Università degli Studi di Torino
Scuola di Dottorato

The Mysteries of Small Exoplanets: Planetary Systems Investigation via Transit Photometry and Doppler Spectroscopy

Elisa Goffo

Università degli Studi di Torino
Scuola di Dottorato

Indirizzo di Fisica ed Astrofisica

The Mysteries of Small Exoplanets: Planetary Systems Investigation via Transit Photometry and Doppler Spectroscopy

Elisa Goffo

Supervisors: Prof. Davide Gandolfi Prof. Artie P. Hatzes

A mio nonno
To my grandpa

Contents

Abstract

The transit and radial velocity methods are two of the most successful techniques for detecting exoplanets. The synergy of both methods gives us access to the orbital geometry and allows us to measure the planetary parameters such as the radius and the mass, leading to the bulk density.

The Kepler space mission - NASA's first space-based survey of transiting planets - has discovered that planets smaller than Neptune are extremely common in our galaxy. Unfortunately, we still know little about their nature, especially in terms of mass and density, which represent the key parameters for studying the planets' composition and internal structures. Precise mass determinations through ground-based Doppler spectroscopy have only been possible for a few Kepler planets, mainly due to the faintness of the stars observed by the Kepler telescope. Launched in 2018, NASA's TESS space mission is observing the light curves of thousands of stars searching for shallow transit signals. Targeting mainly bright stars, TESS is a definite advantage for any radial velocity follow-up program.

In this work, I describe the detection of exoplanets in photometric and spectroscopic measurements, and how to combine the two datasets to determine the fundamental planetary parameters. In addition, I present the results of high-precision RV follow-up observations carried out with the HARPS and CARMENES spectrographs of bright TESS stars ($V \lesssim 11$) hosting transiting planets. The results of the discovery and characterization of planetary systems presented in this work have been and will be published in peer-reviewed journals.

Within this work 6 systems have been investigated providing unprecedented mass and radius determination. This allows us to investigate the internal composition of planets, as well as the formation and evolution history of planetary systems. In particular, the planet GJ 367 b challenges planet formation theories having a ultra high density of 85 % that of the Earth. With these well-characterized systems, this thesis provides a benchmark sample of small exoplanets with high-precision planetary parameters and two promising targets for future atmospheric investigations.

Units

- Solar radius: $\mathrm{R}_\odot = 6.957 \times 10^{10}\,\mathrm{cm}$
- Solar mass: $\mathrm{M}_\odot = 1.988 \times 10^{33}\,\mathrm{g}$
- Solar effective temperature: $\mathrm{T}_{\mathrm{eff}\odot} = 5772\,\mathrm{K}$
- Earth radius: $\mathrm{R}_\oplus = 6.3781 \times 10^{8}\,\mathrm{cm}$
- Earth mass: $\mathrm{M}_\oplus = 5.971 \times 10^{27}\,\mathrm{g}$
- Earth density: $\rho_\oplus = 5.5\,\mathrm{g\,cm^{-3}}$
- Jupiter radius: $\mathrm{R}_\mathrm{J} = 7.1492 \times 10^{9}\,\mathrm{cm} \approx 11.2\ \mathrm{R}_\oplus$
- Jupiter mass: $\mathrm{M}_\mathrm{J} = 1.898 \times 10^{30}\,\mathrm{g} \approx 317\ \mathrm{M}_\oplus$
- Jupiter density: $\rho_\mathrm{J} = 1.33\,\mathrm{g\,cm^{-3}}$
- Astronomical Unit: $1\,\mathrm{au} = 1.496\ \times 10^{13}\,\mathrm{cm}$
- Gravitational constant: $\mathrm{G} = 6.67408\ (\pm 0.00031) \times 10^{11}\,\mathrm{m^3\,kg^1\,s^2}$

Chapter 1

Introduction

Exoplanets in our galaxy have a wide variety of orbital configurations and compositions. They can be inflated gas giants larger than Jupiter or rocky worlds smaller than Mercury and denser than iron. Most of the known planets are larger than Earth but smaller than Neptune – and have no counterpart in our Solar System. In the last decades of exoplanetary research we have discovered a population of rather exotic exoplanets: planets with equilibrium temperatures up to $\sim$4000 K (e.g., Kelt-9 b; Gaudi et al. 2017); "icy planets" (e.g., OGLE-2005-blg-390L b; Beaulieu et al. 2006); "lava worlds" (e.g., 55 Cancri e, Kepler 78 b; Demory et al. 2016; Sanchis-Ojeda et al. 2013); planets denser than iron (e.g., GJ 367 b; Lam et al. 2021; Goffo et al. 2023); or "ocean worlds" (e.g., GJ 1214 b; Charbonneau et al. 2009). Exoplanets that can orbit their stars so closely that a "year" lasts only a few days or even hours, or planets around binaries, are no longer just science fiction but reality.

Our galaxy contains 250 ± 150 billion stars, including our Sun. Most likely each of these stars hosts not just one planet, but a multi-planet system. In the past two decades we have developed exquisite detection methods, most of which measure the effects that an orbiting planet exerts on its host star. The rate of exoplanet discoveries has increased dramatically in recent years due to the development of high-precision techniques with both ground– and space–based facilities.

1.1 What is an exoplanet?

1.1.1 Definition

Before understanding what an exoplanet, also known as extrasolar planet, is, we should start with the definition of a planet. The International Astronomical Union (IAU) agreed on the first official definition of a planet in 2006 (Binzel 2006). They defined a planet as a celestial object that:

1. orbits around the Sun;
2. has sufficient mass for its self-gravity to overcome rigid body forces so that it assumes a hydrostatic equilibrium (nearly round) shape;
3. has cleared the neighborhood around its orbit.

By that definition, our Solar System has eight planets – unfortunately for Pluto.

In 2018 the IAU general assembly established a more general definition of planets, including this time exoplanets in the definition. As discussed in Lecavelier des Etangs & Lissauer (2022), planets are defined as objects:

1. that orbit stars, brown dwarfs or stellar remnants;
2. that have true masses below the limiting mass for thermonuclear fusion of deuterium (currently calculated to be 13 M_J for objects of solar metallicity);
3. that have a mass ratio with the central object below the Lagrangian point instability L4/L5 ($M/M_\mathrm{central} \lesssim 1/25$), where M is the object's mass, no matter how they formed.

Additionally, the extrasolar object must satisfy the hydrostatic equilibrium criteria from the first definition of planet. Free-floating objects in young star clusters with estimated masses below the deuterium-burning threshold are referred to as sub-brown dwarfs. If there is evidence that they formed as planets and were subsequently dynamically ejected from the original host system, they are referred to as free-floating planets (FFPs).

1.1.2 Planet types

Exoplanet discoveries of the last thirty years have unveiled different population of planetary objects. In the exoplanet field, planets are usually categorized by their radius (Borucki et al. 2011) and their mass (Stevens & Gaudi 2013). The boundaries are not strict and it is often difficult to distinguish between different populations. Exoplanets can be classified into the following types:

- **Earth-like** or **terrestrial planets** ($R_\mathrm{p} \lessapprox 1.25\,R_\oplus$, $M_\mathrm{p} \lessapprox 2\,M_\oplus$) have an Earth-like composition, i.e., a metallic core and a silicate mantle, as Venus and Earth, and may have secondary atmospheres.

- **Super-Earths** and **mini-Neptunes** have sizes between that of Earth and that of Neptune ($R_\mathrm{p} \approx 1.25 - 4\,R_\oplus$, $M_\mathrm{p} \approx 2 - 10\,M_\oplus$). This class of planets is absent from the Solar System, although it dominates among the discovered exoplanets.

- **Neptunian planets** ($R_\mathrm{p} \approx 4 - 6\,R_\oplus$, $M_\mathrm{p} \approx 10 - 100\,M_\oplus$), similar to Uranus and Neptune, have significant ices, rocks, as well as hydrogen and helium contents.

- **Gas giant planets** ($R_\mathrm{p} \approx 6 - 15\,R_\oplus$, $M_\mathrm{p} \approx 0.3 - 13\,M_\mathrm{J}$), often referred to as Jupiters or Jovians, are mostly composed of hydrogen and helium ($> 50\%$ H-He of their mass).

1.1.3 Nomenclature

The scientific nomenclature for exoplanets usually consists of two parts. The first part can be an astronomical catalog name for the exoplanet's host star, or the scientific instrument or project that discovered the exoplanet. The second part is a lowercase letter[1]. The letter indicates the order of the planet's discovery (the first discovered is designated with the letter b; the second with c; and

---

[1] `https://www.iau.org/public/themes/naming_exoplanets/`.

so on for every subsequent planet found in the system). If an exoplanet orbits a binary or multiple system, its designation can be, e.g., Kepler-18(AB)b, where A indicates the primary star, and B the secondary one.

1.2 Brief history of exoplanet's discoveries

Historically, a large number of speculations were done on the presence of planets around other stars. The first claimed discoveries were made by Strand (1943) and Reuyl & Holmberg (1943), based on the perturbations in the astrometric motions of the stars 61 Cygni and 70 Ophiuchi. Later van de Kamp (1969) claimed the detection of two planets orbiting Barnards star. Although all these claims were later rejected, they sparked interest in the astronomy community at the time, opening the way for exoplanets' discovery. As a method to discover exoplanets, Struve (1952) proposed to detect the periodic variations of the radial velocity of the star due to the presence of an orbiting planetary companion using the Doppler effect. In the following years, several radial velocity monitoring surveys started. Among them, Campbell et al. (1988) wrote about the tentative detection of Jupiter-like companions around seven stars, using radial velocities variations. One of them, γ Cephei, was later confirmed by Hatzes et al. (2003) to host a gas-giant planet orbiting every 2.5 years.

But it was in the nineties when we had the first confirmed detections of extrasolar planets. With big surprise (and scepticism) from the community Wolszczan & Frail (1992) discovered three Earth-mass planets orbiting the millisecond pulsar PSR B1 257+12 by measuring the nanosecond variations in the timing of its pulses. Three years later Mayor & Queloz (1995) announced the discovery of 51 Pegasi b, the first Jovian-mass planet orbiting a Sun-like star. The discovery was a clear breakthrough for the field. 51 Pegasi b was detected by observing the planet-induced variations in the radial velocity of the host star. In addition, the discovery of a giant planet with a mass of $\sim$0.5 $\mathrm{M_J}$ orbiting the star in 4.2 days surprised the astronomers. All knowledge was based on the only example they had, which was the Solar System. The presence of a Jupiter-like mass planet so close to its host star was therefore impossible for the formation theories of the time. For this breakthrough discovery, Michel Mayor and Didier Queloz received the Nobel Prize in Physics in 2019. Since than, more than 5600 exoplanet have been discovered[2], showing an incredibly broad diversity of strange extrasolar worlds.

1.3 How to discover an exoplanet

Direct observations of an exoplanet are challenging and in most cases we cannot directly see a planet orbiting its host star. The planet's light is hidden in star's light and the angular separation between the two objects is often smaller than the resolution of our current facilities. In order to detect and study exoplanets, we must rely on indirect methods of detection. Exoplanets can be detected with different techniques. Two of the most successful ones are

---

[2] As of April 2024. See, e.g., the Nasa Exoplanet Archive (`https://exoplanetarchive.ipac.caltech.edu`) or the Extrasolar Planets Encyclopaedia (`http://www.exoplanet.eu/`).

the *radial velocity* (RV) and the *transit* methods. Both techniques have been extensively utilized in this thesis. These techniques allow us to derive the fundamental planetary parameters, such as mass, radius, and orbital period. Additionally, we can investigate exoplanets and their host system architectures.

Figure 1.1 shows the planets discovered with different observational techniques in the mass-period and radius-period diagrams. The radial velocity method and the transit methods have been so far the most successful ones. Here I will provide a brief introduction to the different detection methods, and later in Chapters 2 and 3 I will dive into the details of the radial velocity and transit methods.

The radial velocity method

The motion of a planet orbiting its star causes the star to wobble dynamically around the star-planet's center of mass. This involves the periodic perturbation of three observable properties of the star: radial velocity, angular position in the sky, and the time of arrival of some periodic reference signal. The radial velocity method measures the motion projected along the line-of-sight of the primary star as it orbits the center of mass of the system.

A measurement of the stellar radial velocity is given by the small Doppler shift in wavelength of the many absorption lines that make up the stars spectrum. The light we receive from the star is slightly shifted towards the blue or red as the star gets pulled towards or away from us (Figure 1.2). In the classical treatment (non-relativistic case), the radial (line-of-sight) component of the velocity of the star is proportional to this wavelength shift:

$$\frac{\Delta\lambda}{\lambda_{\mathrm{em}}} = \frac{\lambda_{\mathrm{obs}} - \lambda_{\mathrm{em}}}{\lambda_{\mathrm{em}}} = \frac{RV}{c} \tag{1.1}$$

where c is the speed of light, λ_{em} is the emitted wavelength, λ_{obs} is the measured one, and $\Delta\lambda$ is the change in wavelength. The radial velocity semi-amplitude, $K_\star$, of the star can be expressed by

$$K_\star = \frac{1}{\sqrt{1-e^2}} \frac{M_{\mathrm{p}} \sin i}{{M_*}^{2/3}} \left(\frac{2\pi G}{P}\right)^{1/3} \tag{1.2}$$

where e is the eccentricity of the orbit, M_{p} and $M_\star$ are the planetary and stellar masses, respectively, i the orbital inclination, i.e., the angle between the orbital angular momentum and the line of sight to the star, P the orbital period, and G the gravitational constant. The stellar mass $M_\star$ can be determined, e.g., combining spectroscopy, parallax, broad-band photometry and evolutionary tracks. Observationally, we can derive the eccentricity e, the orbital period P, and only the planet's minimum mass, i.e., $M_{\mathrm{p}} \sin i$. If the inclination i is unknown, there is no way to find the true mass of the planet via the RV method. The full derivation of this equation can be found in, e.g., Perryman (2011); Hatzes (2016, 2019). For the sake of completeness, I will give more details in Chapter 2.

According to the equation 1.2, more massive planets result in larger and more easily detected RV semi-amplitudes. Close-in planets are also easier to detect: their orbital periods are shorter (Kepler's third law) and can therefore

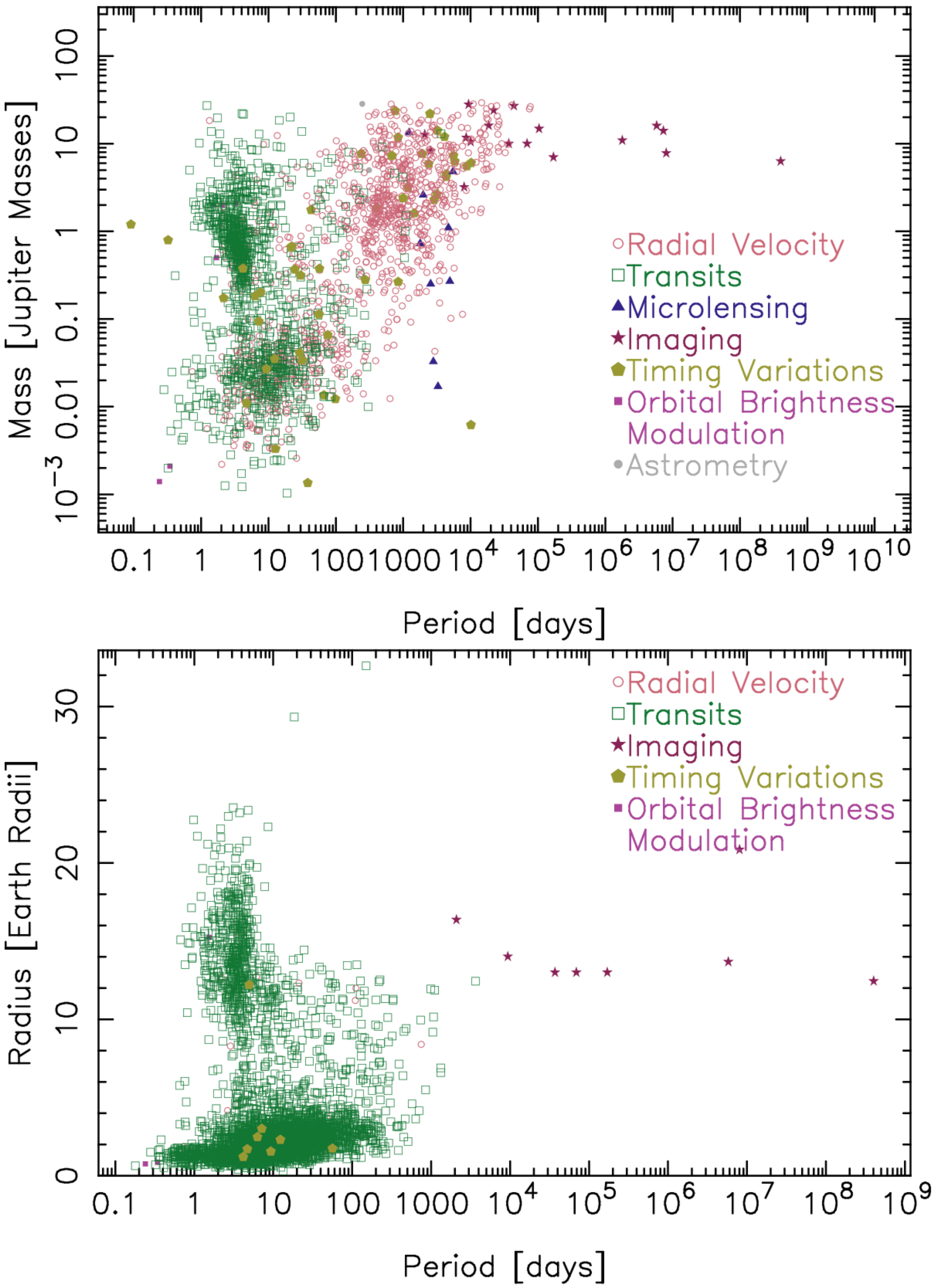

Figure 1.1: *Top*: The period-mass diagram of known exoplanets with mass measurement. Different colors represent different detection methods. A large number of the discovered planets are not shown here due to the fact that many of the transiting planets were discovered by the Kepler mission, which observed stars too faint to follow-up with Doppler spectroscopy and therefore have no mass estimates. Note that for planets detected via the RV method the mass here refers to the minimum mass. *Bottom*: The period-radius diagram of known exoplanets. Different colors refer to different detection methods. From Nasa Exoplanet Archive, as of 12 April 2024.

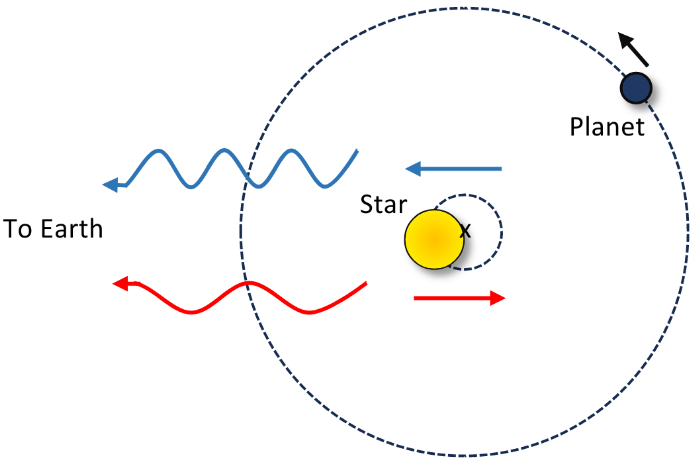

Figure 1.2: The radial-velocity method. As a planet orbits its host star, the star wobbles around the common center of mass. As a result, the starlight received by an observer is Doppler shifted.

be more quickly and easily detected. In our Solar System, Jupiter orbits the Sun at an orbital distance of 5.2 au and induces an 11.2 $\mathrm{m\,s^{-1}}$ stellar reflex motion with a period of 11.9 years. If Jupiter was instead in a 3-day orbit, the induced RV amplitude would be $\sim$150 $\mathrm{m\,s^{1}}$. The Earth at 1 au causes a reflex motion of the Sun of just 10 $\mathrm{cm\,s^{-1}}$, which increases to 0.6 $\mathrm{m\,s^{1}}$ if we could move the Earth to an orbit of just 1 day. To detect the RV of a star induced by the presence of a planet we therefore need instruments with a precision of 0.01–100 $\mathrm{m\,s^{1}}$, depending on the mass and period of the planet we are trying to detect. The majority of planets detected with the RV method have high masses due to the detection limitations, as shown in Figure 1.1.

In the last decades the precision of high-resolution spectrographs, data reduction pipelines, and modeling techniques have improved dramatically, allowing us to detect low-mass planets at more distant orbits from their host star. Instruments like HARPS and HARPS-N (Mayor et al. 2003; Cosentino et al. 2012) reach a precision of $\sim$1 $\mathrm{m\,s^{-1}}$. With a precision of $\sim$10 $\mathrm{cm\,s^{-1}}$, the recently commissioned ESPRESSO spectrograph (Pepe et al. 2010, 2021) will open up the doors to the detection of Earth-like mass planets in Earth-like orbits.

Figure 1.3 shows the evolution of the radial velocity measurement uncertainty as a function of time. In the 1960s we could measure the Doppler reflex motion of a star with a precision of $\sim$1 $\mathrm{km\,s^{-1}}$. Amazingly, the precision improved quickly with time, reaching the sub-$\mathrm{m\,s^{-1}}$ level in recent years. The horizontal red line in Figure 1.3 highlights the precision that was possible to achieve in the mid-1980s, when in fact the first exoplanets were discovered (Hatzes 2019).

The transit method

A planetary transit is a special case of eclipse, i.e., when a planet passes in front of its host star obscuring part of its light. During the transit, the planet occults a fraction of the stellar disk causing a small decrease in the stellar flux.

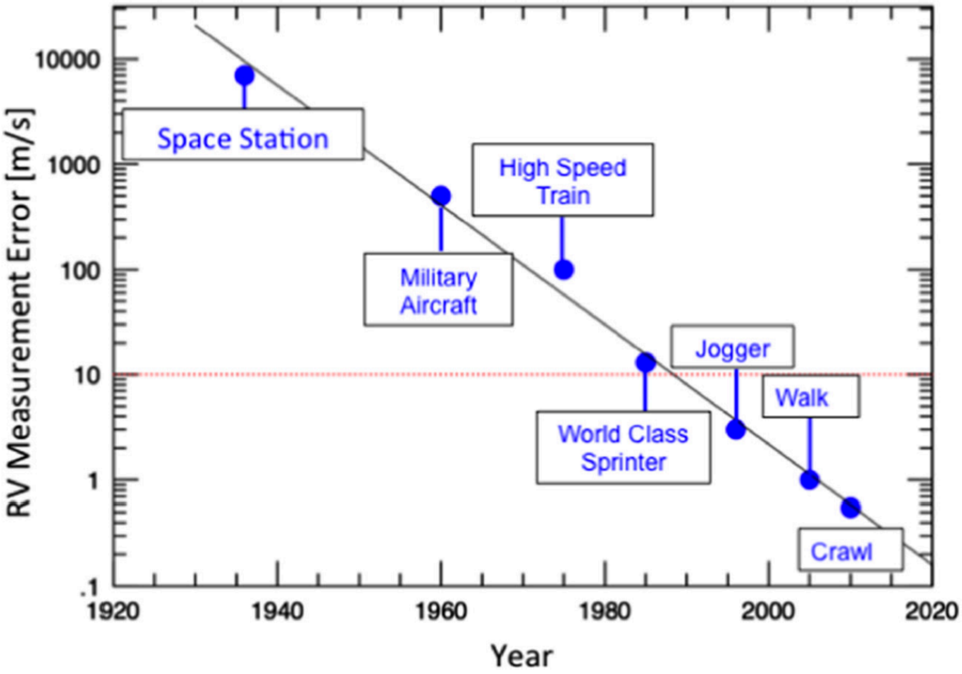

Figure 1.3: The evolution of the radial velocity measurement error as a function of years. The horizontal red line marks the precision that was possible to achieve in the mid-1980s, when in fact the first exoplanets were discovered (Hatzes 2019).

If the orbit has an inclination close to 90°, the presence of a planet can be inferred by detecting the periodic dip in the starlight caused by the passage of the planet in front of the stellar disk (Figure 1.4). The photometric transits provides one of the fundamental parameter of the planet, i.e., its radius R_p. The relative variation of the stellar flux during a planetary transit is indeed proportional to the planet-to-star radius ratio $R_\mathrm{p}/R_\star$ squared (Cameron 2016):

$$\frac{\triangle f}{f} \simeq \left(\frac{R_\mathrm{p}}{R_\star}\right)^2 = 0.0105 \left(\frac{R_\mathrm{p}}{R_\mathrm{J}}\right)^2 \left(\frac{R_\star}{R_\odot}\right)^{-2} . \tag{1.3}$$

The stellar radius $R_\star$ can be determined via, e.g., spectroscopy combined with parallax and broad-band photometry. The probability of observing a transit for any given star, seen in a random direction and at a random time, is extremely small (see Chapter 3). A transit could be visible if the portion of the celestial sphere swept out by the planet's shadow is in the line of sight of an observer on Earth (Cameron 2016). Assuming $R_\mathrm{p} \ll R_\star$, the probability of a transit to happen is

$$p_{tr} \approx 0.0046 \left(\frac{R_\star}{R_\odot}\right) \left(\frac{1\,\mathrm{au}}{a}\right) , \tag{1.4}$$

where a is the semi-major axis of the orbit of the planet relative to the star. This translates into a probability of ∼0.46% to observe a transiting planet at 1 au orbiting a Sun-like star. Taking the distance of Jupiter from the Sun (5.2 au) the probability drops to ∼0.09%, while for short-period planets ($\mathrm{P} \lesssim 10$ days) the transit probability increases up to ∼5-20%.

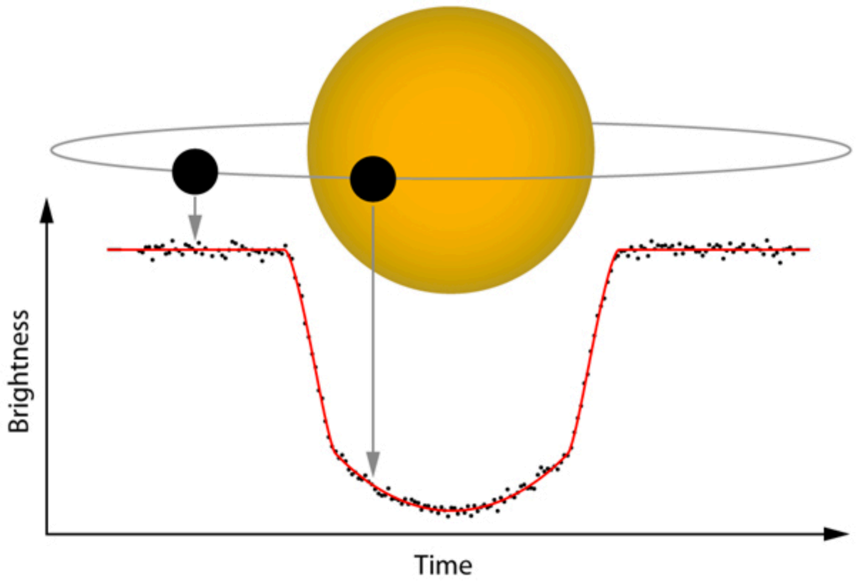

Figure 1.4: The planet obscures the stellar disk when it passes in front of it, thereby reducing the total brightness observed (Credit: ESA).

The first planetary transits were observed by Henry et al. (2000) and Charbonneau et al. (2000) from the photometric monitoring of the known radial-velocity planet HD 209458 b. The authors observed transits with a duration of 2.5 hours and a depth of 1.5%, which occurred at the timings predicted based on the radial velocity ephemeris. These transit observations gave the first confirmation that Jupiter-mass planets in close orbits about their host stars have radii and densities comparable to Jupiter and Saturn, the two gas-giant planets of our Solar System. Since then, the number of known transiting planets has grown dramatically in recent years thanks to both ground- (e.g., Pollacco et al. 2006) and space-based transit surveys (e.g., Baglin et al. 2009; Borucki et al. 2010; Ricker et al. 2015), making the transit technique the most prolific method to detect exoplanets.

The transit method provides also the inclination i of the orbit and the true planetary mass M_p, if the minimum mass $M_\mathrm{p} \sin i$ is known via Doppler monitoring. Combining transit and RV observations together yields a complete set of planetary and orbital parameters. The bulk density of the planet can then be inferred from its mass and radius, allowing us to make a first step towards understanding its internal structure and composition. More insights about the transit method can be found in Chapter 3.

Microlensing

Gravitational microlensing was predicted by Albert Einstein as a consequence of his theory of general relativity. Massive objects can substantially bend light around them. The light from a distant star within the Galaxy traveling towards the Earth can be bent around a foreground aligned star which acts as a lens. In the case of an exoplanetary system (star and planet), the system acts as a

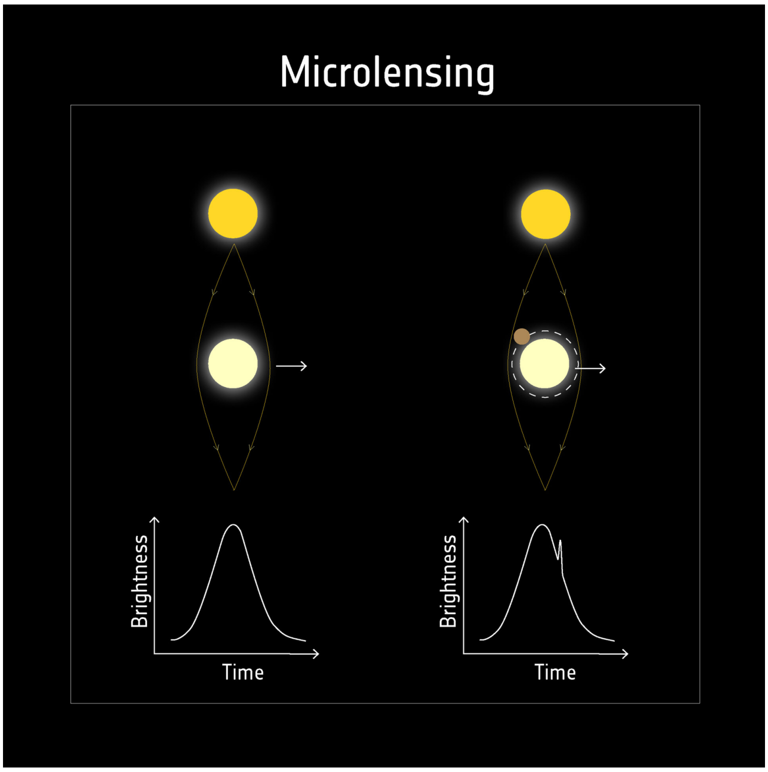

Figure 1.5: Microlensing relies on the chance alignment of two stars with an observer. As one star crosses behind the other, the closer star acts like a lens, bending the light so that the brightness smoothly increases and decreases. If a planet is present around the closer star, its gravity will also bend the light stream, causing a spike. Image credit: ESA.

multiple lens. The magnification varies over time as the alignment geometry changes. This intensity variation over time allows the event to be recognized as a microlensing event (Figure 1.5). Careful monitoring of the light curve as the alignment changes over several hours allows detection of the additional lensing effects of a companion planet. Mao & Paczynski (1991) were the first to propose a search for planetary systems by observing their gravitational lensing effects on the Galactic bulge stars. The first microlensing planet was revealed by Bond et al. (2004). Microlensing is extremely sensitive and could allow us to detect very small planets, although it has one main disadvantage: it is a rare event that will not be repeated.

Imaging

Direct imaging generally refers to the detection of an image of the exoplanet. This may be either in the reflected light from the parent star, in the visible, or through its own thermal emission, in the infrared (Boccaletti 2011). As described by Perryman (2011), the prospects for imaging are high in the case of: (a) nearby young stars (10 − 100 Myr, $d < 100$ pc), around which planets are still forming, warm, and hence self-luminous. Evolutionary models predict young planet luminosities higher than for mature planets by several orders of magnitude depending on mass and age; (b) stars with known planets, for which the increasing temporal baseline of radial velocity surveys are identifying long-period trends suggestive of the existence of high-mass giant planets in

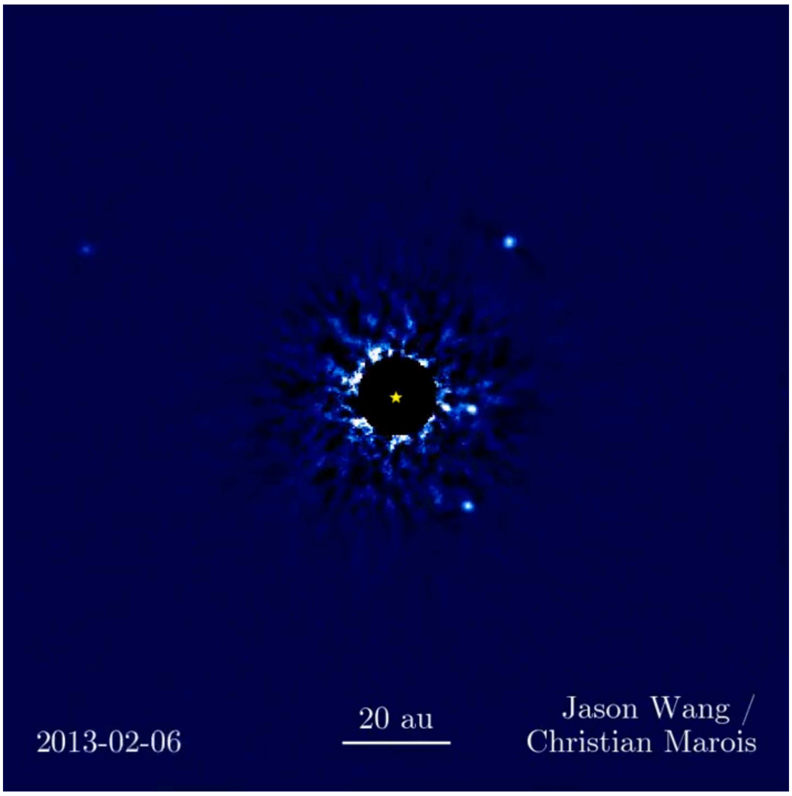

Figure 1.6: Using the Keck telescopes, Marois et al. (2008, 2010) announced the detection of 4 planets orbiting the star HR 8799. HR 8799 is a young (∼30 Myr) star, and the orbiting planets still retain some of the heat of their formation, which is observed at infrared wavelengths.

wide-separation orbits; (c) very close stars, $d < 5$ pc, in which a shorter-period giant planet with significant reflected light might be detected because of its relatively large angular separation from the star due to its proximity. As a show case, Figure 1.6 presents the remarkable result of direct imaging of the four-planet system orbiting the young (∼30 Myr), nearby (∼41 pc) star HR 8799.

Astrometry

As defined in Perryman (2011), astrometry measures the positions and proper motions of solar system bodies, stars within the Galaxy, and also galaxies and galaxy clusters within the Universe. As for exoplanets detection, astrometry aims to determine the transverse component of the host star's displacement due to the gravitational pull of an orbiting planet. If a star hosts a planet, then the gravitational pull of the planet will cause the star itself to move in a tiny orbit around the star-planet's center of mass. As discussed previously, this perturbs periodically the radial velocity and the angular position of the star in the sky. The trajectory of a star orbiting the barycenter of the star-planet system appears projected on the plane of the sky as an ellipse with angular semi-major axis α given by

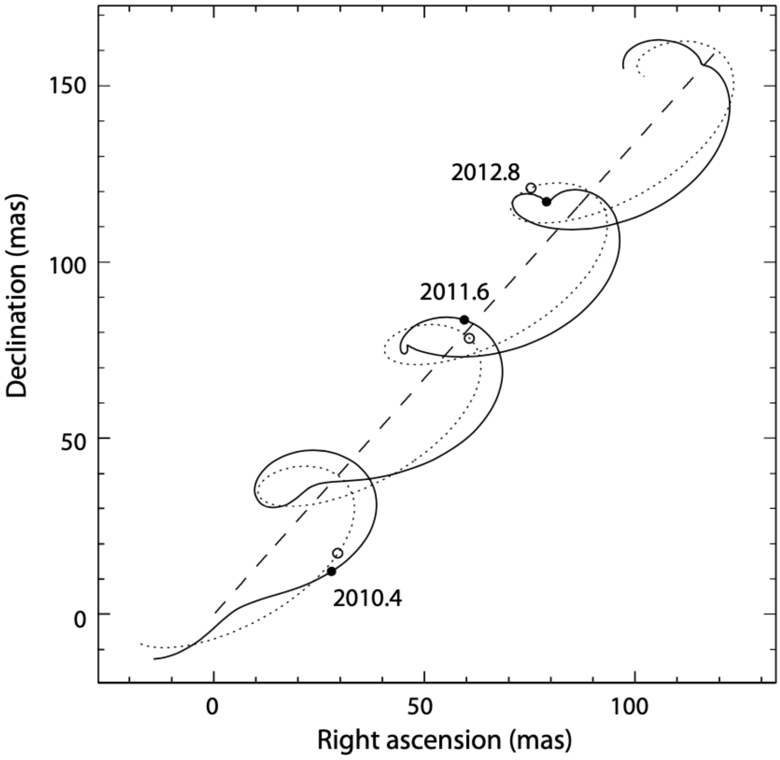

Figure 1.7: Schematic of the path on the sky of a star at d = 50 pc, with a proper motion of $\mu = 50$ mas yr^1, and orbited by a sub-stellar companion of $M_\mathrm{p} = 15\,M_\mathrm{J}$, $e = 0.2$, and $a = 0.6$ au. The straight dashed line shows the systems barycentric motion viewed from the solar system barycentre. The dotted line shows the effect of parallax due to the Earths orbital motion around the Sun (1-year period). The solid line shows the motion of the star as a result of the orbiting planet. The effect is magnified by a factor of 30 for better visibility. Labels indicate (arbitrary) times in years (Perryman 2011).

$$\alpha = \frac{M_\mathrm{p}}{M_\star + M_\mathrm{p}} \frac{a_\mathrm{p}}{d} \simeq \frac{M_\mathrm{p}}{M_\star} \frac{a_\mathrm{p}}{d} \tag{1.5}$$

where a_p is the semi-major axis of the planet orbit relative to the star in au and d is the distance in pc.

This astrometric signature α is the observable for astrometric planet detection, and is proportional to both M_p and a_p, and inversely to d. In fact, astrometry is particularly sensitive to long orbital periods ($P \gtrapprox 1$ yr). This requires, however, observations lasting several years. The method aims to identify an orbiting planet on top of the two other classical astrometric effects: the linear path of the systems barycentre, i.e., its proper motion, combined with the yearly motion, i.e., its parallax, resulting from the Earths orbital motion around the Sun (Figure 1.7).

1.4 Objective of the thesis

Space-based transit surveys have dramatically improved our knowledge of exoplanets, (e.g., CoRoT, *Kepler*, K2; Baglin et al. 2006; Borucki et al. 2010;

Howell et al. 2014), leading us to the new era of comparative planetology in which our Solar System can finally be put into a broader context. The study of transiting planets allows us to measure their radius via transit photometry and their mass via Doppler spectroscopy. The derived bulk density allows us to investigate the internal structure and composition of planets – e.g., by comparing their positions on a mass-radius diagram with theoretical models – and distinguish between gas giants ($\rho \approx 1\,\mathrm{g\,cm^{-3}}$), ice giants ($\rho \approx 1$–$3\,\mathrm{g\,cm^{-3}}$), and terrestrial worlds with or without atmospheric envelopes ($\rho > 3\ \mathrm{g\,cm^{-3}}$).

Radial velocity follow-up observations of transiting planet systems can unveil the architecture of planetary systems, by discovering other planetary companions. The mean density and orbital architecture also give us important insights into the formation and evolution of planets. However, mass determinations with a precision better than 20–25 % are lacking for a large number of transiting planets.

NASA's *Kepler* space mission has unveiled a cornucopia of small planets that have no counterpart in the Solar System. About 25 % of Sun-like stars in our Galaxy host super-Earths and mini-Neptunes with orbital periods shorter than 100 days (see, e.g., Batalha et al. 2013a; Marcy et al. 2014; Silburt et al. 2015; Mulders et al. 2016). Although its exquisite photometry has given us access to the small-radius domain, our knowledge on the composition of super-Earths and sub-Neptunes is still quite limited. Mass determinations with a precision better than 20–25 %, which would allow us to distinguish between different internal compositions, have only been possible for a few dozen *Kepler* small planets. This is because of the small RV variation induced by such planets and the faintness of most *Kepler* host stars ($\mathrm{V} > 13$).

Precise masses and mean densities are especially important for small planets, since a wide diversity of compositions are possible a priori, including terrestrial planets with thin atmospheres and rocky cores with thick envelopes of H_2O, NH_3, H, and He. The Transiting Exoplanet Survey Satellite (TESS) is searching the entire sky for small transiting planets around nearby bright stars ($\mathrm{V} < 11$), which are amenable to mass determination via high-precision Doppler spectroscopy. TESS allows us to detect close-in planets around bright stars to perform detailed characterizations of the planets and their atmospheres. In this regard, high-resolution spectrographs and large numbers of measurements enable us to improve the precision of mass estimation.

The main goal of this thesis work is to combine space-based transit photometry with high-precision RV measurements collected with high-resolution spectrographs to characterize small transiting planets in terms of mass, radius, and bulk density. I focused on the RV follow-up of stars observed by TESS to spectroscopically confirm the planetary nature of the transit signals detected by TESS, measure the mass of the transiting planets, and possibly detect additional planets in the systems. Valuable insights into the planetary system formation and evolution can be gained by determining the internal composition of the planets and the architecture of the systems they belong to.

In details,

- I carried out RV follow-up observations of TESS planet candidates with high-precision spectrographs.

- I used robust data analysis tools.
- I performed joint data analysis once the photometric and RV data have been acquired.
- I published the results of my analyses on the systems GJ 367 and TOI-4438 (Sections 6 and 7), in high-impact factor, peer-reviewed journals.

The thesis is structured as follows: in Chapters 2 and 3 I present in detail the two main detection methods – radial velocity and transit method – which are the basis of this work. In Chapter 4 I present the space telescope TESS and the high-resolution spectrographs HARPS and CARMENES, along with the data used in this thesis; in Chapter 5 I describe the data analysis and the tools I used to determine the system parameters. The results of my first author papers are presented in Chapters 6 and 7, whereas my contributions in other refereed papers are provided in Chapter 8. The conclusions are given in Chapter 9.

Chapter 2

The radial velocity method

The radial velocity method (also known as Doppler method) has been the foundation for the research field of exoplanets, providing a great number of discoveries of planets around stars other than our Sun (Figure 1.1). With this method we are able to determine the minimum mass of an exoplanet ($M_\mathrm{p} \sin i$). If we also known the its radius (R_p) and the inclination of its orbit (i) via transit photometry, we can determine the planet bulk density (ρ_p) and investigate its internal structure and composition.

The basic principle behind the Doppler method consists in measuring the change in the stellar velocity component along the line of sight – also known as radial velocity (RV) – as the star revolves around the center of mass of the system. This velocity is measured via the Doppler effect, i.e., the small systematic shift in wavelength of the spectral lines that make up the stellar spectrum.

Following Perryman (2011), if, in the observer's reference frame, the source moves away with velocity v at an angle θ relative to the direction from observer to source, the change in wavelength

$$\triangle\lambda = \lambda_\mathrm{obs} - \lambda_\mathrm{em}, \tag{2.1}$$

is related to the velocity by the expression for the relativistic Doppler shift

$$\lambda_\mathrm{obs} = \lambda_\mathrm{em} \frac{1 + \beta \cos\theta}{(1 - \beta^2)^{1/2}}, \tag{2.2}$$

where λ_obs, and λ_em are the observed and emitted wavelengths, respectively, and $\beta = v/c$. For $v \ll c$ and $\theta \ll 90^\circ$, we can rewrite the expression 2.2 as

$$RV = v\,\cos\theta \approx \left(\frac{\triangle\lambda}{\lambda_\mathrm{em}}\right) c. \tag{2.3}$$

By convention, radial velocities away from us (redshifts) are positive; those towards us (blueshifts), negative.

For high-precision RV measurements, high-resolution échelle spectrographs with resolving power of $R \equiv \lambda/\triangle\lambda \approx 50\,000$–$150\,000$ and operating in the optical (400–700 nm) are typically used. In such spectrographs many diffraction orders are cross dispersed and recorded simultaneously on charge-coupled devices (CCDs), providing a large number of resolved absorption lines.

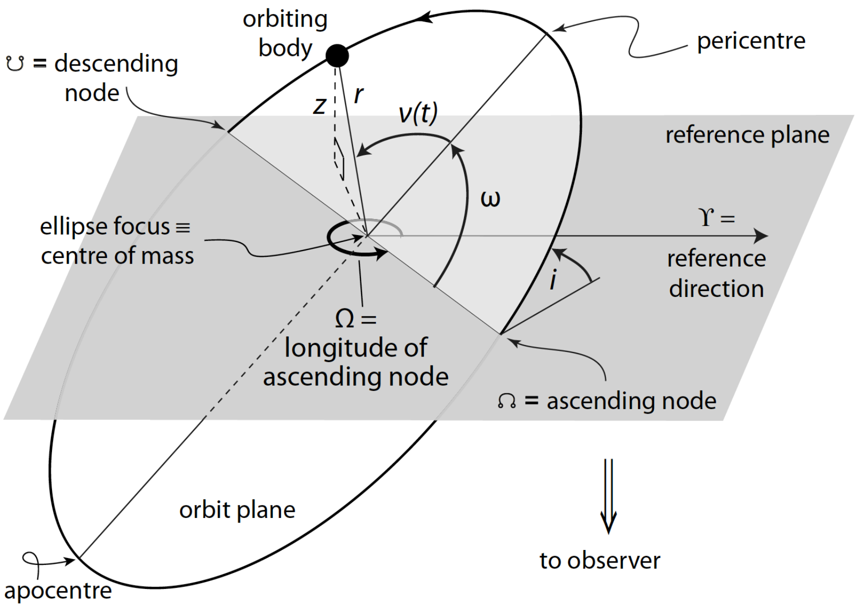

Figure 2.1: The elements of a Keplerian orbit (Perryman 2011).

2.1 Orbital parameters

Following Perryman (2011) and Hatzes (2019), the basic reference elements of a Keplerian orbit are (see Figure 2.1):

- *Reference plane*: the plane tangent to the celestial sphere at the position of the star. This is the so-called plane of the sky.
- *Reference direction*: the direction on the reference plane pointing towards the Vernal Equinox point ♈, i.e., the point on the ecliptic where the Sun crosses from the southern celestial hemisphere to the northern. The point ♈ lies in the intersection between the equatorial plane of the Earth and the ecliptic plane (i.e., the plane that contains the orbit of the Earth around the Sun).
- *Orbital plane*: the plane of the planetary and stellar orbits, which forms the angle i with respect to the reference plane.
- *Line of nodes*: the line defined by the intersection of the orbital plane with the reference plane.
- *Ascending node*: the point on the line of nodes where the planet crosses the reference plane while moving away from the observer.
- *Descending node*: the point on the line of nodes where the planet crosses the reference plane while moving towards the observer.
- *Periastron* (resp. *Apastron*): the point at which the planet is closest (resp. farthest) to (resp. from) its host star.

A Keplerian orbit is described by seven parameters:

- a: the semi-major axis, which defines defines the “size” of the orbit. It is the semi-distance between the periastron and apastron along the long axis of the elliptical orbit.

- e: the eccentricity, which describes the amount of “ellipticity” in the orbit. It is defined as $e = c/a$, where c is the distance between the centre of the ellipse and one of its foci, and a is the semi-major axis. For an elliptical orbit $0 < e < 1$. For a circular orbit $e = 0$. The eccentricity e describes the shape of the orbit and how much it is elongated compared to a circumference.

- Ω: the longitude of the ascending node, i.e., the angle, measured on the plane of the sky and whose vertex is at the star, between the direction of the Vernal Equinox point ♈ and the direction of the ascending node. It defines the orientation of the orbit in the plane of the sky and can assume any values in the range $0 \leq \Omega < 360°$.

- ω: the argument of periastron. Measured on the orbital plane and with its vertex at the star, the argument of periastron in the angle between the direction towards the ascending node and the semi-major axis containing the periastron. It defines the orientation of the orbit on the orbital plane and can assume any value in the range $0 \leq \omega < 360°$. For a circular orbit the argument of periastron of a star is conventionally set to 90°.

- i: the orbit inclination is the angle between the orbital plane and the plane of the sky. Alternatively, it can be defined as the angle between the angular momentum vector and the line of sight to the system. If $i = 0°$ the orbit is seen face-on, i.e., tangential to the celestial sphere. If $i = 90°$ the orbit is seen edge-on.

- P: the orbital period, that is the time taken by the planet and the star to complete one orbit.

- t_{p}: the time (epoch) of periastron passage.

Time-series radial velocity measurements can determine all of these parameters, except for two, namely, the longitude of the ascending node Ω and the orbit inclination i. While Ω is irrelevant for the mass determination, the orbital inclination is important. Since we measure only one component of the stellar motion, we can only get a lower limit on the mass of the planet, i.e., the mass times the sine of the orbital inclination $M_{\mathrm{p}} \sin i$, also known as the minimum mass.

For Keplerian orbits, star and planet move about the center of mass, or barycenter, in elliptical orbits with the center of mass at one focus of the ellipse. As shown in Figure 2.2, a planet moving by a small angle $d\nu$ sweeps out an area $\frac{1}{2}r^2 d\nu$ in a time dt. The *true anomaly* ν is an angular parameter that defines the position of a body moving along a Keplerian orbit, i.e., the angle between the direction of the periastron and the current position of the body as measured from the center of mass. Note that the true anomaly is the same for the planet and the star. By Kepler’s second law, $r^2 d\nu/dt$ is equal to

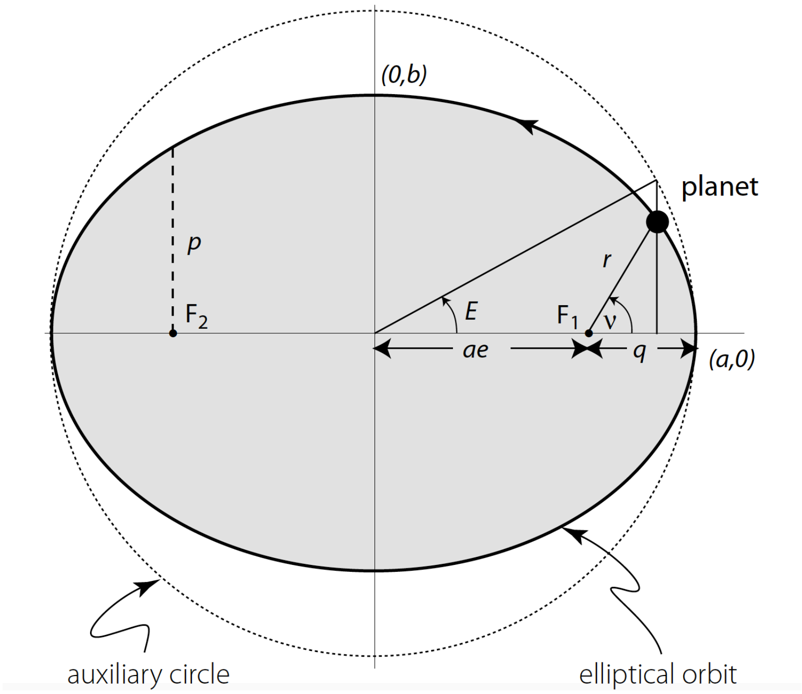

Figure 2.2: Elements of an elliptical orbit (Perryman 2011). The true anomaly, ν, describes points on the orbit. The focus, F1, is the system barycenter.

a constant. The total area of an ellipse is $\pi a^2(1-e^2)^{1/2}$, which is swept by the vector of the orbiting body in a period P. Therefore

$$r^2\frac{d\nu}{dt} = \frac{2\pi\, a^2(1-e^2)^{1/2}}{P} \tag{2.4}$$

We will now refer to the motion of the star and use the subscript "$\star$". The component of $r_\star$ along the line of sight is $z_\star = r_\star \sin(\nu + \omega_\star)\sin i$ (see Figure 2.1). The stellar radial velocity $RV_\star$ is then the projection along the line of sight of the rate of change in $r_\star$:

$$RV_\star = \sin i\left[r_\star \cos(\nu+\omega_\star)\frac{d\nu}{dt} + \sin(\nu+\omega_\star)\frac{dr_\star}{dt}\right] + \gamma \tag{2.5}$$

The above equation refers to the star whose reflected motion we are measuring. The term γ comes from the overall radial velocity of the center of mass and is often called the γ-velocity or the systematic velocity. Since we are only interested in relative velocity measurements for planetary mass determination, the γ-velocity is irrelevant and treated as a mere offset.

Given the equation of an ellipse in polar coordinates

$$r_\star = \frac{a_\star(1-e^2)}{1+e\cos\nu}, \tag{2.6}$$

we can eliminate the time derivatives with Eq. 2.4 and arrive at

$$RV_\star = K_\star\left[\cos(\nu+\omega_\star) + e\cos(\omega_\star)\right] + \gamma, \tag{2.7}$$

where the radial velocity semi-amplitude $K_\star$ is given by

$$K_\star = \frac{2\pi a_\star \sin i}{P(1-e^2)^{1/2}}. \tag{2.8}$$

A radial velocity curve displays the RV time-series, i.e., the RV measurements versus time or orbital phase. The RV curves from Keplerian orbits can have different shapes depending on the eccentricity e and the view angle from the Earth. Figure 2.3 shows four examples of Keplerian orbits. A circular orbit (top left panel) is a sine RV curve. The RV curve changes into a step-like function with higher eccentricities. It is not only eccentricity e that affects the shape of the RV curve, but also the argument of periastron $\omega_\star$. The shape can look significantly different for the same eccentricity, but different values of $\omega_\star$ (Figure 2.3, right panels).

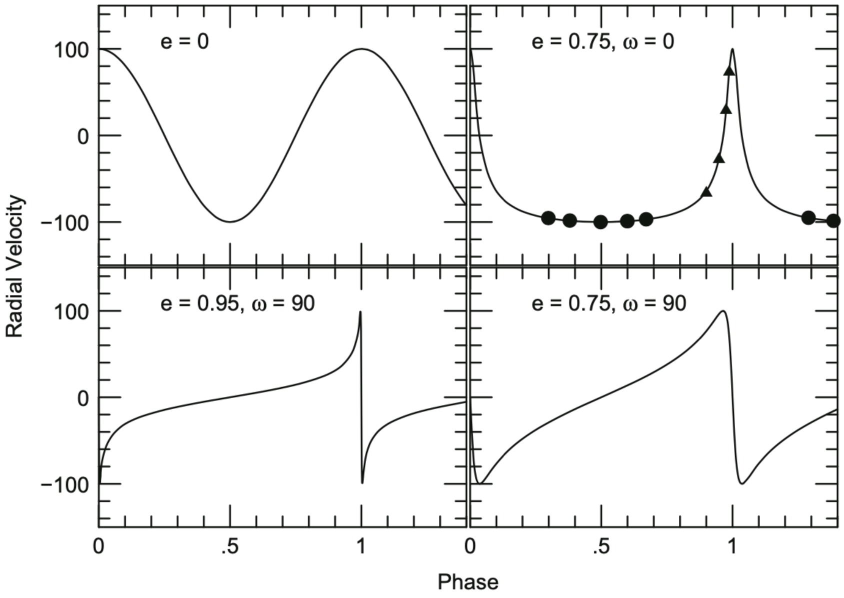

Figure 2.3: Sample RV curves from Keplerian orbits (Hatzes 2016). *Top left:* A circular orbit. *Bottom left:* An eccentric orbit with $e = 0.95$ and $\omega_\star = 90$. *Top right:* An eccentric orbit with $e = 0.75$ and $\omega_\star = 0$. *Bottom right:* Orbit with the same eccentricity but with $\omega_\star = 90$. Note how sparse RV measurements of a star with a planet in an eccentric orbit can have variations that look constant (dots) or mimic a binary companion (triangles).

2.2 The mass function

The Doppler reflex motion of the host star is in general the only observable, because of the small planet-to-star flux ratio ($<10^{-5}$). Radial velocity observations covering all orbital phases are able to measure the orbital period P, the eccentricity e, and the RV semi-amplitude of the host star $K_\star$. From these parameters it is possible to derive the planetary mass through the so-called *mass function*.

Kepler's third law is given by

$$P^2 = \frac{4\pi^2 a^3}{G(M_\star + M_\mathrm{p})} = \frac{4\pi^2 (a_\mathrm{p} + a_\star)^3}{G(M_\star + M_\mathrm{p})}, \tag{2.9}$$

where $M_\star$ is the mass of the star, M_p is the mass of the planet, a the semi-major axis of the relative orbit, and $a_\star$ and a_p are the semi-major axes of the stellar and planetary orbits about the center of mass. We can write Kepler's third law (Eq. 2.9) as

$$\frac{G}{4\pi^2}(M_\star + M_\mathrm{p})P^2 = (a_\star + a_\mathrm{p})^3, \tag{2.10}$$

that can be rewritten using $M_\star \times a_\star = M_\mathrm{p} \times a_\mathrm{p}$ as

$$\frac{G}{4\pi^2}(M_\star + M_\mathrm{p})P^2 \sin^3 i = {a_\star}^3 \sin^3 i \left(\frac{M_\star + M_\mathrm{p}}{M_\mathrm{p}}\right)^3. \tag{2.11}$$

From Eq. (2.8) we can solve for $a_\star \sin i$ in terms of $K_\star$, P, and e. After re-arranging we arrive at

$$f(m) = \frac{{M_\mathrm{p}}^3 \sin^3 i}{(M_\star + M_\mathrm{p})^2} = \frac{{K_\star}^3 P (1-e^2)^{3/2}}{2\pi G} \approx \frac{{M_\mathrm{p}}^3 \sin^3 i}{{M_\star}^2}, \tag{2.12}$$

where for the later expression we have used the fact that $M_\star \gg M_\mathrm{p}$ for planetary companions.

Equation 2.12 is known as the *mass function*, $f(m)$. Empirically, it can be derived from the orbital parameters, namely, $K_\star$, P, and e. Since the mass function depends on the stellar mass, in order to get a good measurement of the mass of our planet, we have to know the mass of the star. Our estimate of stellar mass is generally based on spectroscopic parameters and evolutionary tracks. Only in a few cases we know the stellar mass through asteroseismic measurements, or in the case where the planet host star is a component of an astrometric binary in which both stellar components are visible.

It is also important to note that we cannot derive the true mass of the planet, M_p, but only $M_\mathrm{p} \sin i$, where i is the inclination of the angular momentum vector with respect to the line of sight (for an orbit seen edge-on $i = 90^\circ$). The Doppler effect allows us to get only one component of the velocity of the star, i.e., the velocity component along the line of sight. The orbital inclination can only be measured using astrometric measurements, or for transiting planets (see the following Chapter for the relevant equations behind the transit method). In the latter case the orbital inclination must be near 90° even to see a transit.

From Eq. 2.12 and for a circular orbit we can derive that the RV semi-amplitude variation of the star is given by

$$K_\star = 28.4\,\mathrm{m\,s^{-1}} \left(\frac{P}{1\,\mathrm{yr}}\right)^{-1/3} \left(\frac{M_\mathrm{p} \sin i}{M_\mathrm{Jup}}\right) \left(\frac{M_\star}{M_\odot}\right)^{-2/3}, \tag{2.13}$$

where i is the inclination of the orbital angular momentum with respect to the line of sight.

Planet	**Mass** $[M_\oplus]$	**Distance to the star** [au]	**Orbital period**	$K_\star$ $[\mathrm{m\,s^{-1}}]$
Jupiter	317	5.2	12 years	11.0
Jupiter	317	1.0	1 year	28.0
Jupiter	317	0.04	3 days	150.0
Neptune	17	0.2	36 days	5.0
Super-Earth	5	0.2	36 days	1.4
Earth	1	1.0	1 year	0.09

Table 2.1: Radial velocity semi-amplitude variation $K_\star$ (last column) of a Sun-like mass star for different planetary masses (second column), semi-major axes (third column), and orbital periods (fourth column). Here the orbit eccentricity is assumed to be zero, while the inclination $i = 90°$.

Table 2.1 shows the RV semi-amplitudes induced by planets with different masses, semi-major axes or orbital periods on a Sun-like mass star, assuming the orbits are circular $(e = 0)$ and seen edge-on $(i = 90°)$. In order to detect planets with the RV method, exquisite precision and long-term stability are needed. For instance, to discover a Jupiter-like planet with an orbit of a few days, we need a precision of hundreds of $\mathrm{m\,s^{-1}}$. On the other hand, for an Earth analog at 1 au from a Sun-like mass star, a precision of better than 10 $\mathrm{cm\,s^{-1}}$ is required. Figure 2.4 displays this effect.

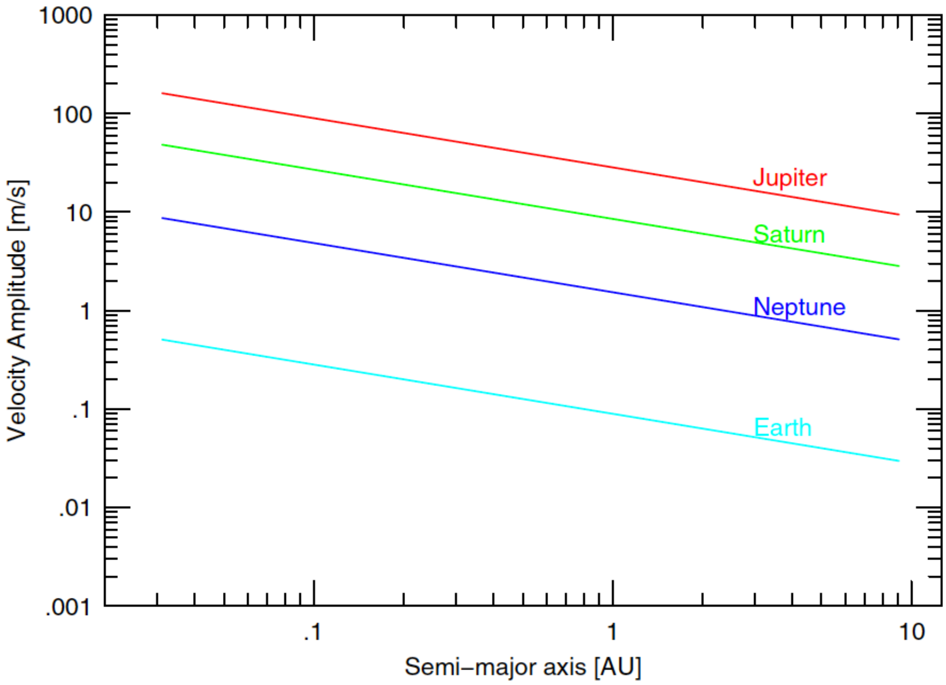

Figure 2.4: The amplitude of the radial velocity variations for a solar-mass star orbited by an Earth, a Neptune, a Saturn, or a Jupiter at different orbital distances (Hatzes 2019).

Chapter 3

The transit method

The transit method has allowed us to discover thousands of transiting planets thank to dedicated ground- (e.g., WASP, HAT-Net, KELT, MASCARA, NGTS) and space-based (e.g., CoRoT, *Kepler*, TESS) transit search surveys. In the following sections, I will present the fundamentals behind the transit method and describe the planetary system parameters that can be inferred from the modelling of a transit light curve.

3.1 Eclipse

An *eclipse* is described as the obscuration of one celestial body by another. When the smaller body (the planet) passes in front of the larger one (the star) we call the eclipse event a *transit*, whereas when the smaller body passes behind the larger one it is an *occultation*, referred often in literature as "secondary eclipse" (see Figure 3.1). If the disk of the smaller body only partially overlaps the disk of the larger one (or if it is not completely hidden), we talk about *grazing* transit (or occultation). We define a transit light curve as the observed stellar flux versus time. During a transit, the observed flux decreases because the planet blocks some of the starlight, producing a dip in the light curve. As the planets dayside comes into view, the flux increases and decreases again each time the planet is occulted by the star.

Transit probability

The probability of observing a transit is geometrically given by the fraction of the celestial sphere swept out by the planets shadow (see Figure 3.2). In the observer's frame of reference, the apparent separation between the planet and the star at mid-transit, i.e., conjunction, is expressed as a dimensionless parameter called the *impact parameter* b, in units of the stellar radius $R_\star$. As presented in Winn et al. (2010) and displayed in Figure 3.3

$$b_{\text{tra}} = \frac{a\cos i}{R_\star}\left(\frac{1-e^2}{1+e\sin\omega}\right), \tag{3.1}$$

$$b_{\text{occ}} = \frac{a\cos i}{R_\star}\left(\frac{1-e^2}{1-e\sin\omega}\right), \tag{3.2}$$

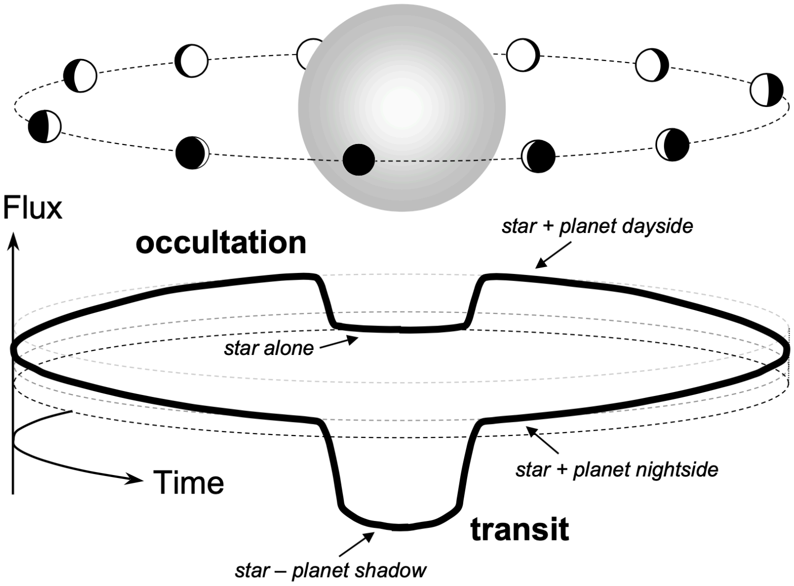

Figure 3.1: Illustration of a transit and an occultation. *Top:* the orbit of the planet around the star. *Bottom:* Its corresponding observed transit light curve. During a transit, the flux drops because the planet blocks a fraction of the starlight. Then the flux rises as the planets dayside comes into view. The flux drops again when the planet is occulted by the star (Winn et al. 2010).

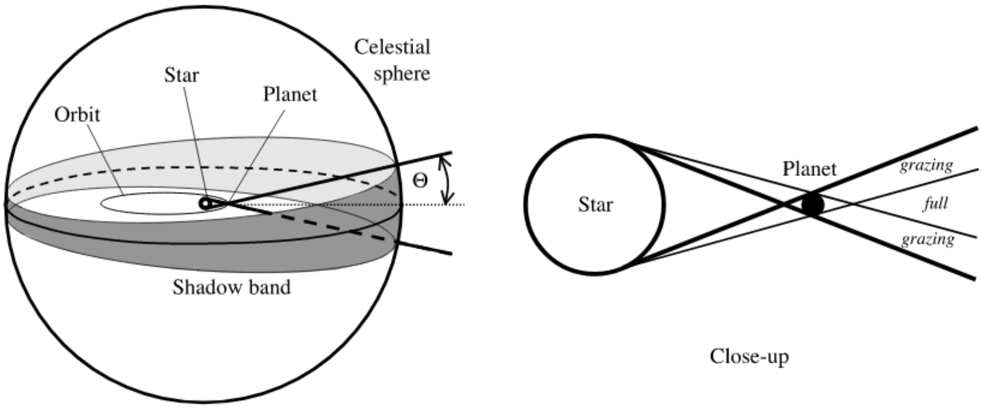

Figure 3.2: The shadow cone of an eclipse (Winn et al. 2010). *Left:* Transits are visible by observers within the penumbra of the planet. *Right:* A close-up showing the penumbra (thick lines), as well as the antumbra (thin lines) within which the transits are full, as opposed to grazing.

where the semi-major axis a and the argument of periastron ω here refer to the orbit of the planet relative to the star, and the subscripts "*tra*" and "*occ*" refer to transits and occultations, respectively.

Transits or occultations are seen only by privileged observers when a planet's orbit is nearly edge-on. As the planet orbits its star, its shadow describes a cone that sweeps out a band on the celestial sphere, as illustrated in Figure 3.2. A distant observer within the shadow band will see transits. The opening angle of the cone, θ, satisfies the condition $\sin\theta = (R_\star + R_\mathrm{p})/r$, where r is the instantaneous star-planet distance. This cone is called the *penumbra*. There is also an interior cone, the *antumbra*, defined by $\sin\theta = (R_\star - R_\mathrm{p})/r$, inside of which the transits are full, i.e., non-grazing.

The transit probability p_tr is calculated from the requirement $|b| < 1 + R_\mathrm{p}/R_\star$. If $R_\mathrm{p} \ll R_\star$ this reduces to $|b| < 1$. Using equation 3.1 and the fact that $\cos i$ is uniformly distributed for a randomly-placed observer, we arrive at

$$p_\mathrm{tr} = \left(\frac{R_\star + R_\mathrm{p}}{a}\right)\left[\frac{1 + e\sin\omega}{1 - e^2}\right], \tag{3.3}$$

Equation 3.3 gives the probability of observing a transiting planet and it depends on the semi-major axis, stellar radius, and, for non-zero eccentricity, on the orbit orientation. For $R_\mathrm{p} \ll R_\star$ and circular orbits ($e = 0$):

$$p_\mathrm{tr} = \left(\frac{R_\star}{a}\right) \approx 0.0046 \left(\frac{R_\star}{R_\odot}\right)\left(\frac{a}{1\,\mathrm{au}}\right)^{-1}. \tag{3.4}$$

More details can be found in Winn et al. (2010). Table 3.1 reports typical values for the transit probability, for a hot Jupiter ($R_\mathrm{p} = 1\,R_\mathrm{J}$) and a hot Neptune ($R_\mathrm{p} \approx 4\,R_\oplus$) on a 3-day circular orbit, as well as for a Earth-sized planet ($R_\mathrm{p} \approx 1\,R_\oplus$) on a Earth-like orbit.

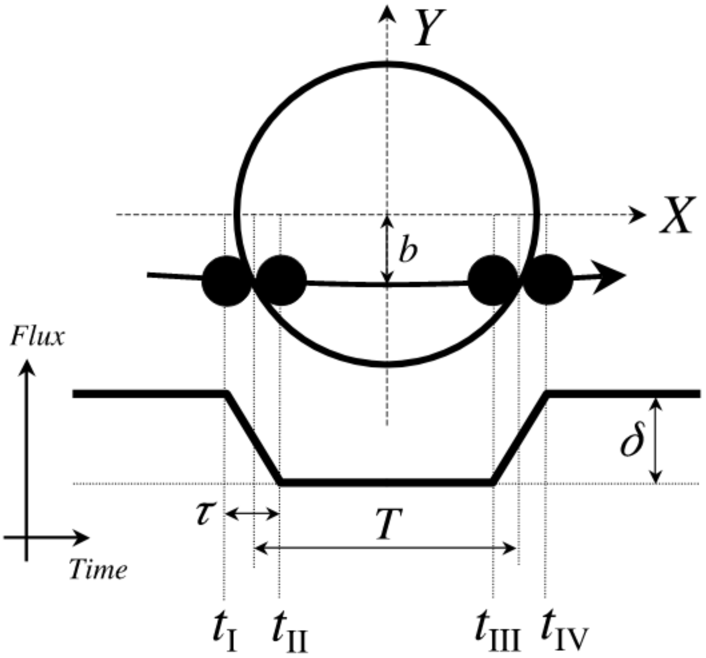

Figure 3.3: Illustration of the main quantities used to describe the orbital configuration: the four contact points and the quantities T and τ, the flux decrease δ, the idealized light curve, and the impact parameter b (Winn et al. 2010).

Transit duration

During the transit event, the disk of the star and the planetary disk are tangent at four contact points $t_\mathrm{I} - t_\mathrm{IV}$, as shown in Figure 3.3. In a grazing transit, the second and third contacts do not occur. Following Winn et al. (2010), we define the total duration as $T_\mathrm{tot} = t_\mathrm{IV} - t_\mathrm{I}$, the full duration as $T_\mathrm{full} = t_\mathrm{III} - t_\mathrm{II}$,

	Hot Jupiter	Hot Neptune	Earth
Period (d)	3	3	365
Transit probability	10	2.5	0.5
Transit duration (h)	3	3	15
Photometric transit depth (%)	1	0.1	0.01

Table 3.1: Transit probability, duration (for a central event), and depth for a Sun-like star transited by a hot Jupiter and a hot Neptune on a 3-day circular orbit, as well as by an Earth-sized planet on a Earth-like orbit.

the ingress duration as $\tau_{\rm ing} = t_{\rm II} - t_{\rm I}$, and the egress duration as $\tau_{\rm egr} = t_{\rm IV} - t_{\rm III}$. In the case of a circular orbit, the total duration $T_{\rm tot}$ and the full duration $T_{\rm full}$ are given by the following equations:

$$T_{\rm tot} = t_{\rm IV} - t_{\rm I} = \frac{P}{\pi} \sin^{-1} \left[\frac{R_\star}{a} \frac{\sqrt{(1+k)^2 - b^2}}{\sin i} \right], \tag{3.5}$$

$$T_{\rm full} = t_{\rm III} - t_{\rm II} = \frac{P}{\pi} \sin^{-1} \left[\frac{R_\star}{a} \frac{\sqrt{(1-k)^2 - b^2}}{\sin i} \right], \tag{3.6}$$

where k is the planet-to-star radius ratio $R_{\rm p}/R_\star$, and b is the impact parameter for a transit (Eq. 3.1).

3.2 Transits equations

During a transit, the stellar flux drops due to the presence of an occulting planet that covers a fraction of the stellar disk. The total flux $F(t)$ is given by

$$F(t) = F_\star(t) + F_{\rm p}(t) - k^2 \alpha(t) F_\star(t), \tag{3.7}$$

where $F_\star(t)$ and $F_{\rm p}(t)$ are the fluxes from the stellar and planetary disk, respectively. The quantity α is a dimensionless function of order unity depending on the overlap area between the stellar and planetary disks (Winn et al. 2010). Due to, e.g., flares, pulsations, rotation of starspots and plages, rotation of the tidal bulge raised by the planet, $F_\star(t)$ may vary over time. Here, however, we consider $F_\star$ to be a constant with time. Only the ratio

$$f(t) = \frac{F(t)}{F_\star} \tag{3.8}$$

is of interest. We define $I_{\rm p}$ and $I_\star$ as the disk-averaged intensities of the planet and star, respectively:

$$\frac{F_{\rm p}}{F_\star} = k^2 \frac{I_{\rm p}}{I_\star}. \tag{3.9}$$

Combining equations 3.7, 3.8, and 3.9, we arrive at:

$$f(t) = 1 + k^2 \frac{I_{\rm p}(t)}{I_\star} - k^2 \alpha(t). \tag{3.10}$$

As a starting approximation, we can consider α as a trapezoid and $f(t)$ is specified by the transit depth δ, the duration T, and the ingress or egress duration τ (Figure 3.3). For transits, the maximum loss of light is given by

$$\delta = k^2 \left[1 - I_{\mathrm{p}}(t)/I_\star\right]. \tag{3.11}$$

When the light from the planetary nightside is negligible (i.e., $I_{\mathrm{p}}(t) \approx 0$) the approximation $\delta \approx k^2$ holds true. In the trapezoidal approximation the flux variation during ingress and egress is linear in time. In reality the bottom of a transit light curve is not flat because real stellar disks do not have a uniform intensity, as discussed in Section 3.3.

Orbital parameters

From the transit duration equations 3.5 and 3.6, we can derive the impact parameter b and the so-called scaled semi-major axis $a/R_\star$ (Seager & Mallén-Ornelas 2003)

$$b \equiv \frac{a}{R_\star}\cos i = \sqrt{\frac{(1-k)^2 - [\sin^2(T_{\mathrm{full}}\pi/P)/\sin^2(T_{\mathrm{tot}}\pi/P)](1+k)^2}{\cos^2(T_{\mathrm{full}}\pi/P)/\cos^2(T_{\mathrm{tot}}\pi/P)}}, \tag{3.12}$$

with

$$\frac{a}{R_\star} = \frac{1}{\tan(T_{\mathrm{tot}}\,\pi/P)}\sqrt{(1+k)^2 - b^2}. \tag{3.13}$$

Using Kepler's third law (Eq. 2.9) and with the reasonable assumption that $M_{\mathrm{p}} \ll M_\star$, the ratio $a/R_\star$ provides an empirical measurement of the stellar mean density:

$$\rho_\star = \frac{3\pi}{GP^2}\left(\frac{a}{R_\star}\right)^3. \tag{3.14}$$

We can compare the stellar density derived from the modeling of the transit light curve with the stellar density estimated through other methods, e.g., spectroscopy, mass-radius relations, or asteroseismology, to select promising transiting candidates (Tingley et al. 2011) and help ruling out false positive scenario[1].

In brief, transit photometry provides a direct measurement of the planet-to-star radius ratio $R_{\mathrm{p}}/R_\star$ (Eq. 3.10). Additionally, it provides the orbital period P, the impact parameter b, the scaled semi-major axis $a/R_\star$, and consequently the orbit inclination i, and the mean density of the host star $\rho_\star$.

3.3 Limb darkening

Real stellar disks are brighter in the center and darker at the edges, or limbs, as shown in Figure 3.4. This phenomenon is known as *limb darkening*. It is a consequence of changes in temperature and opacity with altitude in the stellar atmosphere. The line of sight to the limb follows an oblique path into the stellar atmosphere, and thus an optical depth of unity is reached at a higher

---

[1] False positives are detections of transit-like signals present in time-series photometry that are not due to planetary transits (Brown 2003; Kipping et al. 2014).

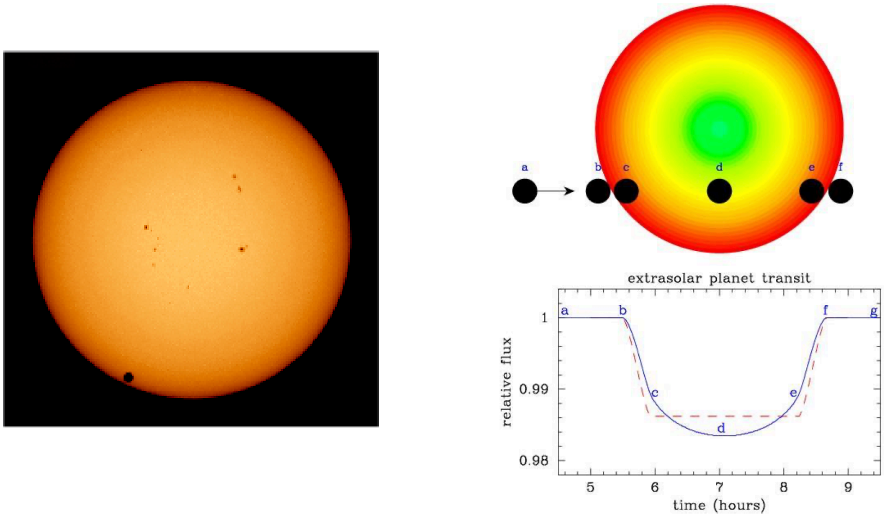

Figure 3.4: *Left:* Limb darkening effect of the solar disk. The edges appear darker than the center; *Right:* As an effect of the limb darkening, the light curve in Figure 3.3 is rounded off at the bottom and smoothed at the second and third contact points.

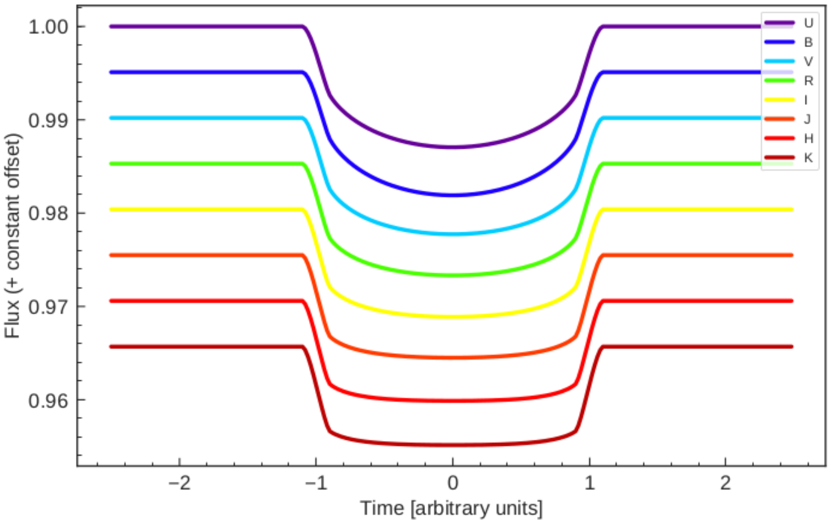

Figure 3.5: Theoretical light curves of a Sun-like star transited by a planet 10% its size. Different colours indicate different filters. It is possible to see that bluer wavelengths correspond to more contrast between the center and the limb, and thus to more round transits (Barragan 2018).

altitude, where the temperature is cooler and the radiation is less intense. Limb darkening affects the shape of the transit light curve that a planet imprints on the observed stellar flux as it passes in front of the host star. For instance, the intensity of the occulted light does not remain constant when the planet is entirely in front of the stellar disk (when $b < 1 - k$). A deeper dip in flux is observed when the planet transits nearer the center of the star than at the edge.

Taking these effects into account, the stellar disk intensity $I_\star$ is parametrized as $I_\star = I_\star(\mu)$, where $\mu = \cos\theta$, and θ is the angle between the line of sight and the normal to a given point on the stellar surface. In this work, the quadratic limb darkening model described by Mandel & Agol (2002) was adopted:

$$I_\star \propto 1 - u_1(1-\mu) - u_2(1-\mu)^2, \tag{3.15}$$

where u_1 and u_2 are the limb darkening coefficients, which satisfy $u_1 + u_2 < 1$. These coefficients depend on the stellar spectral type and wavelength. They can be calculated from stellar atmospheric models or measured from a sufficiently precise transit light curve.

The parameters u_1 and u_2 are different for different bandpasses. Therefore, also the transit shape changes with wavelength. The effect of limb darkening is to round off the bottom and blur the second and the third contact points. Figure 3.5 shows synthetic transit light curves at different wavelengths for a Jupiter-sized planet passing in front of a Sun-like star. For TESS transit light curves, the limb darkening coefficients can be extracted from Claret (2018). Note how a "real" transit light curve does not have a flat bottom, as in the case of an uniform source. Note also how the effects of limb darkening are remarkably stronger at shorter wavelengths (Claret 2018).

Chapter 4

Observations

In this chapter, I shall describe NASA's TESS space telescope (Section 4.1) and the HARPS (Section 4.2.1) and CARMENES (Section 4.2.2) high-resolution spectrographs, whose data were used for this work. TESS time-series photometry is made publicly available to the scientific community by NASA shortly after acquisition, enabling rapid follow-up observations of transiting planets. The high-precision HARPS measurements were acquired as part of two ESO large observing programs coordinated by the University of Turin, that aim at confirming and characterizing small planets from the TESS space mission. The CARMENES high-resolution spectra were collected by the CARMENES consortium. As a member of the team, I have access to the data.

4.1 TESS

The Transiting Exoplanet Survey Satellite (Ricker et al. 2015, TESS) is an all-sky transit survey whose main goal is the detection and characterization of small planets ($1\,R_\oplus \lesssim R_\mathrm{p} \lesssim 4\,R_\oplus$) transiting bright stars ($5 \lesssim V \lesssim 12$). Given the brightness of their host stars, TESS transiting planets are amenable to follow-up observations that aims at determining planetary masses via Doppler spectroscopy, and/or at studying planetary atmospheres via, e.g., transmission and emission spectroscopy. TESS is providing prime targets for further characterization with the James Webb Space Telescope (JWST Greene et al. 2019), as well as with other large ground-based (e.g., the Extremely Large Telescope, or ELT; Evans et al. 2015) and space-based (e.g., the Atmospheric Remote-sensing Infrared Exoplanet Large-survey, or ARIEL; Tinetti et al. 2018) upcoming facilities.

Launched in April 2018, TESS was placed in a highly eccentric, 13.7-day orbit around Earth. The primary mission ended in July 2020, and now the space survey is on an extended mission that is expected to last another two years. As of 12 April 2024, TESS has identified 7138 transiting candidate exoplanets, of which 432 have been confirmed by ground-based observations[1].

The satellite uses an array of wide-field cameras to perform a survey of 85 % of the sky. In order to obtain clear images of both the northern and southern hemispheres of the sky, TESS utilizes a 2:1 lunar resonant orbit called P/2.

---

[1] https://exoplanets.nasa.gov/tess/

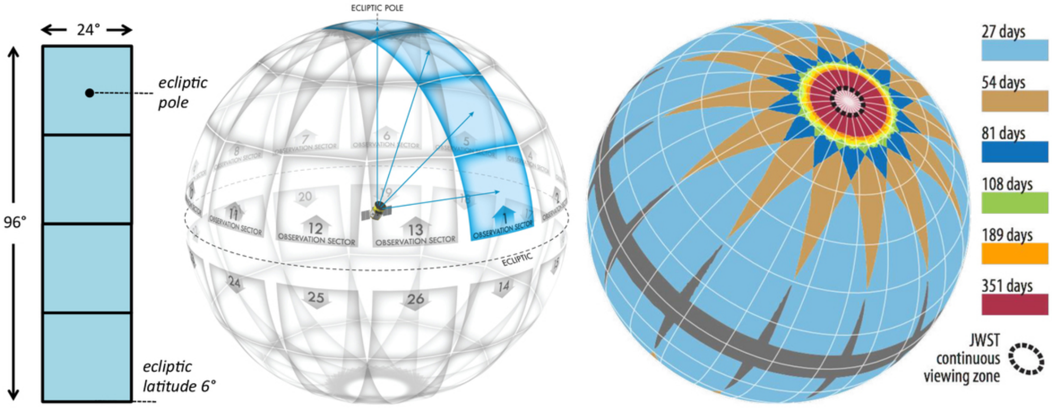

Figure 4.1: *Left:* The four TESS wide-field optical CCD cameras aligned to cover a 24° × 96° sector. *Middle:* Division of the celestial sphere into 26 observation sectors (13 per hemisphere). *Right:* Duration of observations on the celestial sphere, taking into account the overlap between sectors (Credit: NASA).

The highly elliptical orbit has a 373 000 km apogee, timed to be positioned approximately 90° away from the position of the Moon to minimize its perturbations. This orbit should remain stable for decades and keep TESS's cameras in a stable temperature range. The orbit is entirely outside the Van Allen belts to avoid radiation damage. Every 13.7 days, at its perigee of 108 000 km, the satellite transmits data collected during the just-completed orbit to Earth over a period of about 3 hours.

The instrument on TESS includes four wide field-of-view CCD cameras. The four CCDs are arranged in a 2 × 2 detector array for a total of 16 megapixels per camera and 16 CCDs for the entire instrument. Each camera has a wide field of view of 24° × 24°. The TESS lenses have a 10-cm effective aperture and a combined field of view of 24° × 96° (2 300 square degrees, around 5 % of the entire sky) as shown in Figure 4.1. For comparison, *Kepler*'s primary mission only covered an area of the sky measuring 105 square degrees, though the *K2* extension has covered many such areas for shorter times. TESS uses a red-optical bandpass range covering the wavelengths from about 600 nm to 1000 nm.

The primary mission survey was divided into 26 antisolar observing sectors (13 per hemisphere), with an overlap of sectors at the poles of the ecliptic to allow additional sensitivity toward smaller, longer-period exoplanets in that regions of the celestial sphere, where JWST has continuous viewing capabilities. In the extended mission TESS is re-observing the southern and northern hemispheres. The observations of each sector last about 27 days on average. In addition, the TESS team has introduced improvements to the way the satellite collects and processes data. Its cameras now capture a full-frame image every 10 minutes, three times faster than the primary mission. A new fast mode allows it to measure the brightness of thousands of stars every 20 seconds, whereas the previous method involved collecting observations from tens of thousands of stars every 2 minutes. The faster measurements have allowed TESS to better resolve brightness variations caused by stellar oscillations and to capture in greater detail the explosive flares of active stars.

TESS data for each sector become available online about two-three months after the end of the observations. As described in the previous paragraph, TESS obtains time-series photometry at a few different cadences with a baseline ranging from ~ 27 days to a full year, depending on sector overlap and ecliptic latitude. The entirety of the CCDs are downloaded every 30-minutes in files so-called *Full Frame Images* (FFIs). Specific groups of pixels around a selected star are also downloaded at a shorter cadence, known as *Target Pixel* (TP) files.

The photometric data are processed by the TESS data processing pipeline developed by the Science Processing Operations Center (SPOC; Jenkins et al. 2016). The SPOC pipeline uses Simple Aperture Photometry (SAP) to generate stellar light curves, where common instrumental systematics are removed via the Presearch Data Conditioning (PDCSAP) algorithm developed for the *Kepler* space mission (Stumpe et al. 2012; Stumpe et al. 2014; Smith et al. 2012). The PDCSAP is also corrected for dilution effects, e.g., the amount of flux from the target star that falls within the aperture, and the ratio of target flux to total flux in the aperture. The former accounts for the amount of flux captured by the photometric aperture. The latter takes into account the crowding from known nearby sources, i.e., it accounts for the contamination by sources whose light leaks into the photometric mask. TESS's first observed exoplanet was announced in September 2018: a super-Earth transiting the naked-eye star ($V = 5.65$) π Mensae every 6 days (Gandolfi et al. 2018; Huang et al. 2018).

4.2 High-resolution spectrographs

Neutral and ionized atoms in stellar atmospheres produce spectral absorption and emission lines. By measuring the Doppler shift of atmospheric absorption lines, we can measure the radial velocity of a star and look for the tiny signal induced by an orbiting planet. As explained in Section 1.3, the radial velocity semi-amplitude variations induced by Jupiter and Earth in their current positions around the Sun are 11.2 $\mathrm{m\,s^{-1}}$ and 10 $\mathrm{cm\,s^{-1}}$, respectively. To achieve a Doppler precision of few $\mathrm{m\,s^{-1}}$ or even $\mathrm{cm\,s^{-1}}$, and detect exoplanets by the RV method, one needs spectrographs with excellent RV precision coupled with long-term stability (Hatzes 2019).

To obtain spectra of astronomical objects, the spectrograph must be combined with a telescope that collects light. Light from the telescope converges towards the focus of the slit (or fiber) of the spectrograph and then diverges. The light is then collimated onto a dispersing element (usually a reflection grating), which breaks it up into its wavelength components. Finally, the dispersed light is focused on an electronic detector by a camera. CCDs detectors are mostly used for spectrographs working at optical wavelengths ($\approx$300–1000 nm).

The spectral resolution of a spectrograph, $\Delta\lambda$, is defined as the smallest difference in wavelengths that can be resolved by the instrument at a given wavelength λ. The smaller the spectral resolution $\Delta\lambda$, the easier is to distinguish fine spectral features. The spectral resolving power is defined as $R = \lambda/\Delta\lambda$. The larger the resolving power R, the higher the resolution $\Delta\lambda$.

The RV precision depends on the wavelength coverage, the resolving power of the instruments, and the signal-to-noise ratio (S/N) of the data, but also on the spectral type of the observed star, as well as on its projected rotational velocity[2] $v \sin i$. In order to achieve high-precision RV measurements it is therefore necessary to use spectrographs with a large range of wavelengths and high-spectral resolution. For more details, I refer the reader to more specific literature (see, e.g., Hatzes 2019).

4.2.1 HARPS

The High Accuracy Radial Velocity Planet Searcher (Mayor et al. 2003, HARPS) is a high-precision Echelle, planet-finding, spectrograph installed in 2002 on the ESO's 3.6m telescope at La Silla Observatory in Chile (Figure 4.2). The instrument has been built to obtain very high long term radial velocity stability ($< 1\,\mathrm{m\,s^{-1}}$). To achieve this goal, HARPS is designed as an Echelle spectrograph fed by a pair of octagonal fibres and optimized for mechanical stability. It is contained in a vacuum vessel to avoid spectral drift due to temperature and air pressure variations. One of the two fibres collects the star light, while the second is used to simultaneously record either a Th–Ar/Fabry–Pérot reference spectrum, or the background sky. The two HARPS fibres have an aperture on the sky of $1''$. Both fibres are equipped with an image scrambler to provide a uniform spectrograph pupil illumination, independent of pointing decentering. HARPS has a resolving power of 115 000 over a covered spectral range of 378–691 nm. The HARPS detector consists of a mosaic of 2 CCDs (altogether 4k×4k) with a pixel size of 15 μm. The data are usually reduced using the Data Reduction Software (DRS; Lovis & Pepe 2007; Dumusque et al. 2021) available at the telescope. The work presented in this thesis is based on Doppler measurements acquired as part of a large RV follow-up program carried out with the HARPS spectrograph (programs ID: s 1102.C-0923 and 106.21TJ.001).

---

[2] The equatorial velocity projected along the line of sight to the star.

Figure 4.2: *Left*: ESO's 3.6m telescope at La Silla Observatory in Chile with the author. *Right Top*: La Silla Observatory. *Right bottom*: HARPS spectrograph (Credit: ESO).

4.2.2 CARMENES

The Calar Alto high-Resolution search for M dwarfs with Exoearths with Near-infrared and optical Echelle Spectrographs (CARMENES) is an instrument designed, built, and operated by a collaboration of 11 Spanish and German institutions, mounted on the 3.5 m telescope at Calar Alto Observatory, Almería, Spain. The instrument comprises two highly stable, fiber-fed spectrographs (Quirrenbach et al. 2014, 2018). The visible-light spectrograph (VIS) covers the wavelength range 520–960 nm providing a resolving power of $R \approx 94\,600$. The counterpart in the near-infrared (NIR) covers the spectral range 960–1710 nm, with a resolving power of $R \approx 80\,400$.

The two ultra-stable, high-resolution spectrographs were specifically constructed to obtain high long-term stability for delivering high precision radial velocity measurements on the order of 1 $\mathrm{m\,s^{-1}}$. The optical design and layout of the spectrographs are very similar. The light is directed to the Cassegrain focus of the telescope, where it passes a dichroic beam splitter. Sent through a pair of optical fibers, light with wavelengths smaller than 960 nm is fed to the visible-light spectrograph, whereas light with wavelengths greater than 960 nm is fed to the near-infrared spectrograph. In each of the spectrographs, the light is dispersed by an échelle grating and the orders are separated by a grism cross-disperser. The spectra usually follow the standard CARMENES data flow (Caballero et al. 2016) and are reduced with the `caracal` pipeline (Zechmeister et al. 2014). The RV measurements are corrected for barycentric motion, secular acceleration, nightly zero-points, and telluric lines as described by Nagel et al. (2023). Given the low signal-to-noise ratio of the NIR RVs, this work only makes use of the CARMENES VIS data.

Chapter 5

Data analysis

In this chapter I shall briefly described the underlying theory of the data analysis tools used in this work. The analysis mainly focuses on:

1. Frequency analysis of the radial velocity and photometric time series to search for periodic and quasi-periodic signals using the Generalised Lomb-Scargle periodogram implemented by Zechmeister & Kürster (2009).
2. Light curve detrending and joint analysis of the photometric and spectroscopic data to determine planetary and orbital parameters.
3. Handling the presence of stellar activity in time series data.

5.1 Frequency analysis of time series

Light and radial velocity curves are time series and the main mathematical tool to analyse time series is Fourier transform.

Prior to modeling Doppler measurements, possible periodic signals due to planets can be detected in time series data by finding peaks in the corresponding power spectra. As described in Hatzes 2016, finding planets in RV data consists of four major steps:

1. Finding a periodic signal in the data.
2. Determine if the signal is significant, i.e., whether it is real or due to noise.
3. Determine the nature of the variations, i.e., whether they are due to instrumental effects, intrinsic stellar variability, or a bona fide planet.
4. Fit a Keplerian orbit to the RV measurements.

Sometimes a periodic signal in time-series data can be easily detected by eye. This only works if the signal is well-sampled and its amplitude is larger than the noise. If the amplitude of the signal is comparable to the measurement uncertainty, the signal is not so easy to detect by eye as it remains embedded in the noise. The top panel of Figure 5.1 shows a simulated noisy time series of a sampled 2.85-day sine wave with a root mean square (RMS) scatter comparable to the signal amplitude. Despite the noise, the periodogram of the synthetic data (Figure 5.1, lower panel) displays its most significant peak at the frequency of the input sine wave ($1/2.85\,\mathrm{d} = 0.35\,\mathrm{d}^{-1}$). In order to extract signals from such noisy data, customized special methods, which are introduced later in this chapter, have to be used.

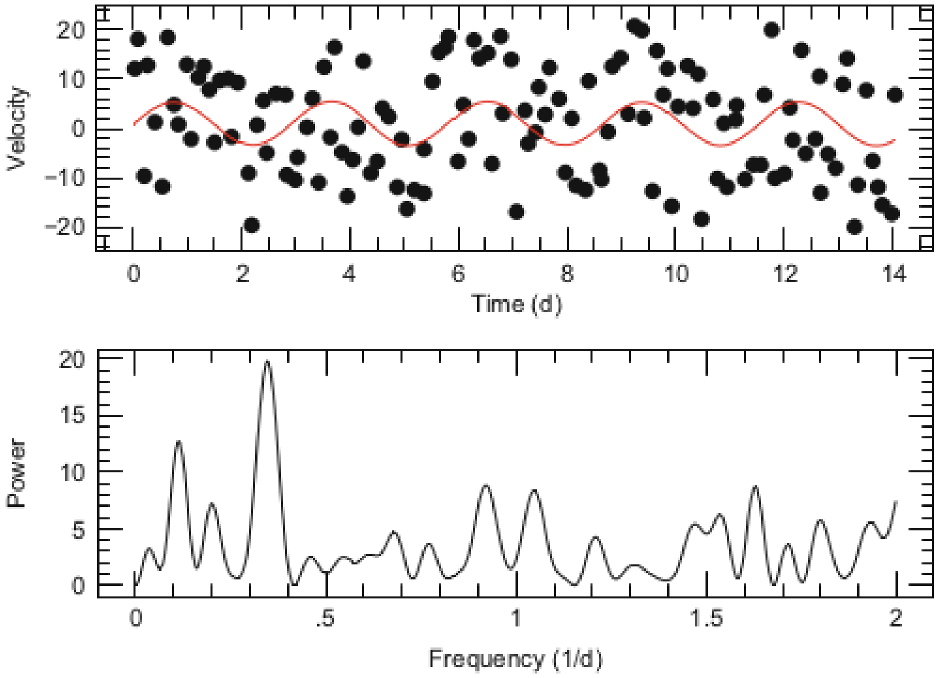

Figure 5.1: *Top:* Time series (dots) of a sampled sine function (red curve) whose amplitude is the same level as the noise. *Bottom:* The Fourier transform of the above time series with a dominant peak at the correct frequency of the input sine wave (Hatzes 2016).

Since we always deal with discrete signals in our experimental data, the most commonly used methods to find possible periodic signals are largely based on the discrete Fourier transform (DFT), often called the classic periodogram. If we have a time series of measurements $X(t_j)$ where t_j is the time of our jth measurements, the DFT is

$$\mathrm{DFT}_X(\omega) = \sum_{j=1}^{N} X(t_j) e^{-i\omega t_j} \tag{5.1}$$

where $e^{i\omega t_j}$ is the complex trigonometric function $\cos(\omega t_j) + i \sin(\omega t_j)$, N is the number of data points sampled at times t_j. As described in Hatzes (2019), ω is referred to the angular frequency related to the period by $\omega = 2\pi/P$. The power is defined by

$$P_X(\omega) = \frac{1}{N}\left[\left(\sum_{j=1}^{N} X(t_j)\cos\omega t_j\right)^2 + \left(\sum_{j=1}^{N} X(t_j)\sin\omega t_j\right)^2\right] \tag{5.2}$$

The DFT is often plotted as a power spectrum $P(\omega)$ or sometimes as the amplitude spectrum $A(\omega)$ where $A = \sqrt{P_X}$.

An alternative form of the DFT, largely used by the exoplanet community, is the generalised Lomb-Scargle periodogram (GLS; Zechmeister & Kürster 2009). In the present case the dominant frequency is found by optimising the chi-square (χ^2) on a grid of frequencies, fitting a periodic function $y(t) =$

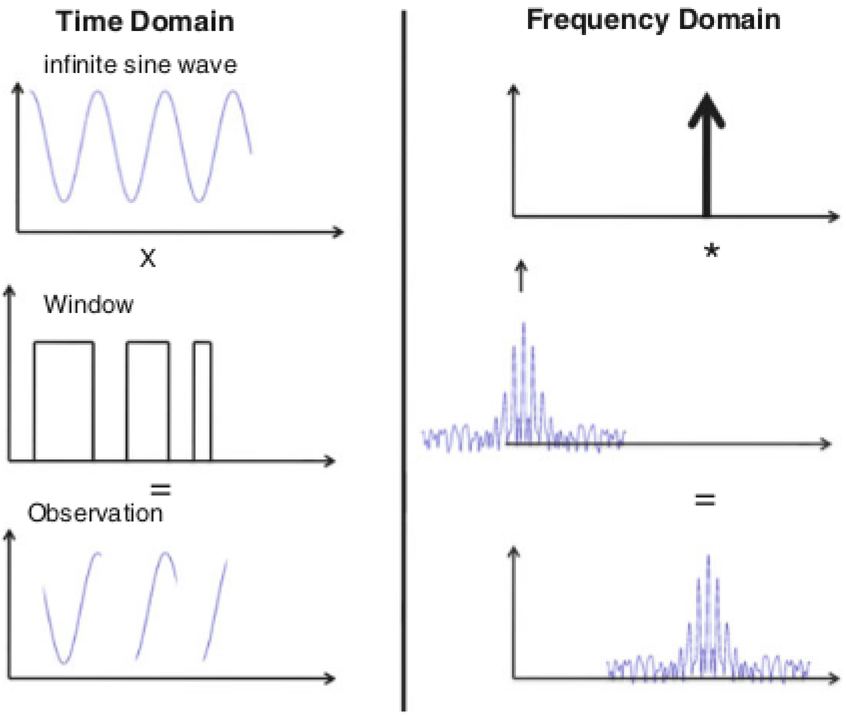

Figure 5.2: *Left:* In the time domain the observations consist of an infinite sine wave multiplied by the sampling window that produces a sine with gaps. *Right:* In the Fourier domain the sine function appears as a δ-function that is convolved (symbolized by the star) with the Fourier transform of the window function (Hatzes 2016).

$a \cos \omega t + b \sin \omega t + c$, with $\omega = 2\pi f$. To perform the frequency analysis of the radial velocity time series, I used the algorithm implemented by Zechmeister & Kürster (2009). Identifying periodic signals is not only limited to the Doppler search for orbiting planets in radial velocity measurements. Frequency analysis techniques are largely employed by the astronomical community to analyze photometric and spectroscopic time series data to, e.g., detect stellar rotation or stellar oscillations.

5.1.1 Spectral windows and aliases

Our time series data have gaps due to diurnal Earth rotation, seasons, bad weather, as well as uneven time sampling due to scheduling constraints. These factors, together with the presence of noise in the data (as shown in the previous section 5.1), can make it challenging to interpret the features in the Fourier domain.

The spectral or sampling window, also known as "window function", is a step (or box) function with unit values at the time stamps of the measurements and zero values elsewhere (Figure 5.2, middle left panel). In time domain, the observations consist on an infinite sine wave (upper left panel) multiplied by the window function (middle left panel) that produces a sine with gaps (lower left panel). The window function and its power spectrum provide important information on the sampling of the data, which in turn has an influence on the features seen in periodograms of our time series.

A narrow function in the time domain will be broad in the Fourier domain. A Gaussian function transforms into another Gaussian in the Fourier domain, while a slit or box function transforms into a sinc function. Therefore, the narrower the slit, the broader the sinc function in the Fourier domain. The convolution of two functions, $f(t)$ and $g(t)$ in the time domain translates into a multiplication of the Fourier transforms of the individual functions, $G(\omega)$ and $F(\omega)$ in the Fourier domain:

$$f(t) * g(t) \equiv F(\omega) \cdot G(\omega). \tag{5.3}$$

This can produce rather complicated periodograms when looking for periodic signals in RV data. For this reason, the window function is important for interpreting the features in the periodogram. For a pure sine wave a DFT or a GLS should produce a δ-function, but that is only the case for an infinite time series (Figure 5.2, upper panels). Real observations are always over a finite time interval and with gaps. In the time domain this is a sine wave that is multiplied by a box function whose width is the time span of our observations. In the Fourier domain (DFT and GLS periodogram) this multiplication turns into a convolution of the Fourier transforms of the individual functions. In Fourier space a sine wave is a delta function, and a box is a sinc function. The convolution causes the δ-function to appear as a sinc function centered on the frequency of our signal and with the same amplitude. This process is shown in Figure 5.2 where several box functions simulates observations over several nights.

The longer the observing window, i.e. longer box, the narrower the sinc function. When trying to resolve two very closely spaced frequencies wide observing window are essential. Such a case may arise if we are trying to extract a planet signal whose period is only slightly different from the rotational period of the star. The length of our observing window, t_{tot}, corresponds to a frequency resolution of $1/t_{tot}$ and this must be much less than the frequency separation of the two signals we are trying to detect.

5.1.2 False alarm probability

How to evaluate the statistical significance of a peak in the GLS periodogram? This question concerns whether noise can produce a peak with power higher than the one we identified in our data, the so-called false alarm probability (FAP).

Bootstrap

A robust estimate of the FAP comes from a bootstrap analysis using two approaches. For the first method we create random noise with a standard deviation equal to the root mean square (RMS) scatter of our data. We compute the GLS periodogram and find the highest peak. We iterate this procedure a large number of times (10 000–100 000) for different random numbers. The fraction of random data sets with GLS power higher than the one we found in our data gives us the FAP. This assumes that our noise is Gaussian and that we have a good handle on our errors.

When the noise is non-Gaussian and/or we suspect that the uncertainties of our data are underestimated, the most common form of the bootstrap method is to take the actual measurements and randomly shuffle the data points, while keeping the time stamps fixed (Murdoch et al. 1993). We calculate the GLS periodogram, find the highest peak, and re-shuffle the time series. The fraction of the shuffled data periodograms having power higher than the one we found in the original data is the FAP. This method preserves the statistical characteristics of the noise in the data to an acceptable level. If there is still a periodic signal in the data, this will create a larger RMS scatter than we would expect due to measurement errors. In this case, the bootstrap will produce a higher FAP, providing a conservative estimate of the FAP.

Windowing bootstrap

The bootstrap method can be utilized to estimate the FAP for a peak at a known frequency (e.g., when we know the orbital frequency of a transiting planet) using narrow frequency windows centered at the frequency of interest. In order to do that we can employ the windowing bootstrap technique. Briefly, this approach consists of taking a relatively large frequency window (at least 10 times the frequency resolution, as suggested by Hatzes 2019) centered on the known frequency and performing the bootstrap shuffling as described before. We successively narrow the spectral window at small steps for, e.g., 10 additional bootstrap randomizations. The fit of the FAP versus window size, extrapolated to the intercept (i.e. the zero window length), yields the FAP at the known frequency.

5.1.3 Multi-periodic signals

Since planets are often found in multi-planet systems, RV time series are often multi-periodic. Prewhitening is a very fast and efficient technique to identify multiple signals in RV data. The procedure is called prewhitening because a time series consisting of only random noise has a power spectrum that is flat or “white”. If a periodic signal is present in our time series, when we remove the signal from the data, we make the power spectrum “whiter” (Hatzes 2019).

The prewhitening procedure consists of the following steps:

1. compute the periodogram of the time series;
2. identify the most significant peak;
3. fit a sine function at the frequency of the dominant peak;
4. subtract the sine fit from the data (this will also remove all the aliases due to this signal);
5. compute the periodogram on the residuals;
6. find the next significant peak and iterate the procedure from point 3. The process stops when there are no significant peaks left in the periodogram of the residuals.

5.2 Joint modeling

We can combine transit photometry and Doppler data to measure the radius and mass of a planet, and thus its bulk density. As we presented in Chapters 2 and 3, light curves and RVs are described by time-dependent parametric equations (Eqs. 2.7 and 3.10). By fitting models to the data we can determine the physical parameters of planetary systems. For a parameter estimation, Bayesian model fitting techniques are widely used, especially in the astronomical community. Markov chain Monte Carlo method (MCMC; Metropolis et al. 1953; Hastings 1970) is one of the most popular and convenient statistical tool of this kind.

However, prior to performing any data modeling another step must be done. In addition to transit signals, the light curve of a star may also exhibit flux variability induced by, e.g., flares, pulsations, starspots, plages, etc. For active stars, the transit signal may be smaller than the photometric variability induced by stellar activity. Since the information we want to extract lies in the depth, duration, and shape of the transit, we must be careful to remove non-transit-related signals. When modeling a transit light curve, it is convenient to remove any trend caused by stellar variability and analyze the normalized light curves. One of the most common methods of detrending a transit light curve is to remove the local trend around each transit. This can be achieved by fitting a polynomial of order N to the out-of-transit data around each transit and dividing each segment of the light curve –including the in-transit data – by the best-fitting polynomial. Other methods consist in using Gaussian process (GP) regression to detrend light curves and remove possible modulations using, e.g., the `python` code `citlalicue`[1] (Barragán et al. 2022).

5.2.1 Bayesian data analysis

The goal of parameter estimation is to determine estimates of the planetary parameters by comparing the models with the observational data. Taking a Bayesian view of probability, we want to estimate the probability that a parametric physical model $M = M(\vec{\theta})$, depending on a set of parameters $\vec{\theta}$, describes our data D. This probability is called *the conditional probability* of M given D, and it is referred to as $P(M|D)$. Bayes' theorem provides us with a simple and powerful mathematical tool to calculate it via:

$$P(M|D) = \frac{P(D|M)P(M)}{P(D)}. \tag{5.4}$$

The term $P(D|M)$ is a function of the model called the *likelihood* of observing the data set D if the model M is true, while $P(M)$ is the *prior* associated to the model M, and $P(D)$ is the *model evidence*. $P(M|D)$ is also called the *joint posterior distribution* (see, e.g., Sharma 2017; Barragán et al. 2019).

Priors are based on previous knowledge about a given model parameter, such as a physical range in which a parameter can be found. Most commonly used priors are the uniform and Gaussian distributions. A *uniform* prior, also called a weakly informative or uninformative prior, is used when the only information available is the interval $[a, b]$ in which a given parameter θ_i is located. If θ_i lies between a and b with equal probability, the uniform prior is given by

---

[1] https://github.com/oscaribv/citlalicue.

$$\mathcal{U}(\theta_i; a, b) = \begin{cases} (b-a)^{-1} & : a < \theta_i < b \\ 0 & : \text{otherwise.} \end{cases} \tag{5.5}$$

If for a given parameter θ_i we have a previous measurement and its 1σ uncertainty we can use this information to weight the probability. A *Gaussian* prior, or informative prior, of a parameter θ_i with mean a and standard deviation b is given as

$$\mathcal{N}(\theta_i; a, b) = \frac{1}{\sqrt{2\pi b^2}} \exp\left[-\frac{(\theta_i - a)^2}{2b^2}\right]. \tag{5.6}$$

The evidence $P(D)$ in equation (5.4) is also called marginal likelihood and simply acts to normalize the posterior distribution. It is calculated by integrating the likelihood and prior distributions in the parameter space as

$$P(D) = \int P(D|M(\vec{\theta}))P(M(\vec{\theta}))d\vec{\theta}. \tag{5.7}$$

For parameter estimation, we are interested on the shape of the posterior distribution of each parameter θ_i more than the normalized probability. The model evidence is important when doing model comparison (Gelman et al. 2004). We can marginalize θ_i by integrating $P(D|M)P(M)$ over the remaining parameters θ_j, with $j \neq i$. We can then infer the model parameters from the marginal posterior distribution for each parameter θ_i.

5.2.2 Markov chain Monte Carlo

A powerful way to find the model that best fits the observed data, and to determine the physical quantities of interest, is to generate a set of points in the parameter space using MCMC methods. They use a Markov chain, that, following Sharma (2017), is a sequence of random variables $X_1, ..., X_n$ such that, given the present state, the future and past are independent. The name of the MCMC method comes from the use of random numbers to generate the Markov chains. These random variables can be the points $\vec{\theta}$ in the parameter space that we want to sample. Starting from a point in the parameter space $\vec{\theta}_1$, we can generate a set of different models $\vec{\theta}_i$ via Markov chains. This creates a set of N models from an initial point $\vec{\theta}_1$ (Barragán et al. 2019).

Several MCMC sampling methods ensure that Markov chains converge to the optimal solution when the posterior reaches a static solution. The converged chains represent a sample of the marginal posterior distribution and the frequencies of the chains can be used to create the posterior distribution of the sampled parameters, e.g., with a histogram. The final marginal posterior distribution for each parameter is called the credible interval. Its median and the 68 % limits defines the best estimate of the parameter and its 1σ uncertainty (see Hogg & Foreman-Mackey 2018), respectively.

5.2.3 Software suite

In this work I used the software suite `pyaneti` (Barragán et al. 2019, 2022). The code is a powerful and user-friendly tool to perform multi-planet radial velocity and transit data fitting. Using Bayesian approaches combined with MCMC samplings, `pyaneti` allows one to estimate the parameters of planetary systems. It is a fast and easy-to-use code that combines the computational power of `Fortran`, the versatility of `Python`, and the parallelization of `OpenMP`. In the following sub-sections I will describe the equations used by the software to extract the parameters from RV time-series and photometric transit data.

Radial velocity equations

As described previously in Section 2.1, the change of the velocity component along the line-of-sight to the host star, induced by the presence of the orbiting planet, is described by the Eq. 2.7. The radial velocity semi-amplitude variation $K_\star$ is given by Eq. 2.12 which provides a relation between $K_\star$ and the planetary M_p and stellar mass $M_\star$. The time dependency of ν is given by

$$\nu(t) = 2 \arctan \left[\sqrt{\frac{1+e}{1-e}} \tan \left(\frac{E(t)}{2} \right) \right]. \tag{5.8}$$

The eccentric anomaly $E(t)$ is defined via Kepler's equation

$$A(t) = E(t) - e \sin[E(t)], \tag{5.9}$$

where

$$A(t) = \frac{2\pi}{P}(t - T_0), \tag{5.10}$$

is the mean anomaly. The latter depends on time t and on T_0, i.e., the time of passage of periastron. For transiting planets T_0 coincides with the mid-time of transit. Eq. 5.9 is transcendent and cannot be solved analytically for $E(t)$. The code solves this using a Newton-Raphson algorithm.

The Doppler reflex motion of a star orbited by more than one planet can thus be described by a general parametric function:

$$M_{RV}(\vec{\theta}; t) = f(\{T_0, P, e, \omega_\star, K_\star\}_j, \gamma_i; t), \tag{5.11}$$

in which the set of parameters $\{T_0, P, e, \omega_\star, K\}$ repeats for each planet j and γ_i accounts for the systemic velocity for each different instrument i.

Transit equations

The code `pyaneti` uses the transit light curve model of Mandel & Agol (2002) in which the stellar intensity is limb-darkened using a quadratic law with coefficients u_1 and u_2 (for more details see Chapter 3). Following the transit equations presented in Chapter 3, the general parametric function that describes transit events in a light curve is

$$M_{tr}(\vec{\theta}; t) = f(\{T_0, P, e, \omega_\star, R_\mathrm{p}/R_\star, a/R_\star, i\}_j, \{u_1, u_2\}_i; t). \tag{5.12}$$

The set of parameters $\{T_0, P, e, \omega_\star, R_\mathrm{p}/R_\star, a/R_\star, i\}$ repeats for each planet j and $\{u_1, u_2\}_i$ repeats for each band i of the light curve.

Multi-planet joint fit

In cases where both Doppler and transit measurements are available, the analysis can be performed with a joint fit. In the RV and the transit parametric functions, 5.11 and 5.12, respectively, T_0, P, e and $\omega_\star$ are shared parameters. In this case the code allows us to fit simultaneously the orbital parameters. Generally, the transit light curves improve the determination of T_0 and P, whereas the RV measurements constrain better e and $\omega_\star$. The final set of parameters involved in the joint fit will be

$$\vec{\theta} = (\{T_0, P, e, \omega_\star, R_\mathrm{p}/R_\star, a/R_\star, i, K_\star\}_j, \{u_1, u_2\}_i, \gamma_k), \tag{5.13}$$

where $\{T_0, P, e, \omega_\star, R_\mathrm{p}/R_\star, a/R_\star, i, K_\star\}_j$ repeats for each planet j, $\{u_1, u_2\}_i$ repeats for each photometric band i and γ_k for each spectrograph k.

Parametrizations

The software `pyaneti` uses a set of convenient parametrizations to improve the exploration of the parameter space and avoid biases due to priors:

- **Eccentricity and angle of periastron**. Because the posterior distribution of the eccentricity is not well sampled for orbits with small eccentricities, a practical solution is to define e and $\omega_\star$ using a polar form. The code adopts the parametrization proposed by Anderson et al. (2010)

  $$ew_1 = \sqrt{e}\sin\omega_\star, \qquad ew_2 = \sqrt{e}\cos\omega_\star, \tag{5.14}$$

  with the advantages that it is not truncated when the eccentricity is close to zero, and that uniform priors on ew_1 and ew_2 imply uniform priors on the eccentricity.

- **Impact parameter**. It is convenient to parametrize the orbital inclination using the impact parameter defined in Eq. 3.1. In this way it is easy to set priors to exclude orbits for which there are no transit when $b > 1 + R_\mathrm{p}/R_\star$, or, if $R_\mathrm{p} \ll R_\star$, when $b > 1$.

- **Limb Darkening coefficients**. The code uses the parameterization proposed by Kipping (2013). An optimal way to sample the parameter space for the limb darkening coefficients of Mandel & Agol (2002) is via the parametrization

  $$q_1 = (u_1 + u_2)^2, \qquad q_2 = \frac{u_1}{2(u_1 + u_2)}. \tag{5.15}$$

  This approach fully accounts for our ignorance about the intensity profile and explores physical solutions by sampling uniformly q_1 and q_2 between 0 and 1. This yields robust and realistic uncertainty estimates. The original coefficients u_1 and u_2 can be recovered with

  $$u_1 = 2q_1\sqrt{q_2}, \qquad u_2 = \sqrt{q_1}(1 - 2q_2). \tag{5.16}$$

- **Stellar density**. From Keplers third law we obtain Eq. 3.14. There is thus a relation between the stellar density and the orbital parameters

P and $a/R_\star$. It is convenient to parametrize $a/R_\star$ with $\rho_\star$. If precise stellar parameters have been derived, it is possible to set tight priors on the stellar density and hence on $a/R_\star$. For a multi-planet system, it is convenient to parameterize the scaled semi-major axis $a_j/R_\star$ of all planets j using the same stellar density. In this way the stellar density is constrained for all planets and Keplers third law is not violated within planets orbiting the same star. `pyaneti` uses the parametrization $\rho_\star^{1/3}$, instead of $\rho_\star$, since $a/R_\star$ and $\rho_\star^{1/3}$ are linearly related.

5.3 Stellar activity

After performing a frequency analysis of the RV time-series, as described in Section 5.1, we detect a significant periodic signal in the data. Prior to performing a Keplerian fit to the data, we should assess whether the signal is due to stellar activity or a bona fide planet. Stellar activity can often induce signals in RV time series which can mimic a planetary signal. For late-type main-sequence stars, stellar activity is the main form of variability in RV measurements. This activity-induced variability can be periodic, like in the case of stellar rotation or activity cycles, or completely stochastic. As described by Hatzes (2019), to confirm the planetary origin of an RV signal we must disprove the stellar origin, remembering that:

1. a Doppler signal due to a planet is stable and coherent. Its amplitude, period, and phase that do not vary with time;
2. the RV amplitude of a planetary signal is independent of wavelength.
3. there are no stellar photometric variability at the period of the planet candidate;
4. there are no changes in the activity indicators (Section 5.3.2) at the period of the planet candidate;
5. there are no changes in the shape of the spectral lines at period of the planet candidate, because planets do not change the shape of the spectral lines;
6. the statistical significance of the planetary signal should increase with the number of measurements in a way that is expected for the quality of the data.

Note that these conditions are necessary but not always sufficient for the planet hypothesis.

The manifestations of stellar activity have an impact on photometric and spectroscopic measurements.

5.3.1 Rotational modulation

Stellar spots appear as dark cool areas on the photosphere of magnetically active stars. They are regions where magnetic flux loops emerge from the stellar surface. Magnetic fields inhibit part of the outgoing convective heat flux, resulting in areas of reduced brightness and temperature. Starspots have temperatures ranging from 500 to 2000 K less than the surrounding photosphere.

As spots grow and decay, they induce photometric and spectroscopic variability that is modulated by stellar rotation. As a star rotates, one half of the disk moves towards us, while the other half moves away. As a result, the flux emitted by the approaching half is blue-shifted, while the receding half is red-shifted. If the stellar surface is featureless, the Doppler shifts on both sides cancel out each other, and the spectral line profile is undisturbed, as pictured in the left diagram of Figure 5.3. A starspot moving in and out of view as the star rotates blocks part of the stellar flux, inducing an imbalance between the redshifted and blueshifted halves of the star. This creates a distortion in the shape of the line profile, thus shifting its centroid by a small amount (Figure 5.3). These perturbations to the spectral line profile translate into RV variations of the order of $1\,\mathrm{m\,s^{-1}}$ for sunspots; RV variations induced by starspots can be much greater for more active and rapidly rotating stars.

The presence of an active region on the stellar photosphere will thus induce an apparent Doppler signal at the rotation period of the star (P_{rot}). A distribution of spots on the stellar surface can produce different rotation harmonics (e.g., $P_{\mathrm{rot}}/2$, $P_{\mathrm{rot}}/3$, $P_{\mathrm{rot}}/4$, etc.) in the periodogram of time series Doppler data. For instance, the presence of two spots separated by $\sim 180^\circ$ in longitude, will induce an apparent Doppler signal at the first harmonic of the rotation period ($P_{\mathrm{rot}}/2$). Similarly, in case of three active regions separated by roughly 120°, one should expect to see a signal at $P_{\mathrm{rot}}/3$, i.e., the second harmonic of the rotation period. Other surface features/structures can influence the RV measurements of a star, e.g., plage, faculae, and granulation (see, e.g., Hatzes 2019 and Haywood 2017).

To exclude that an RV signal is related to rotational modulation, we can check whether the same signal appears in ancillary measurements. The stellar rotation period can be measured (or inferred) through a variety of photometric and spectroscopic measurements: ground– or space–based photometric monitoring, spectral line asymmetry variation and magnetic activity indicators, projected equatorial velocity $v\ \sin(i)$, Ca II H & K lines, etc.

5.3.2 Activity indicators

Radial velocity signals due to stellar magnetic activity often manifest by variations in activity indicators. Periodic variations present in RV observations that are not found in any of the activity indicators may indicate a bona fide Doppler reflex motion of the star induced by an orbiting planet.

In order to measure the RV of a star, all the spectral lines of a spectrum are combined together to produce a mean line profile known as the *cross-correlation function* (CCF). The shape of the CCF reflects that of all the lines in the spectrum, which are affected by the physical processes occurring in the stellar atmosphere, where the lines are formed. Some activity indicators and diagnostics extracted from the CCF are often used to check whether a signal in the RV time series is due to stellar activity or not. As a warning remark, finding a signal in activity indicators is not conclusive evidence against the planet hypothesis. The planet's orbital period could by chance coincide with the stellar rotation period or activity cycle. For example, observing our solar system from a distant planet, extraterrestrial astronomers might mistakenly conclude that Jupiter is not a planet, since the solar cycle of 11 years coincides

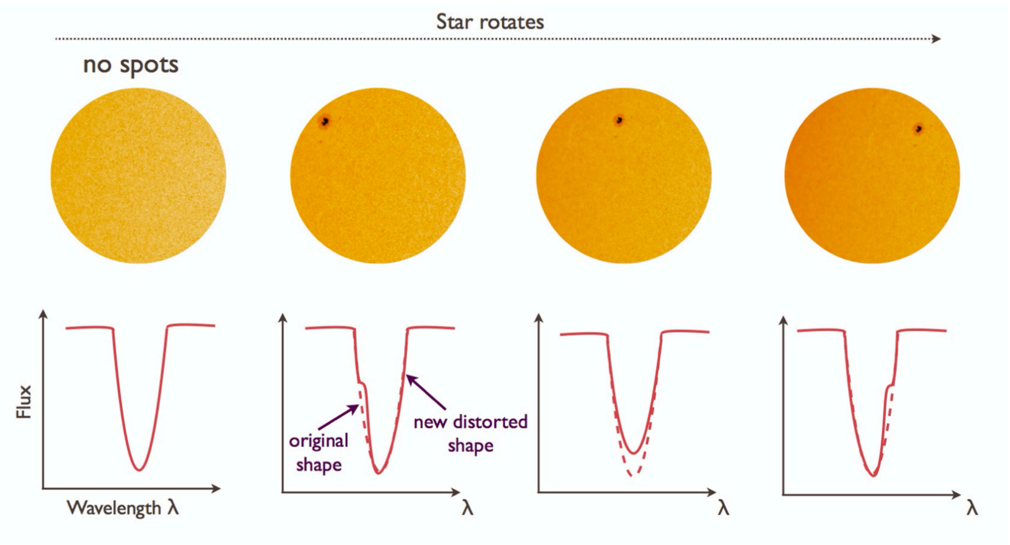

Figure 5.3: Illustration of how asymmetries in the spectral lines are induced by the presence of starspots on the rotating stellar disk, leading to variations in RV measurements (Haywood 2017).

quite well with our giant planet's orbital period of about 12 years. A brief description of some stellar activity indicators used in the course of this work is given below (see e.g., Haywood 2017; Hatzes 2019).

Full width at half-maximum. The full width at half-maximum (FWHM) of the CCF varies as stellar surface features such as spots cross the stellar disk. When a cool spot approaches the limb of the stellar disk, a distortion is produced in the blue wing of the line profile (Figure 5.3). The centroid of the CCF is shifted towards the red, while the line shape is narrower, i.e., the FWHM reaches a minimum. When the spot is in the center of the disk, the distortion occurs in the core of the line, without shifting the centroid. This distortion causes the line profile to appear shallower and larger, resulting in a maximum in the measured FWHM and contrast (see below). Since the FWHM of the CCF is correlated with rotational modulation due to spots, it can be used to measure the rotation period of the star. Other contributions to change in the FWHM are the intrinsic line broadening due to thermal and turbulent motions in the stellar photosphere.

Bisector of the cross-correlation function. The bisector span (BIS) is another activity indicator derived from the shape of the cross-correlation function. It measures the asymmetry of the average spectral line and should correlate with the RV if the observed variability is caused by spots or plages rotating with the star.

Contrast. The third index is the contrast of the CCF, which is the relative depth of the CCF with respect to its baseline level. It is sensitive to changes in the depth of the average spectral line profile.

Ca ii H & K. The Ca ii H & K lines at 3933.7 Å and 3968.5 Å are spectral features used as "classic" indicators of stellar magnetic activity. In the case of the Ca ii lines, the cores of the lines come from the chromosphere, where the source function starts to increase with height (i.e., the temperature increases from the photosphere to the chromosphere). The chromosphere above active regions has an emission spectrum that can partially fills the photospheric absorption lines. For active stars, this results in emission peaks in the cores of the Ca ii lines, which are expected to periodically vary as active regions are carried across the visible hemisphere of the stellar disk due to stellar rotation.

There are two ways of measuring the strength of these emission peaks and thus the level of activity of the star. The first is the S-index, defined as (Hall 2008)

$$S = \alpha \frac{F_{\mathrm{H}} + F_{\mathrm{K}}}{F_{\mathrm{V}} + F_{\mathrm{R}}}, \tag{5.17}$$

where F_{H} and F_{K} refer to the fluxes in the cores of the H and K lines, respectively, and F_{V} and F_{R} refer to the fluxes in the bands on the violet and red sides of the H and K lines. The term α is a calibration constant.

Another measure of the chromospheric activity is the R'_{HK} index:

$$R'_{\mathrm{HK}} = F_{\mathrm{HK}}/F_{\mathrm{bol}}, \tag{5.18}$$

where F_{HK} is the total chromospheric Ca ii H & K surface flux corrected for the photospheric component and F_{bol} is the bolometric flux of the star.

Hα and Na D. These parameters are related to the intensity of the Hα line at 6562.8 Å and the sodium doublet lines at 5895.9 and 5889.9 Å . The Hα line can appear in emission in very active or young stars. In contrast, in less active stars like the Sun, the emission may partially fill the core of the line. The sodium Na I D features have been shown to be useful indicators of stellar activity in cool stars.

Chromaticity. The Chromatic index is defined as the slope of the radial velocity as a function of the logarithm of the wavelength (Zechmeister et al. 2018). The activity-induced RV amplitude depends on the wavelength at which we are observing the star. The amplitude decreases towards longer wavelength, due to the lower contrast between spots and quiet photosphere.

Differential line width. The differential line width (dLW) is an indicator that traces the variations in the stellar line width induced by the presence of active regions co-rotating with the star. The dLW is found to be an alternative indicator to the commonly used FWHM of the CCF.

5.3.3 Handling stellar activity with Gaussian processes

As discussed earlier, stellar activity can cause apparent Doppler variations that can dominate the RV variability and, in the worst case, masquerade as a planet signal (Rajpaul et al. 2015). Especially if we want to discover small planets, e.g., $M_{\mathrm{p}} < 50\,M_{\oplus}$, around active stars, the signal due to magnetic activity may hide the planetary signal. The detection of an exoplanet can therefore be challenging around active stars. We want to filter out the activity signal to be sure that the detected planet signal is true, get more accurate planetary parameters, and finally look for low-mass planets in the Doppler measurements (Hatzes 2019).

In recent years, several methods have been proposed to mitigate or remove stellar activity, e.g., during the RV extraction (e.g., Collier Cameron et al. 2021; Cretignier et al. 2020; Rajpaul et al. 2020), or by filtering the activity induced signal in RV time series (Barragán et al. 2018; Hatzes et al. 2010, 2011; Pepe et al. 2013). Most of these methods work in the case that an orbiting exoplanet is known and one wants to confirm its detection. For instance, stellar activity can be modeled as one or the sum of more sinusoidal functions at the star's rotational period and its harmonics, as a result of a previous frequency analysis of the time series, and can be removed using the prewithening procedure (Section 5.1.3). Activity indicators (Section 5.3.2) can be used to identify whether a signal is due to activity or a bona fide planet.

Stellar activity signals have time scales similar to those associated with planets, e.g., rotational modulations have periods ranging from days to years. In addition, these signals are quasi-periodic and stochastic, e.g., periodic rotation, activity cycles, and evolution of active regions. In this regard, a widely used tool for modeling the RV signal induced by stellar activity is Gaussian processes (GP).

What is a Gaussian process?

A GP is a type of stochastic process based on the Gaussian probability distribution (see, e.g., Rasmussen & Williams 2006; Roberts et al. 2013; Haywood et al. 2014; Rajpaul et al. 2015; Barragán et al. 2022; Aigrain & Foreman-Mackey 2023). A stochastic process is a system that evolves in continuous space while undergoing fluctuations. When the system can be described by a set of random variables, related by a multivariate normal distribution, the stochastic process is a Gaussian process. The joint probability distribution over any finite sample of input points (locations), $\mathbf{t} = t_i$, with $i = 1, ..., N$, is given by a multivariate Gaussian:

$$P(\mathbf{t}) = \frac{1}{\sqrt{(2\pi)^N |\mathbf{K}|}} \exp\left[-\frac{1}{2}(\mathbf{t} - \boldsymbol{\mu})^T \mathbf{K}^{-1} (\mathbf{t} - \boldsymbol{\mu})\right], \tag{5.19}$$

where $\boldsymbol{\mu}$ is a mean vector containing mean values, $\mathbf{K}$ is a covariance matrix, and $|\mathbf{K}| = \det(\mathbf{K})$.

The mean function $\mu(\mathbf{t}; \boldsymbol{\phi})$ is the deterministic part of a GP and depends on a set of parameters, $\boldsymbol{\phi}$, and the variable that describes the continuous space, $\mathbf{t}$. When the GP is used to model a nuisance signal, like in many astrophysical applications, the mean function contains the signal of interest. The covariance matrix $\mathbf{K}$ provides information about the correlation between the random variables, and it needs to be positive semi-definite and symmetric.

In recent years, GPs have been increasingly used and are gaining popularity. Indeed, the central limit theorem suggests that the assumption of a Gaussian distribution is often at least approximately accurate. Another advantage is that Gaussian distributions obey simple mathematical identities for marginalization and conditioning, which enable inference with GPs (the process of marginalizing over the individual functions) to be performed analytically with simple linear algebra (Aigrain & Foreman-Mackey 2023).

The Kernel Function

The covariance matrix $\mathbf{K}$ is computed with a covariance, or kernel function $k(t_i, t_j; \mathbf{\Phi})$, which is controlled by a set of parameters $\mathbf{\Phi}$, referred to as *hyperparameters*. While the mean function represents the information about the deterministic part of the signal, i.e., a Keplerian for the RV curve or a transit model, the kernel function reflects our knowledge about the stochastic part. This function describes how two arbitrary points (locations), t_i and t_j are related according to the parameters Φ. We can use the kernel function to model correlated noise or stochastic signals in the data, e.g., noise, periodicity, long-term evolution, etc. One of the most widely used kernels is the quasi-periodic kernel (QP; Roberts et al. 2013; Nicholson & Aigrain 2022)

$$k(t_i, t_j) = A^2 \exp\left[-\frac{\sin^2\left[\pi(t_i - t_j)/P_{\rm GP}\right]}{2\lambda_{\rm p}^2} - \frac{(t_i - t_j)^2}{2\lambda_{\rm e}^2}\right], \tag{5.20}$$

where A is an amplitude and works as a scale factor, $P_{\rm GP}$ is the characteristic period of the GP, $\lambda_{\rm p}$ is the inverse of the harmonic complexity, that refers to more complex periodic patterns in the data, and $\lambda_{\rm e}$ is the long term evolution timescale. The QP kernel generates a stochastic periodic signal, and it is therefore widely used to model stellar activity signals in both photometry and RVs (Barragán et al. 2022). Figure 5.4 shows examples of functions generated using a QP kernel. Stellar activity can exhibit variability in the period due to, for instance, evolution in the size and distribution of active surface features. In this context, the parameter $P_{\rm GP}$ is interpreted as the stellar rotation period, $\lambda_{\rm p}$ is associated with the distribution of active regions on the stellar surface (Aigrain et al. 2015), and $\lambda_{\rm e}$ is the active region lifetime on the stellar surface.

GP regression

We can perform GP regression assuming that our time series, i.e., a finite set of data points y taken at times t, are samples of a GP (Barragán et al. 2022). As discussed before, the mean function μ is the deterministic part of the signal. It can be a physically motivated parametric model (e.g., Keplerian or transit curves). The covariance kernel function, $k(t_i, t_j)$, includes any intrinsic correlation in our data set due to stellar activity and/or instrumental systematics.

A finite set of variables drawn from a GP is given by a multivariate Gaussian distribution. Therefore, we can write a logarithmic Gaussian likelihood to marginalize over variables as

$$\ln \mathcal{L}(\phi, \Phi) = -\frac{1}{2}\left(N_{\rm obs} \ln 2\pi + \ln|\mathbf{K}| + \mathbf{r}^T \mathbf{K}^{-1} \mathbf{r}\right), \tag{5.21}$$

where ϕ and Φ are the mean and covariance functions parameters, $\mathbf{r} = \mathbf{y} - \boldsymbol{\mu}$ is the vector of residuals between the data $\mathbf{y}$ and the mean function $\boldsymbol{\mu} = \boldsymbol{\mu}(t)$ evaluated at each time stamps t, $\mathbf{K}$ is the covariance matrix, and finally, $N_{\rm obs}$ is the number of observations. To infer the parameters of the mean and covariance functions, we can sample Eq. 5.21 with several numerical methods.

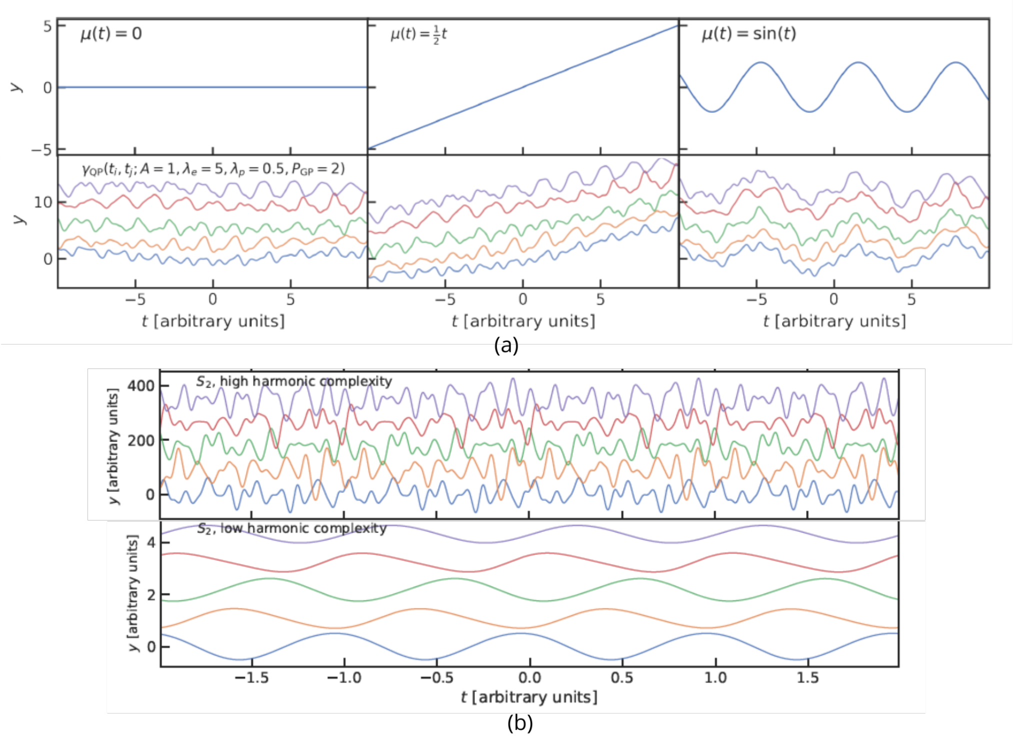

(a)

(b)

Figure 5.4: Example of functions generated by GPs using a QP kernel. (a) functions with different mean and covariance functions. (b) example of a sample S_2 created with a QP kernel with $P_{\rm GP} = 1$, $\lambda_{\rm e} = 10$, and high ($\lambda_{\rm p} = 0.1$, top pannel) and low ($\lambda_{\rm p} = 10$, lower pannel) levels of harmonic complexity (compiled from Barragán et al. 2022).

Inference with a GP

After evaluating the likelihood function of the model (Eq. 5.21), we can perform inference and use our observations to update our prior beliefs about the system we are studying (see, e.g., Aigrain & Foreman-Mackey 2023). We then choose a prior distribution that includes our prior beliefs about the model parameters and use Bayes theorem to obtain the posterior distribution of the parameters given the data. Instead of calculating the posterior distribution analytically, we can use sampling methods such as MCMC (Section 5.2.2) to perform Bayesian inference. In this work, I have used the MCMC sampling, as implemented in the code `pyaneti`.

Stochastic signals in astronomical time series, e.g., RV data, can result from physical or instrumental factors. In our case, we want to remove them to identify the signals of interest, i.e., those induced by planets, and accurately measure the planetary parameters. We evaluate the posterior distribution over the GP hyperparameters. Markov chain Monte Carlo samples are used to approximate the posterior probability distributions for specific hyperparameters of interest. For this purpose, we marginalize the posterior distribution over the nuisance parameters.

Multi-dimensional GP

Multi-dimensional GPs arise from the idea that the same GP can describe correlations in multiple continuous spaces that are somehow related to each other.

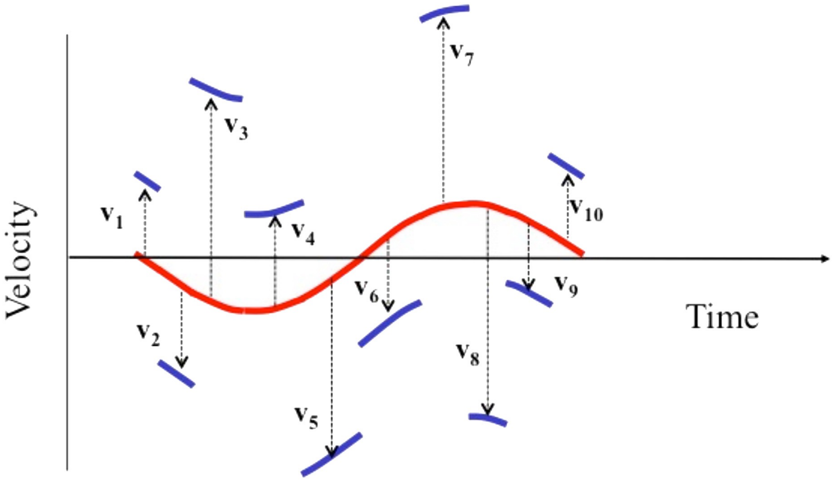

Figure 5.5: Schematic of the floating chunk offset method (Hatzes 2019). Observations of a short-period planet on a given night appear as short segments of a sinusoidal function for circular orbits. The segment on a given night has an offset, v_i, due to long period phenomena. By finding the appropriate offset and subtracting it, one can line up the segments to recover the planets orbit (shown here as a red curve).

One application of this framework is regression (Rajpaul et al. 2015; Barragán et al. 2022). The time series of activity indicators are usually simultaneous with those of RVs. These indicators are sensitive only to stellar activity, making them particularly suitable for mitigating the activity signal from RV data and disentangling the planetary signals. A multi-dimensional GP approach can be used to model stellar activity in RV time series simultaneously with the activity indicators. This approach assumes that the signals due to the stars activity in all the time series can be described by the same underlying GP, the function $G(t)$, and its time derivatives. The function $G(t)$ represents the projected area of the visible stellar disk that is covered by active regions at a given time.

Active regions on the stellar surface affect photometric and spectroscopic observables differently. For instance, some are influenced only by the projected area covered by the regions and can be described only by $G(t)$, while others are influenced by how the regions evolve over time and are described by $G(t)$ and at least its first derivative $\dot{G}(t)$.

Radial velocity measurements are affected by both the position and temporal evolution of active regions (see, e.g., Dumusque et al. 2014). Most activity indicators are influenced only by the fraction of the stellar surface covered by active regions and thus need only $G(t)$ for their description (e.g., log R'_{HK} or S-index). Other indices, on the other hand, such as BIS, are affected by the evolution of active regions, and thus require higher time derivatives of $G(t)$ to be described. The multidimensional GP approach was used to model the RVs and determine the planetary parameters of the GJ 367 system, which will be presented and discussed in Chapter 6.

5.3.4 Floating Chunk Offset

Transit surveys have observed a large population of planets with orbital periods of less than a few days. Among them, the ultra-short period (USP) planets have periods shorter than 1 day (Sanchis-Ojeda et al. 2014). The orbital period of these planets is therefore much smaller than the periods of the stellar rotation or activity cycles.

We can exploit this fact to filter out the activity signal. On this basis, Hatzes et al. (2011) used the floating chunk offset (FCO) method to determine the mass of the USP planet CoRoT-7 b ($P \approx 20\,\mathrm{hr}$). Within a single night ($\approx 8\,\mathrm{hr}$), the RV variation of the star is mainly induced by the USP planet rather than stellar rotation, activity cycles, or additional long-period planets. The RV contribution due to these longer period phenomena can thus be considered constant in a given night. We can then introduce nightly velocity offsets that will include all the longer period signals (i.e., signals with time scales much longer than 8 hr). This method allows us to filter out any long-term RV variations to disentangle the reflex motion of the planet. An illustrative explanation of the method is shown in Figure 5.5.

Chapter 6

GJ 367

Hundreds of ultra-short period (USP) planets have been discovered so far, but only a few of them have a radius and a mass estimate. USP planets are defined as planets that orbit their host star in less than 1 day (Sahu et al. 2006; Sanchis-Ojeda et al. 2014). Close-in planets with orbital periods of a few days, or even hours, challenge formation and evolution theories of planetary system (Winn & Fabrycky 2015; Zhu & Dong 2021). How these planets reach their current position around the star is currently unclear, and the formation processes are not yet fully understood. Several scenarios have been proposed in recent years to explain their close-in position:

1. dynamical interactions in multi-planet systems (Schlaufman et al. 2010);
2. low-eccentricity migration due to secular planet-planet interactions (Pu & Lai 2019);
3. high-eccentricity migration due to secular dynamical chaos (Petrovich et al. 2019);
4. tidal orbital decay of USP planets formed in situ (Lee & Chiang 2017);
5. obliquity-driven tidal migration (Millholland & Spalding 2020).

USP planets present their own advantages in terms of observations: they are easier to detect! Their transit probability (Section 3.1) is higher and the planet induced Doppler reflex motion is larger (Section 2.1). In addition, because their orbital period is typically shorter than the stellar rotation period, we can disentangle their signal from stellar activity using, e.g., the FCO method, Section 5.3.4. Radial velocity follow up of these types of systems can help us understand their formation and evolution mechanism by exploring the inner architecture of the host system.

GJ 367 is an M1 V star hosting a transiting ultra-short period hot sub-Earth on a ∼7.7 hr (∼0.32 days) orbit. The planet GJ 367 b was detected during TESS' primary mission and confirmed as a bona fide sub-Earth by Lam et al. (2021). Its radius was found to be $R_\mathrm{b} = 0.718 \pm 0.054\,R_\oplus$ and the mass $M_\mathrm{b} = 0.546 \pm 0.078\,M_\oplus$, resulting in a bulk density of $\rho_\mathrm{b} = 8.1 \pm 2.2\,\mathrm{g\,cm^{-3}}$.

As Dai et al. (2021) suggested, most of well-characterized USP planets are found to have additional planetary companions. GJ 367 was then likely to host more than one planet. With the aim of refining the planetary mass and radius of GJ 367 b, and searching for external companions, probing the outer architecture of the system, we performed an intensive RV follow-up campaign with the HARPS spectrograph (Goffo et al. 2023). We collected 371 high-

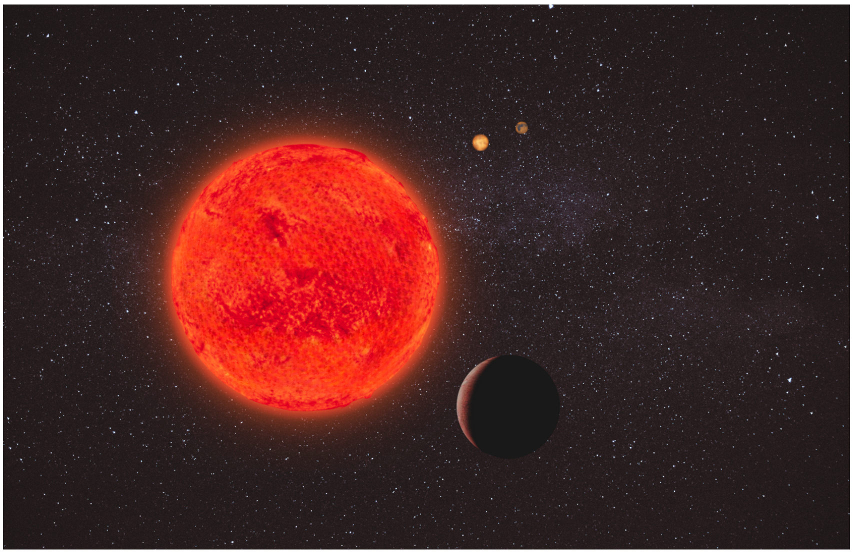

Figure 6.1: The author's illustration of the planetary system orbiting the star GJ 367, which comprises the inner ultra-dense planet GJ 367 b, and the two outer low-mass planets GJ 367 c and d. See the press release available at the University of Turin webpage `https://www.unito.it/sites/default/files/draft_press_release_gj_367_b_unito_english.pdf`.

precision radial velocities covering a baseline of nearly 3 years.

I combined our Doppler measurements with TESS observations from 3 sectors. I found that the hot (equilibrium temperature of about 1365 K) sub-Earth GJ 367 b has a mass of $M_{\mathrm{b}} = 0.633 \pm 0.050\,M_{\oplus}$ (8 %), and a radius of $R_{\mathrm{b}} = 0.699 \pm 0.024\,R_{\oplus}$ (3.4 %). This implies a bulk density of $\rho_{\mathrm{b}} = 10.2 \pm 1.3$ g cm^{-3}, i.e., 85 % higher than Earth's density. GJ 367 b joins the small class of high-density planets, i.e., super-Mercuries, being the densest ultra-short period small planet known to date. Given its precise mass and radius, we explored the potential internal composition, and found that GJ 367 b is expected to have an iron core with a mass fraction of $0.91^{+0.07}_{-0.23}$.

Two additional low-mass companions were also discovered: GJ 367 c and GJ 367 d have orbital periods of about 11.5 days and 34 days and minimum masses of $\sim 4\,M_{\oplus}$ and $6\,M_{\oplus}$, respectively. Unfortunately, they were not found to transit their host star.

The presence of outer planetary companions could be responsible for the migration processes that moved USP planets to their current positions (Pu & Lai 2019; Petrovich et al. 2019). The GJ 367 system proves to be an excellent target for studying the formation and evolution scenarios of USP planet systems. We explored secular migration scenarios that could explain the current system architecture of GJ 367. We tested whether the low-eccentricity secular forcing proposed by Pu & Lai (2019) could explain the observed position of GJ 367 b. We found that an alternative migration history, such as by high-eccentricity secular chaos (Petrovich et al. 2019), can better account for the architecture of the system.

How a low-mass high-density planet like GJ 367 b could have formed is currently unclear. For instance, the planet could have simply formed from iron-rich materials in protoplanetry disks (Dullemond & Monnier 2010; Aguichine et al. 2020; Adibekyan et al. 2021). Another possibility is the formation of a larger planet later differentiated into a denser core and less dense outer layers. These outer layers are then removed either by collisional stripping, i.e., by a giant collision, or by the strong stellar radiation. Figure 6.1 shows an artistic illustration of the system GJ 367.

The star GJ 367 was recently observed by the Mid-Infrared Instrument (MIRI) on board the James Webb Space Telescope (JWST) to obtain a mid-infrared (5–12 μm) phase curve of its transiting planet GJ 367 b (Zhang et al. 2024). GJ 367 b is the first sub-Earth with thermal emission observations. The JWST observations suggest a planet with no detectable atmosphere, lack of heat redistribution, and a dark surface in the MIRI bandpass (albedo of about 0.1), with a blackbody emission spectrum.

The results presented in Goffo et al. (2023) were fundamental for the analysis of the MIRI data. Given the 200 transits observed by TESS over a baseline of nearly 2 years, the calculated ephemeris and transit parameters are extremely well determined, providing strong constraints to the MIRI observations. The high-precision estimates of the planetary mass, radius, and density were important for the modeling of the planets atmosphere. The uncertainty on the radius dominates the error on the brightness temperature, which is one of the parameters used to assess whether the planet has an atmosphere or not. The surface gravity also affects the temperature/pressure profile of any putative atmosphere, which in turn affects the emission spectrum.

The following refereed paper, published on the Astrophisical Journal Letter, is the core result of this PhD work. All the methods described in the previous chapters were utilized for the analysis of the data presented in the paper.

The Astrophysical Journal Letters, 955:L3 (20pp), 2023 September 20 https://doi.org/10.3847/2041-8213/ace0c7

Company for the Ultra-high Density, Ultra-short Period Sub-Earth GJ 367 b: Discovery of Two Additional Low-mass Planets at 11.5 and 34 Days*

Elisa Goffo[1,2], Davide Gandolfi[1], Jo Ann Egger[3], Alexander J. Mustill[4,5], Simon H. Albrecht[6], Teruyuki Hirano[7,8], Oleg Kochukhov[9], Nicola Astudillo-Defru[10], Oscar Barragan[11], Luisa M. Serrano[1], Artie P. Hatzes[2], Yann Alibert[3,12], Eike Guenther[2], Fei Dai[13,14,34], Kristine W. F. Lam[15], Szilárd Csizmadia[15], Alexis M. S. Smith[15], Luca Fossati[16], Rafael Luque[17], Florian Rodler[18], Mark L. Winther[6], Jakob L. Rørsted[6], Javier Alarcon[18], Xavier Bonfils[19], William D. Cochran[20], Hans J. Deeg[21,22], Jon M. Jenkins[23], Judith Korth[4], John H. Livingston[7,8,24], Annabella Meech[25], Felipe Murgas[21,22], Jaume Orell-Miquel[21,22], Hannah L. M. Osborne[26], Enric Palle[21,22], Carina M. Persson[27], Seth Redfield[28], George R. Ricker[29], Sara Seager[30,31,32], Roland Vanderspek[31], Vincent Van Eylen[26], and Joshua N. Winn[33]

[1] Dipartimento di Fisica, Universitá degli Studi di Torino, via Pietro Giuria 1, I-10125, Torino, Italy; elisa.goffo@unito.it, elisa@tls-tautenburg.de
[2] Thüringer Landessternwarte Tautenburg, Sternwarte 5, D-07778 Tautenburg, Germany
[3] Physikalisches Institut, University of Bern, Gesellschaftsstrasse 6, 3012 Bern, Switzerland
[4] Lund Observatory, Division of Astrophysics, Department of Physics, Lund University, Box 43, SE-221 00 Lund, Sweden
[5] Lund Observatory, Department of Astronomy and Theoretical Physics, Lund University, Box 43, SE-221 00 Lund, Sweden
[6] Stellar Astrophysics Centre, Department of Physics and Astronomy, Aarhus University, Ny Munkegade 120, DK-8000 Aarhus C, Denmark
[7] Astrobiology Center, 2-21-1 Osawa, Mitaka, Tokyo 181-8588, Japan
[8] National Astronomical Observatory of Japan, 2-21-1 Osawa, Mitaka, Tokyo 181-8588, Japan
[9] Department of Physics and Astronomy, Uppsala University, Box 516, SE-75120 Uppsala, Sweden
[10] Departamento de Matemática y Física Aplicadas, Universidad Católica de la Santísima Concepción, Alonso de Rivera 2850, Concepción, Chile
[11] Sub-department of Astrophysics, Department of Physics, University of Oxford, Oxford, OX1 3RH, UK
[12] Center for Space and Habitability, University of Bern, Gesellsschaftsstr. 6 CH3012, Bern, Switzerland
[13] Division of Geological and Planetary Sciences, 1200 E California Boulevard, Pasadena, CA, 91125, USA
[14] Department of Astronomy, California Institute of Technology, Pasadena, CA 91125, USA
[15] Institute of Planetary Research, German Aerospace Center (DLR), Rutherfordstrasse 2, D-12489 Berlin, Germany
[16] Space Research Institute, Austrian Academy of Sciences, Schmiedlstrasse 6, A-8042, Graz, Austria
[17] Department of Astronomy and Astrophysics, University of Chicago, Chicago, IL 60637, USA
[18] European Southern Observatory, Alonso de Cordova 3107, Vitacura, Santiago de Chile, Chile
[19] Université Grenoble Alpes, CNRS, IPAG, F-38000 Grenoble, France
[20] McDonald Observatory and Center for Planetary Systems Habitability, The University of Texas, Austin Texas USA
[21] Instituto de Astrofísica de Canarias (IAC), E-38205 La Laguna, Tenerife, Spain
[22] Departamento de Astrofísica, Universidad de La Laguna (ULL), E-38206 La Laguna, Tenerife, Spain
[23] NASA Ames Research Center, Moffett Field, CA 94035, USA
[24] Department of Astronomical Science, School of Physical Sciences, The Graduate University for Advanced Studies (SOKENDAI), 2-21-1, Osawa, Mitaka, Tokyo, 181-8588, Japan
[25] Department of Physics, University of Oxford, Keble Road, Oxford, OX1 3RH, UK
[26] Mullard Space Science Laboratory, University College London, Holmbury St Mary, Dorking, Surrey RH5 6NT, UK
[27] Department of Space, Earth and Environment, Chalmers University of Technology, Onsala Space Observatory, SE-439 92 Onsala, Sweden
[28] Astronomy Department and Van Vleck Observatory, Wesleyan University, Middletown, CT 06459, USA
[29] MIT Kavli Institute for Astrophysics and Space Research & MIT Physics Department, USA
[30] Department of Earth, Atmospheric, and Planetary Sciences, Massachusetts Institute of Technology, Cambridge, MA 02139, USA
[31] Department of Physics and Kavli Institute for Astrophysics and Space Research, Massachusetts Institute of Technology, Cambridge, MA 02139, USA
[32] Department of Aeronautics and Astronautics, Massachusetts Institute of Technology, Cambridge, MA 02139, USA
[33] Department of Astrophysical Sciences, Princeton University, Princeton, NJ 08544, USA

Received 2023 February 16; revised 2023 June 15; accepted 2023 June 21; published 2023 September 14

Abstract

GJ 367 is a bright ($V \approx 10.2$) M1 V star that has been recently found to host a transiting ultra-short period sub-Earth on a 7.7 hr orbit. With the aim of improving the planetary mass and radius and unveiling the inner architecture of the system, we performed an intensive radial velocity follow-up campaign with the HARPS spectrograph—collecting 371 high-precision measurements over a baseline of nearly 3 yr—and combined our Doppler measurements with new TESS observations from sectors 35 and 36. We found that GJ 367 b has a mass of $M_b = 0.633 \pm 0.050\,M_\oplus$ and a radius of $R_b = 0.699 \pm 0.024\,R_\oplus$, corresponding to precisions of 8% and 3.4%, respectively. This implies a planetary bulk density of $\rho_b = 10.2 \pm 1.3\,\mathrm{g\,cm^{-3}}$, i.e., 85% higher than Earth's density. We revealed the presence of two additional non-transiting low-mass companions with orbital periods of ~11.5 and 34 days and minimum masses of $M_c \sin i_c = 4.13 \pm 0.36\,M_\oplus$ and $M_d \sin i_d = 6.03 \pm 0.49\,M_\oplus$,

---

* Based on observations made with the ESO-3.6 m telescope at La Silla Observatory under programs 1102.C-0923 and 106.21TJ.001.

[34] NASA Sagan Fellow.

respectively, which lie close to the 3:1 mean motion commensurability. GJ 367 b joins the small class of high-density planets, namely the class of super-Mercuries, being the densest ultra-short period small planet known to date. Thanks to our precise mass and radius estimates, we explored the potential internal composition and structure of GJ 367 b, and found that it is expected to have an iron core with a mass fraction of $0.91^{+0.07}_{-0.23}$. How this iron core is formed and how such a high density is reached is still not clear, and we discuss the possible pathways of formation of such a small ultra-dense planet.

Unified Astronomy Thesaurus concepts: Exoplanet detection methods (489); Exoplanet systems (484); Exoplanets (498); Extrasolar rocky planets (511)

Supporting material: machine-readable table

1. Introduction

Close-in planets with orbital periods of a few days challenge planet formation and evolution theories and play a key role in the architecture of exoplanetary systems (Winn & Fabrycky 2015; Zhu & Dong 2021). To date, about 132 ultra-short period (USP) planets, namely planets with orbital periods shorter than 1 day (Sahu et al. 2006; Sanchis-Ojeda et al. 2014), have been validated, and only 36 of these were confirmed and have measured radii and masses.[35] USPs are preferred targets for transit and radial velocity (RV) planet search surveys, as the transit probability is higher—it scales as $P_{\rm orb}^{-2/3}$—and the Doppler reflex motion is larger—it scales as $P_{\rm orb}^{-1/3}$. In addition, their orbital period is typically 1 order of magnitude shorter than the rotation period of the star, allowing one to disentangle bona fide planetary signals from stellar activity (Hatzes et al. 2011; Hatzes 2019; Winn et al. 2018).

Sanchis-Ojeda et al. (2014) found that the occurrence rate of rocky USP planets seems to depend on the spectral type of the host star, being $0.15 \pm 0.05\%$ for F dwarfs, $0.51\% \pm 0.07\%$ for G dwarfs, and $1.10\% \pm 0.40\%$ for M dwarfs. In this context, low-mass stars, such as M dwarfs, are particularly suitable to search for close-in terrestrial planets. Given the relatively small stellar radius and mass, a planet transiting an M-dwarf star induces both a deeper transit and a larger RV signal, increasing its detection probability (Cifuentes et al. 2020).

The formation process of USP planets is still not fully understood, and different scenarios have been proposed to explain their short-period orbits: dynamical interactions in multiplanet systems (Schlaufman et al. 2010); low-eccentricity migration due to secular planet–planet interactions (Pu & Lai 2019); high-eccentricity migration due to secular dynamical chaos (Petrovich et al. 2019); tidal orbital decay of USP planets formed in situ (Lee & Chiang 2017); and obliquity-driven tidal migration (Millholland & Spalding 2020). Intensive follow-up observations of systems hosting USP planets can help us to understand the formation and evolution mechanisms of short-period objects and other phenomena related to star–planet interactions (Serrano et al. 2022).

Sanchis-Ojeda et al. (2014), Adams et al. (2017), and Winn et al. (2018) found that most USP planets have nearby planetary companions. In multiplanet systems, USP planets show wider-than-usual period ratios with their nearest companion, and appear to have larger mutual inclinations than planets on outer orbits (Rodriguez et al. 2018; Dai et al. 2018). These observations suggest that USP planets experienced a change in their orbital parameters, such as inclination increase and orbital shrinkage, suggesting the presence of long-period planets.

During its primary mission, NASA's Transiting Exoplanet Survey Satellite (TESS; Ricker et al. 2015) discovered a shallow (∼300 ppm) transit event repeating every ∼7.7 hr (∼0.32 days) and associated to a USP small planet candidate orbiting the bright ($V \approx 10.2$), nearby ($d \approx 9.4$ pc), M1 V star GJ 367. Lam et al. (2021) recently confirmed GJ 367 b as a bona fide USP sub-Earth with a radius of $R_{\rm b} = 0.718 \pm 0.054\, R_{\oplus}$ and a mass of $M_{\rm b} = 0.546 \pm 0.078\, M_{\oplus}$.

As the majority of well-characterized USP systems are consistent with having additional planetary companions (Dai et al. 2021), it is quite realistic to believe that the GJ 367 hosts more than one planet. As part of the RV follow-up program carried out by the KESPRINT consortium,[36] we here present the results of an intensive RV campaign conducted with the HARPS spectrograph to refine the mass determination of the transiting USP planet and search for external planetary companions, while probing the architecture of the GJ 367 planetary system.

The paper is organized as follows: we provide a summary of the TESS data and describe our HARPS spectroscopic follow-up in Section 2. Stellar fundamental parameters are presented in Section 3. We report on the RV and transit analysis in Sections 4 and 5, along with the frequency analysis of our HARPS time series. Discussion and conclusions are given in Sections 6 and 7, respectively.

2. Observations

2.1. TESS Photometry

TESS observed GJ 367 in Sector 9 as part of its primary mission, from 2019 February 28 to 2019 March 26, with CCD 1 of camera 3 at a cadence of 2 minutes. These observations have been presented in Lam et al. (2021). About 2 yr later, TESS re-observed GJ 367 as part of its extended mission in Sectors 35 and 36, from 2021 February 9 to 2021 April 2, with CCD 1 and 2 of camera 3 at a higher cadence of 20 s as well as at 2 minutes. The photometric data were processed by the TESS data processing pipeline developed by the Science Processing Operations Center (SPOC; Jenkins et al. 2016). The SPOC pipeline uses Simple Aperture Photometry (SAP) to generate stellar light curves, where common instrumental systematics are removed via the Presearch Data Conditioning (PDCSAP) algorithm developed for the Kepler space mission (Stumpe et al. 2012, 2014; Smith et al. 2012).

We retrieved TESS Sector 9, 35, and 36 data from from the Mikulski Archive for Space Telescopes (MAST)[37] and performed our data analyses using the PDCSAP light curve. We ran the Détection Spécialisée de Transits (DST;

---

[35] See https://exoplanetarchive.ipac.caltech.edu, as of May 2023.

[36] https://kesprint.science/

[37] https://mast.stsci.edu/portal/Mashup/Clients/Mast/Portal.html

Cabrera et al. 2012) algorithm to search for additional transit signals and found no significant detection besides the 7.7 h signal associated to GJ 367 b, suggesting that there are no other transiting planets in the system observed in TESS Sector 9, 35, and 36, consistent with the SPOC multitransiting planet search.

2.2. HARPS High-precision Doppler Follow-up

GJ 367 was observed with the High Accuracy Radial velocity Planet Searcher (HARPS) spectrograph (Mayor et al. 2003), mounted at the ESO-3.6 m telescope of La Silla Observatory in Chile. We collected 295 high-resolution ($R \approx 115{,}000$, $\lambda \in$378–691 nm) spectra between 2020 November 9 and 2022 April 18 (UT), as part of our large observing program 106.21TJ.001 (PI: Gandolfi) to follow-up TESS transiting planets. When added to the 77 HARPS spectra published in Lam et al. (2021), our data includes 371 HARPS spectra.

The exposure time varied between 600 and 1200 s, depending on weather conditions and observing schedule constraints, leading to a signal-to-noise ratio (S/N) per pixel at 550 nm ranging between 20 and 90, with a median of ∼55. We used the second fiber of the instrument to simultaneously observe a Fabry–Perot interferometer and trace possible nightly instrumental drifts (Wildi et al. 2010, 2011). The HARPS data were reduced using the Data Reduction Software (DRS; Lovis & Pepe 2007) available at the telescope. The RV measurements, as well as the Hα, Hβ, Hγ, Na D activity indicators, log $R'_{\rm HK}$, the differential line width (DLW), and the chromaticity index (CRX), were extracted using the codes NAIRA (Astudillo-Defru et al. 2017b) and SERVAL (Zechmeister et al. 2017). NAIRA and SERVAL feature template matching algorithms that are suitable to derive precise RVs for M-dwarf stars, when compared to the cross-correlation function technique implemented in the DRS. We tested both the NAIRA and SERVAL RV time series and found no significant difference in the fitted parameters. While we have no reason to prefer one code over the other, we used the RV data extracted with NAIRA for the analyses described in the following sections.

Table A1 lists the HARPS RVs, including those previously reported in Lam et al. (2021), along with the activity indicators and line profile variation diagnostics extracted with NAIRA and SERVAL. Time stamps are given in Barycentric Julian Date in the Barycentric Dynamical Time (BJD$_{\rm TDB}$).

2.3. HARPS Spectropolarimetric Observations

With the aim of measuring the magnetic field of GJ 367, we performed a single circular polarization observation with the HARPSpol polarimeter (Piskunov et al. 2011; Snik et al. 2011) on 2022 November 16 (UT), as part of the our ESO HARPS program 1102.C-0923 (PI: Gandolfi). We used an exposure time of 3600 s split in four $T_{\rm exp} = 900$ s subexposures obtained with different configuration of polarization optics to ensure cancellation of the spurious instrumental signals (see Donati et al. 1997; Bagnulo et al. 2009). The data reduction was carried out with the REDUCE code (Piskunov & Valenti 2002) following the steps described in Rusomarov et al. (2013). The resulting Stokes I (intensity) and Stokes V (circular polarization) spectra cover approximately the same wavelength interval as the usual HARPS observations at a slightly reduced resolving power ($R \approx 110{,}000$). We also derived a diagnostic null spectrum (e.g., Bagnulo et al. 2009), which is useful for assessing the presence of instrumental artifacts and non-Gaussian noise in the Stokes V spectra.

Table 1
Fundamental Parameters of GJ 367

Parame2ter	Value	Reference
Name	GJ 367	
	TOI-731	
	TIC 34068865	
R.A. (J2000)	09:44:29.15	[1]
Decl. (J2000)	−45:46:44.46	[1]
TESS-band magnitude	8.032 ± 0.007	[2]
V-band magnitude	10.153 ± 0.044	[3]
Parallax (mas)	106.173 ± 0.014	[1]
Distance (pc)	9.413 ± 0.003	[1]
Star mass M_* ($M_\odot$)	0.455 ± 0.011	[4]
Star radius R_* ($R_\odot$)	0.458 ± 0.013	[4]
Effective temperature T$_{\rm eff}$ (K)	3522 ± 70	[4]
Stellar density ρ_* ($\rho_\odot$)	$4.75^{+0.44}_{-0.39}$	[4]
Metallicity [Fe/H]	−0.01 ± 0.12	[4]
Surface gravity log $g_\star$	4.776 ± 0.026	[4]
Luminosity L_* ($L_\odot$)	$0.0289^{+0.0029}_{-0.0027}$	[4]
log $R'_{\rm HK}$	−5.169 ± 0.068	[4]
Spectral type	M1.0 V	[5]

Note. [1] Gaia Collaboration et al. (2021), [2] TESS input catalog (TIC; Stassun et al. 2018, 2019), [3] Paegert et al. (2022), [4] This work, [5] Koen et al. (2010).

3. Stellar Parameters

3.1. Photospheric and Fundamental Parameters

We derived the spectroscopic parameters using the new coadded HARPS spectrum for GJ 367. Following the prescription in Hirano et al. (2018), we first estimate the stellar effective temperature $T_{\rm eff}$, metallicity [Fe/H], and radius $R_\star$ using `SpecMatch-Emp` (Yee et al. 2017). The code attempts to find a subset of best-matching template spectra from the library to the input spectrum and derives the best empirical values for the above parameters. `SpecMatch-Emp` returned $T_{\rm eff} = 3522 \pm 70$ K, $R_\star = 0.452 \pm 0.045\,R_\odot$, and $[{\rm Fe/H}] = -0.01 \pm 0.12$. We then used those parameters to estimate the other stellar parameters as well as refine $R_\star$. As described in Hirano et al. (2021), we implemented a Markov Chain Monte Carlo (MCMC) simulation and derived the parameters in a self-consistent manner, making use of the empirical formulae by Mann et al. (2015) and Mann et al. (2019) for the derivations of the stellar mass $M_\star$ and radius $R_\star$. We found that GJ 367 has a mass of $M_\star = 0.455 \pm 0.011\,M_\odot$ and a radius of $R_\star = 0.458 \pm 0.013\,R_\odot$, with the latter in very good agreement with the value derived using `SpecMatch-Emp`. In the MCMC implementation, we also derived the stellar density $\rho_\star$, surface gravity $\log g_\star$, and luminosity $L_\star$ of the star. Results of our analysis are listed in Table 1. As the quoted uncertainties of the stellar parameters do not account for possible unknown systematic errors—which in turn might affect the estimates of the planetary parameters—we performed a sanity check and determined the stellar mass and radius using the code BASTA (Aguirre Børsen-Koch et al. 2022). We fitted the derived stellar parameters to the BaSTI isochrones (Hidalgo et al. 2018; science case 4 in Table 1 of the BASTA paper). Starting from the effective temperature, metallicity, and radius, as derived from `SpecMatch-Emp`, yielded a mass of $M_\star = 0.435^{+0.035}_{-0.040}\ M_\odot$

and radius of $R_\star = 0.411^{+0.032}_{-0.034}\ R_\odot$. The stellar mass is in good agreement with the previous result. The new estimate of the stellar radius is smaller than the value reported in Table 1, but it is still consistent within ~1.4 σ (where σ is the sum in quadrature of the two nominal uncertainties) with a p-value of ~15%. Assuming a significance level of 5%, the two radii are consistent, providing evidence that our estimates might not be significantly affected by inaccuracy.

3.2. Rotation Period

Using archival photometry from the Wide Angle Search for Planets survey (WASP), Lam et al. (2021) found a photometric modulation with a period of 48 ± 2 days. Lam et al. (2021) also measured a Ca II H & K chromospheric activity index of $\log R'_{\rm HK} = -5.214 \pm 0.074$ from their 77 HARPS spectra. Based on the $\log R'_{\rm HK}$–rotation empirical relationship for M dwarfs from Astudillo-Defru et al. (2017a), they estimated a stellar rotation period of $P_{\rm rot} = 58.0 \pm 6.9$ days.

We independently derived a Ca II H & K chromospheric activity index of $\log R'_{\rm HK} = -5.169 \pm 0.068$ from the 371 HARPS spectra and estimated the rotation period of GJ 367 using the same empirical relationship. We found a rotation period of $P_{\rm rot} = 54 \pm 6$ d, in good agreement with the previous estimated value. We note that our estimate is consistent within 1σ with the value of $P_{\rm rot} = 51.30 \pm 0.13$ d recovered by our sinusoidal signal analysis described in Section 5.2, and with the period of $P_{\rm rot} = 53.67^{+0.65}_{-0.53}$ d derived by our multidimensional Gaussian process (GP) analysis described in Section 5.3.

3.3. Magnetic Field

Our spectropolarimetric observation of GJ 367 achieved a median S/N of about 90 over the red HARPS chip. This is insufficient for detecting Zeeman polarization signatures in individual lines even for the most active M dwarfs. To boost the signal, we made use of the least-squares deconvolution procedure (LSD; Donati et al. 1997) as implemented by Kochukhov et al. (2010). The line mask required for LSD was obtained from the VALD database (Ryabchikova et al. 2015) using the atmospheric parameters of GJ 367 and assuming solar abundances (Section 3.1). We used about 5000 lines deeper than 20% of the continuum for LSD, reaching an S/N of 7250 per 1 km s^{-1} velocity bin. The resulting Stokes V profile has a shape compatible with a Zeeman polarization signature with an amplitude of ≈0.04% (Figure 1). However, with a false-alarm probability (FAP) = 2.3%, detection of this signal is not statistically significant according to the usual detection criteria employed in high-resolution spectropolarimetry (Donati et al. 1997). The mean longitudinal magnetic field, which represents the disk-averaged line-of-sight component of the global magnetic field, derived from this Stokes V profile is $\langle B_z \rangle = -7.3 \pm 3.2$ G.

Our spectropolarimetric observation of GJ 367 suggests that this object is not an active M dwarf. Its longitudinal magnetic field was found to be below 10 G, which is much weaker than ⩾100–700 G longitudinal fields typical of active M dwarfs (Donati et al. 2008; Morin et al. 2008). Considering that the strength and topology of the global magnetic fields of M dwarfs is systematically changing with the stellar mass (Kochukhov 2021), it is appropriate to compare GJ 367 with early-M dwarfs. To this end, the well-known ~20 Myr old M1V star AU Mic was observed with HARPSpol in the same configuration and with a similar S/N as our GJ 367 observations (Kochukhov & Reiners 2020), yielding consistent detections of polarization signatures and longitudinal fields of up to 50 G. The magnetic activity of GJ 367 is evidently well below that of AU Mic.

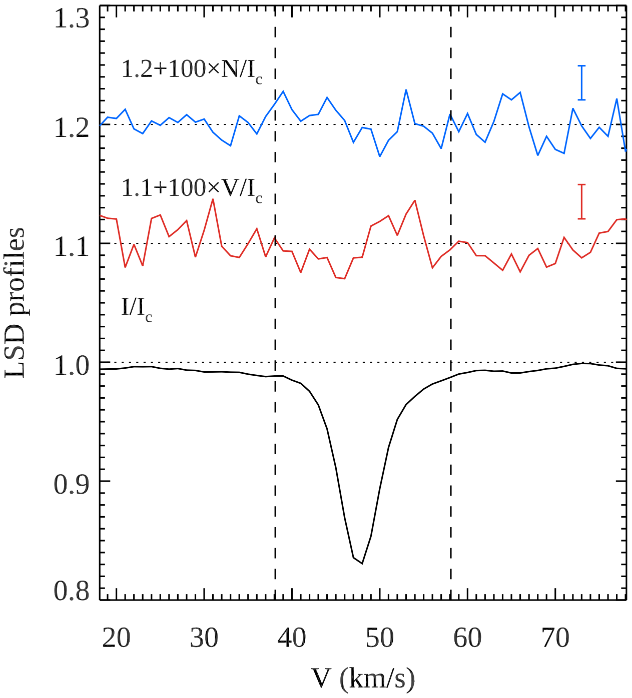

Figure 1. Least-squares deconvolved (LSD) Stokes I, V and null profiles of GJ 367. The polarization profiles are shifted vertically and expanded by a factor of 100 relative to the intensity profile. The vertical dashed lines indicate velocity interval adopted for the longitudinal field measurement.

3.4. Age

Determining the age of M-dwarf stars is especially challenging and depends on the methods being utilized. Lam et al. (2021) estimated an isochronal age of $8.0^{+3.8}_{-4.6}$ Gyr and a gyrochronological age of 4.0 ± 1.1 Gyr for GJ 367. More recently, Brandner et al. (2022) gave two different estimates: (1) by comparing Gaia EDR3 parallax and photometric measurements with theoretical isochrones, they suggested a young age < 60 Myr. However, as pointed out by the authors, this is not in line with the star's Galactic kinematics that exclude membership to any nearby young moving group; (2) by considering the Galactic dynamical evolution, which indicates an age of 18 Gyr.

In this respect, the results presented in our study shows compelling evidence that GJ 367 is not a young star:

1. The time series of our HARPS RVs and activity indicators give a clear detection of a spot-induced rotation modulation with a period of about 52–54 days, which translates into a gyrochronological age of ~4.6–4.8 Gyr (Barnes 2010; Barnes & Kim 2010).
2. The HARPS spectra of GJ 367 show no significant lithium absorption line at 6708 Å. Figure 2 displays the coadded HARPS spectrum of AU Mic (Zicher et al. 2022; Klein et al. 2022) in the spectral region around the Li I 6708 Å line. AU Mic is a well-known 22-Myr-old M1 star located in the β Pictoris moving group

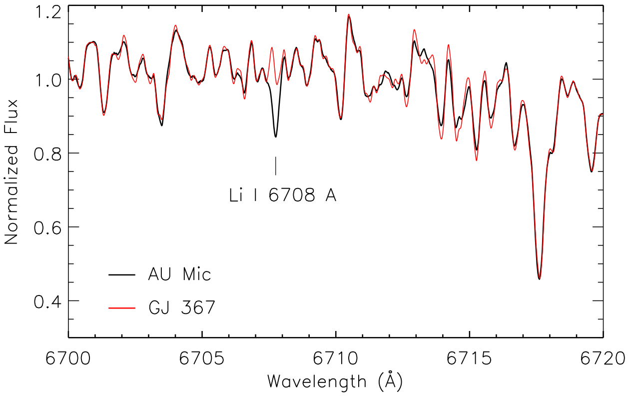

Figure 2. Coadded HARPS spectrum of AU Mic (black line) in the spectral region encompassing the Li I 6708 Å absorption line. Superimposed with a thick red line is the coadded HARPS spectrum of GJ 367, which has been rotationally broadened to match the $v \sin i_\star = 7.8$ km s^{-1} of AU Mic.

(Mamajek & Bell 2014). Superimposed with a thick red line is GJ 367's coadded HARPS spectrum, which has been broadened to match the projected rotational velocity of AU Mic ($v \sin i_\star = 7.8$ km s^{-1}). Since lithium is quickly depleted in young GKM stars, the lack of lithium in the spectrum of GJ 367 suggests an age $\gtrsim$50 Myr (Binks & Jeffries 2014; Binks et al. 2021).

3. The low level of magnetic activity inferred by the Ca H & K indicator $\log R'_{\rm HK}$ (Section 3.2) and the weak magnetic field (Section 3.3) are consistent with an old, inactive M-dwarf scenario (Pace 2013).
4. We measured an average Hα equivalent width of EW $= 0.0638 \pm 0.0014$ Å. Using the empirical relation that connects the Hα equivalent width with stellar age (Kiman et al. 2021), this translates into an age $\gtrsim$300 Myr.

We therefore conclude that GJ 367 is a rather slowly rotating, old star with a low magnetic activity level, rather than a young M dwarf. This conclusion is consistent with a recent study by Gaidos et al. (2023), who measured an age of 7.95 ± 1.31 Gyr from the M-dwarf rotation–age relation.

4. Frequency Analysis of the HARPS Time Series

In order to search for the Doppler reflex motion induced by the USP planet GJ 367 b and unveil the presence of potential additional signals associated with other orbiting companions and/or stellar activity, we performed a frequency analysis of the HARPS RV measurements and activity indicators. For this analysis we did not include the HARPS measurements[38] presented in Lam et al. (2021) and used only the Doppler data collected between 2020 November 9 and 2022 April 18 (UT) as part of our HARPS large program, to avoid spurious peaks introduced by the poor sampling of the existing old data set, and to avoid having to account for the RV offset caused by the refurbishment of the instrument.

Figure 3 shows the generalized Lomb–Scargle (GLS; Zechmeister & Kürster 2009) periodograms of the HARPS RVs and activity indicators in two frequency ranges, i.e., 0.000–0.130 day^{-1} (left panels) and 3.075–3.125 day^{-1} (right panels), with the former including the frequencies at which we expect to see activity signals at the rotation period of the star, and the latter encompassing the orbital frequency of the transiting planet GJ 367 b. The horizontal dashed lines mark the GLS powers at the 0.1%, 1%, and 10% FAP. The FAP was estimated following the bootstrap method described in Murdoch et al. (1993), i.e., by computing the GLS periodogram of 10^6 mock time series obtained by randomly shuffling the measurements and their uncertainties, while keeping the time stamps fixed. In this work we assumed a peak to be significant if its FAP $< 0.1\%$.

The GLS periodogram of the HARPS RVs (Figure 3, upper panel) shows its most significant peak at $f_1 = 0.086$ day^{-1}, corresponding to a period of about 11.5 days. This peak is not detected in the activity indicators, providing evidence that the 11.5 days signal is caused by a second planet orbiting the host star, hereafter referred to as GJ 367 c.

We used the pre-whitening technique (Hatzes et al. 2010) to identify additional significant signals and successively remove them from the RV time series. We employed the code `pyaneti` (Barragán et al. 2019, 2022) to subtract the 11.5 day signal from the HARPS RVs assuming a circular model, adopting uniform priors centered around the period and phase derived from the periodogram analysis, while allowing the systemic velocity and RV semiamplitude to uniformly vary over a wide range.

The periodogram of the RV residuals following the subtraction of the signal at f_1 (Figure 3, second panel) shows its most significant peak at $f_2 = 0.019$ day^{-1} (52.2 days). Iterating the pre-whitening procedure and removing the signal at f_2, we found a significant peak at $f_3 = 0.029$ day^{-1} (34 days). This peak has no significant counterpart in the activity indicators, suggesting it is associated to a third planet orbiting the star, hereafter referred as GJ 367 d (Figure 3, third panel). The periodograms of the CRX, DLW, Hα, Hβ, Hγ, $\log R'_{\rm HK}$, and Na D show significant peaks in the range 48–54 days (Figure 3, lower panels), i.e., close to the rotation period of the star, suggesting that the peak at $f_2 = 0.019$ day^{-1} (52.2 days) seen in the RV residuals is very likely associated to the presence of active regions appearing and disappearing on the visible stellar hemisphere as the star rotates about its axis.

After removing the signal at f_3, we found significant power at $f_4 = 0.009$ day^{-1} (~115 days; Figure 3, fourth panel). The periodograms of the activity indicators show also significant power around f_4, providing evidence this signal is associated to stellar activity. As we will discuss in Section 5.3, we interpreted the power at f_4 as the evolution timescale of active regions. Finally, we found that the RV residuals also show a significant fifth peak at $f_5 = f_{\rm b} = 3.106$ day^{-1} (0.322 day), the orbital frequency of the USP planet GJ 367 b, further confirming the planetary nature of the transit signal identified in the TESS data and announced by Lam et al. (2021).

Finally, we computed the GLS periodogram of the HARPS RVs including all of the available data, i.e., the data acquired before and after the refurbishment of the instrument. Adding the old data points increases the baseline of our observations and, consequently, the frequency resolution. However, the resulting periodogram is "jagged," owing to the presence of aliases with very small frequency spacing, making it more difficult to identify the true peaks.

---

[38] Twenty-four measurements taken with the old fiber bundle between 2003 December 12 and 2010 February 7 (UT) and 77 measurements acquired between 2019 June 23 and 2020 March 23 (UT) with the new fiber bundle.

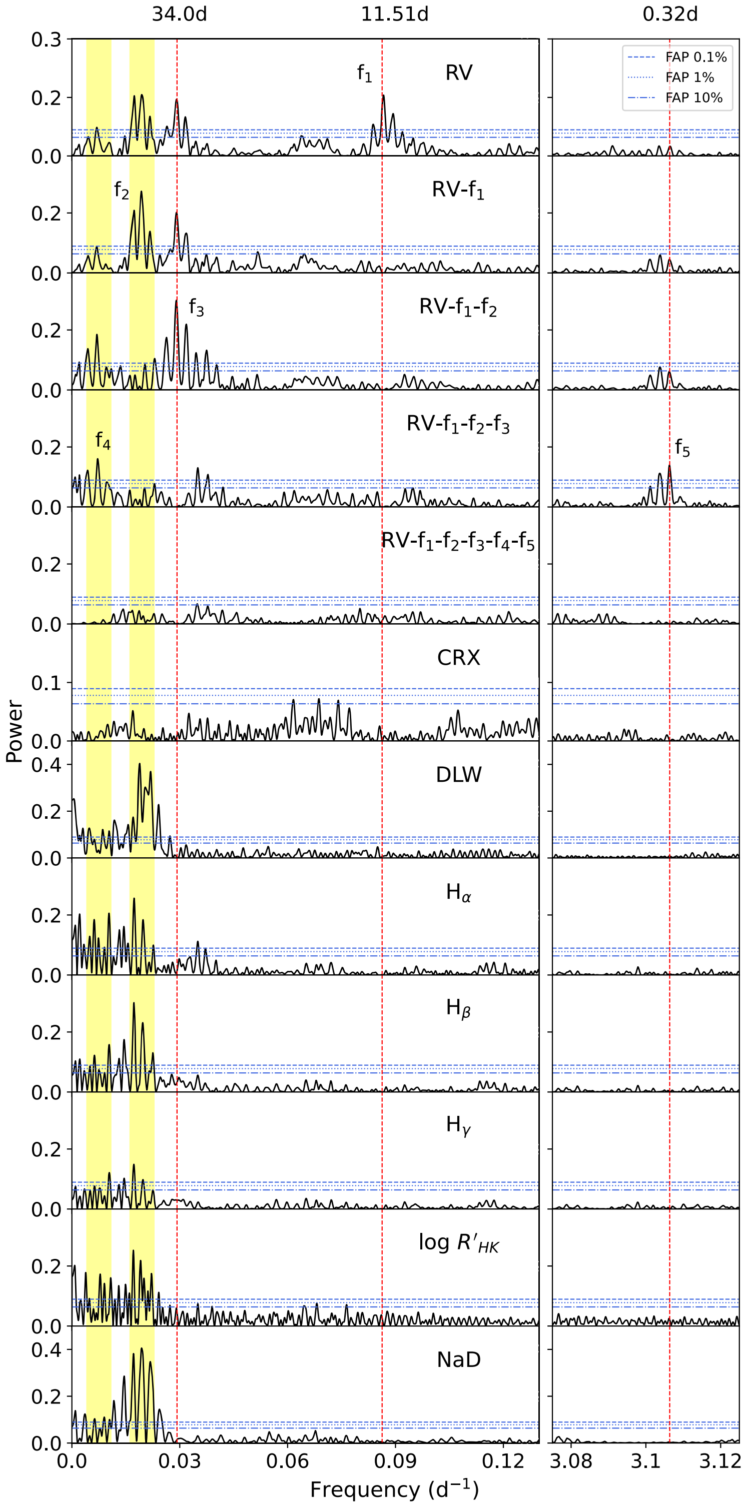

Figure 3. Generalized Lomb–Scargle (GLS) periodograms of the HARPS RV measurements (upper panel); RV residuals after subtracting the f_1 signal at 11.5 days (second panel), the f_2 signal related to stellar activity at 52.2 days (third panel), the f_3 signal at 34 days (fourth panel), and the f_4 and $f_5 = f_{\rm b}$ signals at 115 days and 0.322 days (fifth panel). Also shown are periodograms of the activity indicators (remaining panels). The 10%, 1%, and 0.1% false-alarm probabilities (FAPs) estimated using the bootstrap method are shown with horizontal blue lines. The red vertical lines mark the orbital frequencies of the transiting planet GJ 367 b ($f_5 = f_{\rm b} = 3.106$ day^{-1}), and of the additional Doppler signals we found in the HARPS data, which are associated to the presence of two additional orbiting planets ($f_1 = f_{\rm c} = 0.086$ day^{-1} and $f_3 = f_{\rm d} = 0.029$ day^{-1}). The shaded yellow bands indicate the rotation period of the star centered around f_2, and the long-period stellar signal f_4.

5. Data Analysis

We modeled the TESS transit light curves and HARPS RV measurements using three different approaches. The methods differ in the way the Doppler data are fitted, as described in the following subsections.

5.1. Floating Chunk Offset Method

We used the floating chunk offset (FCO) method to determine the semiamplitude K_{b} of the Doppler reflex motion induced by the USP planet GJ 367 b. Pioneered by Hatzes et al. (2011) for the mass determination of the USP planet CoRoT-7 b, the FCO method relies on the reasonable assumption that, within a single night, the RV variation of the star is mainly induced by the orbital motion of the USP planet rather than stellar rotation, magnetic cycles, or orbiting companions on longer-period orbits. As the RV component due to long-period phenomena can thus be treated as constant within a given night, introducing nightly offsets filters out any long-term RV variations, allowing one to disentangle the reflex motion of the USP planet from additional long-period Doppler signals.

With an orbital period of only 7.7 hr, the USP planet GJ 367 b is suitable to the FCO method (see, e.g., Gandolfi et al. 2017; Barragán et al. 2018). GJ 367 is accessible for up to 8 hr at an airmass < 1.5 (i.e., altitude $> 40°$) from La Silla Observatory, allowing one to cover one full orbit in one single night by acquiring multiple HARPS spectra per night. Within the nightly visibility window of GJ 367, the phase of the long-term signals does not change significantly, the variation being 0.029, 0.010, and 0.006 for the 11.5, 34, and 52 day signals, respectively.

We simultaneously modeled the TESS transit light curves and HARPS RV measurements using the open source software suite `pyaneti` (Barragán et al. 2019, 2022). The code utilizes a Bayesian approach in combination with MCMC sampling to infer the parameters of planetary systems. The photometric data included in the analysis are subsets of the TESS light curve. We selected 2.5 hr of TESS data points centered around each transit and detrended each light-curve segment by fitting a second-order polynomial to the out-of-transit data. Following Hatzes et al. (2011), we divided the HARPS RVs into subsets ("chunks") of nightly measurements and analyzed only those chunks containing at least two RVs per observing night, leading to a total of 96 chunks.

The RV model includes one Keplerian orbit for the transiting planet GJ 367 b and 96 nightly offsets. We fitted for a nonzero eccentricity adopting the parameterization proposed by Anderson et al. (2010) for the eccentricity e and the argument of periastron of the stellar orbit $\omega_\star$ (i.e., $\sqrt{e}\,\sin\omega_\star$ and $\sqrt{e}\,\cos\omega_\star$). We fitted for a photometric and an RV jitter term to account for any instrumental noise not included in the nominal TESS and HARPS uncertainties. We used the limb-darkened quadratic model by Mandel & Agol (2002) for the transit light curve. We adopted Gaussian priors for the limb-darkening coefficients, using the values derived by Claret (2017) for the TESS passband, and we imposed conservative error bars of 0.1 on both the linear and the quadratic limb-darkening term. As the shallow transit light curve of GJ 367 b poorly constrains the scaled semimajor axis ($a_{\mathrm{b}}/R_\star$), we sampled for the stellar density $\rho_\star$ using a Gaussian prior on the star's mass and radius as derived in Section 3, and recovered the scaled semimajor axis of the planet using the orbital period and Kepler's third law of planetary motion (see, e.g., Winn 2010). We adopted uniform priors over a wide range for all of the remaining model parameters. We ran 500 independent Markov chains. The posterior distributions were created using the last 5000 iterations of the converged chains with a thin factor of 10, leading to a distribution of 250,000 data points for each model parameter. The chains were initialized at random values within the priors ranges. This ensured a homogeneous sampling of the parameter space. We followed the same procedure and convergence test as described in Barragán et al. (2019). The final estimates and their 1σ uncertainties were taken as the median and 68% of the credible interval of the posterior distributions. Table 2 reports prior ranges and posterior values of the fitted and derived system parameters. Figure 5 displays the phase-folded RV curve with our HARPS data, along with the best-fitting Keplerian model. Different colors refer to different nights. Figure 4 shows the phase-folded transit light curve of GJ 367 b, along with the TESS data and best-fitting transit model. We found an RV semiamplitude variation of $K_{\mathrm{b}} = 1.003 \pm 0.078\ \mathrm{m\,s^{-1}}$, which translates into a planetary mass of $M_{\mathrm{b}} = 0.633 \pm 0.050\,M_\oplus$ (7.9% precision). The depth of the transit light curve implies a radius of $R_{\mathrm{b}} = 0.699 \pm 0.024\ R_\oplus$ (3.4% precision) for GJ 367 b. When combined together, the planetary mass and radius yield a mean density of $\rho_{\mathrm{b}} = 10.2 \pm 1.3\ \mathrm{g\,cm^{-3}}$ (12.7% precision). The eccentricity of the USP planet ($e_{\mathrm{b}} = 0.06^{+0.07}_{-0.04}$) is consistent with zero, as expected given the short tidal evolution timescale and the age of the system. Assuming a circular orbit, our fit gives an RV semiamplitude of $K_{\mathrm{b}} = 1.001 \pm 0.077\ \mathrm{m\,s^{-1}}$, in excellent agreement with the values listed in Table 2.

We note that 27 of the HARPS RV measurements were taken during transits of GJ 367 b. Assuming the star is seen equator-on ($i_\star = 90°$), its rotation period of $P_{\mathrm{rot}} \approx 51$–$54$ days (Section 3.2) implies an equatorial rotational velocity of $v_{\mathrm{rot}} \approx 0.45\ \mathrm{km\,s^{-1}}$. Using the equations in Triaud (2018), we estimated the semiamplitude of the Rossiter-McLaughlin effect to be $\approx 0.05\ \mathrm{m\,s^{-1}}$, which is too small to cause any detectable effect given our RV uncertainties.

5.2. Sinusoidal Activity Signal Modeling

Using the FCO method, we cannot determine the semiamplitude of the Doppler signals induced by the two outer planets and by stellar activity (Section 4). In the analysis described in this section, we treated the RV signals associated with stellar activity as coherent sinusoidal signals. Once again, we used the code `pyaneti` and performed an MCMC analysis similar to the one described in Section 5.1. The RV model includes three Keplerians, to account for the Doppler reflex motion induced by the three planets GJ 367 b, c, and d, and two additional sine functions, to account for the activity-induced signals at the rotation period of the star (~52 days) and at the evolution timescale of active regions (~115 days), as described in Section 4. We used Gaussian priors for the orbital period and time of first transit of GJ 367 b as derived in Section 5.1, and uniform wide priors for all of the remaining parameters. We fitted for an RV jitter term, as well as for a nonzero eccentricity both for the USP planet, and for the two outer companions, following the e-$\omega_\star$ parameterization proposed by Anderson et al. (2010). Details of the fitted parameters and prior ranges are given in Table 3. We used 500 independent Markov chains initialized randomly inside the prior ranges. Once all chains converged, we used the last 5000 iterations and saved the chain

Table 2
GJ 367 b Parameters from the Joint FCO and Transit Modeling with `pyaneti`

GJ 367 b	Prior	Derived Value
Model parameters		
Orbital period $P_{\mathrm{orb,\ b}}$ [days]	$\mathcal{U}$[0.3219221,0.3219229]	0.3219225 ± 0.0000002
Transit epoch $T_{0,\mathrm{b}}$ [BJD$_{\mathrm{TDB}}$ − 2,450,000]	$\mathcal{U}$[8544.13235,8544.14035]	8544.13635 ± 0.00040
Planet-to-star radius ratio $R_{\mathrm{b}}/R_{\star}$	$\mathcal{U}$[0.001,0.025]	0.01399 ± 0.00028
Impact parameter b_{b}	$\mathcal{U}$[0,1]	$0.584^{+0.034}_{-0.037}$
$\sqrt{e_{\mathrm{b}}}\,\sin\omega_{\star,\mathrm{b}}$	$\mathcal{U}$[-1.0,1.0]	$0.16^{+0.17}_{-0.22}$
$\sqrt{e_{\mathrm{b}}}\,\cos\omega_{\star,\mathrm{b}}$	$\mathcal{U}$[-1.0,1.0]	0.04 ± 0.14
Radial velocity semiamplitude variation K_{b} [m s^{-1}]	$\mathcal{U}$[0,50]	1.003 ± 0.078
Derived parameters		
Planet mass M_{b} [$M_{\oplus}$]	…	0.633 ± 0.050
Planet radius R_{b} [$R_{\oplus}$]	…	0.699 ± 0.024
Planet mean density ρ_{b} [g cm^{-3}]	…	10.2 ± 1.3
Semimajor axis of the planetary orbit a_{b} [au]	…	0.00709 ± 0.00027
Orbit eccentricity e_{b}	…	$0.06^{+0.07}_{-0.04}$
Argument of periastron of stellar orbit $\omega_{\star,\mathrm{b}}$ [deg]	…	66^{+41}_{-108}
Orbit inclination i_{b} [deg]	…	$79.89^{+0.87}_{-0.85}$
Transit duration $\tau_{14,\mathrm{b}}$ [hr]	…	0.629 ± 0.008
Equilibrium temperature $\mathrm{T}_{\mathrm{eq,b}}$ [K][a]	…	1365 ± 32
Received irradiance F_{b} [$\mathrm{F}_{\oplus}$]	…	579^{+57}_{-52}
Additional model parameters		
Stellar density $\rho_{\star}$ [g cm^{-3}]	$\mathcal{N}$[6.68,0.59]	6.76 ± 0.59
Parameterized limb-darkening coefficient q_1	$\mathcal{N}$[0.3766,0.1000]	0.343 ± 0.095
Parameterized limb-darkening coefficient q_2	$\mathcal{N}$[0.1596,0.1000]	$0.163^{+0.096}_{-0.088}$
Radial velocity jitter term $\sigma_{RV,HARPS}$ [m s^{-1}]	$\mathcal{J}$[0,100]	0.43 ± 0.08
TESS jitter term σ_{TESS}	$\mathcal{J}$[0,100]	0.00004 ± 0.00003

Note. $\mathcal{U}[a, b]$ refers to uniform priors between a and b; $\mathcal{N}[a, b]$ refers to Gaussian priors with mean a and standard deviation b; $\mathcal{J}[a, b]$ refers to Jeffrey's priors between a and b. Inferred parameters and uncertainties are defined as the median and the 68.3% credible interval of their posterior distributions.

[a] Assuming zero albedo and uniform redistribution of heat.

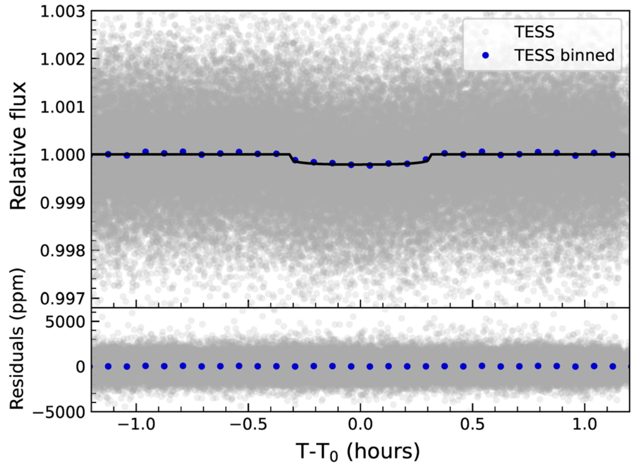

Figure 4. TESS transit light curve of GJ 367 b and best-fitting model folded at the orbital period of the planet.

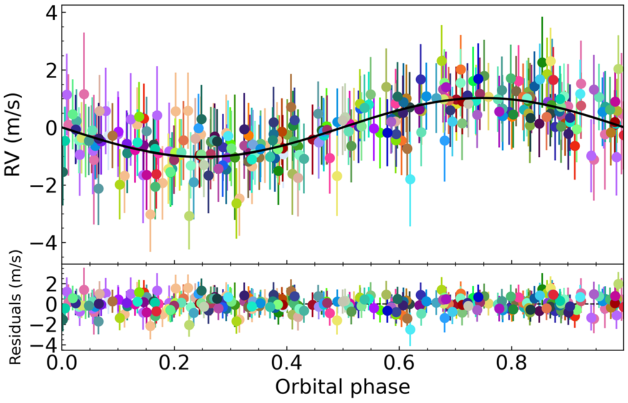

Figure 5. HARPS RVs of GJ 367 phase-folded at the orbital period of the USP planet and best-fitting model as derived using the FCO method. The different colors refer to the 96 different nightly chunks, which include at least two measurements per night.

states every 10 iterations. This approach generated a posterior distribution of 250,000250000 points for each fitted parameter.

The RV semiamplitude variations induced by the three planets are $K_{\mathrm{b}} = 1.10 \pm 0.14\,\mathrm{m\,s^{-1}}$, $K_{\mathrm{c}} = 2.01 \pm 0.15\,\mathrm{m\,s^{-1}}$, and $K_{\mathrm{d}} = 1.98 \pm 0.15\,\mathrm{m\,s^{-1}}$, which imply planetary masses and minimum masses of $M_{\mathrm{b}} = 0.699 \pm 0.083\,M_{\oplus}$, $M_{\mathrm{c}}\sin i_{\mathrm{c}} = 4.08 \pm 0.30\,M_{\oplus}$, and $M_{\mathrm{d}}\sin i_{\mathrm{d}} = 5.93 \pm 0.45\,M_{\oplus}$ for GJ 367 b, c, and d, respectively, whereas the RV semiamplitudes induced by stellar activity signals at 51.3 and 138 days are of $K_{\star,\mathrm{Rot}} = 2.52 \pm 0.13\,\mathrm{m\,s^{-1}}$ and $K_{\star,\mathrm{Evol}} = 1.25 \pm 0.69\,\mathrm{m\,s^{-1}}$. The RV time series along with the best-fitting model are shown in Figure 6. The phase-folded RV curves for each signal are displayed in Figure 7.

5.3. Multidimensional Gaussian Process Approach

We also followed a multidimensional GP approach to account for the stellar signals in our RV time series (Rajpaul et al. 2015). This approach models the RVs along with time

Table 3
System Parameters as Derived Modeling the Stellar Signals with Two Sine Functions

Parameter	Prior	Derived Value
GJ 367 b		
Model parameters		
Orbital period $P_{\rm orb,\ b}$ [days]	$\mathcal{N}$[0.3219225, 0.0000002]	0.3219225 ± 0.0000002
Transit epoch $T_{0,\rm b}$ [BJD$_{\rm TDB}$-2,450,000]	$\mathcal{N}$[8544.1364,0.0004]	8544.13632 ± 0.00040
$\sqrt{e_{\rm b}}\ \sin\omega_{\star,\rm b}$	$\mathcal{U}$[-1.0,1.0]	$-0.23^{+0.30}_{-0.23}$
$\sqrt{e_{\rm b}}\ \cos\omega_{\star,\rm b}$	$\mathcal{U}$[-1.0,1.0]	-0.07 ± 0.13
Radial velocity semiamplitude variation $K_{\rm b}$ [m s^{-1}]	$\mathcal{U}$[0.00, 0.05]	1.10 ± 0.14
Derived parameters		
Planet mass $M_{\rm b}$ [$M_\oplus$][a]	⋯	0.699 ± 0.083
Orbit eccentricity $e_{\rm b}$	⋯	$0.10^{+0.14}_{-0.07}$
Argument of periastron of stellar orbit $\omega_{\star,\rm b}$ [deg]	⋯	251^{+23}_{-102}
GJ 367 c		
Model parameters		
Orbital period $P_{\rm orb,\ c}$ [days]	$\mathcal{U}$[11.4858,11.5858]	11.543 ± 0.005
Time of inferior conjunction T$_{0,\rm c}$ [BJD$_{\rm TDB}$-2,450,000]	$\mathcal{U}$[9152.6591,9154.6591]	9153.46 ± 0.21
$\sqrt{e_{\rm c}}\ \sin\omega_{\star,\rm c}$	$\mathcal{U}$[-1,1]	$0.38\ ^{+0.10}_{-0.13}$
$\sqrt{e_{\rm c}}\ \cos\omega_{\star,\rm c}$	$\mathcal{U}$[-1,1]	$0.27\ ^{+0.11}_{-0.14}$
Radial velocity semiamplitude variation $K_{\rm c}$ [m s^{-1}]	$\mathcal{U}$[0.00, 0.05]	2.01 ± 0.15
Derived parameters		
Planet minimum mass $M_{\rm c}\sin i_{\rm c}$ [$M_\oplus$]	⋯	4.08 ± 0.30
Orbit eccentricity $e_{\rm c}$	⋯	0.23 ± 0.07
Argument of periastron of stellar orbit $\omega_{\star,\rm c}$ [deg]	⋯	55 ± 18
GJ 367 d		
Model parameters		
Orbital period $P_{\rm orb,\ d}$ [days]	$\mathcal{U}$[34.0016,34.6016]	34.39 ± 0.06
Time of inferior conjunction $T_{0,\rm d}$ [BJD$_{\rm TDB}$-2,450,000]	$\mathcal{U}$[9179.2710,9183.2710]	$9180.90\ ^{+0.70}_{-0.81}$
$\sqrt{e_{\rm d}}\ \cos\omega_{\star,\rm d}$	$\mathcal{U}$[-1,1]	$-0.10^{+0.20}_{-0.18}$
$\sqrt{e_{\rm d}}\ \cos\omega_{\star,\rm d}$	$\mathcal{U}$[-1,1]	$0.16^{+0.16}_{-0.20}$
Radial velocity semiamplitude variation $K_{\rm d}$ [m s^{-1}]	$\mathcal{U}$[0.00, 0.05]	1.98 ± 0.15
Derived parameters		
Planet minimum mass $M_{\rm d}\sin i_{\rm d}$ [$M_\oplus$]	⋯	5.93 ± 0.45
Orbit eccentricity $e_{\rm d}$	⋯	$0.08^{+0.07}_{-0.05}$
Argument of periastron of stellar orbit $\omega_{\star,\rm d}$ [deg]	⋯	277^{+58}_{-242}
Stellar activity-induced RV signal		
Rotation period $P_{\star,\rm Rot}$ [days]	$\mathcal{U}$[50.0903,52.0903]	51.30 ± 0.13
Rotation RV semiamplitude $K_{\star,\rm Rot}$ [m s^{-1}]	$\mathcal{U}$[0.00, 0.05]	2.52 ± 0.13
Active region evolution period $P_{\star,\rm Evol}$ [days]	$\mathcal{U}$[103.1797,163.1797]	138 ± 2
Active region evolution RV semiamplitude $K_{\star,\rm Evol}$ [m s^{-1}]	$\mathcal{U}$[0.00, 0.05]	1.25 ± 0.14
Additional model parameters		
Systemic velocity γ_{HARPS} [m s^{-1}]	$\mathcal{U}$[47.806,48.025]	47.91674 ± 0.00013
Radial velocity jitter term $\sigma_{RV,HARPS}$ [m s^{-1}]	$\mathcal{J}$[0,100]	1.59 ± 0.07

Note. $\mathcal{U}[a, b]$ refers to uniform priors between a and b; $\mathcal{N}[a, b]$ refers to Gaussian priors with mean a and standard deviation b; $\mathcal{J}[a, b]$ refers to Jeffrey's priors between a and b. Inferred parameters and uncertainties are defined as the median and the 68.3% credible interval of their posterior distributions.

[a] Assuming an orbital inclination of $i_{\rm b} = 79.89^{+0.87}_{-0.85}$°, from the modeling of TESS transit light curves (Section 5.1).

series of activity indicators assuming that the same GP, a function $G(t)$, can describe them both. The function $G(t)$ represents the projected area of the visible stellar disk that is covered by active regions at a given time. For our best GP analysis, we selected the activity indicator that shows the strongest signal in the periodograms, i.e., the DLW, and modeled the RVs alongside this activity index. We created a two-dimensional GP model via

$$\mathrm{RV} = A_{\rm RV}\,G(t) + B_{\rm RV}\,\dot{G}(t), \qquad (1)$$

$$\mathrm{DLW} = A_{\rm DLW}\,G(t). \qquad (2)$$

The amplitudes $A_{\rm RV}$, $B_{\rm RV}$, and $A_{\rm DLW}$ are free parameters, which relate the individual time series to $G(t)$. The RV data are modeled as a function of $G(t)$ and its time derivative $\dot{G}(t)$, since they depend both on the fraction of the stellar surface covered by active regions, and on how these regions evolve and migrate on the disk. The DLW, which measures the width of the spectral lines, has been proven to be a good tracer of the fraction of the surface covered by active regions, and is thus

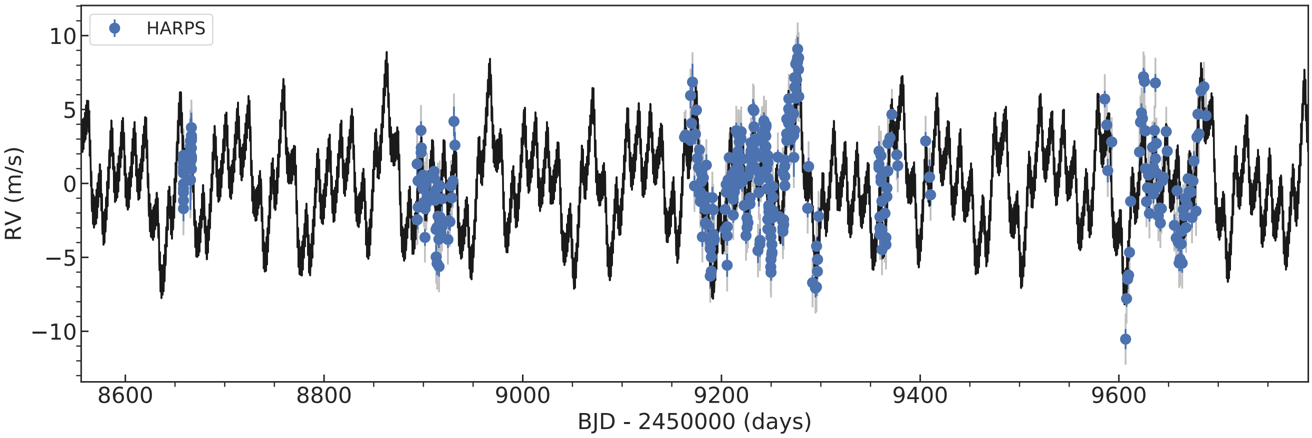

Figure 6. HARPS RV time series of GJ 367 along with the best-fitting five-signal model (three planets + stellar rotation + long-period stellar signal). Data are shown as blue filled circles with their nominal uncertainties. The vertical gray lines mark the error bars including the RV jitter.

expected to be solely proportional to $G(t)$ (Zicher et al. 2022). For our covariance matrix, we used a quasiperiodic kernel

$$\gamma(t_i, t_j) = \exp\left[-\frac{\sin^2[\pi(t_i - t_j)/P_{\rm GP}]}{2\lambda_{\rm p}^2} - \frac{(t_i - t_j)^2}{2\lambda_{\rm e}^2}\right] \quad (3)$$

and its derivatives (Barragán et al. 2022; Rajpaul et al. 2015). The parameter $P_{\rm GP}$ in Equation (3) is the characteristic period of the GP, which is interpreted as the stellar rotation period; $\lambda_{\rm p}$ is the inverse of the harmonic complexity, which is associated with the distribution of active regions on the stellar surface (Aigrain et al. 2015); $\lambda_{\rm e}$ is the long-term evolution timescale, i.e., the active region lifetime on the stellar surface. We performed the multidimensional GP regression using `pyaneti` (described in Barragán et al. 2022), adding three Keplerians to account for the Doppler reflex motion of the three planets, as described in Section 5.2.

We performed an MCMC analysis setting informative Gaussian priors based on the transit ephemeris of the innermost planet GJ 367 b, as derived in Section 5.1, and uniform priors for all of the remaining parameters. We also used uniform priors to sample for the multidimensional GP hyper-parameters. We included a jitter term to the diagonal of the covariance for each time series.

We performed our fit with 500 Markov chains to sample the parameter space. The posterior distributions were created using the last 5000 iterations of the converged chains with a thin factor of 10, leading to a distribution of data points for each fitted parameter. The chains were initialized at random values within the priors ranges. This ensured a homogeneous sampling of the parameter space.

Priors and results are listed are listed in Table 4. Planets GJ 367 b, c, and d are significantly detected in the HARPS RV time series with Doppler semiamplitudes of $K_{\rm b} = 0.86 \pm 0.15\ {\rm m\,s^{-1}}$, $K_{\rm c} = 1.99 \pm 0.17\ {\rm m\,s^{-1}}$, and $K_{\rm d} = 2.03 \pm 0.16\ {\rm m\,s^{-1}}$, respectively. These imply planetary masses and minimum masses of $M_{\rm b} = 0.546 \pm 0.093\,M_\oplus$, $M_{\rm c}\sin i_{\rm c} = 4.13 \pm 0.36\,M_\oplus$, and $M_{\rm d}\sin i_{\rm d} = 6.03 \pm 0.49\,M_\oplus$. The resulting GP hyper-parameters are $P_{\rm GP} = 53.67^{+0.65}_{-0.53}$ days, $\lambda_{\rm p} = 0.44 \pm 0.05$, and $\lambda_{\rm e} = 114 \pm 19$ days. The characteristic period $P_{\rm GP}$ is in agreement with the stellar rotation period, as discussed in Section 3.2, as well as the long-term evolution timescale $\lambda_{\rm e}$, which is in agreement with the long-period signal found in the analyses of Sections 4 and 5.2.

Figure 8 shows the RV and DLW time series, along with the inferred models, whereas Figure 9 displays the phase-folded RV curves of the three planets and the best-fitting models.

6. Discussion

The three techniques used to determine the mass of GJ 367 b give results that are consistent to within $\sim 1\sigma$. We adopted the results from the FCO method, which gives a planetary mass of $M_{\rm b} = 0.633 \pm 0.050\,M_\oplus$ (7.9% precision). Our result differs by about $\sim 1\sigma$ from the mass of $M_{\rm b} = 0.546 \pm 0.078\,M_\oplus$ reported by Lam et al. (2021), which was also derived using the FCO method applied on 20 HARPS data chunks that do not entirely cover the orbital phase of the USP planet, as opposed to our 96 chunks. We found that GJ 367 b has a radius of $R_{\rm b} = 0.699 \pm 0.024\,R_\oplus$ (3.4% precision), consistent with the value of $R_{\rm b} = 0.718 \pm 0.054\,R_\oplus$ from Lam et al. (2021), but more precise, thanks to the additional TESS photometry and increased cadence. Lam et al. (2021) reported a density of $\rho_{\rm b} = 8.1 \pm 2.2\ {\rm g\,cm^{-3}}$. The higher mass but similar radius measured in this work make the USP planet denser, with a ultra-high density of $\rho_{\rm b} = 10.2 \pm 1.3\ {\rm g\,cm^{-3}}$.

GJ 367 b belongs to the handful of small USP planets ($R_{\rm p} < 2\,R_\oplus$, $M_{\rm p} < 10\,M_\oplus$) whose masses and radii are known with a precision better than 20%. Figure 10 shows the mass–radius diagram for small USP planets along with the theoretical composition models for rocky worlds (Zeng et al. 2016). GJ 367 b is the smallest and densest USP planet known to date. The position of the planet on the mass–radius diagram suggests that its composition is dominated by iron. Taking into account its mean density, GJ 367 b leads the class of super-Mercuries, namely, extremely dense planets containing an excess of iron, analogous to Mercury: K2-229 b (Santerne et al. 2018), K2-38 b (Toledo-Padrón et al. 2020), K2-106 b (Guenther et al. 2017), Kepler-107 c (Bonomo et al. 2019), Kepler-406 b (Marcy et al. 2014), HD 137496b (Azevedo Silva et al. 2022), HD 23472b (Barros et al. 2022), and TOI-1075b (Essack et al. 2022).

The two nontransiting planets GJ 367 c and GJ 367 d have orbital periods of ∼11.5 d and 34.4 days, respectively, and minimum masses of $M_{\rm c}\sin i_{\rm c} = 4.13 \pm 0.36\,M_\oplus$ and $M_{\rm d}\sin i_{\rm d} = 6.03 \pm 0.49\,M_\oplus$, as derived adopting the multidimensional GP

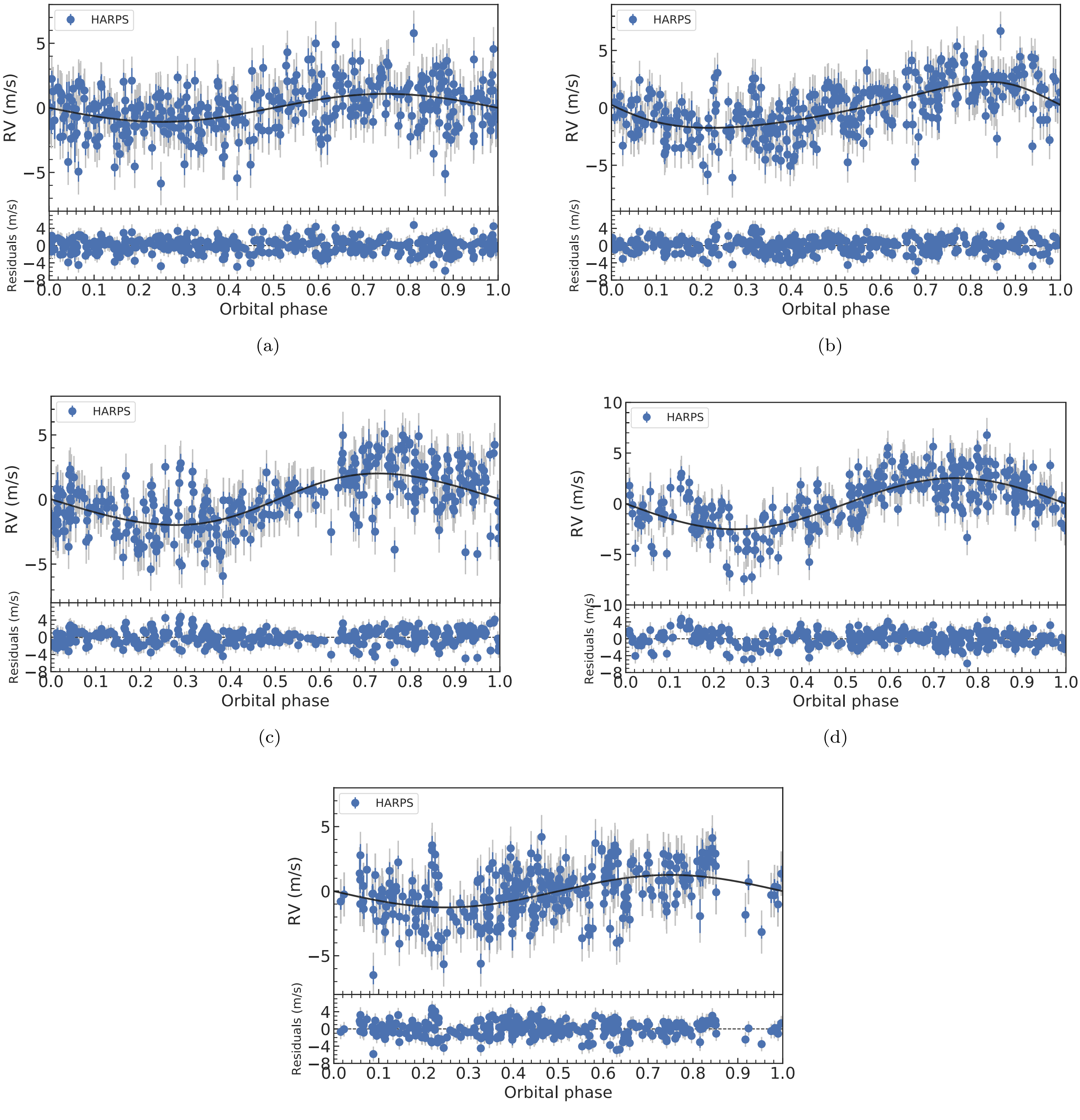

(a)

(b)

(c)

(d)

(e)

Figure 7. Phase-folded RV curves of GJ 367 b (a), GJ 367 c (b), GJ 367 d (c), stellar rotation (d), and long-period stellar signal (e). Data are shown as blue filled circles with their nominal uncertainties. The vertical gray lines mark the error bars including the RV jitter.

approach to model stellar activity (Section 5.3). We note that our minimum mass determinations are in very good agreement with those of $M_{\rm c} \sin i_{\rm c} = 4.08 \pm 0.30\, M_\oplus$ and $M_{\rm d} \sin i_{\rm d} = 5.93 \pm 0.45\, M_\oplus$ that we determined modeling stellar activity with two sinusoidal components (Section 5.2).

If the orbits of GJ 367 b, c, and d were coplanar ($i_{\rm b} = i_{\rm c} = i_{\rm d} = 79\overset{\circ}{.}9$), planets c and d would have true masses of $M_{\rm c} = 4.19 \pm 0.35\, M_\oplus$ and $M_{\rm d} = 6.12 \pm 0.48\, M_\oplus$, respectively. Using the mass–radius relation for small rocky planets from Otegi et al. (2020), we found that GJ 367 c and d are expected to have radii of ∼1.6 and ∼1.7 $R_\oplus$, respectively, making them two super-Earths with mean densities of $\sim 6\,{\rm g\,cm^{-3}}$. We searched the TESS light curves for possible transits of the two outer companions with the DST code (Section 2.1) masking out the transits of the UPS planet, but we found no other significant transit signals. Under the assumption that the orbits of the three planets are coplanar, the impact parameters of planets c and d would be $b_{\rm c} \approx 6$ and $b_{\rm d} \approx 13$, respectively. This would account for the nondetection of the transit signals of GJ 367 c and GJ 367 d in the TESS light curves. In this scenario, GJ 367 c and d would transit their host star only if their radii were unphysically large, i.e., $R_c > 1.9\, R_\odot$ and $R_d > 5\, R_\odot$. The other configuration for the outer planets to transit is if they are mutually inclined with planet b ($i_{\rm c} \neq i_{\rm b}$; $i_{\rm d} \neq i_{\rm b}$). This is not an

Table 4
System Parameters as Derived Modeling the Stellar Signals with a GP

Parameter	Prior	Derived Value
GJ 367 b		
Model parameters		
Orbital period $P_{\mathrm{orb,b}}$ [days]	$\mathcal{N}[0.3219225, 0.0000002]$	0.3219225 ± 0.0000002
Transit epoch $T_{0,\mathrm{b}}$ [$\mathrm{BJD_{TDB}} - 2{,}450{,}000$]	$\mathcal{N}[8544.1364, 0.0004]$	8544.13631 ± 0.00038
$\sqrt{e_b}\,\sin\omega_{\star,\mathrm{b}}$	$\mathcal{U}[-1.0,1.0]$	$0.13^{+0.29}_{-0.32}$
$\sqrt{e_b}\,\cos\omega_{\star,\mathrm{b}}$	$\mathcal{U}[-1.0,1.0]$	-0.05 ± 0.21
Radial velocity semiamplitude variation K_{b} [m s^{-1}]	$\mathcal{U}[0.00, 0.05]$	0.86 ± 0.15
Derived parameters		
Planet mass M_{b} [$M_\oplus$][a]	...	0.546 ± 0.093
Orbit eccentricity e_{b}	...	$0.10^{+0.13}_{-0.07}$
Argument of periastron of stellar orbit $\omega_{\star,\mathrm{b}}$ [deg]	...	71^{+60}_{-173}
GJ 367 c		
Model parameters		
Orbital period $P_{\mathrm{orb,c}}$ [days]	$\mathcal{U}[11.4, 11.6]$	11.5301 ± 0.0078
Time of inferior conjunction $T_{0,\mathrm{c}}$ [$\mathrm{BJD_{TDB}} - 2{,}450{,}000$]	$\mathcal{U}[9153.0, 9155.0]$	9153.84 ± 0.30
$\sqrt{e_{\mathrm{c}}}\,\sin\omega_{\star,\mathrm{c}}$	$\mathcal{U}[-1.0,1.0]$	$-0.11^{+0.23}_{-0.20}$
$\sqrt{e_{\mathrm{c}}}\,\cos\omega_{\star,\mathrm{c}}$	$\mathcal{U}[-1.0,1.0]$	$0.14^{+0.19}_{-0.15}$
Radial velocity semiamplitude variation K_{c} [m s^{-1}]	$\mathcal{U}[0.00, 0.05]$	1.99 ± 0.17
Derived parameters		
Planet minimum mass $M_{\mathrm{c}}\sin i_{\mathrm{c}}\,[M_\oplus]$	...	4.13 ± 0.36
Orbit eccentricity e_{c}	...	0.09 ± 0.07
Argument of periastron of stellar orbit $\omega_{\star,\mathrm{c}}$ [deg]	...	-34^{+74}_{-54}
GJ 367 d		
Model parameters		
Orbital period $P_{\mathrm{orb,d}}$ [days]	$\mathcal{U}[30.0,40.0]$	34.369 ± 0.073
Time of inferior conjunction $T_{0,\mathrm{d}}$ [$\mathrm{BJD_{TDB}} - 2{,}450{,}000$]	$\mathcal{U}[9173.0, 9180.0]$	9181.82 ± 1.10
$\sqrt{e_{\mathrm{d}}}\,\sin\omega_{\star,\mathrm{d}}$	$\mathcal{U}[-1.0,1.0]$	-0.09 ± 0.19
$\sqrt{e_{\mathrm{d}}}\,\cos\omega_{\star,\mathrm{d}}$	$\mathcal{U}[-1.0,1.0]$	$-0.30^{+0.20}_{-0.13}$
Radial velocity semiamplitude variation K_{d} [m s^{-1}]	$\mathcal{U}[0.00, 0.05]$	2.03 ± 0.16
Derived parameters		
Planet minimum mass $M_{\mathrm{d}}\sin i_{\mathrm{d}}\,[M_\oplus]$	...	6.03 ± 0.49
Orbit eccentricity e_{d}	...	0.14 ± 0.09
Argument of periastron of stellar orbit $\omega_{\star,\mathrm{d}}$ [deg]	...	-126^{+287}_{-38}
Additional model parameters		
Characteristic period of the GP P_{GP} [days]	$\mathcal{U}[35.0,65.0]$	$53.67^{+0.65}_{-0.53}$
Inverse of the harmonic complexity λ_{p}	$\mathcal{U}[0.1,3.0]$	0.44 ± 0.05
Long-term evolution timescale λ_{e} [days]	$\mathcal{U}[1,300]$	114 ± 19
Amplitude A_{RV} [km s^{-1}]	$\mathcal{U}[0.0,0.005]$	0.0016 ± 0.0004
Amplitude B_{RV} [km s^{-1}]	$\mathcal{U}[-0.05,0.05]$	$0.009^{+0.0025}_{-0.0019}$
Amplitude A_{DLW}	$\mathcal{U}[0.0,30.0]$	$6.31^{+1.42}_{-1.02}$
Systemic velocity γ_{HARPS} [km s^{-1}]	$\mathcal{U}[47.40,48.42]$	47.9168 ± 0.0005
Offset DLW [10^3 m^2 s^{-2}]	$\mathcal{U}[-16.90,14.11]$	$-0.11^{+2.02}_{-1.98}$
Radial velocity jitter term σ_{HARPS} [m s^{-1}]	$\mathcal{J}[0,100]$	1.83 ± 0.08
DLW jitter term σ_{DLW} [m^2 s^{-2}]	$\mathcal{J}[0,1000]$	378^{+145}_{-335}

Note. $\mathcal{U}[a, b]$ refers to uniform priors between a and b; $\mathcal{N}[a, b]$ refers to Gaussian priors with mean a and standard deviation b; $\mathcal{J}[a, b]$ refers to Jeffrey's priors between a and b. Inferred parameters and uncertainties are defined as the median and the 68.3% credible interval of their posterior distributions.

[a] Assuming an orbital inclination of $i_{\mathrm{b}} = 79.89^{+0.87}_{-0.85}$°, from the modeling of TESS transit light curves (Section 5.1).

unusual architecture for systems with USP planets (Dai et al. 2018). With minimum masses of 4.13 $M_\oplus$ and 6.03 $M_\oplus$, GJ 367 c and d are expected to have a minimum radius of ∼1.5 $R_\oplus$ given the maximum collisional stripping limit (Marcus et al. 2009, 2010). The inclination of their orbits should be larger than ∼86.5° to produce nongrazing transits. If the two planets had radii of 1.5 $R_\oplus$, the transit depths would be ∼900 ppm. For 2.5 $R_\oplus$, the nongrazing transit depth is expected to be ∼2500 ppm. Similarly, transit depth of a 4 $R_\oplus$ planet is ∼6400 ppm. The rms of the TESS light curve of GJ 367 is approximately 500 ppm. The expected transit times of planets c and d also fall well within the baseline of the TESS data. Therefore, GJ 367 c and d would be easily detected if they produced nongrazing transits.

The presence of two additional planetary companions to GJ 367 b is in line with the tendency of USP planets to belong

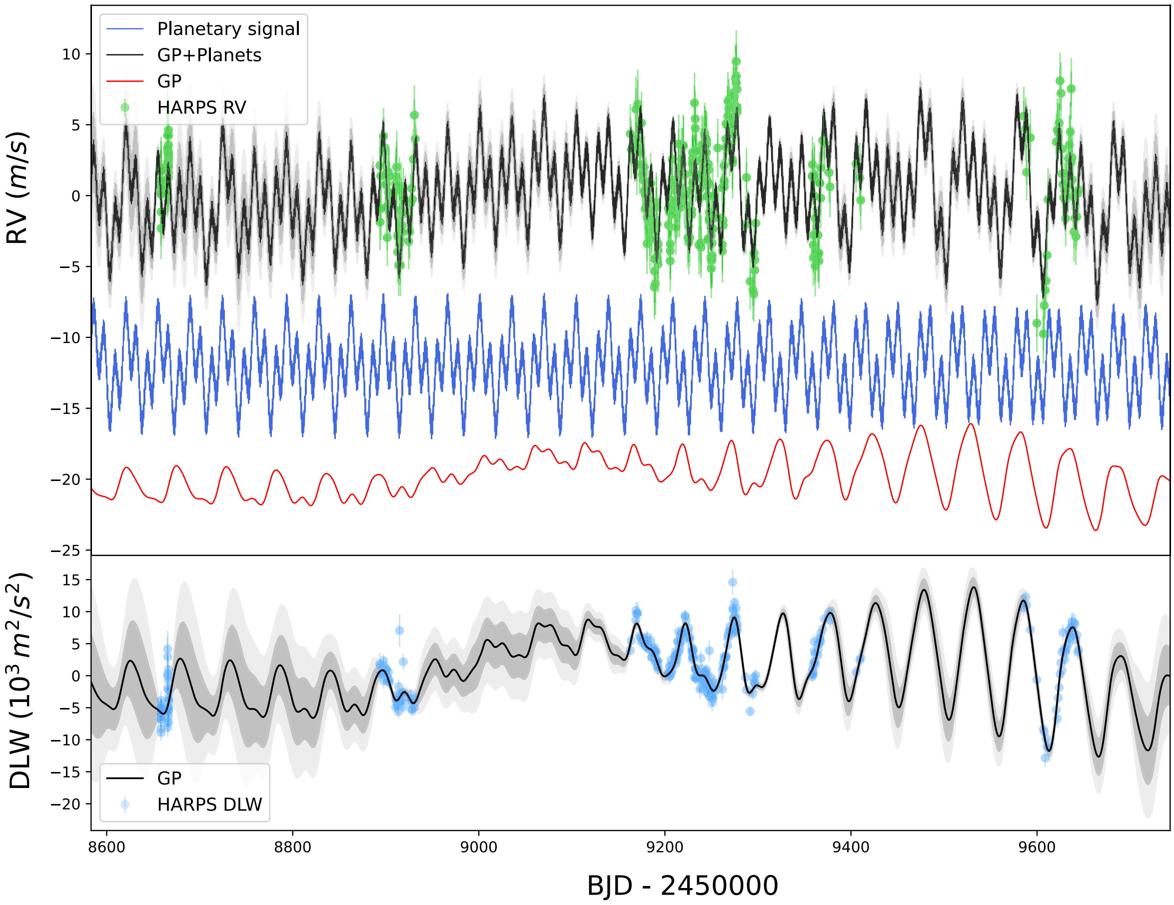

Figure 8. RV and differential line width (DLW) time series with best-fitting models from the multi-GP (solid black lines) and the 1σ and 2σ credible intervals of the corresponding GP models (light gray shaded areas). The upper panel shows the RV data with the full model in black, while the planetary signal (blue), and stellar (red) inferred models are shown with a vertical offset for clarity. The lower panel shows the DLW along with the stellar inferred model. Data are shown with filled circles, with their nominal error bars and semitransparent error bar extensions accounting for the inferred jitter term.

to multiplanet systems (Dai et al. 2021). While the origin of USP planets is debated, it is likely that the presence of outer companions could be responsible for the migration processes that carried USP planets to their current positions (Pu & Lai 2019; Petrovich et al. 2019), which would lie inside the magnetospheric cavity of a typical protoplanetary disk. In these models, planet migration occurs after the dissipation of the protoplanetary disk, by a combination of eccentricity forcing from the planetary companions and tidal dissipation in the innermost planet's interior, although the precise dynamical forcing mechanisms are debated. Serrano et al. (2022) showed, for TOI-500, that the low-eccentricity secular forcing proposed by Pu & Lai (2019) can explain the migration of that system's USP planet from a formation radius of ∼0.02 au to its observed location. For GJ 367 b, we tested this migration scenario with similar initial conditions (USP planet starting at 0.02 au, initial eccentricities of all planets set to 0.2), and found only modest migration of planet b, from 0.02 au to ∼0.01 au, short of the observed 0.007 au. This would support an alternative migration history, such as by high-eccentricity secular chaos (Petrovich et al. 2019). However, we note that GJ 367 c and GJ 367 d lie close to a 3:1 mean motion commensurability, having a period ratio of 2.98, and that the dynamics may be affected by the 3:1 resonance, which can provide additional eccentricity forcing in the system. A deeper analysis would be needed to draw definite conclusions on the formation, migration, and dynamics of the system. The GJ 367 system is thus an excellent target for studying planetary system formation and evolution scenarios.

6.1. Internal Structure of GJ 367 b

Given the high precision of both the derived mass and radius, we used a Bayesian analysis to infer the internal structure of GJ 367 b. We followed the method described in Leleu et al. (2021), which is based on Dorn et al. (2017). Prior to presenting the results of our modeling, we provide the reader with a brief overview over the used model.

Modeling the interior of an exoplanet is a degenerate problem: there is a multitude of different compositions that could explain the observed planetary density. This is why a Bayesian modeling approach is used, with the goal of finding posterior distributions for the internal structure parameters. We assumed a planet that is made up of four fully distinct layers: an inner iron core, a silicate mantle, a water layer, and a gas layer made up of hydrogen and helium. In our forward model, this atmospheric layer is modeled separately from the rest of the planet following Lopez & Fortney (2014), and it is assumed that it does not influence the inner layers. While the presence of a gas and water layer is not expected given the high equilibrium temperature of GJ 367 b, we still included them in the initial model setup, as this is the most general way to model the planet and give us all possible compositions that could lead to the

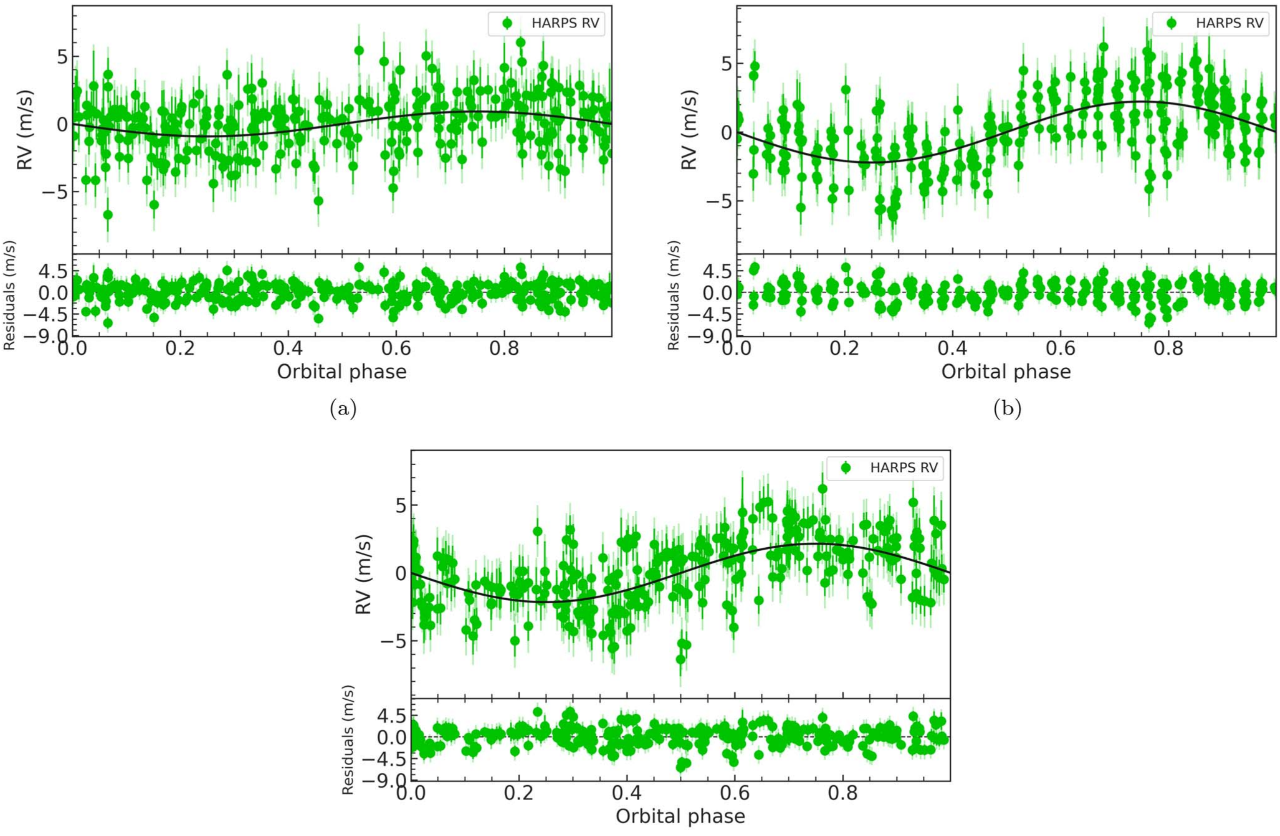

(a) (b)

(d)

Figure 9. Phase-folded RVs curve of GJ 367 b (a), GJ 367 c (b), and GJ 367 d (c). Data are shown as filled green circles with the error bars and the light-green error bars accounting for the inferred RV jitter term.

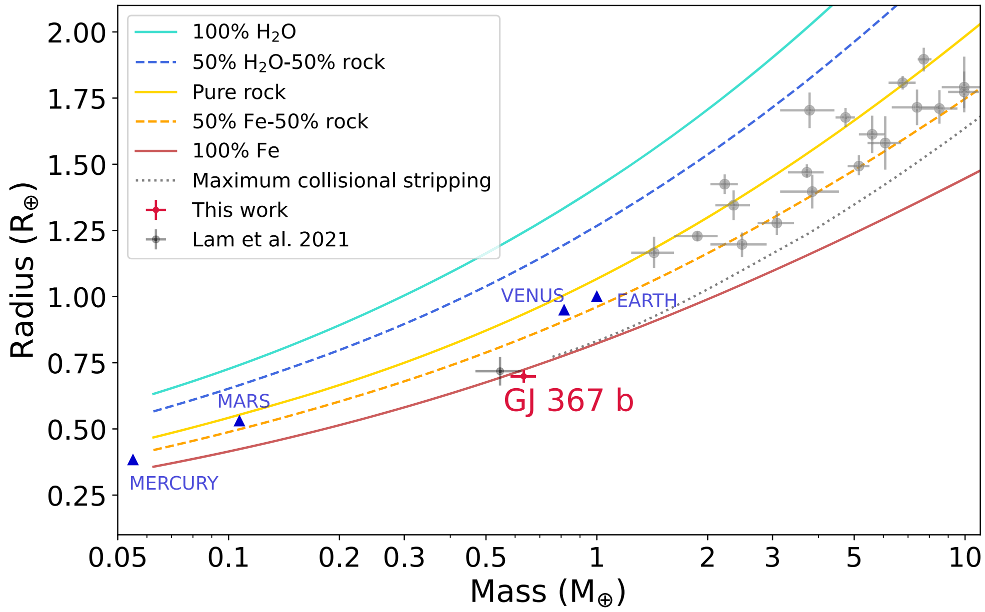

Figure 10. Mass–radius diagram of small USP planets ($P < 1$ days, $R < 2\,R_\oplus$, $M < 10\,M_\oplus$) with masses and radii known with a precision better than 20%, as retrieved from the Transiting Extrasolar Planet Catalogue (Southworth 2011). From bottom to top, the solid and dashed curves are theoretical models from Zeng et al. (2016). We highlighted GJ 367 b with a red dot and the previous position on the diagram with a black dot (Lam et al. 2021).

observed planetary density. As input parameters, we used the planetary and stellar parameters listed in Tables 1 and 2, i.e., the transit depth, RV semiamplitude and period of the planet and the mass, radius, effective temperature, and metallicity of the star. In addition, we chose a prior distribution of 5 ± 5 Gyr for the age of the star.

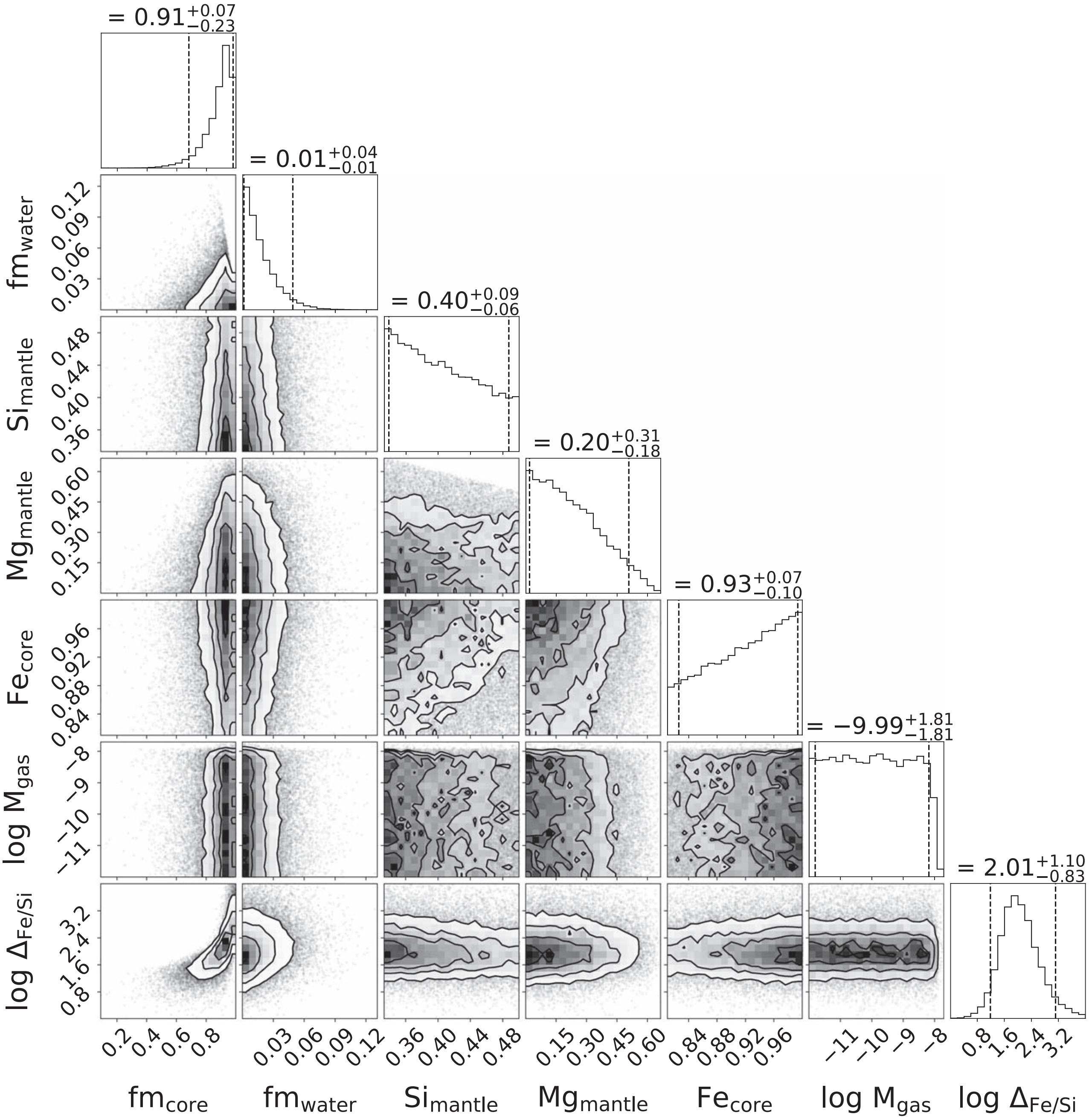

Figure 11. Results of a Bayesian analysis of the internal structure of GJ 367 b. The depicted internal structure parameters are as follows: the mass fractions of the inner iron core and a possible water layer with respect to the solid planet without a possible H/He layer), the molar fractions of Si and Mg within the silicate mantle layer, the molar fraction of iron in the inner core, the logarithm with base 10 of the mass of the H/He layer in Earth masses, and the shift in the Fe/Si ratio of the planet with respect to the Fe/Si ratio in the host star, again in a logarithmic scale. The titles in each column show the median of the posterior distributions and the 5th and 95th percentiles.

For our Bayesian analysis, we chose a prior that is uniform in log for the gas mass fraction of the planet. For the mass fractions of the inner iron core, the silicate mantle, and the water layer (all with respect to the solid part of the planet without the H/He gas layer), our chosen prior is a distribution that is uniform on the simplex on which these three mass fractions add up to one. Additionally, we added an upper limit of 0.5 for the water mass fraction in the planet, as a planet with a pure water composition is not physical (Thiabaud et al. 2014; Marboeuf et al. 2014). Note that choosing very different priors influences the results of the internal structure analysis.

There are multiple studies that show a correlation between the composition of planets and their host star (e.g., Thiabaud et al. 2015; Adibekyan et al. 2021), but it is not clear if this correlation is 1:1 or has a different slope. As a first step, we assumed the composition of the planet to match that of its host star exactly. Since we do not have measured values for the stellar [Si/H] and [Mg/H], we left them unconstrained and sampled the stellar parameters from [Si/H] = [Mg/H] = 0^{+1}_{-1}. However, our analysis showed that the observed mass and radius values of GJ 367 b are not compatible with a 1:1 relationship between the Si/Mg/Fe ratios of the planet and of these sampled synthetic host stars, as it is not possible to reach such a high density under these constraints. The same is true when assuming the steeper slope between stellar and planetary Fe/(Si+Mg) ratios found by Adibekyan et al. (2021). We then repeated our analysis allowing the iron to silicon and iron to magnesium ratios in the planet to be up to a factor 1000 higher than in the sampled stars.

The results of this second analysis are summarized in Figure 11. Indeed, we can see that the Fe/Si ratio in the planet (and therefore also the Fe/Mg ratio) was a factor of 10 to the power of $2.01^{+1.10}_{-0.83}$ higher than in the sampled host star. We further expect GJ 367 b to host no H/He envelope and no significant water layer. Conversely, we expect the mass fraction of the inner iron core with $0.91^{+0.07}_{-0.23}$ (median with 5th and 95th percentiles) to be very high.

6.2. Formation and Evolution of the Ultra-high Density Sub-Earth GJ 367 b

It is not clear how a low-mass high-density planet like GJ 367 b forms. Possible pathways may include the formation out of material significantly more iron rich than thought to be normally present in protoplanetry disks. Although it is not clear if disks with such a large relative iron content specifically near the inner edge (where most of the material might be obtained from) exist (Dullemond & Monnier 2010; Aguichine et al. 2020; Adibekyan et al. 2021)

Another possibility is the formation of a larger planet with a lower bulk density. Subsequently the planet differentiates into a denser core and less dense outer layers. These outer layers are then removed. This may be accomplished through two processes.

(i) A first process is collisional stripping. The preferred removal of outer material in giant collisions (e.g., Marcus et al. 2009; Reinhardt et al. 2022) might have increased the bulk density. Indeed, this is what might have lead to the high iron fraction and therefore high density of Mercury for its small size (Benz et al. 1988, 2007), as a Mercury with a chondritic composition would have a lower density. The amount of maximum stripping is governed by the mass, impact velocity, and impact parameter of the impactor (Marcus et al. 2010; Leinhardt & Stewart 2012). Preferable removal of outer layers requires the right mass ratio (close to unity), right impact parameter (close to grazing), and right relative velocity. There is also evidence that, at least in some systems, densities have been altered by collisions (Kepler-107; Bonomo et al. 2019) A problem to effectively remove mass might be the removal of collision debris and the avoidance of a re-accretion of debris material onto the planet, as re-accretion would leave the bulk density largely unchanged. However, this might not be as large a problem as originally thought (Spalding & Adams 2020). Our measurement of the bulk density of GJ 367 b suggests that collisional stripping has to be remarkably effective in removing non-iron material from the planet if it is the only process at work.

(ii) A second process that might have played a role in shaping GJ 367 b after core formation is removal of outer layers of material facilitated by the enormous stellar radiation to which this planet is subjected. At the equilibrium temperature of 1365 ± 32 K, material might sublimate, be uplifted, and transported away from the surface.

Of course, all of the above discussed processes could have contributed to create the nearly pure ball of iron, known as GJ 367 b.

7. Conclusions

We report refined mass and radius determinations for GJ 367 b, the ultra-high density, USP sub-Earth planet transiting the M-dwarf star GJ 367 recently discovered by Lam et al. (2021). We used new TESS observations from sectors 35 and 36 combined with 371 Doppler measurements collected as part of an intensive RV follow-up campaign with the HARPS spectrograph. We derived a precise planetary mass of $M_{\rm b} = 0.633 \pm 0.050\,M_{\oplus}$ (7.9% precision) and a radius of $R_{\rm b} = 0.699 \pm 0.024\,R_{\oplus}$ (3.4% precision), resulting in an ultra-high density of $\rho_{\rm b} = 10.2 \pm 1.3$ g cm^{-3} (∼13%). According to our internal structure analysis, GJ 367 b is predominantly composed of iron with an iron core mass fraction of $0.91^{+0.07}_{-0.23}$, which accounts for the aforementioned planetary density. In addition, our HARPS RV follow-up observations, which span a period of nearly ∼3 yr, allowed us to discover two additional nontransiting small companions with orbital periods of ∼11.5 and 34.4 days, and minimum masses of $M_{\rm c} \sin i_{\rm c} = 4.13 \pm 0.36\,M_{\oplus}$ and $M_{\rm d} \sin i_{\rm d} = 6.03 \pm 0.49\,M_{\oplus}$. GJ 367 joins the small group of well-characterized multiplanetary systems hosting a USP planet, with the inner planet GJ 367 b being the densest and smallest USP planet known to date. This unique multiplanetary system hosting this ultra-high density, USP sub-Earth is an extraordinary target to further investigate the formation and migration scenarios of USP systems.

Acknowledgments

We thank the anonymous referee for a thoughtful review of our paper and very positive feedback. This work was supported by the KESPRINT collaboration, an international consortium devoted to the characterization and research of exoplanets discovered with space-based missions (www.kesprint.science). Based on observations made with the ESO-3.6 m telescope at La Silla Observatory under programs 1102.C-0923 and 106.21TJ.001. We are extremely grateful to the ESO staff members for their unique and superb support during the observations. We acknowledge the use of public TESS data from pipelines at the TESS Science Office and at the TESS Science Processing Operations Center. TESS data presented in this paper were obtained from the Milkulski Archive for Space Telescopes (MAST) at the Space Telescope Science Institute. The specific observations analyzed can be accessed via doi:10.17909/rkwv-t847. Resources supporting this work were provided by the NASA High-End Computing (HEC) Program through the NASA Advanced Supercomputing (NAS) Division at Ames Research Center for the production of the SPOC data products. E.G. acknowledges the generous support from Deutsche Forschungsgemeinschaft (DFG) of the grant HA3279/14-1. D.G. gratefully acknowledges financial support from the *Cassa di Risparmio di Torino* (CRT) foundation under Grant No. 2018.2323 “Gaseous or rocky? Unveiling the nature of small worlds”. Y.A. and J.A.E. acknowledge the support of the Swiss National Fund under grant 200020_192038. C.M.P. gratefully acknowledges the support of the Swedish National Space Agency (DNR 65/19). R.L. acknowledges funding from University of La Laguna through the Margarita Salas Fellowship from the Spanish Ministry of Universities ref. UNI/551/2021-May 26, and under the EU Next Generation funds. K.W.F.L. was supported by Deutsche Forschungsgemeinschaft grants RA714/14-1 within the DFG Schwerpunkt SPP 1992, Exploring the Diversity of Extrasolar Planets. S.A. acknowledges the support from the Danish Council for Independent Research through grant No. 2032-00230B. O.B. received funding from the ERC under the European Union's Horizon 2020 research and innovation program (grant agreement No. 865624). H.J.D. acknowledges support from the Spanish Research Agency of the Ministry of Science and Innovation (AEI-MICINN) under grant 'Contribution of the IAC to the PLATO Space Mission' with reference PID2019-107061GB-C66. A.J.M. acknowledges support from the Swedish National Space Agency (career grant 120/19C). O.K. acknowledges support by the Swedish Research Council (grant agreement No. 2019-03548), the Swedish National Space Agency, and the Royal Swedish Academy of Sciences. J.K. gratefully acknowledges the support of the Swedish National Space Agency (SNSA; DNR 2020-00104) and of the Swedish Research Council (VR: Etableringsbidrag 2017-04945).

Appendix

We report here the HARPS RVs, including those previously reported in Lam et al. (2021), along with the activity indicators and line profile variation diagnostics extracted with NAIRA and serval (Table A1). Time stamps are given in Barycentric Julian Date in the Barycentric Dynamical Time (BJD_{TDB}).

Table A1

Radial Velocities and Spectral Activity Indicators

$\mathrm{BJD_{TBD}}$ −2450000	RV (km $\mathrm{s^{-1}}$)	σ_{RV} (km $\mathrm{s^{-1}}$)	Hα (Ang)	$\sigma_{\mathrm{H}\alpha}$ (Ang)	Hβ (Ang)	$\sigma_{\mathrm{H}\beta}$ (Ang)	Hγ (Ang)	$\sigma_{\mathrm{H}\gamma}$ (Ang)	log R'_{HK}	$\sigma_{\log \mathrm{R}'\mathrm{HK}}$	NaD (Ang)	σ_{NaD} (Ang)	DLW ($\mathrm{m^2\ s^{-2}}$)	σ_{DLW} ($\mathrm{m^2\ s^{-2}}$)	CRX (m $\mathrm{s^{-1}}$)	σ_{CRX} (m $\mathrm{s^{-1}}$)
8658.45473	47.91637	0.00084	0.06472	0.00012	0.05217	0.00026	0.11412	0.00081	−5.222	0.077	0.01038	0.00007	−7.9	1.3	−10.2	11.1
8658.46195	47.91814	0.00082	0.06421	0.00011	0.05180	0.00025	0.11147	0.00078	−5.180	0.077	0.01040	0.00007	−10.0	1.2	3.4	9.3
8658.46946	47.91502	0.00085	0.06424	0.00012	0.05180	0.00026	0.11413	0.00084	−5.221	0.077	0.01045	0.00007	−6.8	1.2	−17.2	10.7
8658.47642	47.91611	0.00079	0.06417	0.00011	0.05257	0.00025	0.11363	0.00078	−5.130	0.077	0.01041	0.00007	−7.1	1.3	2.8	10.9
8658.48401	47.91860	0.00090	0.06454	0.00012	0.05315	0.00028	0.11124	0.00088	−5.139	0.077	0.01040	0.00008	−7.5	1.4	3.5	11.0
8658.49105	47.91862	0.00087	0.06499	0.00012	0.05417	0.00027	0.11592	0.00086	−5.136	0.077	0.01054	0.00007	−6.1	1.3	4.4	10.9
8658.49842	47.91780	0.00086	0.06548	0.00012	0.05403	0.00027	0.11601	0.00088	−5.151	0.077	0.01074	0.00007	−7.9	1.1	−11.5	10.4
8658.50565	47.91753	0.00091	0.06500	0.00012	0.05374	0.00029	0.11864	0.00092	−5.137	0.077	0.01066	0.00008	−5.0	1.5	9.4	11.2
8658.51297	47.91784	0.00089	0.06466	0.00012	0.05302	0.00028	0.11529	0.00091	−5.175	0.077	0.01057	0.00008	−9.3	1.3	−15.4	10.6
8658.52049	47.91557	0.00083	0.06464	0.00011	0.05272	0.00026	0.11484	0.00085	−5.151	0.077	0.01069	0.00007	−5.7	1.3	6.2	11.1
…	…	…	…	…	…	…	…	…	…	…	…	…	…	…	…	…

Note. The entire RV data set is available in its entirety in machine-readable form. Only a portion of this table is shown here to demonstrate its form and content. A machine-readable version of the full table is available.

(This table is available in its entirety in machine-readable form.)

ORCID iDs

Elisa Goffo https://orcid.org/0000-0001-9670-961X
Davide Gandolfi https://orcid.org/0000-0001-8627-9628
Jo Ann Egger https://orcid.org/0000-0003-1628-4231
Alexander J. Mustill https://orcid.org/0000-0002-2086-3642
Simon H. Albrecht https://orcid.org/0000-0003-1762-8235
Teruyuki Hirano https://orcid.org/0000-0003-3618-7535
Oleg Kochukhov https://orcid.org/0000-0003-3061-4591
Nicola Astudillo-Defru https://orcid.org/0000-0002-8462-515X
Oscar Barragan https://orcid.org/0000-0003-0563-0493
Luisa M. Serrano https://orcid.org/0000-0001-9211-3691
Artie P. Hatzes https://orcid.org/0000-0002-3404-8358
Yann Alibert https://orcid.org/0000-0002-4644-8818
Eike Guenther https://orcid.org/0000-0002-9130-6747
Fei Dai https://orcid.org/0000-0002-8958-0683
Kristine W. F. Lam https://orcid.org/0000-0002-9910-6088
Szilárd Csizmadia https://orcid.org/0000-0001-6803-9698
Alexis M. S. Smith https://orcid.org/0000-0002-2386-4341
Luca Fossati https://orcid.org/0000-0003-4426-9530
Rafael Luque https://orcid.org/0000-0002-4671-2957
Florian Rodler https://orcid.org/0000-0003-0650-5723
Mark L. Winther https://orcid.org/0000-0003-1687-3271
Jakob L. Rørsted https://orcid.org/0000-0001-9234-430X
William D. Cochran https://orcid.org/0000-0001-9662-3496
Hans J. Deeg https://orcid.org/0000-0003-0047-4241
Jon M. Jenkins https://orcid.org/0000-0002-4715-9460
Judith Korth https://orcid.org/0000-0002-0076-6239
John H. Livingston https://orcid.org/0000-0002-4881-3620
Annabella Meech https://orcid.org/0000-0002-7500-7173
Felipe Murgas https://orcid.org/0000-0001-9087-1245
Jaume Orell-Miquel https://orcid.org/0000-0003-2066-8959
Hannah L. M. Osborne https://orcid.org/0000-0002-4143-4767
Enric Palle https://orcid.org/0000-0003-0987-1593
Carina M. Persson https://orcid.org/0000-0003-1257-5146
Seth Redfield https://orcid.org/0000-0003-3786-3486
George R. Ricker https://orcid.org/0000-0003-2058-6662
Sara Seager https://orcid.org/0000-0002-6892-6948
Roland Vanderspek https://orcid.org/0000-0001-6763-6562
Vincent Van Eylen https://orcid.org/0000-0001-5542-8870
Joshua N. Winn https://orcid.org/0000-0002-4265-047X

References

Adams, E. R., Jackson, B., Endl, M., et al. 2017, AJ, 153, 82
Adibekyan, V., Dorn, C., Sousa, S. G., et al. 2021, Sci, 374, 330
Aguichine, A., Mousis, O., Devouard, B., & Ronnet, T. 2020, ApJ, 901, 97
Aguirre Børsen-Koch, V., Rørsted, J. L., Justesen, A. B., et al. 2022, MNRAS, 509, 4344
Aigrain, S., Llama, J., Ceillier, T., et al. 2015, MNRAS, 450, 3211
Anderson, D. R., Cameron, A. C., Hellier, C., et al. 2010, ApJL, 726, L19
Astudillo-Defru, N., Delfosse, X., Bonfils, X., et al. 2017a, A&A, 600, A13
Astudillo-Defru, N., Forveille, T., Bonfils, X., et al. 2017b, A&A, 602, A88
Azevedo Silva, T., Demangeon, O. D. S., Barros, S. C. C., et al. 2022, A&A, 657, A68
Bagnulo, S., Landolfi, M., Landstreet, J. D., et al. 2009, PASP, 121, 993
Barnes, S. A. 2010, ApJ, 722, 222
Barnes, S. A., & Kim, Y.-C. 2010, ApJ, 721, 675
Barragán, O., Aigrain, S., Rajpaul, V. M., & Zicher, N. 2022, MNRAS, 509, 866
Barragán, O., Gandolfi, D., & Antoniciello, G. 2019, MNRAS, 482, 1017
Barragán, O., Gandolfi, D., Dai, F., et al. 2018, A&A, 612, A95
Barros, S. C. C., Demangeon, O. D. S., Alibert, Y., et al. 2022, A&A, 665, A154
Benz, W., Anic, A., Horner, J., & Whitby, J. A. 2007, SSRv, 132, 189
Benz, W., Slattery, W. L., & Cameron, A. G. W. 1988, Icar, 74, 516
Binks, A. S., & Jeffries, R. D. 2014, MNRAS, 438, L11
Binks, A. S., Jeffries, R. D., Jackson, R. J., et al. 2021, MNRAS, 505, 1280
Bonomo, A. S., Zeng, L., Damasso, M., et al. 2019, NatAs, 3, 416
Brandner, W., Calissendorff, P., Frankel, N., & Cantalloube, F. 2022, MNRAS, 513, 661
Cabrera, J., Csizmadia, S., Erikson, A., Rauer, H., & Kirste, S. 2012, A&A, 548, A44
Cifuentes, C., Caballero, J. A., Cortés-Contreras, M., et al. 2020, A&A, 642, A115
Claret, A. 2017, A&A, 600, A30
Dai, F., Howard, A. W., Batalha, N. M., et al. 2021, AJ, 162, 62
Dai, F., Masuda, K., & Winn, J. N. 2018, ApJL, 864, L38
Donati, J. F., Morin, J., Petit, P., et al. 2008, MNRAS, 390, 545
Donati, J. F., Semel, M., Carter, B. D., Rees, D. E., & Collier Cameron, A. 1997, MNRAS, 291, 658
Dorn, C., Venturini, J., Khan, A., et al. 2017, A&A, 597, A37
Dullemond, C. P., & Monnier, J. D. 2010, ARA&A, 48, 205
Essack, Z., Burt, J., Shporer, A., et al. 2022, BAAS, 54, 102.59
Gaidos, E., Claytor, Z., Dungee, R., Ali, A., & Feiden, G. A. 2023, MNRAS, 520, 5283
Gandolfi, D., Barragán, O., Hatzes, A. P., et al. 2017, AJ, 154, 123
Guenther, E. W., Barragán, O., Dai, F., et al. 2017, A&A, 608, A93
Gaia Collaboration, Smart, R. L., Sarro, L. M., et al. 2021, A&A, 649, A6
Hatzes, A. P. 2019, in The Doppler Method for the Detection of Exoplanets, ed. Vishniac (Bristol: IOP Publishing)
Hatzes, A. P., Dvorak, R., Wuchterl, G., et al. 2010, A&A, 520, A93
Hatzes, A. P., Fridlund, M., Nachmani, G., et al. 2011, ApJ, 743, 75
Hidalgo, S. L., Pietrinferni, A., Cassisi, S., et al. 2018, ApJ, 856, 125
Hirano, T., Dai, F., Gandolfi, D., et al. 2018, AJ, 155, 127
Hirano, T., Livingston, J. H., Fukui, A., et al. 2021, AJ, 162, 161
Jenkins, J. M., Twicken, J. D., McCauliff, S., et al. 2016, Proc. SPIE, 9913, 99133E
Kiman, R., Faherty, J. K., Cruz, K. L., et al. 2021, AJ, 161, 277
Klein, B., Zicher, N., Kavanagh, R. D., et al. 2022, MNRAS, 512, 5067
Kochukhov, O. 2021, A&ARv, 29, 1
Kochukhov, O., Makaganiuk, V., & Piskunov, N. 2010, A&A, 524, A5
Kochukhov, O., & Reiners, A. 2020, ApJ, 902, 43
Koen, C., Kilkenny, D., van Wyk, F., & Marang, F. 2010, MNRAS, 403, 1949
Lam, K. W. F., Csizmadia, S., Astudillo-Defru, N., et al. 2021, Sci, 374, 1271
Lee, E. J., & Chiang, E. 2017, ApJ, 842, 40
Leinhardt, Z. M., & Stewart, S. T. 2012, ApJ, 745, 79
Leleu, A., Alibert, Y., Hara, N. C., et al. 2021, A&A, 649, A26
Lopez, E. D., & Fortney, J. J. 2014, ApJ, 792, 1
Lovis, C., & Pepe, F. 2007, A&A, 468, 1115
Mamajek, E. E., & Bell, C. P. M. 2014, MNRAS, 445, 2169
Mandel, K., & Agol, E. 2002, ApJL, 580, L171
Mann, A. W., Dupuy, T., Kraus, A. L., et al. 2019, ApJ, 871, 63
Mann, A. W., Feiden, G. A., Gaidos, E., Boyajian, T., & von Braun, K. 2015, ApJ, 804, 64
Marboeuf, U., Thiabaud, A., Alibert, Y., Cabral, N., & Benz, W. 2014, A&A, 570, A36
Marcus, R. A., Sasselov, D., Hernquist, L., & Stewart, S. T. 2010, ApJL, 712, L73
Marcus, R. A., Stewart, S. T., Sasselov, D., & Hernquist, L. 2009, ApJL, 700, L118
Marcy, G. W., Isaacson, H., Howard, A. W., et al. 2014, ApJS, 210, 20
Mayor, M., Pepe, F., Queloz, D., et al. 2003, Msngr, 114, 20
Millholland, S. C., & Spalding, C. 2020, ApJ, 905, 71
Morin, J., Donati, J. F., Petit, P., et al. 2008, MNRAS, 390, 567
Murdoch, K. A., Hearnshaw, J. B., & Clark, M. 1993, ApJ, 413, 349
Otegi, J. F., Bouchy, F., & Helled, R. 2020, A&A, 634, A43
Pace, G. 2013, A&A, 551, L8
Paegert, M., Stassun, K. G., Collins, K. A., et al. 2022, yCat, IV/39
Petrovich, C., Deibert, E., & Wu, Y. 2019, AJ, 157, 180
Piskunov, N., Snik, F., Dolgopolov, A., et al. 2011, Msngr, 143, 7
Piskunov, N. E., & Valenti, J. A. 2002, A&A, 385, 1095
Pu, B., & Lai, D. 2019, MNRAS, 488, 3568
Rajpaul, V., Aigrain, S., Osborne, M. A., Reece, S., & Roberts, S. 2015, MNRAS, 452, 2269
Reinhardt, C., Meier, T., Stadel, J. G., Otegi, J. F., & Helled, R. 2022, MNRAS, 517, 3132
Ricker, G. R., Winn, J. N., Vanderspek, R., et al. 2015, JATIS, 1, 014003
Rodriguez, J. E., Becker, J. C., Eastman, J. D., et al. 2018, AJ, 156, 245

Rusomarov, N., Kochukhov, O., Piskunov, N., et al. 2013, A&A, 558, A8
Ryabchikova, T., Piskunov, N., Kurucz, R. L., et al. 2015, PhyS, 90, 054005
Sahu, K. C., Casertano, S., Bond, H. E., et al. 2006, Natur, 443, 534
Sanchis-Ojeda, R., Rappaport, S., Winn, J. N., et al. 2014, ApJ, 787, 47
Santerne, A., Brugger, B., Armstrong, D. J., et al. 2018, NatAs, 2, 393
Schlaufman, K. C., Lin, D. N. C., & Ida, S. 2010, ApJL, 724, L53
Serrano, L. M., Gandolfi, D., Mustill, A. J., et al. 2022, NatAs, 6, 736
Smith, J. C., Stumpe, M. C., Van Cleve, J. E., et al. 2012, PASP, 124, 1000
Snik, F., Kochukhov, O., Piskunov, N., et al. 2011, in ASP Conf. Ser. 437, Solar Polarization 6, ed. J. R. Kuhn et al. (San Francisco, CA: ASP), 237
Southworth, J. 2011, MNRAS, 417, 2166
Spalding, C., & Adams, F. C. 2020, PSJ, 1, 7
Stassun, K. G., Oelkers, R. J., Paegert, M., et al. 2019, AJ, 158, 138
Stassun, K. G., Oelkers, R. J., Pepper, J., et al. 2018, AJ, 156, 102
Stumpe, M. C., Smith, J. C., Catanzarite, J. H., et al. 2014, PASP, 126, 100
Stumpe, M. C., Smith, J. C., Van Cleve, J. E., et al. 2012, PASP, 124, 985
Thiabaud, A., Marboeuf, U., Alibert, Y., et al. 2014, A&A, 562, A27
Thiabaud, A., Marboeuf, U., Alibert, Y., Leya, I., & Mezger, K. 2015, A&A, 580, A30
Toledo-Padrón, B., Lovis, C., Suárez Mascareño, A., et al. 2020, A&A, 641, A92
Triaud, A. H. M. J. 2018, in Handbook of Exoplanets, ed. H. J. Deeg & J. A. Belmonte (Springer, Cham: Springer), 2
Wildi, F., Pepe, F., Chazelas, B., Lo Curto, G., & Lovis, C. 2010, Proc. SPIE, 7735, 77354X
Wildi, F., Pepe, F., Chazelas, B., Lo Curto, G., & Lovis, C. 2011, Proc. SPIE, 8151, 81511F
Winn, J. N. 2010, arXiv:1001.2010
Winn, J. N., & Fabrycky, D. C. 2015, ARA&A, 53, 409
Winn, J. N., Sanchis-Ojeda, R., & Rappaport, S. 2018, NewAR, 83, 37
Yee, S. W., Petigura, E. A., & von Braun, K. 2017, ApJ, 836, 77
Zechmeister, M., & Kürster, M. 2009, A&A, 496, 577
Zechmeister, M., Reiners, A., Amado, P. J., et al. 2017, A&A, 609, A12
Zeng, L., Sasselov, D. D., & Jacobsen, S. B. 2016, ApJ, 819, 127
Zhu, W., & Dong, S. 2021, ARA&A, 59, 291
Zicher, N., Barragán, O., Klein, B., et al. 2022, MNRAS, 512, 3060

Chapter 7

TOI-4438

The space-based transit survey *Kepler* discovered that about 25 % of Sun-like stars in our galaxy host planets that have no counterparts in our Solar System. Their sizes are between the ones of Earth and Neptune ($1.0 \lesssim R_{\rm p} \lesssim 4.0\,R_\oplus$; Batalha et al. 2013b). Small planets with radii $1.8 \lesssim R_{\rm p} \lesssim 4.0\,R_\oplus$, the so-called mini-Neptunes, seem to host hydrogen-dominated atmospheres. However, the composition of their upper atmosphere, as well as their internal structure are still not well understood, as mini-Neptunes could be explained by several composition and internal structure models (Zeng et al. 2019). Atmospheric follow-up observations are needed to break the degeneracy between various composition models.

Current and forthcoming space- and ground-based telescopes, such as the JWST, ARIEL, and ELT, will allow us to explore the composition of the upper gaseous layer of exoplanets. To select the best mini-Neptunes amenable to future atmospheric characterization, we need to determine precise planetary masses and radii. Kempton et al. (2018) proposed a methodology to estimate the expected signal-to-noise ratio of transmission spectra for a transiting planet with the Near Infrared Imager and Slitless Spectrograph (NIRISS) on JWST, i.e., the transmission spectroscopy metric (TSM).

In the paper presented in this chapter, I report on the confirmation and characterization of the TESS planet TOI-4438 b, a transiting mini-Neptune planet orbiting the M3.5 V star TOI-4438 every 7.44 days (Goffo et al. 2024). A transit signal was detected with NASA's TESS space mission in three sectors. In order to confirm the planet TOI-4438 b, and determine its fundamental parameters, I combined TESS and MuSCAT2 (Narita et al. 2019) time series photometry with CARMENES high-resolution spectroscopy measurements (Section 4.2.2) spanning almost one year of Doppler monitoring. I found that TOI-4438 b has a radius of $R_{\rm b} = 2.52 \pm 0.13\,R_\oplus$ (5 % precision), which together with its mass of $M_{\rm b} = 5.4 \pm 1.1\ M_\oplus$ (20 % precision), yields a bulk density of $\rho_{\rm b} = 1.85^{+0.51}_{-0.44}\,{\rm g\,cm^{-3}}$ (∼28 % precision), suggesting that TOI-4438 b might be volatile-rich planet.

Our interior structure retrieval with a pure water envelope yields a minimum water mass fraction of 46%. TOI-4438 b is a volatile-rich mini-Neptune with a likely H/He-dominated atmosphere containing H_2O, CO_2, and CH_4. TOI-4438 b has a high transmission spectroscopy metric (TSM) of 136 ± 13. Taking into account its relatively warm equilibrium temperature of $T_{\rm eq} = 435 \pm 15$ K, and the low activity level of its host star, TOI-4438 b is one of the most suitable targets for future atmospheric observations with JWST. We performed spectral simulations to explore the planet's potential for transmission spectroscopy. A single transit observation of TOI-4438 with NIRISS-SOSS or NIRSpec-G395H should be adequate to detect an H/He atmosphere, while at least two transits may be needed to reveal a secondary H_2O dominated atmosphere.

The following paper is accepted for publication in the Astronomy & Astrophysics journal. Some of the methods described in the previous chapters were utilized for the analysis of the photometric and spectroscopic data presented in the paper.

Astronomy & Astrophysics manuscript no. output
April 12, 2024

TOI-4438 b: a transiting mini-Neptune amenable to atmospheric characterization

E. Goffo[1,2], P. Chaturvedi[2], F. Murgas[3,4], G. Morello[5,3,7], J. Orell-Miquel[3,4], L. Acuña[6], L. Peña-Moñino[7], E. Pallé[3,4], A. P. Hatzes[2], S. Geraldía-González[3,4], F. J. Pozuelos[7], A. F. Lanza[8], D. Gandolfi[1], J. A. Caballero[9], M. Schlecker[10], M. Pérez-Torres[7,29,30], N. Lodieu[3,4], A. Schweitzer[11], C. Hellier[12], S. V. Jeffers[13], C. Duque-Arribas[14], C. Cifuentes[9], V. J. S. Béjar[3,4], M. Daspute[15], F. Dubois[16,17], S. Dufoer[16], E. Esparza-Borges[3,4], A. Fukui[18,3], Y. Hayashi[19], E. Herrero[20], M. Mori[19], N. Narita[18,21,3], H. Parviainen[3,4], L. Tal-Or[15], S. Vanaverbeke[16,17,22], I. Hermelo[23], P. J. Amado[7], S. Dreizler[24], Th. Henning[6], J. Lillo-Box[9], R. Luque[25,7], M. Mallorquín[3,4], E. Nagel[24], A. Quirrenbach[26], S. Reffert[26], A. Reiners[24], I. Ribas[20,27], P. Schöfer[7], H. M. Tabernero[14,28], M. Zechmeister[24]

(Affiliations can be found after the references)

Received 30 December 2023 / Accepted dd Month 2024

ABSTRACT

We report the confirmation and mass determination of a mini-Neptune transiting the M3.5 V star TOI-4438 (G 182-34) every 7.44 days. A transit signal was detected with NASA's *TESS* space mission in the sectors 40, 52, and 53. In order to validate the planet TOI-4438 b and to determine the system properties, we combined *TESS* data with high-precision radial velocity measurements from the CARMENES spectrograph, spanning almost one year, and ground-based transit photometry. We found that TOI-4438 b has a radius of $R_\mathrm{b} = 2.52 \pm 0.13$ R$_\oplus$ (5% precision), which together with a mass of $M_\mathrm{b} = 5.4 \pm 1.1$ M$_\oplus$ (20% precision), results in a bulk density of $\rho_\mathrm{b} = 1.85^{+0.51}_{-0.44}$ g cm^{-3} (~28% precision), aligning the discovery with a volatile-rich planet. Our interior structure retrieval with a pure water envelope yields a minimum water mass fraction of 46% (1σ). TOI-4438 b is a volatile-rich mini-Neptune with likely H/He mixed with molecules, such as water, CO_2, and CH_4. The primary star has a J-band magnitude of 9.7, and the planet has a high transmission spectroscopy metric (TSM) of 136 ± 13. Taking into account the relatively warm equilibrium temperature of $T_\mathrm{eq} = 435 \pm 15$ K, and the low activity level of its host star, TOI-4438 b is one of the most promising mini-Neptunes around an M dwarf for transmission spectroscopy studies.

Key words. planetary systems – planets and satellites: individual: TOI-4438 b – planets and satellites: atmospheres – methods: radial velocity – techniques: spectroscopic – stars: low-mass

1. Introduction

Precise and accurate planetary mass and radius measurements are necessary to enable the atmospheric characterization of exoplanets. Current and forthcoming telescopes such as the James Webb Space Telescope (*JWST*), the Atmospheric Remote-sensing Infrared Exoplanet Large-survey (*Ariel*), and the Extremely Large Telescope ELT will expand our frontiers of planetary science, allowing us to explore the composition of the upper gaseous layer of exoplanets. Selecting the best targets amenable to future atmospheric characterization is therefore crucial.

Since the beginning of this century, the *CoRoT* (Baglin et al. 2006), *Kepler* (Borucki et al. 2010), *K2* (Howell et al. 2014), and *TESS* (Ricker et al. 2015) space-based telescopes have opened our eyes to several thousands of transiting exoplanets in our galaxy. Surprisingly, most of these planets have no counterparts within our solar system, since their sizes are between the ones of Earth and Neptune ($1.0 \lesssim R_\mathrm{p} \lesssim 4.0\,\mathrm{R}_\oplus$; Batalha et al. 2013). Small planets with radii $1.8 \lesssim R_\mathrm{p} \lesssim 4.0\,\mathrm{R}_\oplus$, the so-called mini-Neptunes, seem to host hydrogen-dominated atmospheres. The composition of the outer atmosphere as well as the internal planetary structure are still not well understood, as they could be explained by several degenerate models (Zeng et al. 2019). Atmospheric follow-up observations are needed to solve the discrepancy between various composition models. With the methodology proposed by Kempton et al. (2018), one can calculate the expected signal-to-noise ratio (S/N) of transmission spectra for a transiting planet, based on the strength of spectral features and the brightness of the host star, assuming cloud-free atmospheres, namely the transmission spectroscopy metric (TSM). The TSM is used for determining which transiting exoplanets are the best targets for atmospheric characterization via transmission spectroscopy, especially with the Near Infrared Imager and Slitless Spectrograph (NIRISS) on *JWST*.

Small planets including mini-Neptunes happen to be common around M-type dwarf stars (Dressing & Charbonneau 2013; Sabotta et al. 2021; Ribas et al. 2023), as found also in data from the *TESS* mission (Chaturvedi et al. 2022; Espinoza et al. 2022; Kawauchi et al. 2022; González-Álvarez et al. 2023; Barkaoui et al. 2023). Follow-up observations focused on M dwarfs have their own advantages as these are abundant compared to F, G, and K stars. Their smaller stellar radii and masses produce deeper transit signals (the transit depth δ is inversely proportional to $R_\star^2$) and larger Doppler reflex motions (the radial velocity semi-amplitude $K_\star$ is inversely proportional to $M_\star^{2/3}$), increasing our capability to detect small low-mass planets (see, e.g., Ribas et al. 2023).

Here, we present the characterisation of TESS object of interest (TOI)-4438 b, a transiting mini-Neptune orbiting the M3.5 V star TOI-4438 (G 182-34). We used CARMENES precise radial velocities (RVs) and ground-based transit observations to confirm the planet and to derive its fundamental parameters, such as mass, radius, orbital period, semi-major axis, and equilibrium temperature. TOI-4438 b with a score of ∼136 scales very high on TSM, thereby, making it a promising target for future atmospheric observations with *JWST*. This work is part of the *TESS* follow-up program within the CARMENES observations survey (see, e.g., González-Álvarez et al. 2023; Kossakowski et al. 2023; Mallorquín et al. 2023; Murgas et al. 2023; Palle et al. 2023).

2. Observations

2.1. TESS photometry

TESS observed TOI-4438 in sector 40, from 25 June to 23 July 2021, with CCD#2 of camera 1 with an integration time of 2 min. TOI-4438 had more observations taken in sector 52, from 19 May to 12 June 2022, and in sector 53, from 13 June to 8 July 2022. The observations were done again at the same cadence of 2 min with CCD#1 of camera 1 in sector 52, and with CCD#2 of camera 1 in sector 53. We retrieved the *TESS* data from the Mikulski Archive for Space Telescopes (MAST)[1] The data were processed by Science Processing Operations Center (SPOC, Jenkins et al. 2016) pipeline using the Presearch Data Conditioning Simple Aperture Photometry (PDCSAP) algorithm. For details, refer Stumpe et al. (2012, 2014); Smith et al. (2012).

In order to correct for the photometric contamination caused by *TESS*'s large pixel size of 21″, a photometric mask is used to extract the *TESS* Simple Aperture Photometry (SAP) light curve. We plotted the target pixel files (TPFs; Fig. 1) of TOI-4438 using the code `tpfplotter`[2] (Aller et al. 2020). The TPFs include all the *Gaia* Data Release 3 (DR3, Gaia Collaboration et al. 2023) sources, down to $\Delta G = 10$ mag fainter than the target star and spatially located within the field of view of the *TESS* aperture. No bright sources fall inside the photometric aperture of TOI-4438. For the analysis presented in this paper, we used the *TESS* contamination corrected PDCSAP light curves (Fig. 2).

2.2. CARMENES radial velocity follow-up

We spectroscopically monitored TOI-4438 with the Calar Alto high-Resolution search for M dwarfs with Exoearths with Near-infrared and optical Echelle Spectrographs (CARMENES) installed at the 3.5 m telescope at Calar Alto Observatory, Almería, Spain. The instrument comprises two highly stable, fiber-fed spectrographs (Quirrenbach et al. 2014, 2018), one covering the wavelength range 520–960 nm (VIS) with a resolving power of R ≈ 94 600, the other covering the near-infrared range 960–1710 nm (NIR), with a resolving power of R ≈ 80 400.

We collected 34 high-resolution spectra between 21 May 2022 and 2 May 2023. Depending on the sky condition and observing constraints, each of the spectra was exposed between 700 and 1800 s. The resultant average S/N was ∼47 at 740 nm. We followed the standard `caracal` pipeline (Zechmeister et al. 2014) to reduce the CARMENES data.

The precise relative RVs were computed using the `serval`[3] pipeline (Zechmeister et al. 2018) with the standard corrections for barycentric and secular motions. The ancillary corrections applied for the nightly drift by incorporating the nightly zero-points and the atmospheric effects using the telluric lines are described by Nagel et al. (2023). In our analysis we also used the `serval` produced spectral activity indicators, namely, the chromatic index (CRX), the differential line width (dLW), the Hα index, the Ca II infrared triplet (IRT) index, and the Na I D doublet index.

We discarded two data points in the CARMENES VIS RV time series due to their low signal-to-noise ratio (S/N < 21). The final CARMENES dataset includes 32 measurements with a root mean square (RMS) of $\approx 2\,\mathrm{m\,s^{-1}}$. We did not include the NIR RVs in our further analysis, given their low signal-to-noise ratio. Table A.1 lists the CARMENES VIS RV measurements with the time information in the Barycentric Julian Date- Barycentric Dynamical Time ($\mathrm{BJD_{TDB}}$) units.

2.3. Ground-based photometry

2.3.1. MuSCAT2

TOI-4438 was observed on three nights, namely, on 17 May 2022, 2 May 2023, and 8 July 2023, with the multi-band imager MuSCAT2 (Narita et al. 2019) mounted on the 1.5 m Telescopio Carlos Sánchez (TCS) at Teide Observatory, Tenerife, Spain. MUSCAT2 is equipped with four 1k×1k pixel CCDS, with each having a field of view of 7.4′×7.4′. The cameras can simultaneously observe in the g', r', i', and z_s bands. We observed two complete transits and one partial transit of TOI-4438 b in each band. The times for exposure varied between 10 s to 30 s. The data reduction were carried out using the standard pipeline as described by Parviainen et al. (2019); Parviainen (2015).

2.3.2. SuperWASP

The SuperWASP transit search (Pollacco et al. 2006) observed the field of TOI-4438 in 2004 and then every year from 2007 to 2010. The eight cameras have each 2048×2048 CCDs with f/1.8 lenses. A total of 71 000 photometric data points were obtained over a period of of ∼ 120 nights in the visible passband of 400–700 nm. At $V = 13.7$ mag, TOI-4438 is relatively faint for WASP, though it is the brightest star in the 48″ extraction aperture.

2.3.3. TJO

We carried out a dedicated photometry monitoring campaign of TOI-4438 on 49 different nights from April to September 2023 with the 0.8 m Telescopi Joan Oró (TJO; Colomé et al. 2010) at the Montsec Observatory, Lleida, Spain. A total of 285 data points were observed using the Johnson *R* filter of the LAIA imager on a 4k×4k CCD with a 30′ field of view. The standard reduction process was followed using the `AstroImageJ`(Collins et al. 2017) package and the `icat` pipeline (Colome & Ribas 2006) of the TJO. We used indigenous pipelines for removal of outliers for observations made during poor sky conditions. We obtained an effective rms of ∼9 ppt in the *R* filter.

2.3.4. LCOGT

We performed photometric monitoring of TOI-4438 in the *V* band between 2 August and 6 November 2023, using the SBIG camera of one of the 40 cm telescope of Las Cumbres Observatory Global Telescope (LCOGT; Brown et al. 2013) providing a field of view of 29.2′×19.5′. We took three exposures of 600 s in each of the 71 different observing epochs during 96 d. The observing conditions were mostly good and the average seeing varied from 2.0 to 6.0″. Raw data were processed using the `BANZAI` pipeline (McCully et al. 2018) and differential aperture photom-

---

[1] `https://mast.stsci.edu/portal/Mashup/Clients/Mast/Portal.html`.

[2] `https://github.com/jlillo/tpfplotter`.

[3] `https://github.com/mzechmeister/serval`.

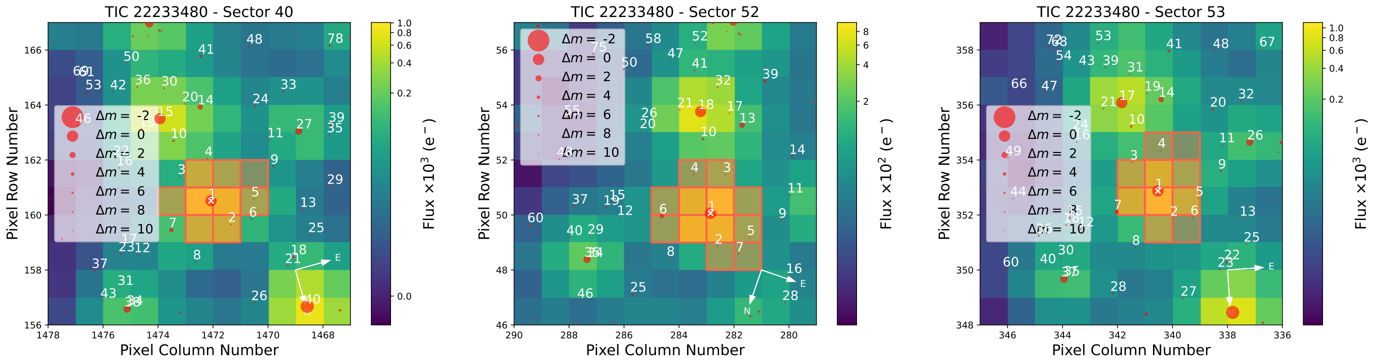

Fig. 1: TPFs of TOI-4438 in TESS sectors 40, 52, and 53. The red bordered squares mark the optimal photometric aperture used to extract the SAP fluxes. The different sizes of the red circles show the G-band magnitudes from *Gaia* DR3 for all nearby stars with respect to TOI-4438 (marked with an "×") up to $\Delta G = 10$ mag fainter.

etry of TOI-4438 was performed using the `AstroImageJ` software. An optimal aperture of 8 pixels ($\sim 4.5''$) was adopted to minimize the dispersion of the differential light curves.

We used the 1 m LCOGT telescopes from 9 June to 4 November 2023, to observe TOI-4438 in the B filter with an exposure time of 120 s until JD = 2460156, and of 77 s afterwards. This produced 88 images, out of which nine were found to be bad. The final light curve has an rms of 0.57% ∼ with 79 data points, spanning 148 d.

2.3.5. ASAS-SN

TOI-4438 was photometrically monitored by the All-Sky Automated Survey for Supernovae (ASAS-SN; Shappee et al. 2014; Kochanek et al. 2017). ASAS-SN consists of a network of 24 robotic telescopes with a diameter of 14 cm, distributed around the world. We retrieved the ASAS-SN light curve from the webpage of the project[4]. There are 246 V-band photometry measurements taken for the star between 3 May 2013 and 25 September 2018 with a rms scatter of ~0.021 mag.

2.3.6. e-EYE

TOI-4438 was also observed by e-EYE (Entre Encinas y Estrellas)[5] 16″ ODK corrected-Dall-Kirkham reflector, located at Fregenal de la Sierra in Badajoz, Spain. V band observations were taken between 12 September and 13 November 2023 with a Kodak KAF-16803 CCD chip mounted on ASA DDM85. The images were reduced using the `LesvePhotometry` package[6]. The rms of the data was ~0.006 mag.

2.3.7. ADONIS

TOI-4438 was observed by the privately owned ADONIS observatory in the V filter from 30 September to 6 December 2023. The telescope used is 0.25 m skywatcher Quattro Newtonian telescope with a Moravian CCD camera. `LesvePhotometry` is used to perform the aperture photometry.

3. Stellar properties

The star TOI-4438 was originally discovered as a high-proper motion star (34th in the plate 182 in Hercules) in the northern hemisphere at the Lowell Observatory by Giclas (1966). The star has been identified as G 182–34 (Giclas et al. 1971) and has been tabulated by a number of catalogs on proper motion (Luyten 1979; Lépine & Shara 2005; Schneider et al. 2016), parallax (Dahn et al. 1988, 2002; van Altena et al. 1995), or the solar neighborhood (Reid & Cruz 2002; Lépine & Gaidos 2011; Frith et al. 2013; Gaia Collaboration et al. 2021).

3.1. Stellar parameters

We derived the stellar parameters as discussed in Schweitzer et al. (2019). The total luminosity was computed by summing over the spectral energy distribution with `VOSA` (Bayo et al. 2008). Broadband photometry from passbands Johnson (B) to AllWISE ($W4$) and astrometry from *Gaia* DR3 catalog were utilized. The stellar atmospheric parameters ($T_{\rm eff}$, $\log g$, and [Fe/H]) were derived with the `SteParSyn`[7] code (Tabernero et al. 2022) using the line list and model grid described by Marfil et al. (2021). The mass of the star was derived using the the linear mass-radius relation (Schweitzer et al. 2019) whereas the radius of the star was derived from Stefan-Boltzmann's law assuming the bolometric luminosity and the spectroscopic temperature. The stellar parameters of TOI-4438 are listed in Table 1. The effective temperature of $T_{\rm eff} = 3422 \pm 81$ K and surface gravity of $\log g_\star = 4.68 \pm 0.04$ (cgs) match the ∼ M3 V spectral-type from the spectro-photometric relations of Pecaut & Mamajek (2013) and Cifuentes et al. (2020) and, the M3.5±0.5 V spectral type from low-resolution optical spectroscopy by Reid et al. (2003).

3.2. Stellar activity

The broad wavelength range coverage offered by the CARMENES VIS and NIR channels allows us to study a total of sixteen spectral activity indicators. These are pEW(Hα) (from which we derived $\log {\rm H}\alpha/L_{\rm bol}$ as Jeffers et al. 2018), HeD3, NaD, Ca IRT-a,-b,-c, He ɪλ10830, Pa β, CaH2, CaH3, TiO 7050, TiO 8430, TiO 8860, VO 7436, VO 7942, and FeH Wing-Ford, and they were computed following the methods described by Schöfer et al. (2019). In addition, the output parameters from `serval` also include the CRX and dLW pa-

---

[4] https://asas-sn.osu.edu/.

[5] www.e-eye.es/.

[6] www.dppobservatory.net.

[7] https://github.com/hmtabernero/SteParSyn/.

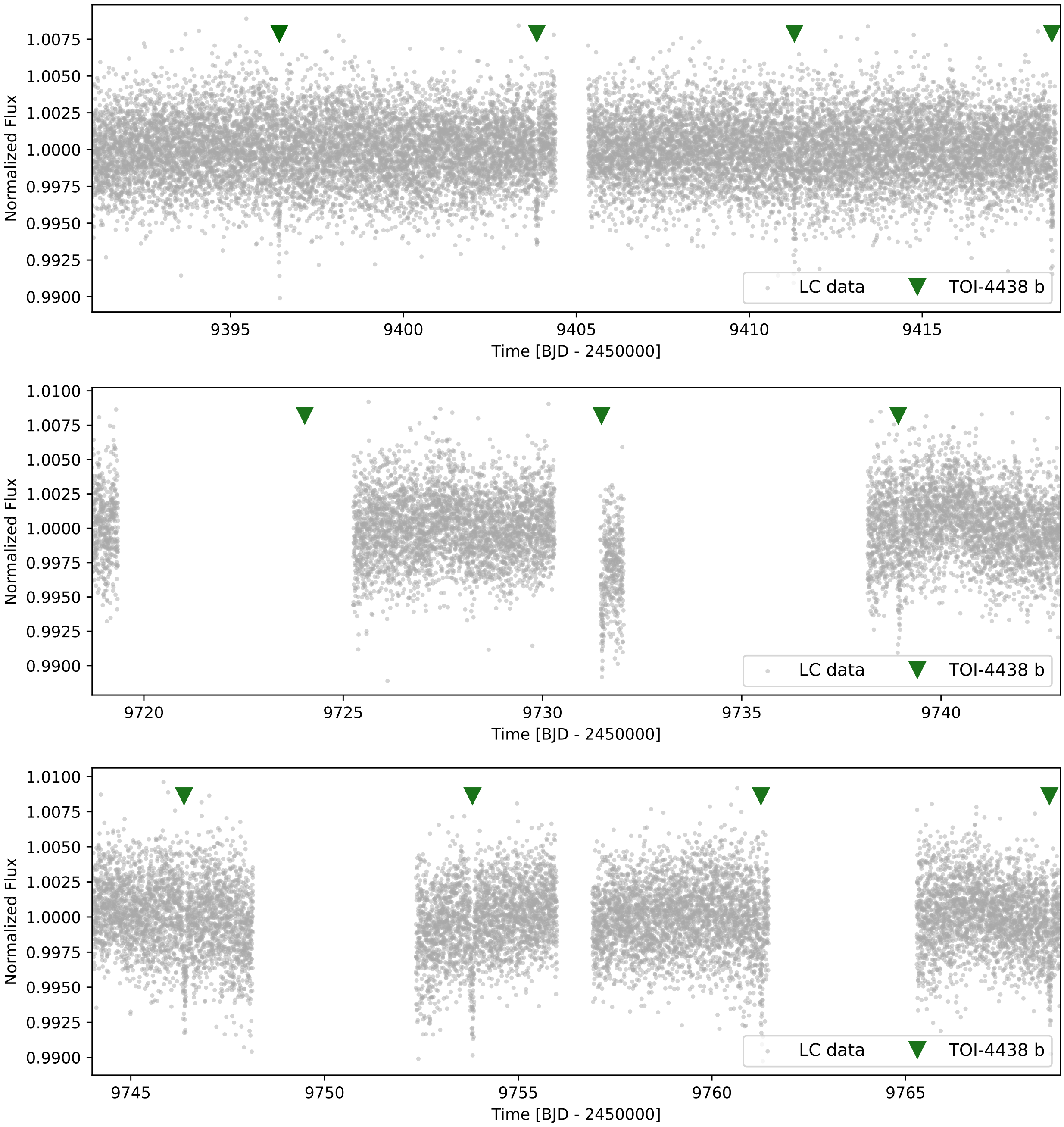

Fig. 2: *TESS* PDCSAP light curve of TOI-4438 from sectors 40, 52, and 53. The green triangles mark the timings of the transits of TOI-4438 b.

rameters for both channels (Zechmeister et al. 2018), resulting in twenty activity diagnostics.

In all CARMENES spectra we found that Hα is in absorption, indicating that TOI-4438 is a weakly active star with undetectable levels of activity-induced emission in the Hα line. We also did not detect Hα emission due to flaring in the CARMENES spectra. Jeffers et al. (2018) showed that only about one third of M3 dwarfs are Hα active. Given the M3.5 V spectral type, the low activity level of TOI-4438 is therefore not surprising. We also computed Pearson's r correlation coefficient between the measured RVs and the spectral activity indicators as described in Jeffers et al. (2020) and confirmed the star to be least active.

3.3. Rotation period of the star

We inspected the SuperWASP light curves for rotational modulations as discussed in Maxted et al. (2011). There appears to be significant power at long periods (see Fig. 3), although the periodograms are hard to interpret. In each observation season, the amplitude of the modulations is variable, and the data covered only about two cycles. There are likely to be profile and phase changes between years. We found a rotational modulation with an amplitude of ~ 6 mmag, and a period of 68 ± 6 d. The first harmonic is also present at ~ 34 d in the years 2004 and 2010.

In addition, we computed the generalized Lomb-Scargle (GLS; Zechmeister & Kürster 2009) periodograms of the TJO, LCOGT (in V- and B- filters), ASAS-SN, e-EYE, and ADONIS

Table 1: Stellar parameters of TOI-4438.

Parameter	Value	Reference
Identifiers	G 182-34	Gic71
	Karmn J18012+355	Cab16
	TIC 22233480	TIC
Sp. type	M3.5 V	Reid03
α (ICRS, epoch 2016.0)	18:01:16.14	*Gaia* DR3
δ (ICRS, epoch 2016.0)	+35:35:41.6	*Gaia* DR3
$\mu_\alpha \cos\delta$ (mas yr^{-1})	$+29.212 \pm 0.017$	*Gaia* DR3
μ_δ (mas yr^{-1})	-517.512 ± 0.018	*Gaia* DR3
ϖ (mas)	33.2642 ± 0.0154	*Gaia* DR3
d (pc)	30.0623 ± 0.0139	*Gaia* DR3
γ (km s^{-1})	-35.81 ± 0.47	*Gaia* DR3
$T_{\rm eff}$ [K]	3422 ± 81	This work
$\log g_\star$ [cgs]	4.68 ± 0.04	This work
[Fe/H] [dex]	-0.19 ± 0.05	This work
$L_\star$ [$L_\odot$]	0.01706 ± 0.00007	This work
$R_\star$ [$R_\odot$]	0.372 ± 0.018	This work
$M_\star$ [$M_\odot$]	0.368 ± 0.021	This work
$\rho_\star$ [g cm^{-3}]	10.06 ± 1.62	This work
$v \sin i_\star$ [km s^{-1}]	< 2	This work
$P_{\rm rot}$ [d]	68 ± 6	This work
Age [Gyr]	5.1 ± 2.8	This work
G [mag]	12.50 ± 0.68	*Gaia* DR3
T [mag]	11.2695 ± 0.0073	TIC
J [mag]	9.695 ± 0.021	2MASS
K_s [mag]	8.869 ± 0.018	2MASS

References. Gic71: Giclas et al. (1971); Cab16: Caballero et al. (2016); TIC: Stassun et al. (2019); *Gaia* DR3: Gaia Collaboration et al. (2023); 2MASS: Skrutskie et al. (2006); Reid03: Reid et al. (2003).

light curves of TOI-4438, as shown in Fig. 4. The periodogram of the TJO light curve shows its highest peak at ~34 d, and a second high peak at ~64 d, consistent with the SuperWASP results. The same applies to the periodogram of the LCOGT data (V-filter), where we found the highest signal at 68 ± 10 d, and the ASAS-SN photometry, which shows a modulation at around 57 d. LCOGT B-filter data show a peak at 22 ± 1 d with a false alarm probability of <0.1%, which could be related to the second harmonic of the stellar rotation period. Since the e-EYE and ADONIS data covered a shorter baseline, the periodograms displayed no significant signals around 68 or 34 d. We concluded that TOI-4438 has a rotation period of 68 ± 6 d, as derived from SuperWASP photometry.

3.4. Age

With a rotation period of 68 ± 6 d, TOI-4438 is very likely an old star. From the relations of Bouma et al. (2023), a maximum rotation period of 25 d is detected for members of the Praesepe cluster (500–700 Myr; Lodieu et al. 2019). The rotation period of TOI-4438 is at least twice longer, so the age is expected to be much older, although the relation is not linear. Similarly, Curtis et al. (2020) showed that field stars with spectral types between K0 and M1–M2 and ages of 6 ± 2 Gyr have rotation periods around 35–45 d, again much shorter than TOI-4438. Eventually, we used the rotation–age relations applicable to M2.5–6.5 dwarfs from the recent study by Engle & Guinan (2023) and derived an age of 5.1 ± 2.8 Gyr.

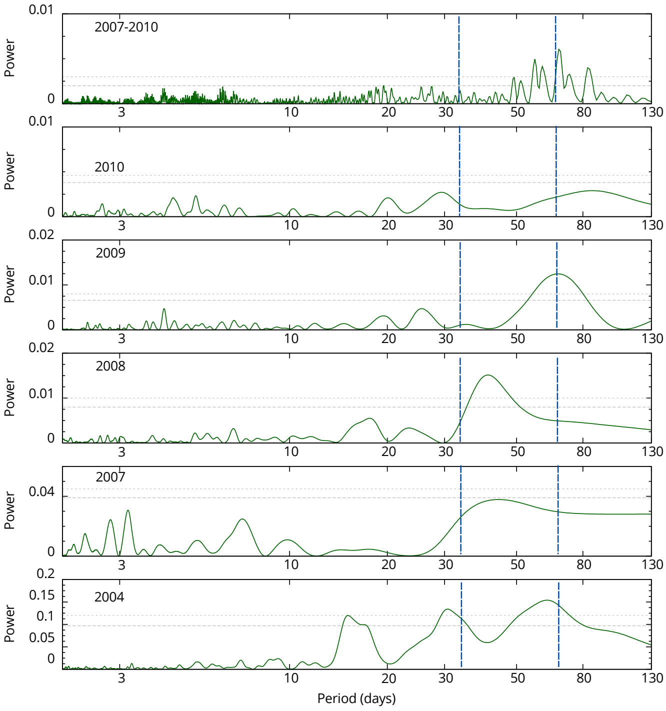

Fig. 3: Periodogram of the SuperWASP data for TOI-4438 from each year and (top) the periodogram of 2007–2010 combined. The horizontal dashed lines indicate the estimated 10%- and 1%-likelihood false-alarm levels. The blue vertical dashed lines mark the stellar rotation period and its first harmonic.

To constrain the age of an M-type dwarf we can also look for wide, higher-mass, gravitationally bound companions. We searched for possible co-moving common proper motion companions to TOI-4438 in the *Gaia* Data Release 3 (DR3) in a radius of five degrees. The search was based on the proximity in parallax, using a very conservative interval of 3.25 pc, 200 times more than the error bar on the parallax reported in DR3. Ten sources were returned but none of them shows a proper motion in right ascension consistent with the large motion of TOI-4438 ($\mu_\alpha \cos\delta \approx -517.5$ mas yr^{-1}). Moreover, we checked several parameters that may indicate departure from a single star astrometric model, such as the renormalized unit weight error (RUWE), the excess noise of the source and its significance, and the percent of successful-IPD windows with more than one peak. None of them point toward the presence of an unseen companion around TOI-4438. This is consistent with the null results on TOI-4438 of the laser-guided, adaptive-optics, Robo-AO M-dwarf multiplicity survey of Lamman et al. (2020).

4. Analysis

4.1. Transit light curve modeling

Prior to performing a joint analysis of the photometric and Doppler time series (Sect. 4.4), we performed a preliminary analysis of the available transit light curves to check whether the different passbands provide consistent transit depths. With this aim, we used the code `pyaneti` (Barragán et al. 2017, 2022) to model the *TESS* light curve from sectors 40, 52,

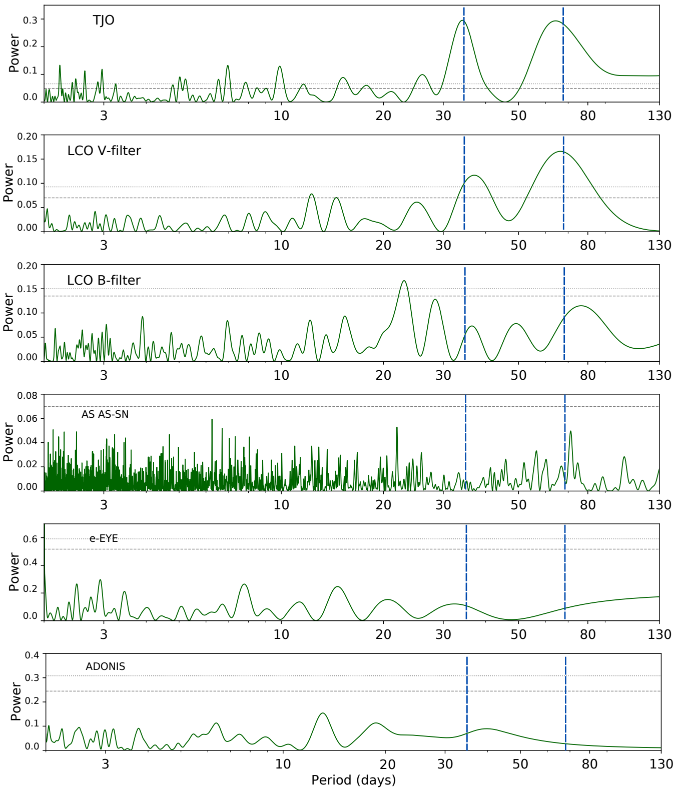

Fig. 4: Periodograms of the TJO, LCOGT (*V* and *B*), ASAS-SN, e-EYE, and ADONIS data for TOI-4438. The horizontal dashed lines indicate the estimated 10%- and 1%-likelihood false-alarm levels. The blue vertical dashed lines mark the stellar rotation period and its first harmonic.

and 53 (Sect. 2.1), and MuSCAT2 ground-based photometry (Sect. 2.3.1). The *TESS* data included in the analysis are subsets of 8 h of the PDCSAP light curves, centered around each transit epoch, and detrended by fitting a second-order polynomial to the out-of-transit data.

Based on the period and ephemeris reported by SPOC ($P_{\rm orb,b} = 7.446303 \pm 0.000023$ d and $T_{0,b} = 2459396.40958 \pm 0.00075$ BJD$_{\rm TDB}$), we allowed the period to vary between 7.2 and 7.7 d, and the epoch of reference transit between BJD$_{\rm TDB}$ = 2459396.16 and 2459396.66 d. We adopted the parameterization proposed by Anderson et al. (2010) for the eccentricity e and the argument of periastron of the stellar orbit $\omega_\star$ (i.e., $\sqrt{e}\sin\omega_\star$ and $\sqrt{e}\cos\omega_\star$). `pyaneti` uses Mandel & Agol (2002)'s limb-darkened quadratic model for the transit light curve and the limb-darkening parameterization proposed by Kipping (2013). We adopted Gaussian priors for the linear and quadratic limb-darkening coefficients (q_1, q_2) using the values calculated with the `Python Limb Darkening Toolkit`[8] (PyLDTk, Parviainen & Aigrain 2015) for *TESS* and MuSCAT2 bands. We set uniform priors for all of the remaining parameters. A photometric jitter term was added to account for any instrumental noise not included in the nominal uncertainties. We sampled the parameter space with 500 walkers using the Markov chain Monte Carlo (MCMC) ensemble sampler algorithm implemented in `pyaneti`. We created the posterior distributions using the last 5000 iterations of the converged chains with a thin factor of 10, giving a distribution of 250 000 data points for each sampled parameter. We followed the procedure and the convergence test as described by Barragán et al. (2017).

In order to check for uniform transit depths in the *TESS* and MuSCAT2 bands, and determine the chromaticity of the transits in each available filter, we performed two analyses: (1) we allowed an independent scaled planetary radius $R_{\rm b}/R_\star$ for each passband; (2) we modeled a single scaled planetary radius, namely assuming the same transit depth in all passbands. Table 2 lists the adopted priors and posterior values of the sampled parameters. For the parameter estimates and their 1σ uncertainties, we took the median and the 68.3% credibility interval of the posterior distributions. Fig. 5 shows the phase-folded *TESS* and MuSCAT2 transit light curves of TOI-4438 b. We measured an orbital period of $P_{\rm orb,b} = 7.4462800 \pm 0.0000087$ d, an epoch of reference transit of $T_{0,\rm b} = 2459396.4116 \pm 0.0006$ d (BJD$_{\rm TDB}$), and a radius of $R_{\rm b} = 2.51 \pm 0.12\,R_\oplus$ from the unique scaled planet radius fit (case 2).

Fig. 6 displays the posterior distributions for the sampled scaled planetary radii $R_{\rm p}/R_\star$ for each passband. We found that the posterior distributions for the *TESS* and MuSCAT2 bands overlap, except for the g' and r' filters.

We also found a color dependence, given the deeper transits in the g' and r' filters. Assuming an astrophysical origin, this color trend could be caused by contamination from a cooler dwarf (Parviainen et al. 2019) or unocculted star spots (Ballerini et al. 2012). Potential inaccuracies due to the stellar limb-darkening parameterization (Morello et al. 2017) or planetary atmospheric signatures (Chen et al. 2021) should be negligible compared to the error bars. In order to check the hypothesis of astrophysical contamination, we fitted the measured planetary radii in multiple bands by assuming a unique planet-to-star radius ratio $R_{\rm b}/R_\star$ and different star spots configurations modeled with `ExoTETHyS` (Morello et al. 2021). The stellar spectrum was modeled as the sum of two components, namely the quiet photosphere and the spots, characterized by different values of $T_{\rm eff}$ and $\log g_\star$, and neglecting stellar limb-darkening effects (Cracchiolo et al. 2021; Thompson et al. 2023). We adopted the `PHOENIX-COND` and `PHOENIX-DRIFT` libraries of stellar spectra (Claret et al. 2012, 2013; Husser et al. 2013). Technical details are given in Appendix B. It turned out that a spot filling factor of ~40% and temperature contrast of ~500 K are needed to explain the different measurements between g' and *TESS* filters, but they struggle to maintain the uniform transit depth observed in i', z_s, and *TESS*. Furthermore, these values would denote a very high level of stellar activity, in contrast with all other indicators (see Sect. 3.2). This scenario is mathematically equivalent to that of a cooler M-type contaminant with similar brightness to that of the host star, following the model by Morello et al. (2023). Such a bright contaminant is also unlikely to be unseen (see Sect. 3.4). Another possibility is that the transit measurements in g' and r' bands are affected by systematic bias, due to the low S/N of the MuSCAT2 light curves obtained with these filters. Therefore, we ignored the bluer g' and r', and used i' and z_s only for the following analysis. We discuss an alternative solution including all bands and potential color contamination in Appendix B.

4.2. Additional planet search and detection limits

We adopted the box least-square (`BLS`; (Kovács et al. 2002; Hartman & Bakos 2016) method to look for additional transits in the PDCSAP *TESS* light curves. Before applying the BLS we de-

---

[8] `https://github.com/hpparvi/ldtk`.

Table 2: TOI-4438 b parameters from the transit light curve modeling with `pyaneti`.[(a)]

Parameter	Prior	Derived value (multi-radii)	Derived value (single radius)
Model parameters			
$P_{\rm orb,b}$ [d]	$\mathcal{U}[7.2, 7.7]$	7.4462801 ± 0.0000091	7.4462800 ± 0.0000087
$T_{0,\rm b}$ [BJD$_{\rm TDB}$−2,450,000]	$\mathcal{U}[9396.16, 9396.66]$	9396.4116 ± 0.0007	9396.4116 ± 0.0006
$R_{\rm b}/R_\star$	$\mathcal{U}[0.001, 0.09]$	...	$0.0619^{+0.0006}_{-0.0005}$
$R_{\rm b}/R_\star$TESS	$\mathcal{U}[0.001, 0.09]$	0.0606 ± 0.0012	...
$R_{\rm b}/R_\star$MuSCAT2 g′	$\mathcal{U}[0.001, 0.09]$	0.0678 ± 0.0026	...
$R_{\rm b}/R_\star$MuSCAT2 r′	$\mathcal{U}[0.001, 0.09]$	0.0661 ± 0.0019	...
$R_{\rm b}/R_\star$MuSCAT2 i′	$\mathcal{U}[0.001, 0.09]$	0.0622 ± 0.0013	...
$R_{\rm b}/R_\star$MuSCAT2 z$_{\rm s}$	$\mathcal{U}[0.001, 0.09]$	0.0624 ± 0.0010	...
$b_{\rm b}$	$\mathcal{U}[0, 1]$	$0.38^{+0.16}_{-0.24}$	$0.15^{+0.14}_{-0.10}$
$a/R_\star$	$\mathcal{U}[1, 50]$	$28.6^{+4.0}_{-4.9}$	30 ± 5
$\sqrt{e_{\rm b}}\sin\omega_{\star,\rm b}$	$\mathcal{U}[-1, 1]$	$-0.13^{+0.38}_{-0.25}$	$-0.14^{+0.40}_{-0.27}$
$\sqrt{e_{\rm b}}\cos\omega_{\star,\rm b}$	$\mathcal{U}[-1, 1]$	-0.004 ± 0.447	-0.02 ± 0.47
Derived parameters			
$R_{\rm b}$ [$R_\oplus$]	...	...	2.51 ± 0.12
$R_{\rm b,TESS}$ [$R_\oplus$]	...	2.46 ± 0.13	...
$R_{\rm b,MuSCAT2\,g'}$ [$R_\oplus$]	...	2.75 ± 0.17	...
$R_{\rm b,MuSCAT2\,r'}$ [$R_\oplus$]	...	2.68 ± 0.15	...
$R_{\rm b,MuSCAT2\,i'}$ [$R_\oplus$]	...	2.52 ± 0.13	...
$R_{\rm b,MuSCAT2\,z_s}$ [$R_\oplus$]	...	2.53 ± 0.13	...
$a_{\rm b}$ [au]	...	$0.0492^{+0.0074}_{-0.0086}$	0.053 ± 0.009
$e_{\rm b}$	...	$0.21^{+0.24}_{-0.14}$	$0.23^{+0.25}_{-0.15}$
$\omega_{\star,\rm b}$ [deg]	...	-34^{+134}_{-111}	-37^{+139}_{-108}
$i_{\rm b}$ [deg]	...	$89.22^{+0.50}_{-0.53}$	$89.71^{+0.35}_{-0.21}$
$\tau_{14,\rm b}$ [h]	...	2.02 ± 0.03	2.01 ± 0.02
$T_{\rm eq,b}$ [K] $^{(b)}$	...	453^{+46}_{-30}	438^{+45}_{-32}
$S_{\rm b}$ [S$_\oplus$]	...	$7.04^{+3.3}_{-1.7}$	$6.1^{+2.9}_{-1.6}$
Additional model parameters			
Parameterized limb-darkening coefficients			
$q_{1,\rm TESS}$	$\mathcal{N}[0.276, 0.1]$	0.30 ± 0.08	0.30 ± 0.08
$q_{2,\rm TESS}$	$\mathcal{N}[0.261, 0.1]$	0.26 ± 0.10	0.26 ± 0.10
$q_{1,\rm MuSCAT2\,g'}$	$\mathcal{N}[0.629, 0.1]$	0.64 ± 0.10	0.64 ± 0.10
$q_{2,\rm MuSCAT2\,g'}$	$\mathcal{N}[0.312, 0.1]$	0.35 ± 0.10	0.35 ± 0.10
$q_{1,\rm MuSCAT2\,r'}$	$\mathcal{N}[0.572, 0.1]$	0.55 ± 0.16	0.55 ± 0.16
$q_{2,\rm MuSCAT2\,r'}$	$\mathcal{N}[0.317, 0.1]$	0.33 ± 0.10	0.33 ± 0.10
$q_{1,\rm MuSCAT2\,i'}$	$\mathcal{N}[0.334, 0.1]$	0.37 ± 0.08	0.37 ± 0.08
$q_{2,\rm MuSCAT2\,i'}$	$\mathcal{N}[0.260, 0.1]$	0.31 ± 0.10	0.31 ± 0.10
$q_{1,\rm MuSCAT2\,z_s}$	$\mathcal{N}[0.241, 0.1]$	0.16 ± 0.08	0.16 ± 0.08
$q_{2,\rm MuSCAT2\,z_s}$	$\mathcal{N}[0.240, 0.1]$	0.19 ± 0.10	0.19 ± 0.10
Jitter terms			
$\sigma_{\rm TESS}$	$\mathcal{J}[0,100]$	0.000058 ± 0.000054	0.000058 ± 0.000054
$\sigma_{MuSCAT2\,g'}$	$\mathcal{J}[0,100]$	0.00021 ± 0.00020	0.00021 ± 0.00020
$\sigma_{\rm MuSCAT2\,r'}$	$\mathcal{J}[0,100]$	0.00030 ± 0.00026	0.00030 ± 0.00026
$\sigma_{\rm MuSCAT2\,i'}$	$\mathcal{J}[0,100]$	0.00014 ± 0.00012	0.00014 ± 0.00012
$\sigma_{\rm MuSCAT2\,z_s}$	$\mathcal{J}[0,100]$	0.00018 ± 0.00026	0.00018 ± 0.00026

Notes. [a] $\mathcal{U}[a, b]$ refers to uniform priors between a and b; $\mathcal{N}[a, b]$ refers to Gaussian priors with mean a and standard deviation b; $\mathcal{J}[a, b]$ refers to Jeffrey's priors between a and b. Inferred parameters and uncertainties are defined as the median and the 68.3% credible interval of their posterior distributions. [b] Assuming zero albedo and uniform redistribution of heat.

trended the data using the package `citlalique`[9], which allows to detrend light curves using Gaussian processes (GPs) to remove low frequency signals in the light curves (Barragán et al. 2022).

We used the `BoxLeastSquares` class of the `astropy.timeseries` python package. Whenever the program identified a transit signal, we removed the in-transit data points and ran the algorithm again to search for additional transiting planets. The BLS periodograms of the *TESS* light curves were evaluated over periods from 0.5 d to half the total length of the observations, namely ~190 d. The first transit signal was identified at 7.44 d, corresponding to the orbital period of TOI-4438 b. We found no other signals in the data corresponding to additional transiting planets.

To identify possible additional companions that might perturb the orbit of TOI-4438 b, we analysed the available transit light curves for transit timing variation (TTVs). We used the ten *TESS* transits from sectors 40, 52, and 53, and the two full tran-

---

[9] https://github.com/oscaribv/citlalicue

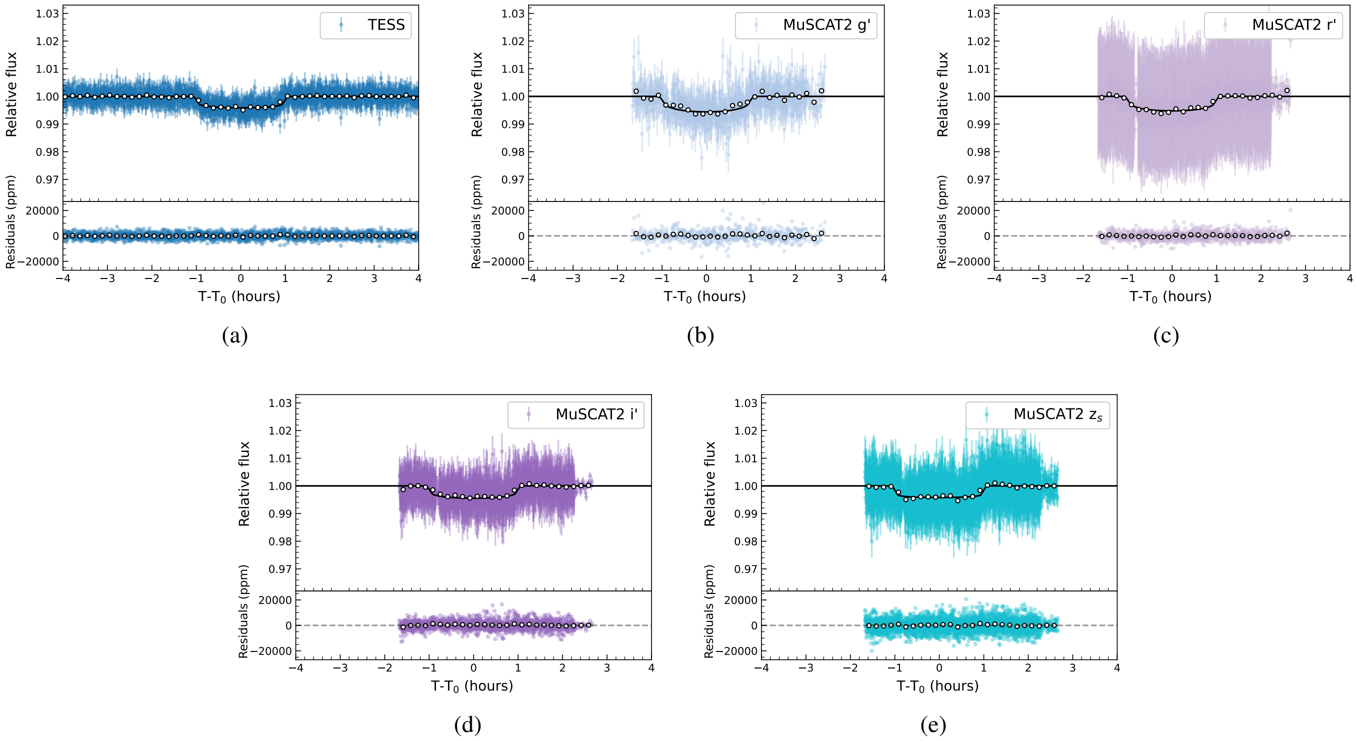

(a)

(b)

(c)

(d)

(e)

Fig. 5: Phase-folded transit light curves of TOI-4438 b from the (a) *TESS*, and (b) g', (c) r', (d) i', and (e) z_s MuSCAT2 bands. Data are shown as filled circles with their nominal uncertainties. The 10-min binned data points are marked with white circles.

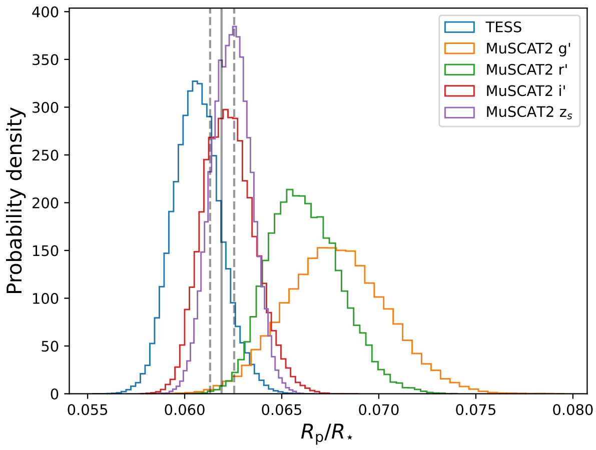

Fig. 6: Posterior distributions of the sampled scaled planetary radii $R_b/R_\star$ for the *TESS* and MuSCAT2 g', r', i', z_s bands. The solid and dotted, vertical, gray lines mark the median and the 68.3% credibility interval of the $R_p/R_\star$'s posterior distribution, as derived in case 2 (see Sect. 4.1).

sits observed with MuSCAT2 on 2 May and 8 July 2023. We co-added the data from MuSCAT2 passbands z_s and i' prior to the analysis. We individually modeled the mid-time of each transit with the code `pyaneti` (Barragán et al. 2022). We found no significant TTV in the ~770 d baseline of our observations, as shown in Fig. 7.

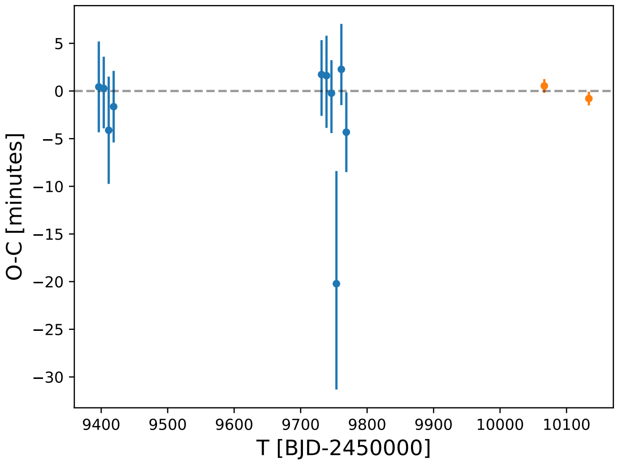

Fig. 7: Transit-timing variations of TOI-4438 b. Blue points correspond to TESS transits while the orange points correspond to the full MuSCAT2 transits.

The lack of extra signals attributable to transiting planets in the *TESS* data might be due to one of the following scenarios (see, e.g., Wells et al. 2021; Schanche et al. 2022; Delrez et al. 2022; Pozuelos et al. 2023): (1) no other planets exist in the system; (2) they do exist, but they do not transit; (3) they do exist and transit the host star, but have orbital periods longer than the ones explored in this study; (4) they do exist and transit, but the photometric precision of the data is not high enough to detect them. Scenarios (1) and (2) might be further explored by em-

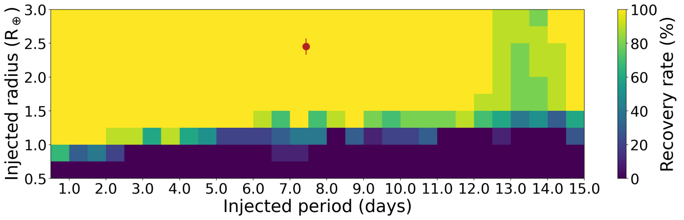

Fig. 8: The resulting detectability map from the injection-and-retrieval experiment. Each pixel corresponds to ten of the 3000 different scenarios, that is, ten light curves with injected planets having different $P_{\rm planet}$, $R_{\rm planet}$, and T_0. Larger recovery rates are presented in yellow and green colors, while lower recovery rates are shown in blue and darker hues. The red dot refers to TOI-4438 b, which has a recovery rate of 100%, highlighting the ease of detecting mini-Neptunes in this *TESS* data set with orbital periods shorter than 15 d.

ploying RV follow-up data as discussed in Sect. 2.2. Scenario (3) can be tested when *TESS* will reobserve TOI-4438 in sectors 79 and 80 (June-July 2024), extending the available time baseline[10]. To evaluate scenario (4), we studied the detection limits of the current *TESS* photometry conducting injection-and-recovery experiments with the `MATRIX` code[11] (Dévora-Pajares & Pozuelos 2023). We used the `MATRIX` code to inject synthetic planets over the PDCSAP light curves corresponding to the three *TESS* sectors used in this study, combining a unique set of radius, orbital period, and phase for each synthetic planet. We explored the $R_{\rm planet}$–$P_{\rm planet}$ parameter space in the ranges of 0.5–3.0 $R_\oplus$ with steps of 0.25 $R_\oplus$, and 0.5–15.0 d with steps of 0.25 d. Moreover, for each combination of $R_{\rm planet}$–$P_{\rm planet}$ `MATRIX` produces five different phases, that is, different values of T_0. In total, we explored 3000 scenarios. For simplicity, the injected planets had impact parameters and eccentricities equal to zero.

Once the synthetic planets were injected in `MATRIX` , we detrended the light curves using a bi-weight filter with a window size of 0.5 d, which was found to be the optimal value to recover the known planet TOI-4438 b. Moreover, existing transits in the data were masked out to evaluate the ease of finding TOI-4438 b-like planets. In `MATRIX` , a synthetic planet is recovered when its epoch matches the injected epoch with 1 hour accuracy, and its period is within 5 % of the injected period. Since we injected the synthetic signals in the PDCSAP light curve, these signals were not affected by the PDCSAP systematic corrections; hence, the detection limits that we found represent the most optimistic scenario (see, e.g., Pozuelos et al. 2020).

The resulting detectability map from this injection-and-retrieval experiment is shown in Fig. 8. On the one hand, we found that transiting Earth- and sub-Earth size planets would remain unnoticed for the complete set of periods explored with recovery rates ranging from 50 to 0%. On the other hand, mini-Neptunes such as TOI-4438 b, seem to be easily detectable, with recovery rates higher than 80% for all the periods, that is, the presence of additional transiting planets in the system with sizes larger than 1.5 $R_\oplus$ and with orbital periods between 0.5 and 15.0 d seems unlikely.

4.3. Frequency analysis of the RV data

We performed a frequency analysis to search for periodic signals due to orbiting planets or stellar activity. We computed the GLS periodograms of the CARMENES RVs and activity indicators, as shown in Fig. 9. We estimated the false alarm probability (FAP) using the bootstrap method as described by Murdoch et al. (1993). We calculated the periodogram of 10^6 time series obtained by randomly shuffling the data and their error bars, keeping the time values fixed. We determined that a peak is significant when it has a FAP < 0.1% (Cochran & Hatzes 1996).

The GLS periodogram of the CARMENES RVs in the VIS band (Fig. 9, upper panel) shows the highest peak at $f_1 = 0.13\,{\rm d}^{-1}$, corresponding to a period of about 7.44 d. This signal is not significant (FAP < 10%) within the frequency range 0.0–0.3 ${\rm d}^{-1}$. However, the peak was found at a known frequency, namely the orbital frequency of the planet, providing strong evidence that the signal is related to TOI-4438 b. We estimated the FAP of the peak at orbital frequency of TOI-4438 b using the "windowing bootstrap" method described by Hatzes (2019) and following the procedure done in Osborne et al. (2024). We found a FAP = 0.002% for f_1, which confirms the planetary nature of the signal discovered by *TESS*.

We also used a pre-whitening technique (Hatzes et al. 2010) to find additional signals. We subtracted the 7.44 d signal from the VIS RVs. The periodogram of the RV residuals following the subtraction of the signal at f_1 (second panel) shows no other significant signal.

Finally, we performed a frequency analysis of the activity indicators obtained using the `serval` pipeline. The GLS periodograms show peaks at periods > 30 d, with a FAP > 10% (lower panels of Fig. 9). Although not significant, peaks at ~68 d and ~34 d are present in the periodograms of the CRX, the Ca II IRT2, Hα, and Na I D indices. The peaks appear at the periods observed in the ground-based photometry analysis of Sect. 3.3, corroborating the stellar rotational period, and its first and second harmonic at 68 d, 34 d, and 22 d, respectively.

4.4. Joint fit of the transit light curves and RV measurements

We performed a joint modeling combining *TESS*, MuSCAT2 i' and z_s transit light curves, and CARMENES VIS RV measurements, following the results presented in Sect. 4.1 and 4.3. We used the code `pyaneti` to perform an MCMC analysis. We followed the procedures described previously in Sect. 4.1, adopting uniform priors for the orbital period and reference transit epoch of TOI-4438 b. We used the same parameterizations and prior distributions as in Sect. 4.1. We performed two analyses: (i) we assumed a circular orbit fixing $\sqrt{e}\sin\omega_\star$ and $\sqrt{e}\cos\omega_\star$ to zero; (ii) we fitted for an eccentric orbit. In a preliminary analysis we used a uniform prior for the stellar density $\rho_\star$. The modeling of the transit light curves gave a mean stellar density consistent with the density of Table. 1, which corroborates the planetary nature of the transit signals. We then sampled for the stellar density $\rho_\star$ using a Gaussian prior on the stellar mass and radius, derived in Sect. 3.1, and used wide uniform priors for the remaining model parameters. We fitted for photometric and RV jitter terms to account for possible signals not captured by our models, or instrumental noise not included in the nominal error bars.

We explored the parameter space with 500 Markov chains initialized randomly inside the prior ranges. Once all chains converged, we used the last 5000 iterations of the converged chains with a thin factor of 10 to create the posterior distributions, lead-

---

[10] See the *TESS*-point Web Tool available at https://heasarc.gsfc.nasa.gov/wsgi-scripts/TESS/TESS-point_Web_Tool/TESS-point_Web_Tool/wtv_v2.0.py/.

[11] The `MATRIX` (**M**ulti-ph**A**se **T**ransits **R**ecovery from **I**njected e**X**oplanets) code is open access on GitHub at https://github.com/PlanetHunters/tkmatrix.

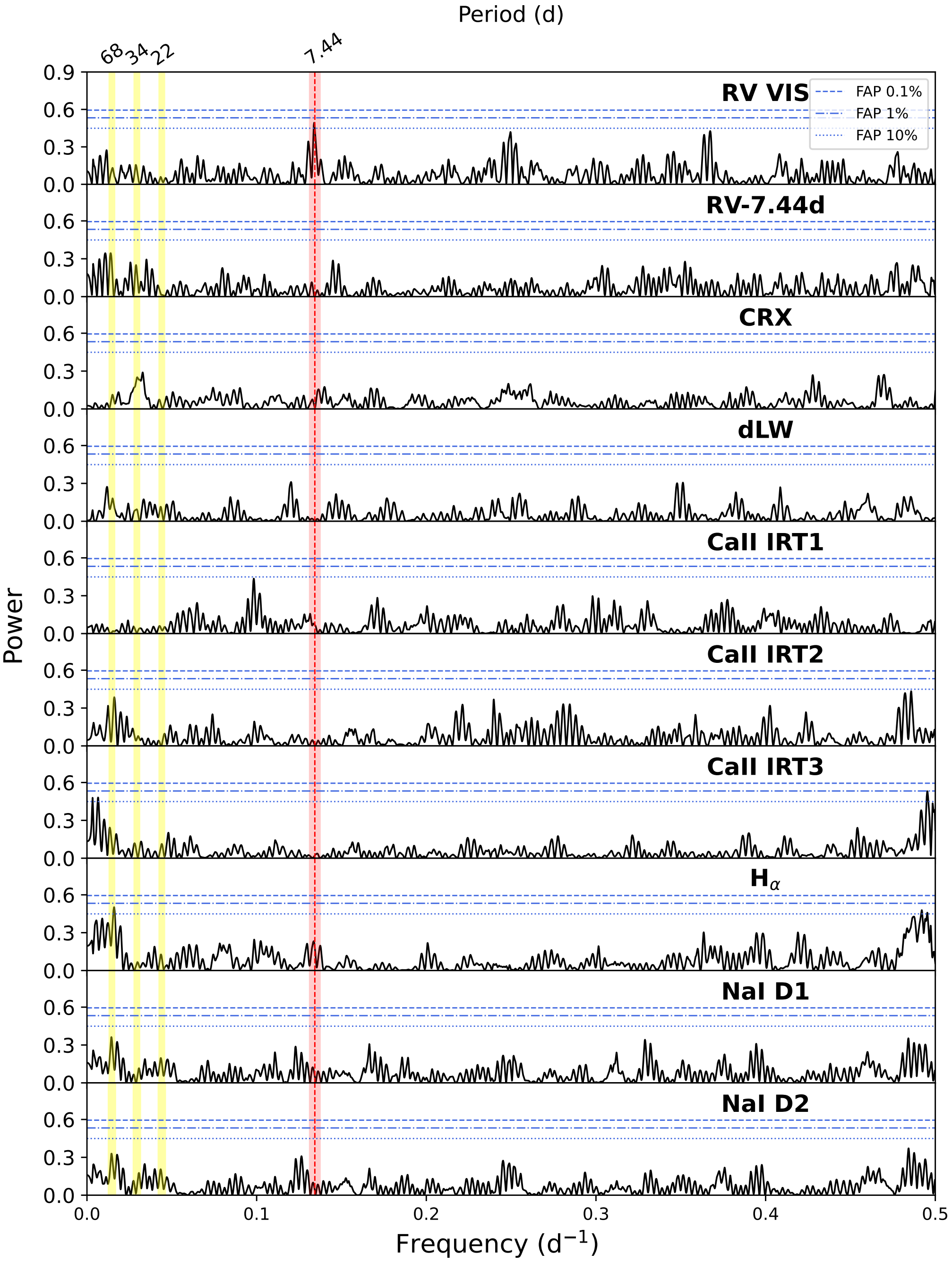

Fig. 9: GLS periodograms of the CARMENES VIS RV measurements (*upper panel*), and RV residuals after subtracting f_1 (*second panel*). The periodograms of the activity indicators are shown in the remaining panels. The 10%, 1%, and 0.1% FAPs are shown with horizontal blue lines. The red vertical line marks the orbital frequency of the transiting planet TOI-4438 b. The yellow vertical lines mark the stellar rotation period at ~ 68 d, and its first and second harmonics.

ing to a distribution of 250 000 data points for each sampled parameter. This procedure ensured a homogeneous sampling of the parameter space. We followed the same procedure and convergence test as described by Barragán et al. (2017).

Results and prior ranges of the fitted and derived parameters are reported in Table 3. Since the planet is not close enough to the star to expect tidal circularization and there are no other reasons to assume so (Sect. 4.5), we chose the eccentric model as the best-fit, although the resulting eccentricity is consistent with zero.

Figs. 10 and 11 display the CARMENES VIS time series and the RV curve phase-folded at the orbital period of TOI-4438 b, respectively, along with the best-fitting Doppler model. We found an RV semi-amplitude variation of $K_b = 3.50 \pm 0.72$ m s^{-1}, and a planetary mass of $M_b = 5.4 \pm 1.1$ M$_\oplus$ (20% precision). We measured a radius of $R_b = 2.52 \pm 0.13$ R$_\oplus$ (5% precision). Combining the planetary mass and radius, we calculated a mean density of $\rho_b = 1.85^{+0.51}_{-0.44}$ g cm^{-3} (~28% precision).

Although the results obtained with `pyaneti` are robust, we performed a second joint analysis of the light curves and RVs with `juliet` (Espinoza et al. 2019) as a sanity check. The derived planetary parameters are consistent within errors with those presented in Table 4.4. The `juliet` planetary radius and mass are $R_b = 2.54 \pm 0.12\,\mathrm{R}_\oplus$ (∼5 %), and $M_b = 5.7 \pm 1.1\,\mathrm{M}_\oplus$ (∼20 %), respectively.

4.5. Tidal damping of the eccentricity and its consequences

We estimated the current eccentricity decay timescale of TOI-4438b adopting the model by Leconte et al. (2010). We assumed that its current value is $e = 0.14$, although its actually measured value is compatible with zero at the 2σ level. To apply the tidal model, we expressed the product of the constant tidal time lag Δt_p, adopted by Leconte et al. (2010), by the Love number of the planet $k_{2,\mathrm{p}}$:

$$k_{2,\mathrm{p}}\Delta t_\mathrm{p} = \frac{3}{2Q'_\mathrm{p}n}, \tag{1}$$

where Q'_p is the modified tidal quality factor of the planet itself, $n = 2\pi/P$ is the orbit mean motion, and P the orbital period.

The rheology of mini-Neptune planets is unknown, thus we investigated two extreme cases. The former assumed $Q'_\mathrm{p} = 10^5$, which is comparable to the modified tidal quality factor of Uranus or Neptune as estimated by for example Tittemore & Wisdom (1990) and Ogilvie (2014), and is appropriate for a body where the dissipation of the tidal energy occurs in a fluid interior; the latter assumed that tides are mainly dissipated inside a rocky core encompassing the whole mass of the planet 5.4 $\mathrm{M}_\oplus$, but having a radius of 1.3 $\mathrm{R}_\odot$. This hypotetical core radius corresponds to the peak of the smallest radius component of the distribution of the transiting planets as observed by Kepler (Fulton et al. 2017). According to the model by Owen & Wu (2017) such a radius corresponds to the mean size of the bare core that remains after the gaseous envelope of a mini-Neptune has been removed by photoevaporation after the first few 100 Myr after its host star settled on the main sequence. In the latter case, we adopted $Q'_\mathrm{p} = 300$ as in the case of our Earth (Henning et al. 2009) and neglected the small mass and tidal dissipation in the fluid outer envelope of the planet in comparison with that in its rocky core. The present eccentricity tidal decay timescale was found to be $\tau_\mathrm{e} \equiv |e/(de/dt)| \sim 24$ Gyr in the former case, while $\tau_\mathrm{e} \sim 2$ Gyr in the latter case. We noted that tidal dissipation inside the star has a negligible effect on the evolution of the eccentricity because of the relatively large separation of the planet and its small mass. Our results on the eccentricity decay timescale are critically dependent on the Q'_p of the planet, and therefore, it is difficult to reach a conclusion on the possibility that the current eccentricity is primordial or is still excited, for example, by the gravitational perturbation of a distant companion or by other effects (see, e.g., Correia et al. 2020).

An interesting consequence of the eccentric orbit of TOI-4438b is its expected pseudosynchronization with the orbital motion, that is, its rotation is predicted to be faster than the orbital mean motion n because tides tend to synchronize its rotation with the orbital velocity at periastron where they are stronger. Using the formalism of Leconte et al. (2010), we predicted a rotation period of the planet of 6.7 d, that is, 1.12 times shorter than its orbital period. Such a state of pseudosynchronization is reached after a timescale of ∼ 0.26 Myr for $Q'_\mathrm{p} = 10^5$ or 5.6 kyr for $Q'_\mathrm{p} = 300$, that is, on timescales much shorter than the system lifetime. We expect tides to dissipate energy inside the planet due to its eccentric orbit and pseudosynchronous rotation. The maximum dissipated power is predicted for $Q'_\mathrm{p} = 300$ and is $\sim 6.3 \times 10^{16}$ W giving a heat flux of ~ 20 W m^{-2} at the top of its atmosphere with a radius of 2.5 $\mathrm{R}_\oplus$. Such a flux is significantly larger than in the case of Jupiter, where the heat flux from the interior of the planet is $\sim$ 5.4 W m^{-2} (Guillot et al. 2004). Therefore, it can play a relevant role in the atmospheric dynamics of the planet. On the other hand, adopting $Q'_\mathrm{p} = 10^5$, we found a dissipated power of 5.2×10^{15} W and a surface flux of only ~ 1.6 W m^{-2}.

5. Discussion

TOI-4438 b has a mass of $M_b = 5.4 \pm 1.1\,\mathrm{M}_\oplus$, and a radius of $R_b = 2.52 \pm 0.13\,\mathrm{R}_\oplus$, with precision of 20% and 5%, respectively. Its bulk density of $\rho_b = 1.85^{+0.51}_{-0.44}$ g cm^{-3}, is close to Neptune's of 1.638 g cm^{-3} and 32% that of Earth's density. We calculated an equilibrium temperature of 435 K, assuming zero albedo. TOI-4438 b belongs to the small group ($\lesssim 50$) of planets around M-dwarf stars whose masses and radii are known with a precision better than 25%. Fig. 12 shows the mass-radius diagram with different theoretical composition models (Zeng et al. 2016). TOI-4438 b lies in the mini-Neptunes domain.

The position of TOI-4438 b in the mass-radius diagram is consistent with a high volatile content; it joins a group of low-density planets abundantly predicted in planet population syntheses based on the core accretion paradigm (e.g., Venturini et al. 2020; Burn et al. 2021; Schlecker et al. 2021a,b), where they correspond to planets with high (∼50 %) water ice mass fractions that accreted the bulk of their mass outside the water ice line (e.g., Mordasini 2018; Bitsch et al. 2021). However, the planet's bulk density is also compatible with an extended atmosphere.

With an instellation of $S_\mathrm{b} = 6.00^{+0.90}_{-0.77}\,S_\oplus$, TOI-4438 b is orbiting significantly closer to its host star than the predicted inner edge of the habitable zone (Kopparapu et al. 2014). As such, it may either have undergone an instellation-induced runaway greenhouse transition (e.g., Kasting 1988; Nakajima et al. 1992) and lost all its water to space, or currently be in a post-runaway state and host an extended steam atmosphere. The latter scenario is consistent with the planet's low bulk density (Turbet et al. 2020; Dorn & Lichtenberg 2021) and gains credibility through the expected long durations of runaway greenhouse phases in planets orbiting M dwarfs (Luger & Barnes 2015). With a derived instellation of a few times that of Earth, TOI-4438 b is well within the runaway greenhouse regime but close to the habitable zone inner edge. As such, and through the precise density estimate presented here, TOI-4438 b contributes to the currently small sample of planets suited to probe the habitable zone inner edge discontinuity, a predicted demographic imprint of the habitable zone inner edge in the radius–density distribution of small exoplanets (Turbet et al. 2019; Schlecker et al. 2023).

5.1. Interior modeling

Given the planet mass and radius obtained in our transit and radial velocity analyses, we derived the interior composition of TOI-4438 b. The forward model favoured an interior structure model for water-dominated sub-Neptunes (Acuña et al. 2021; Aguichine et al. 2021). The interior structure of the planet was assumed to consist of three layers: a Fe-rich core, a silicate mantle, and a water layer. The phases of water present in the top layer were determined self-consistently with the irradiation received by the planet from its host star and an atmospheric model. To compute the temperature in the deep water layer, we used the k-correlated atmospheric model initially introduced in Marcq

Table 3: TOI-4438 b parameters from the joint RVs and transit modeling with `pyaneti`.[a]

Parameter	Prior	Derived value ($e = 0$)	Derived value ($e \neq 0$)
Model parameters			
$P_{\rm orb,b}$ [d]	$\mathcal{U}[7.2,7.7]$	7.44628 ± 0.000009	7.44628 ± 0.000009
$T_{0,\rm b}$ [BJD$_{\rm TDB}-2{,}450{,}000$]	$\mathcal{U}[9396.16, 9396.66]$	9396.41178 ± 0.00066	9396.41168 ± 0.00065
$R_{\rm b}/R_\star$	$\mathcal{U}[0.001,0.09]$	0.0613 ± 0.0007	0.062 ± 0.001
$b_{\rm b}$	$\mathcal{U}[0,1]$	$0.18^{+0.15}_{-0.13}$	$0.39^{+0.16}_{-0.24}$
$\sqrt{e_{\rm b}} \sin \omega_{\star,\rm b}$	$\mathcal{U}[-1,1]$	0.0	$-0.31^{+0.20}_{-0.14}$
$\sqrt{e_{\rm b}} \cos \omega_{\star,\rm b}$	$\mathcal{U}[-1,1]$	0.0	$0.11^{+0.14}_{-0.19}$
$K_{\rm b}$ [m s^{-1}]	$\mathcal{U}[0,50]$	3.23 ± 0.69	3.50 ± 0.72
Derived parameters			
$M_{\rm b}$ [$M_\oplus$]	...	5.1 ± 1.1	5.4 ± 1.1
$R_{\rm b}$ [$R_\oplus$]	...	2.48 ± 0.12	2.52 ± 0.13
$\rho_{\rm b}$ [g cm^{-3}]	...	$1.80^{+0.53}_{-0.44}$	$1.85^{+0.51}_{-0.44}$
$a_{\rm b}$ [au]	...	0.0509 ± 0.0028	0.0534 ± 0.0037
$e_{\rm b}$	...	0.0	0.14 ± 0.09
$\omega_{\star,\rm b}$ [deg]	...	0.0	-70^{+36}_{-32}
$i_{\rm b}$ [deg]	...	$89.64^{+0.25}_{-0.31}$	$89.34^{+0.39}_{-0.21}$
$\tau_{14,\rm b}$ [h]	...	2.002 ± 0.018	$2.021^{+0.033}_{-0.025}$
$T_{\rm eq,b}$ [K] (a=0)	...	446 ± 13	435 ± 15
$T_{\rm eq,b}$ [K] (a=0.6)	...	354 ± 7	347 ± 5
$S_{\rm b}$ [S$_\oplus$]	...	$6.57^{+0.81}_{-0.68}$	$6.00^{+0.90}_{-0.77}$
Additional model parameters			
$\rho_\star$ [g cm^{-3}]	$\mathcal{N}[10.06,1.62]$	$8.92^{+0.49}_{-0.99}$	$10.1^{+1.7}_{-1.4}$
$\gamma_{\rm CARMENES}$ [m s^{-1}]	$\mathcal{U}[-2,2]$	-0.2 ± 0.5	-0.3 ± 0.5
RV jitter term $\sigma_{\rm RV,CARMENES}$ [m s^{-1}]	$\mathcal{J}[0,100]$	$1.48^{+0.72}_{-0.79}$	$1.33^{+0.71}_{-0.80}$
Phot. jitter term $\sigma_{\rm TESS}$	$\mathcal{J}[0,100]$	0.000060 ± 0.000055	0.000060 ± 0.000055
Phot. jitter term $\sigma_{\rm MuSCAT2\,i'}$	$\mathcal{J}[0,100]$	0.00014 ± 0.00011	0.00013 ± 0.00011
Phot. jitter term $\sigma_{\rm MuSCAT2\,z_s}$	$\mathcal{J}[0,100]$	0.00018 ± 0.00016	0.00017 ± 0.00016

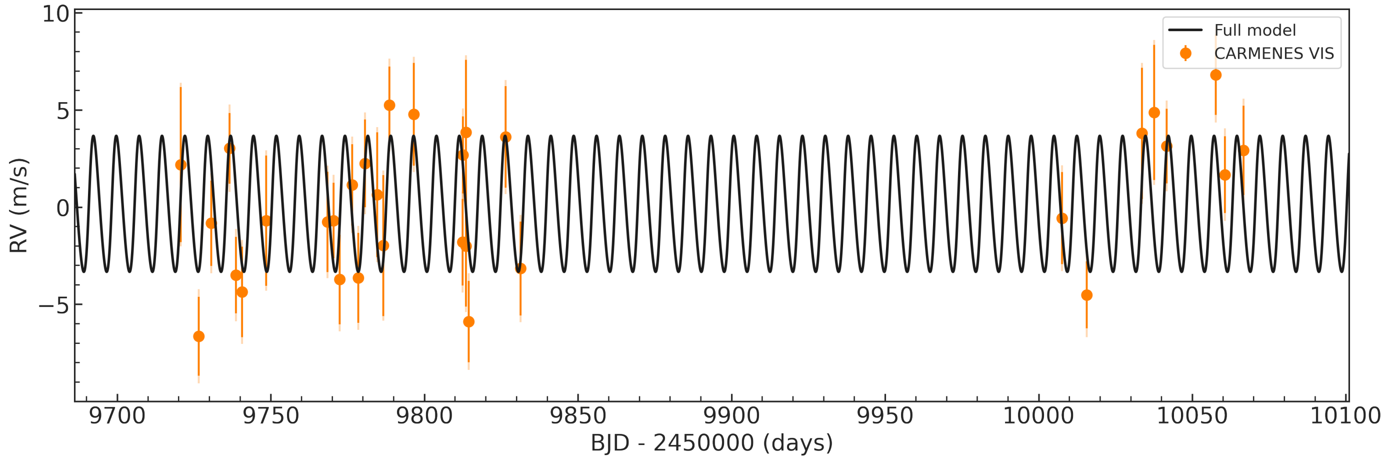

Fig. 10: CARMENES RV time series of TOI-4438 along with the best-fitting model. Data are shown as orange filled circles with their nominal uncertainties and semitransparent error bar extensions accounting for the jitter term.

et al. (2017) and Pluriel et al. (2019), with up-to-date opacity and equation of state data from Acuña et al. (2023). The atmospheric model computed the temperature profile and the radius contribution of the upper water envelope (from 300 bar to 20 mbar). The interior and the atmospheric models were coupled self-consistently assuming radiative-convective equilibrium in the atmosphere, and with an iterative algorithm (Acuña et al. 2021). A water-dominated upper envelope was inferred with 99% H_2O and 1% CO_2.

TOI-4438 b's instellation is high enough to have molecules such as water in gas and supercritical phases. Fig. 13 shows the posterior distribution functions of the free parameters in our interior composition retrieval. Due to the low density of the planet and its distance from the star, the refractory elements probably consist of silicates instead of a Si and Fe mixture (Aguichine et al. 2020). Therefore, in our analysis we set the Fe mass fraction to zero. We obtained a water mass fraction of $0.62^{+0.34}_{-0.16}$. With a composition between 46% and 96% H_2O (1σ), TOI-4438 b is volatile-rich. Moreover, it is very likely to have H/He atmosphere

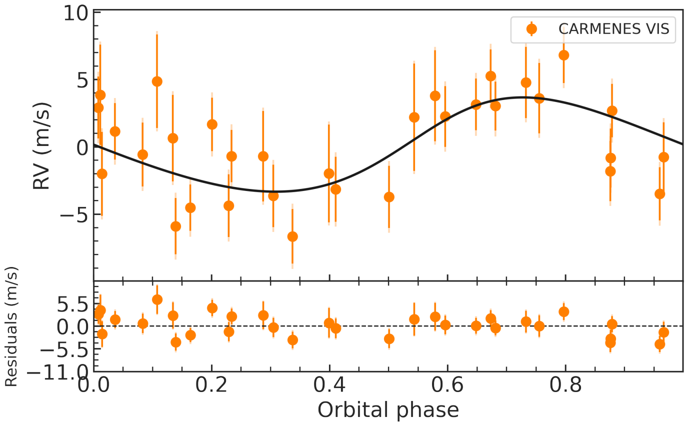

Fig. 11: Same as Fig. 10 but phase-folded at the orbital period of TOI-4438 b.

mixed with molecules, such as H_2O, CO_2, and CH_4. In the Solar System, comets and other small bodies with up to 80% of pure water have been found (McKay et al. 2019). However, low-mass planets with more than 50% water in mass are not a natural outcome of planetesimal accretion and other planet formation mechanisms (Kimura & Ikoma 2020; Miguel et al. 2020). Thus, atmospheric characterization is required to break the degeneracy between the mass and the composition of the envelope, and to determine whether TOI-4438 b has a massive, high metallicity envelope (i.e H_2O envelope scenario), or a less massive, low metallicity atmosphere (i.e H/He-dominated envelope scenario).

5.2. Prospects for atmospheric characterization

We used the metric proposed by Kempton et al. (2018) to identify the transiting planets most amenable for atmospheric characterization via transmission spectroscopy with the *JWST*. For TOI-4438 b the derived transmission spectroscopy metric (TSM) is 136 ± 13, which is well above the threshold value of 92 defined for the respective planetary categories (small mini-Neptunes; $1.5\,R_\oplus < R_p < 2.75\,R_\oplus$) for follow-up studies (Kempton et al. 2018). In this regard, TOI-4438 b is placed in the second quartile (rank 25–50%) of *JWST* targets with the strongest predicted atmospheric detections, and it is among the first five planets with the highest TSM, whose host stars have *J*-band magnitudes of 8.5 mag < J < 11.5 mag. Therefore, TOI-4438 b is one of the best small mini-Neptune targets for atmospheric characterization. Fig. 14 shows the TSM value of TOI-4438 b along with the TSMs of known transiting planets smaller than $4\,R_\oplus$ with measured masses, as retrieved from the Transiting Extrasolar Planet Catalogue (Southworth 2011). We also calculated the emission spectroscopy metric (ESM) following Kempton et al. (2018) finding an ESM of ∼4, which instead is below the suggested threshold value (i.e., ESM = 7.5). The planet TOI-4438 b is not a high priority target for emission spectroscopy of terrestrial planets with JWST.

We explored the potential of TOI-4438 b for transmission spectroscopy with the *JWST* through spectral simulations for a set of model atmospheres consistent with the planetary mass, radius, and equilibrium temperature. We adopted `TauREx 3` (Al-Refaie et al. 2021) to generate the synthetic transmission spectra. TOI-4438 b could have a rocky core surrounded by an H/He envelope or be a waterworld (Sect 5.1). We modeled H/He atmospheres with 1× and 100× scaled solar abundances using the atmospheric chemical equilibrium module (Agúndez et al. 2012), including collisionally induced absorption by H_2–H_2 and H_2–He (Abel et al. 2011, 2012; Fletcher et al. 2018), and Rayleigh scattering. For each chemical setup, we considered the cases of clear and hazy atmospheres. The haze was modeled by Mie scattering with the formalism of Lee et al. (2013), assuming a particle size of $\alpha = 0.05\,\mu$m, a mixing ratio of $\chi_c = 10^{-12}$, and an extinction coefficient of $Q_0 = 40$. While this assumption has some limitations in reproducing the actual behavior of scattered light due to using spherical particles instead of non-spherical ones (see, e.g., Mishchenko et al. 1996), this strategy was motivated by its low computational cost. The same haze parameters were chosen in previous atmospheric simulation studies (e.g. Orell-Miquel et al. 2023). We note that a super-solar metallicity is expected from planetary formation theories (e.g., Fortney et al. 2013; Thorngren et al. 2016). The equilibrium temperature within ∼400–600 K also points to a high degree of haziness due to inefficient haze removal (Gao & Zhang 2020; Ohno & Tanaka 2021; Yu et al. 2021). Additionally, we modeled the case of a steam H_2O atmosphere.

We used `ExoTETHyS` (Morello et al. 2021) to simulate the corresponding *JWST* spectra, as observed with the NIRISS-SOSS (0.6–2.8 μm), NIRSpec-G395H (2.88–5.20 μm), and MIRI-LRS (5–12 μm) instrumental modes. The spectroscopic error bars obtained with `ExoTETHyS` are consistent with those calculated using the Exoplanet Characterization Toolkit (ExoCTK, Bourque et al. 2021) and `PandExo` (Batalha et al. 2017), as proven in previous studies (Murgas et al. 2021; Espinoza et al. 2022; Luque et al. 2022a,b; Chaturvedi et al. 2022; Lillo-Box et al. 2023; Orell-Miquel et al. 2023; Palle et al. 2023). We conservatively increased the error estimates by 20%. We chose the sizes of the wavelength bins following the recommendations from recent *JWST* data synthesis papers that adopted a spectral resolution of R ∼100 for NIRISS and NIRSpec (Carter et al., under review), and a constant bin size of 0.25 μm for MIRI-LRS observations (Powell et al. 2024).

Fig. 15 shows the synthetic transmission spectra for the atmospheric configurations above. The H/He model atmospheres exhibit strong H_2O and CH_4 absorption features of $\gtrsim$100–1000 parts per million (ppm), depending on metallicity and haze, while the steam H_2O atmosphere has absorption features $\lesssim$100 ppm. The predicted error bars for a single transit observation are 31–123 ppm (mean error 53 ppm) for NIRISS-SOSS, 38–82 ppm (mean error 56 ppm) for NIRSpec-G395H, and 47–89 ppm (mean error 64 ppm) for MIRI-LRS. Our simulations suggest that a single transit observation with NIRISS-SOSS or NIRSpec-G395H is well suited to detect an H/He atmosphere, while at least two transit observations may be needed to reveal a secondary H_2O– dominated atmosphere.

5.3. Expected radio emission from star-planet interaction

Here we assess the feasibility of detecting radio emission arising from magnetic star-planet interaction (SPI) between TOI-4438b and its host star. The physical phenomenon responsible for this kind of emission is the electron cyclotron maser (ECM) instability (Melrose & Dulk 1982), which can generate auroral radio emission on the star and also the planet itself.

The characteristic frequency associated with ECM is given by the electron gyrofrequency, $\nu_G = 2.8\,B$ MHz, where B is the local magnetic field in Gauss. This non-thermal emission is coherent and circularly polarized (reaching up to 100% in some instances), and may reach a large bandwidth ($\Delta\nu \sim \nu_G/2$).

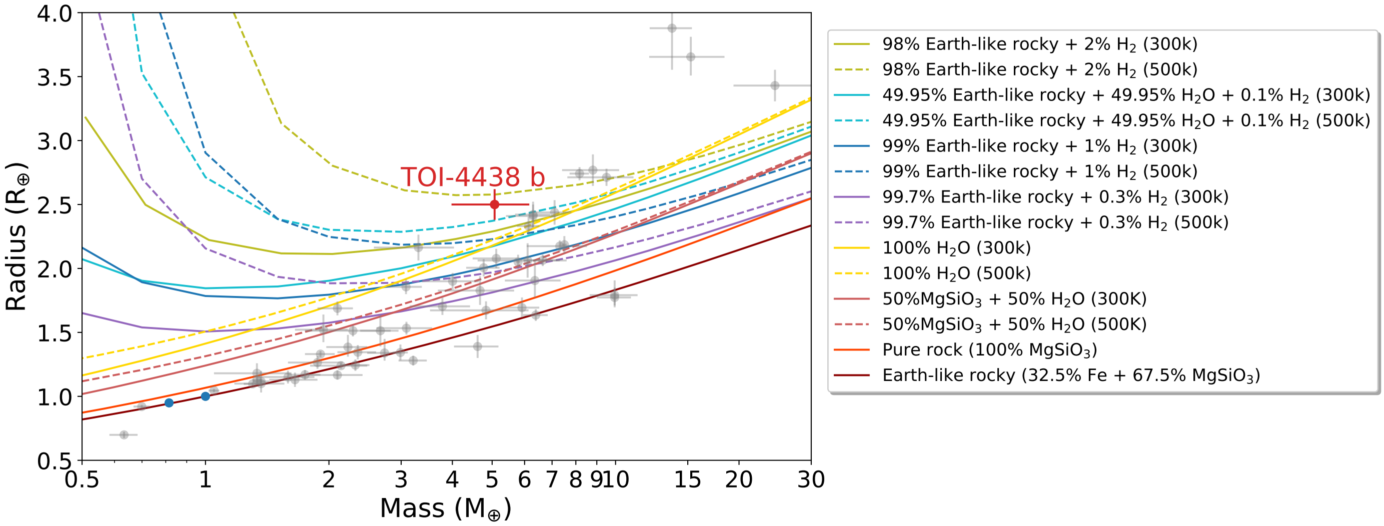

Fig. 12: Mass-radius diagram for well-characterized planets (R< 4 $R_\oplus$, M< 13 $M_\oplus$) around M-dwarf stars ($T_{\rm eff}$ <4000 K), as retrieved from the Transiting Extrasolar Planet Catalogue (Southworth 2011). The masses and radii are known with a precision better than 30% and 10%, respectively. The theoretical composition models from Zeng et al. (2019) are displayed from bottom to top, with solid and dashed curves. The location of TOI-4438 b is marked with a red dot.

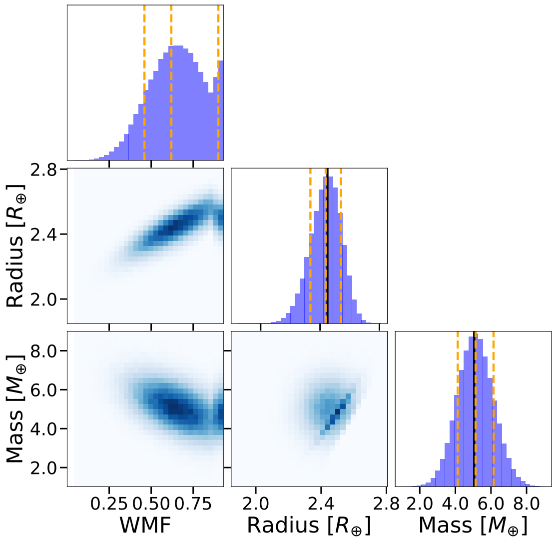

Fig. 13: Posterior probability distributions of the mass, radius and water mass fraction (WMF) derived from in the interior structure retrieval. The diagonal panels show the marginalized probability distributions of the individual parameters. For the observable parameters (mass and radius), the mean observed value is indicated with a black line. The mean and the 1σ interval of the posterior distributions retrieved in the MCMC are shown as orange dashed lines for all parameters. The PDFs agree well with the mean and uncertainties of the observed mass and radius.

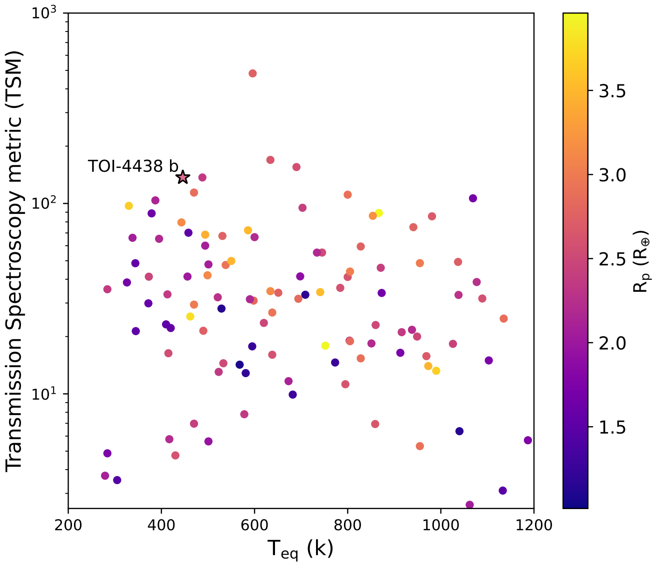

Fig. 14: TSM for planets with radii smaller than 4 $R_\oplus$ and measured masses, whose host stars have J-band magnitudes of 8.5 mag < J < 11.5 mag. TOI-4438 b is displayed with a star symbol. The color indicates the radius of the planets.

We note, however, that any kind of SPI emission coming from the planet itself would be undetectable with current instrumentation. The reason is that the magnetic field of a planet is merely a few Gauss, so the resulting emission would be blocked by the Earth's ionosphere. We therefore studied the auroral emission on the star TOI-4438 induced by the presence of its planet b, since the global magnetic field of the star is of the order of a few hundreds of Gauss or larger. As a result, the corresponding electron gyrofrequency would be of several hundreds or thousands of MHz, a frequency range that can be studied with current observatories. This phenomenon takes place in the sub-Alfvénic regime, that is, when the planet is close enough to the star that the speed of the plasma wind is lower than the Alfvén speed, enabling energy and momentum to travel back from the planet onto the star in the form of Alfvèn wings, triggering the radio emission close to the stellar surface.

To estimate the magnetic field of TOI-4438, we used the relation from Reiners et al. (2022), who estimated the Rossby number as a function of the stellar mass with the relations from

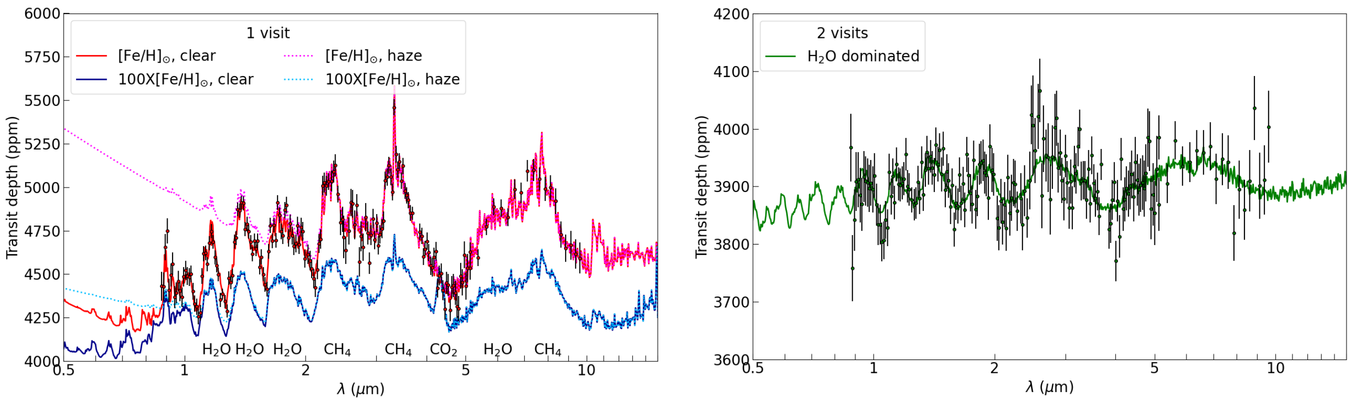

Fig. 15: Synthetic atmospheric transmission spectra of TOI-4438 b. *Left:* fiducial models for clear or hazy H/He atmospheres with scaled solar abundances. *Right:* model for a steam H_2O atmosphere. Simulated measurements with error bars are shown for the observation of one (*left*) or two (*right*) transits with *JWST* NIRISS-SOSS, NIRSpec-G395H, and MIRI-LRS configurations.

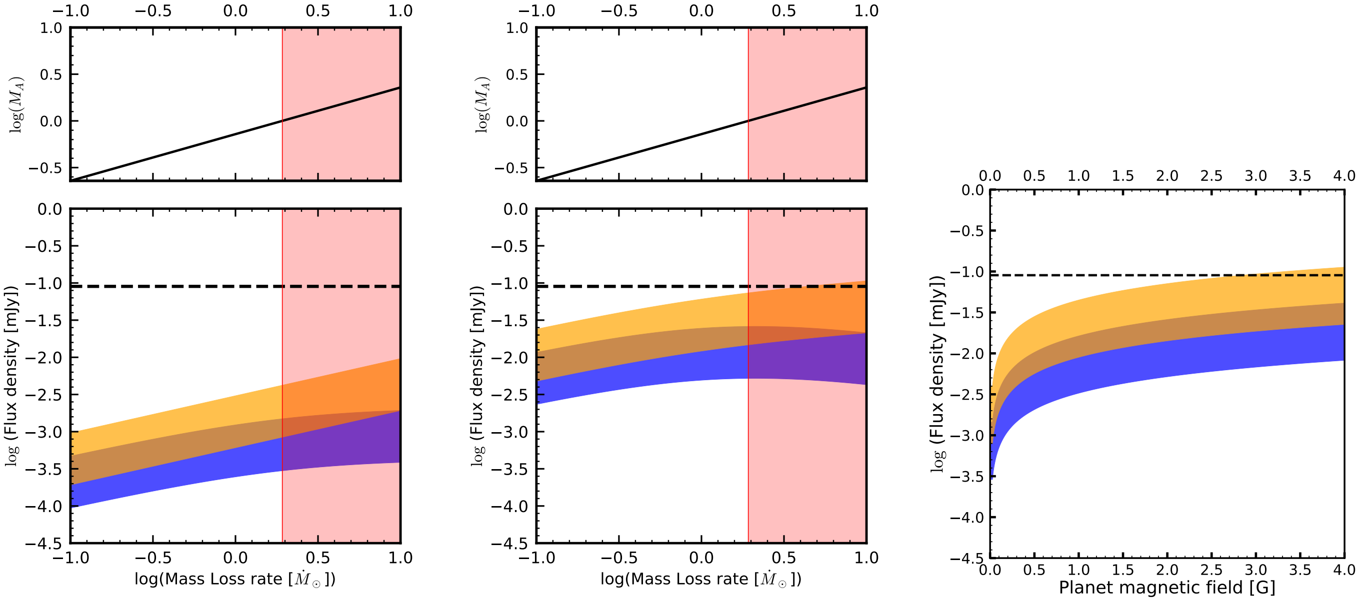

Fig. 16: Flux density arising from star planet interaction as a function of stellar mass-loss rate (*left* and *center*) and the magnetic field of the planet (*right*). The emission expected from Saur–Turnpenney's model is shown in orange, while the emission expected from Zarka–Lanza's model is shown in blue. The overlap between both models is shown in brown. We show in pale red color the region when the planet is in the super-Alfvènic regime. The dashed black line represents an assumed detection threshold of 100 μJy. For the variation with respect to the magnetic field of the planet we used $\dot{M} = 1.92\dot{M}_\odot$, which is the maximum value for the mass loss rate before entering the sub-Alfvènic regime. *Left*: Expected flux density for an unmagnetized planet in a closed dipolar geometry, as a function of the stellar wind mass loss. The pale red colored region indicates the super-Alfvénic case, when our approach no longer applies. *Center*: The same as in the left panel, but for a magnetized planet with $B_\mathrm{p} = 2$ G. *Right*: Expected flux density for a closed dipolar geometry

Wright et al. (2018), which yields a value of $B_\star \approx 191.9$ G. We then used the code described in Pérez-Torres et al. (2021) to estimate the flux density arising from the sub-Alfvénic interaction between an exoplanet and its host star, for an isothermal wind. For our calculations, we assumed an isothermal wind with coronal temperature equal to that of the solar corona, $T = 2 \times 10^6$ K, and which is also adequate for M dwarf stars. We took the solid angle covered by the ECM emission to be 1.6 sterradians, in conformity with observations of the Jupiter-Io decametric radio emission (Ray & Hess 2008). We worked with two different emission models, Saur–Turnpenney (Saur et al. 2013; Turnpenney et al. 2018) and Zarka–Lanza (Zarka 2007; Lanza 2009), and in both cases we considered an efficiency in the conversion from Poynting flux to radio emission in the range from 0.2 to 1%.

In the left panels of Fig. 16, we show the radio flux density from sub-Alfvénic star-planet interaction as a function of the mass-loss rate of the star for an unmagnetized planet and a planet with a magnetic field of 2 G. In this regime, our approach does not apply and, therefore, no radio emission from SPI can reach us. In the right panel of Fig. 16 we show the emission as a function of the magnetic field of the planet. Despite the planet being rather large in size, the expected radio emission is too low to be detectable in essentially all scenarios due to the large distance to the system (30 pc). Only in the case when the planet is highly magnetized and the stellar wind is relatively powerful there could be marginal chances of detecting a signal from SPI.

6. Conclusions

We have reported the confirmation and characterization of TOI-4438 b, a mini-Neptune around an M3.5 V star (G 182-34) on a 7.44 d orbit. We performed a joint modeling of the *TESS* and MuSCAT2 light curves with CARMENES high-resolution spectroscopy measurements. We found a radius of 2.52 ± 0.13 $R_\oplus$ and a mass of 5.4 ± 1.1 $M_\oplus$, resulting in a bulk density of $1.85\,^{+0.51}_{-0.44}\,\mathrm{g\,cm^{-3}}$. The equilibrium temperature of the planet is 435 ± 15 K.

Our interior structure retrieval with a pure water envelope yields a minimum water mass fraction of 46% (1σ). The volatile-rich mini-Neptune TOI-4438 b has likely H/He mixed with molecules, such as water, CO_2, and CH_4. TOI-4438 b presents a high transmission spectroscopy metric of 136 ± 13, which places the planet among the most suitable targets for atmospheric observations with *JWST*. We performed spectral simulations to explore the potential for transmission spectroscopy with *JWST*. A single transit observation of TOI-4438 with NIRISS-SOSS or NIRSpec-G395H should be adequate to detect an H/He atmosphere, while at least two transits may be needed to reveal a secondary H_2O dominated atmosphere.

Acknowledgements. We acknowledge the use of public *TESS* data from pipelines at the *TESS* Science Office and at the TESS Science Processing Operations Center. TESS data presented in this paper were obtained from the Milkulski Archive for Space Telescopes (MAST) at the Space Telescope Science Institute. Resources supporting this work were provided by the NASA High-End Computing (HEC) Program through the NASA Advanced Supercomputing (NAS) Division at Ames Research Center for the production of the SPOC data products. CARMENES is an instrument at the Centro Astronómico Hispano en Andalucía (CAHA) at Calar Alto (Almería, Spain), operated jointly by the Junta de Andalucía and the Instituto de Astrofísica de Andalucía (CSIC). CARMENES was funded by the Max-Planck-Gesellschaft (MPG), the Consejo Superior de Investigaciones Científicas (CSIC), the Ministerio de Economía y Competitividad (MINECO) and the European Regional Development Fund (ERDF) through projects FICTS-2011-02, ICTS-2017-07-CAHA-4, and CAHA16-CE-3978, and the members of the CARMENES Consortium (Max-Planck-Institut für Astronomie, Instituto de Astrofísica de Andalucía, Landessternwarte Königstuhl, Institut de Ciències de l'Espai, Institut für Astrophysik Göttingen, Universidad Complutense de Madrid, Thüringer Landessternwarte Tautenburg, Instituto de Astrofísica de Canarias, Hamburger Sternwarte, Centro de Astrobiología and Centro Astronómico Hispano-Alemán), with additional contributions by the MINECO, the Deutsche Forschungsgemeinschaft (DFG) through the Major Research Instrumentation Programme and Research Unit FOR2544 "Blue Planets around Red Stars", the Klaus Tschira Stiftung, the states of Baden-Württemberg and Niedersachsen, and by the Junta de Andalucía. The results reported herein benefitted from collaborations and/or information exchange within NASA's Nexus for Exoplanet System Science (NExSS) research coordination network sponsored by NASA's Science Mission Directorate under Agreement No. 80NSSC21K0593 for the program "Alien Earths". The Joan Oró Telescope (TJO) of the Montsec Observatory (OdM) is owned by the Catalan Government and operated by the Institute for Space Studies of Catalonia (IEEC). G.M. has received fundings from the Ariel Postdoctoral Fellowship program of the Swedish National Space Agency (SNSA). S.V.J. acknowledges the support of the DFG priority program SPP 1992 "Exploring the Diversity of Extrasolar Planets (JE 701/5-1). M.P.T. and L.P.M. acknowledge financial support through grants CEX2021-001131-S and PID2020-117404GB-C21, funded by MCIU/AEI/10.13039/501100011033. L.P.M. also acknowledges funding through the grant PRE2020-095421, funded by MCIU/AEI/10.13039/501100011033 and by FSE Investing in your future. This work is partly supported by JSPS KAKENHI Grant Number JP18H05439, JST CREST Grant Number JPMJCR1761. This article is based on observations made with the MuSCAT2 instrument, developed by ABC, at Telescopio Carlos Sánchez operated on the island of Tenerife by the IAC in the Spanish Observatorio del Teide. We acknowledge financial support from the Agencia Estatal de Investigación (AEI/10.13039/501100011033) of the Ministerio de Ciencia e Innovación and the ERDF "A way of making Europe" through projects PID2022-137241NB-C4[1:4], PID2021-125627OB-C31, PID2019–109522GB–C5[1:4], and the Centre of Excellence "Severo Ochoa" and "María de Maeztu" awards to the Instituto de Astrofísica de Canarias (CEX2019-000920-S), Instituto de Astrofísica de Andalucía (CEX2021-001131-S) and Institut de Ciències de l'Espai (CEX2020-001058-M). This work was also funded by the Generalitat de Catalunya/CERCA programme, the DFG through grant HA3279/14-1 and the priority program SPP 1992 "Exploring the Diversity of Extrasolar Planets" (JE 701/5-1), the JSPS KAK-ENHI through grant JP18H05439, the JST CREST through grant JPMJCR1761, and the Israel Science Foundation through grant 1404/22.

References

Abel, M., Frommhold, L., Li, X., & Hunt, K. L. C. 2011, Journal of Physical Chemistry A, 115, 6805
Abel, M., Frommhold, L., Li, X., & Hunt, K. L. C. 2012, J. Chem. Phys., 136, 044319
Acuña, L., Deleuil, M., & Mousis, O. 2023, A&A, 677, A14
Acuña, L., Deleuil, M., Mousis, O., et al. 2021, A&A, 647, A53
Aguichine, A., Mousis, O., Deleuil, M., & Marcq, E. 2021, ApJ, 914, 84
Aguichine, A., Mousis, O., Devouard, B., & Ronnet, T. 2020, ApJ, 901, 97
Agúndez, M., Venot, O., Iro, N., et al. 2012, A&A, 548, A73
Al-Refaie, A. F., Changeat, Q., Waldmann, I. P., & Tinetti, G. 2021, ApJ, 917, 37
Aller, A., Lillo-Box, J., Jones, D., Miranda, L. F., & Barceló Forteza, S. 2020, A&A, 635, A128
Anderson, D. R., Cameron, A. C., Hellier, C., et al. 2010, ApJL, 726, L19
Baglin, A., Auvergne, M., Boisnard, L., et al. 2006, in 36th COSPAR Scientific Assembly, Vol. 36, 3749
Ballerini, P., Micela, G., Lanza, A. F., & Pagano, I. 2012, A&A, 539, A140
Barkaoui, K., Timmermans, M., Soubkiou, A., et al. 2023, A&A, 677, A38
Barragán, O., Aigrain, S., Rajpaul, V. M., & Zicher, N. 2022, MNRAS, 509, 866
Barragán, O., Gandolfi, D., & Antoniciello, G. 2017, pyaneti: Multi-planet radial velocity and transit fitting, Astrophysics Source Code Library, record ascl:1707.003
Batalha, N. E., Mandell, A., Pontoppidan, K., et al. 2017, PASP, 129, 064501
Batalha, N. M., Rowe, J. F., Bryson, S. T., et al. 2013, ApJS, 204, 24
Bayo, A., Rodrigo, C., Barrado Y Navascués, D., et al. 2008, A&A, 492, 277
Bitsch, B., Raymond, S. N., Buchhave, L. A., et al. 2021, 1
Borucki, W. J., Koch, D., Basri, G., et al. 2010, Science, 327, 977
Bouma, L. G., Palumbo, E. K., & Hillenbrand, L. A. 2023, ApJ, 947, L3
Bourque, M., Espinoza, N., Filippazzo, J., et al. 2021, The Exoplanet Characterization Toolkit (ExoCTK), Zenodo
Brown, T. M., Baliber, N., Bianco, F. B., et al. 2013, PASP, 125, 1031
Burn, R., Schlecker, M., Mordasini, C., et al. 2021, Astronomy & Astrophysics, 656, A72
Caballero, J. A., Guàrdia, J., López del Fresno, M., et al. 2016, in Society of Photo-Optical Instrumentation Engineers (SPIE) Conference Series, Vol. 9910, Observatory Operations: Strategies, Processes, and Systems VI, ed. A. B. Peck, R. L. Seaman, & C. R. Benn, 99100E
Chaturvedi, P., Bluhm, P., Nagel, E., et al. 2022, A&A, 666, A155
Chen, G., Pallé, E., Parviainen, H., et al. 2021, MNRAS, 500, 5420
Cifuentes, C., Caballero, J. A., Cortés-Contreras, M., et al. 2020, A&A, 642, A115
Claret, A., Hauschildt, P. H., & Witte, S. 2012, A&A, 546, A14
Claret, A., Hauschildt, P. H., & Witte, S. 2013, A&A, 552, A16
Cochran, W. D. & Hatzes, A. P. 1996, Ap&SS, 241, 43
Collins, K. A., Kielkopf, J. F., Stassun, K. G., & Hessman, F. V. 2017, AJ, 153, 77
Colomé, J., Casteels, K., Ribas, I., & Francisco, X. 2010, in Society of Photo-Optical Instrumentation Engineers (SPIE) Conference Series, Vol. 7740, Software and Cyberinfrastructure for Astronomy, ed. N. M. Radziwill & A. Bridger, 77403K
Colome, J. & Ribas, I. 2006, IAU Special Session, 6, 11
Correia, A. C. M., Bourrier, V., & Delisle, J. B. 2020, A&A, 635, A37
Cracchiolo, G., Micela, G., Morello, G., & Peres, G. 2021, MNRAS, 507, 6118
Curtis, J. L., Agüeros, M. A., Matt, S. P., et al. 2020, ApJ, 904, 140
Dahn, C. C., Harrington, R. S., Kallarakal, V. V., et al. 1988, AJ, 95, 237
Dahn, C. C., Harris, H. C., Vrba, F. J., et al. 2002, AJ, 124, 1170
Delrez, L., Murray, C. A., Pozuelos, F. J., et al. 2022, A&A, 667, A59
Dévora-Pajares, M. & Pozuelos, F. J. 2023, MATRIX: Multi-phAse Transits Recovery from Injected eXoplanets toolkit, Astrophysics Source Code Library, record ascl:2309.007
Dorn, C. & Lichtenberg, T. 2021, The Astrophysical Journal Letters, 922, L4
Dressing, C. D. & Charbonneau, D. 2013, ApJ, 767, 95
Engle, S. G. & Guinan, E. F. 2023, ApJ, 954, L50
Espinoza, N., Kossakowski, D., & Brahm, R. 2019, MNRAS, 490, 2262
Espinoza, N., Pallé, E., Kemmer, J., et al. 2022, AJ, 163, 133
Fletcher, L. N., Gustafsson, M., & Orton, G. S. 2018, ApJS, 235, 24

Foreman-Mackey, D. 2016, The Journal of Open Source Software, 1, 24
Foreman-Mackey, D., Hogg, D. W., Lang, D., & Goodman, J. 2013, PASP, 125, 306
Fortney, J. J., Mordasini, C., Nettelmann, N., et al. 2013, ApJ, 775, 80
Frith, J., Pinfield, D. J., Jones, H. R. A., et al. 2013, MNRAS, 435, 2161
Fulton, B. J., Petigura, E. A., Howard, A. W., et al. 2017, AJ, 154, 109
Gaia Collaboration, Smart, R. L., Sarro, L. M., et al. 2021, A&A, 649, A6
Gaia Collaboration, Vallenari, A., Brown, A. G. A., et al. 2023, A&A, 674, A1
Gao, P. & Zhang, X. 2020, ApJ, 890, 93
Giclas, H. 1966, Vistas in Astronomy, 8, 23
Giclas, H. L., Burnham, R., & Thomas, N. G. 1971, Lowell proper motion survey Northern Hemisphere. The G numbered stars. 8991 stars fainter than magnitude 8 with motions > 0".26/year
González-Álvarez, E., Zapatero Osorio, M. R., Caballero, J. A., et al. 2023, A&A, 675, A177
Guillot, T., Stevenson, D. J., Hubbard, W. B., & Saumon, D. 2004, in Jupiter. The Planet, Satellites and Magnetosphere, ed. F. Bagenal, T. E. Dowling, & W. B. McKinnon, Vol. 1, 35–57
Hartman, J. D. & Bakos, G. Á. 2016, Astronomy and Computing, 17, 1
Hatzes, A. P. 2019, The Doppler Method for the Detection of Exoplanets
Hatzes, A. P., Dvorak, R., Wuchterl, G., et al. 2010, Astronomy and Astrophysics, 520, A93
Henning, W. G., O'Connell, R. J., & Sasselov, D. D. 2009, ApJ, 707, 1000
Howell, S. B., Sobeck, C., Haas, M., et al. 2014, PASP, 126, 398
Husser, T. O., Wende-von Berg, S., Dreizler, S., et al. 2013, A&A, 553, A6
Jeffers, S. V., Dreizler, S., Barnes, J. R., et al. 2020, Science, 368, 1477
Jeffers, S. V., Schöfer, P., Lamert, A., et al. 2018, A&A, 614, A76
Jenkins, J. M., Twicken, J. D., McCauliff, S., et al. 2016, in Proc. SPIE, Vol. 9913, Software and Cyberinfrastructure for Astronomy IV, 99133E
Kasting, J. F. 1988, Icarus, 74, 472
Kawauchi, K., Murgas, F., Palle, E., et al. 2022, A&A, 666, A4
Kempton, E. M. R., Bean, J. L., Louie, D. R., et al. 2018, PASP, 130, 114401
Kimura, T. & Ikoma, M. 2020, MNRAS, 496, 3755
Kipping, D. M. 2013, MNRAS, 435, 2152
Kochanek, C. S., Shappee, B. J., Stanek, K. Z., et al. 2017, PASP, 129, 104502
Kopparapu, R. K., Ramirez, R. M., SchottelKotte, J., et al. 2014, The Astrophysical Journal Letters, 787, L29
Kossakowski, D., Kürster, M., Trifonov, T., et al. 2023, A&A, 670, A84
Kovács, G., Zucker, S., & Mazeh, T. 2002, A&A, 391, 369
Lamman, C., Baranec, C., Berta-Thompson, Z. K., et al. 2020, AJ, 159, 139
Lanza, A. F. 2009, A&A, 505, 339
Leconte, J., Chabrier, G., Baraffe, I., & Levrard, B. 2010, A&A, 516, A64
Lee, J.-M., Heng, K., & Irwin, P. G. J. 2013, ApJ, 778, 97
Lépine, S. & Gaidos, E. 2011, AJ, 142, 138
Lépine, S. & Shara, M. M. 2005, AJ, 129, 1483
Lillo-Box, J., Gandolfi, D., Armstrong, D. J., et al. 2023, A&A, 669, A109
Lodieu, N., Pérez-Garrido, A., Smart, R. L., & Silvotti, R. 2019, A&A, 628, A66
Luger, R. & Barnes, R. 2015, Astrobiology, 15, 119
Luque, R., Fulton, B. J., Kunimoto, M., et al. 2022a, A&A, 664, A199
Luque, R., Nowak, G., Hirano, T., et al. 2022b, A&A, 666, A154
Luyten, W. J. 1979, LHS catalogue. A catalogue of stars with proper motions exceeding 0"5 annually
Mallorquín, M., Goffo, E., Pallé, E., et al. 2023, A&A, 680, A76
Mandel, K. & Agol, E. 2002, ApJL, 580, L171–L175
Marcq, E., Salvador, A., Massol, H., & Davaille, A. 2017, Journal of Geophysical Research (Planets), 122, 1539
Marfil, E., Tabernero, H. M., Montes, D., et al. 2021, A&A, 656, A162
Maxted, P. F. L., Anderson, D. R., Collier Cameron, A., et al. 2011, PASP, 123, 547
McCully, C., Volgenau, N. H., Harbeck, D.-R., et al. 2018, in Society of Photo-Optical Instrumentation Engineers (SPIE) Conference Series, Vol. 10707, Proc. SPIE, 107070K
McKay, A. J., DiSanti, M. A., Kelley, M. S. P., et al. 2019, AJ, 158, 128
Melrose, D. B. & Dulk, G. A. 1982, ApJ, 259, 844
Miguel, Y., Cridland, A., Ormel, C. W., Fortney, J. J., & Ida, S. 2020, MNRAS, 491, 1998
Mishchenko, M. I., Travis, L. D., & Mackowski, D. W. 1996, J. Quant. Spectr. Rad. Transf., 55, 535
Mordasini, C. 2018, in Handbook of Exoplanets (Cham: Springer International Publishing), 2425–2474
Morello, G., Parviainen, H., Murgas, F., et al. 2023, A&A, 673, A32
Morello, G., Tsiaras, A., Howarth, I. D., & Homeier, D. 2017, AJ, 154, 111
Morello, G., Zingales, T., Martin-Lagarde, M., Gastaud, R., & Lagage, P.-O. 2021, AJ, 161, 174
Murdoch, K. A., Hearnshaw, J. B., & Clark, M. 1993, The Astrophysical Journal, 413, 349
Murgas, F., Astudillo-Defru, N., Bonfils, X., et al. 2021, A&A, 653, A60
Murgas, F., Castro-González, A., Pallé, E., et al. 2023, A&A, 677, A182
Nagel, E., Czesla, S., Kaminski, A., et al. 2023, A&A, 680, A73
Nakajima, S., Hayashi, Y.-Y., & Abe, Y. 1992, Journal of the Atmospheric Sciences, 49, 2256
Narita, N., Fukui, A., Kusakabe, N., et al. 2019, Journal of Astronomical Telescopes, Instruments, and Systems, 5, 015001
Ogilvie, G. I. 2014, ARA&A, 52, 171
Ohno, K. & Tanaka, Y. A. 2021, ApJ, 920, 124
Orell-Miquel, J., Nowak, G., Murgas, F., et al. 2023, A&A, 669, A40
Osborne, H. L. M., Van Eylen, V., Goffo, E., et al. 2024, MNRAS, 527, 11138
Owen, J. E. & Wu, Y. 2017, ApJ, 847, 29
Palle, E., Orell-Miquel, J., Brady, M., et al. 2023, A&A, 678, A80
Parviainen, H. 2015, Monthly Notices of the Royal Astronomical Society, 450, 3233
Parviainen, H. & Aigrain, S. 2015, MNRAS, 453, 3821
Parviainen, H., Tingley, B., Deeg, H. J., et al. 2019, A&A, 630, A89
Pecaut, M. J. & Mamajek, E. E. 2013, ApJS, 208, 9
Pérez-Torres, M., Gómez, J. F., Ortiz, J. L., et al. 2021, A&A, 645, A77
Pluriel, W., Marcq, E., & Turbet, M. 2019, Icarus, 317, 583
Pollacco, D. L., Skillen, I., Collier Cameron, A., et al. 2006, PASP, 118, 1407
Powell, D., Feinstein, A. D., Lee, E. K. H., et al. 2024, Nature
Pozuelos, F. J., Suárez, J. C., de Elía, G. C., et al. 2020, A&A, 641, A23
Pozuelos, F. J., Timmermans, M., Rackham, B. V., et al. 2023, A&A, 672, A70
Quirrenbach, A., Amado, P. J., Caballero, J. A., et al. 2014, in Proc. SPIE, Vol. 9147, Ground-based and Airborne Instrumentation for Astronomy V, 91471F
Quirrenbach, A., Amado, P. J., Ribas, I., et al. 2018, in Society of Photo-Optical Instrumentation Engineers (SPIE) Conference Series, Vol. 10702, Ground-based and Airborne Instrumentation for Astronomy VII, 107020W
Ray, L. C. & Hess, S. 2008, Journal of Geophysical Research (Space Physics), 113, A11218
Reid, I. N. & Cruz, K. L. 2002, AJ, 123, 2806
Reid, I. N., Cruz, K. L., Allen, P., et al. 2003, AJ, 126, 3007
Reiners, A., Shulyak, D., Käpylä, P. J., et al. 2022, A&A, 662, A41
Ribas, I., Reiners, A., Zechmeister, M., et al. 2023, A&A, 670, A139
Ricker, G. R., Winn, J. N., Vanderspek, R., et al. 2015, Journal of Astronomical Telescopes, Instruments, and Systems, 1, 014003
Sabotta, S., Schlecker, M., Chaturvedi, P., et al. 2021, A&A, 653, A114
Saur, J., Grambusch, T., Duling, S., Neubauer, F. M., & Simon, S. 2013, A&A, 552, A119
Schanche, N., Pozuelos, F. J., Günther, M. N., et al. 2022, A&A, 657, A45
Schlecker, M., Apai, D., Lichtenberg, T., et al. 2023, Bioverse: The Habitable Zone Inner Edge Discontinuity as an Imprint of Runaway Greenhouse Climates on Exoplanet Demographics
Schlecker, M., Mordasini, C., Emsenhuber, A., et al. 2021a, Astronomy & Astrophysics, 656, A71
Schlecker, M., Pham, D., Burn, R., et al. 2021b, Astronomy & Astrophysics, 656, A73
Schneider, A. C., Greco, J., Cushing, M. C., et al. 2016, ApJ, 817, 112
Schöfer, P., Jeffers, S. V., Reiners, A., et al. 2019, A&A, 623, A44
Schweitzer, A., Passegger, V. M., Cifuentes, C., et al. 2019, A&A, 625, A68
Shappee, B. J., Prieto, J. L., Grupe, D., et al. 2014, ApJ, 788, 48
Skrutskie, M. F., Cutri, R. M., Stiening, R., et al. 2006, AJ, 131, 1163
Smith, J. C., Stumpe, M. C., Van Cleve, J. E., et al. 2012, PASP, 124, 1000
Southworth, J. 2011, MNRAS, 417, 2166
Stassun, K. G., Oelkers, R. J., Paegert, M., et al. 2019, AJ, 158, 138
Stumpe, M. C., Smith, J. C., Catanzarite, J. H., et al. 2014, PASP, 126, 100
Stumpe, M. C., Smith, J. C., Van Cleve, J. E., et al. 2012, PASP, 124, 985
Tabernero, H. M., Marfil, E., Montes, D., & González Hernández, J. I. 2022, A&A, 657, A66
Thompson, A., Biagini, A., Cracchiolo, G., et al. 2023, arXiv e-prints, arXiv:2302.04574
Thorngren, D. P., Fortney, J. J., Murray-Clay, R. A., & Lopez, E. D. 2016, ApJ, 831, 64
Tittemore, W. C. & Wisdom, J. 1990, Icarus, 85, 394
Turbet, M., Bolmont, E., Ehrenreich, D., et al. 2020, Astronomy & Astrophysics, Volume 638, id.A41, 638, A41
Turbet, M., Ehrenreich, D., Lovis, C., Bolmont, E., & Fauchez, T. 2019, Astronomy & Astrophysics, 628, A12
Turnpenney, S., Nichols, J. D., Wynn, G. A., & Burleigh, M. R. 2018, ApJ, 854, 72
van Altena, W. F., Lee, J. T., & Hoffleit, E. D. 1995, The general catalogue of trigonometric [stellar] parallaxes
Venturini, J., Guilera, O. M., Haldemann, J., Ronco, M. P., & Mordasini, C. 2020, Astronomy & Astrophysics, 643, L1
Wells, R. D., Rackham, B. V., Schanche, N., et al. 2021, A&A, 653, A97
Wright, N. J., Newton, E. R., Williams, P. K. G., Drake, J. J., & Yadav, R. K. 2018, Monthly Notices of the Royal Astronomical Society, 479, 2351
Yu, X., He, C., Zhang, X., et al. 2021, Nature Astronomy, 5, 822
Zarka, P. 2007, Planet. Space Sci., 55, 598
Zechmeister, M., Anglada-Escudé, G., & Reiners, A. 2014, A&A, 561, A59
Zechmeister, M. & Kürster, M. 2009, Astronomy & Astrophysics, 496, 577–584
Zechmeister, M., Reiners, A., Amado, P. J., et al. 2018, A&A, 609, A12

Zeng, L., Jacobsen, S. B., Sasselov, D. D., et al. 2019, Proceedings of the National Academy of Science, 116, 9723
Zeng, L., Sasselov, D. D., & Jacobsen, S. B. 2016, ApJ, 819, 127

---

[1] Dipartimento di Fisica, Università degli Studi di Torino, via Pietro Giuria 1, I-10125, Torino, Italy
[2] Thüringer Landessternwarte Tautenburg, 07778 Tautenburg, Germany
[3] Instituto de Astrofísica de Canarias (IAC), Calle Vía Láctea s/n, 38205 La Laguna, Tenerife, Spain
[4] Departamento de Astrofísica, Universidad de La Laguna (ULL), 38206 La Laguna, Tenerife, Spain
[5] Department of Space, Earth and Environment, Chalmers University of Technology, SE-412 96 Gothenburg, Sweden
[6] Max-Planck-Institut für Astronomie, Königstuhl 17, 69117 Heidelberg, Germany
[7] Instituto de Astrofísica de Andalucía (IAA-CSIC), Glorieta de la Astronomía s/n, 18008 Granada, Spain
[8] INAF – Osservatorio Astrofisico di Catania, Via S. Sofia 78, 95123 Catania, Italy
[9] Centro de Astrobiología, (CSIC-INTA), ESAC Campus, Camino bajo del castillo s/n, 28692 Villanueva de la Cañada, Madrid, Spain
[10] Steward Observatory and Department of Astronomy, The University of Arizona, Tucson, AZ 85721, USA
[11] Hamburger Sternwarte, Gojenbergsweg 112, 21029 Hamburg, Germany
[12] Astrophysics Group, Keele University, Staffordshire ST5 5BG, United Kingdom
[13] Max Planck Institut für Sonnensystemforschung, Justus-von-Liebig-Weg 3, 37077 Göttingen, Germany
[14] Departamento de Física de la Tierra y Astrofísica and IPARCOS-UCM (Instituto de Física de Partículas y del Cosmos de la UCM), Facultad de Ciencias Físicas, Universidad Complutense de Madrid, 28040 Madrid, Spain
[15] Department of Physics, Ariel University, Ariel 40700, Israel
[16] Vereniging Voor Sterrenkunde, Oude Bleken 12, 2400 Mol, Belgium
[17] AstroLAB IRIS, Provinciaal Domein "De Palingbeek", Verbrandemolenstraat 5, 8902 Zillebeke, Ieper, Belgium
[18] Komaba Institute for Science, The University of Tokyo, 3-8-1 Komaba, Meguro, Tokyo 153-8902, Japan
[19] Department of Multi-Disciplinary Sciences, Graduate School of Arts and Sciences, The University of Tokyo, 3-8-1 Komaba, Meguro, Tokyo, 153-8902, Japan
[20] Institut d'Estudis Espacials de Catalunya (IEEC), Calle Gran Capita 2-4, 08034, Barcelona, Spain
[21] Astrobiology Center, 2-21-1 Osawa, Mitaka, Tokyo 181-8588, Japan
[22] Centre for Mathematical Plasma-Astrophysics, Department of Mathematics, KU Leuven, Celestijnenlaan 200B, 3001 Heverlee, Belgium
[23] Centro Astronómico Hispano en Andalucía (CAHA), Observatorio de Calar Alto, Sierra de los Filabres, 04550 Gérgal, Spain
[24] Institut für Astrophysik und Geophysik, Georg-August-Universität Göttingen, Friedrich-Hund-Platz 1, 37077 Göttingen, Germany
[25] Department of Astronomy & Astrophysics, University of Chicago, Chicago, IL 60637, USA
[26] Landessternwarte, Zentrum für Astronomie der Universität Heidelberg, Königstuhl 12, 69117 Heidelberg, Germany
[27] Institut de Ciéncies de l'Espai (CSIC-IEEC), Campus UAB, de Can Magrans s/n, 08193 Bellaterra, Barcelona, Spain
[28] Centro de Astrobiología (CSIC-INTA), Carretera de Ajalvir km 4, 28850 Torrejón de Ardoz, Madrid, Spain
[29] Center for Astroparticles and High Energy Physics (CAPA), Universidad de Zaragoza, E-50009 Zaragoza, Spain
[30] School of Sciences, European University Cyprus, Diogenes street, Engomi, 1516 Nicosia, Cyprus

Appendix A: Radial velocity data

Table A.1: RV data from CARMENES VIS.

Time [$\mathrm{BJD_{TDB}}$]	RV [$\mathrm{m\,s^{-1}}$]	σ [$\mathrm{m\,s^{-1}}$]
2459720.6490	1.90	3.99
2459726.5607	–6.93	2.02
2459730.5751	–1.11	2.20
2459736.5664	2.74	1.81
2459738.6403	–3.77	1.97
2459740.6490	–4.64	2.32
2459748.5283	–0.98	3.35
2459768.4734	–1.05	2.57
2459770.4685	–0.97	1.94
2459772.4574	–4.01	2.31
2459776.4443	0.86	2.09
2459778.4424	–3.92	2.31
2459780.6099	1.97	2.25
2459784.6203	0.36	3.21
2459786.5898	–2.26	3.63
2459788.6297	4.97	1.98
2459796.5221	4.49	2.64
2459812.4809	–2.08	2.23
2459812.5016	2.40	1.98
2459813.4895	3.57	3.72
2459813.5105	–2.29	3.12
2459814.4412	–6.17	2.09
2459826.4745	3.32	2.61
2459831.3528	–3.44	2.42
2460007.6296	–0.85	2.37
2460015.6770	–4.80	1.72
2460033.6556	3.51	3.38
2460037.5939	4.58	3.48
2460041.6186	2.86	1.92
2460057.6177	6.53	2.07
2460060.6283	1.38	1.98
2460066.6401	2.64	2.30

Appendix B: Photometric fit with unocculted star spots

We fitted the color dependent transit depths that appear when considering the measurements from TESS and all MuSCAT2 filters, including g' and r', following the method described in Sect. 4.1. For simplicity, we fixed the stellar parameters of the quiet photosphere to those of TOI-4438, as reported in Table 1. The free parameters in our fit were the geometric radius ratio $R_b/R_\star$, the star spot photospheric parameters $T_{\rm spot}$ and $\log g_{\rm spot}$, and filling factor $f_{\rm spot}$. We run `emcee` (Foreman-Mackey et al. 2013) with 16 walkers and 30 000 iterations to sample the posterior distribution, then applying a conservative burn-in of 10 000 iterations, which is more than 20 times the maximum autocorrelation length. For each parameters set from the chains, we also computed the apparent transit depth in each passband using the formulae from Ballerini et al. (2012).

Fig. B.1 compares the measured transit depths in each passband with those derived from the fit with unocculted star spots and the posterior distribution for the model parameters. While the unocculted star spots may explain the larger transit depths in g' and r', they would also cause a difference between the i' and z_s that is not seen in the data. As a compromise, the model tends to underestimate the g' and r' transit depths to keep a small difference between i' and z_s. The modelled transit depths are consistent within 1σ with the measured ones, owing to the large error bars in g' and r'. The spot temperature contrast is -490^{+380}_{-640} K and the filling factor is $0.44^{+0.24}_{-0.17}$. In this scenario, the planet-to-star radius ratio is $R_b/R_\star = 0.055^{+0.004}_{-0.011}$, that is significantly smaller and with order-of-magnitude larger error bars than those obtained discarding the g' and r' bands and neglecting star spots.

If we accepted this solution, the planetary radius would be $R_b = 2.24^{+0.28}_{-0.55}\,R_\oplus$. This slightly smaller radius would not significantly change the predicted composition, which is volatile-rich. With a smaller TSM of 96, TOI-4438 b would remain a top target for atmospheric characterization with *JWST*.

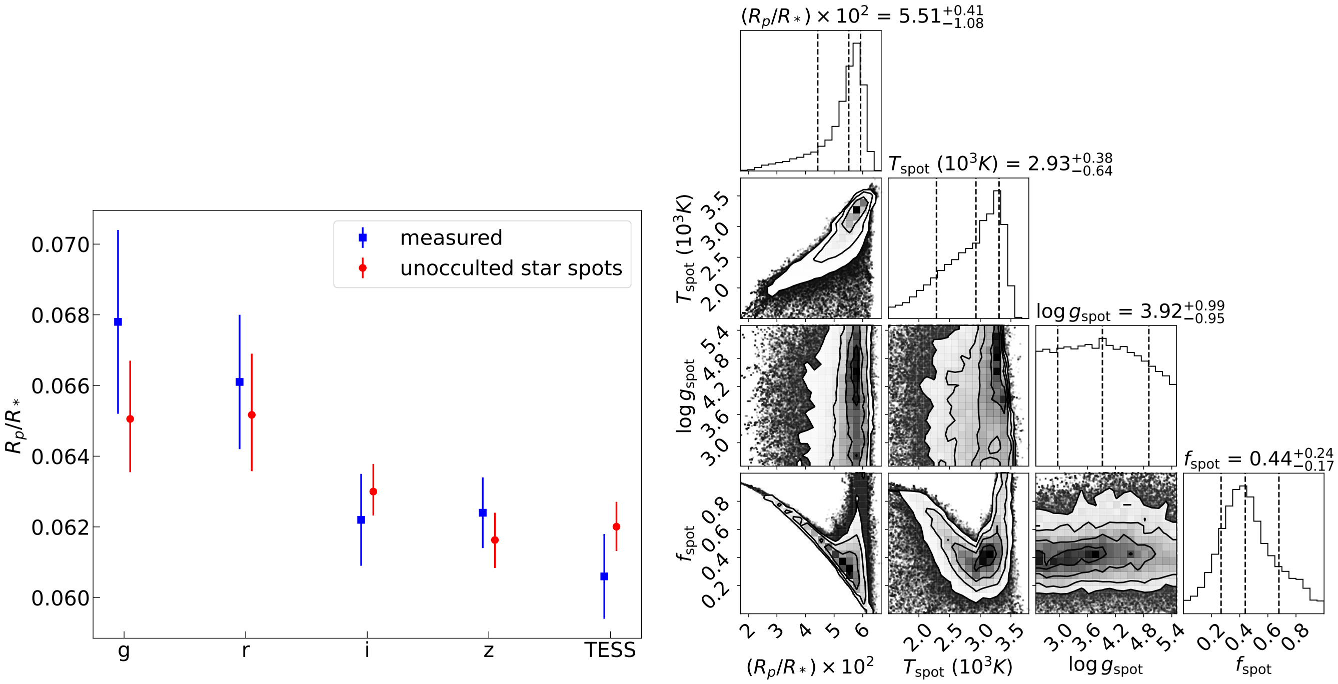

Fig. B.1: Results of the photometric fit with unocculted star spots. *Left*: Individual transit depths derived from photometric observations (blue squares) and best-fit model assuming that the color-dependence is due to unocculted star spots. *Right*: corner plot with the posterior distribution of the model parameters, generated with the `corner` package (Foreman-Mackey 2016).

Chapter 8

Other Contributions

In this chapter I present the papers in which I have substantially contributed with the analysis of photometric and spectroscopic data, as well as with the paper writing:

1. “TOI-1801b: a temperate super-earth around a young M5 dwarf”, Mallorquin, Goffo, et al., 2023, A&A, 680, A76; Section 8.1.
2. “A Different-Twin Pair of Sub-Neptunes orbiting TOI-1064 Discovered by TESS, Characterised by CHEOPS and HARPS”, Wilson, Goffo et al., 2021, MNRAS, 511, 1043; Section 8.2.
3. “TOI-544 b: a potential water-world inside the radius valley in a two-planet system”, Osborne, Van Eylen, Goffo et al., 2023, MNRAS, 527, 11138; Section 8.3.
4. “A new mass and radius determination of the ultra-short period planet K2-106b and the fluffy planet K2-106c”, Günther, Goffo et al., 2024, MNRAS, 529, 141. Section 8.4.

8.1 TOI-1801

In the paper by Mallorquín et al. (2023), we reported the discovery and characterization of TOI-1801 b, a temperate mini-Neptune, with an equilibrium temperature of ∼490 K, orbiting a young M0.5 V star every ∼10.6 days. TESS observed the star TOI-1801 in two sectors and reported the presence of a transiting planet candidate on a 21.3-day orbit. Through ground-based photometric follow-up observations, and CARMENES and HIRES high-precision RV measurements, we found that the true orbital period is about 10.6 days, i.e., half the value reported by the TESS team.

TOI-1801 b has a mass of $5.74 \pm 1.46\, M_{\oplus}$ and a radius of $2.08 \pm 0.12\, R_{\oplus}$. The planet is likely composed of water and rocks, with an upper limit of 2 % by mass of H_2 in its atmosphere. We measured a stellar rotation period of 16 days using the RV time series and ground-based photometry. The stellar age was found to be 600–800 Myr. If the planet had a larger atmosphere in the past, it must have been removed by some evolutionary mechanism, such as photo-evaporation (Owen & Wu 2017), in less than 1 Gyr.

I performed a frequency analysis of the ground-based photometric data from several telescopes, which allowed me to measure the rotational period of the star. I also did the frequency analysis of the RV measurements and activity indicators, and performed the joint analysis with `pyaneti` as a sanity check of the results presented in the article. I wrote the relevant sections and revised the manuscript.

8.2 TOI-1064

Wilson et al. (2022) reported on the discovery and characterization of a two-planet system transiting the bright K dwarf star TOI-1064. TESS, CHEOPS, ground-based photometry, HARPS high-resolution spectroscopy, and Gemini speckle images were used. The paper presents a novel method to detrend photometric data based on modeling the shape variation of the point-spread function (PSF), and successfully applied it to correct CHEOPS photometry for instrumental systematics.

The planets were found to be two warm sub-Neptunes with orbital periods of 6.443868 ± 0.000025 days and 12.226574 ± 0.000045 days, and equilibrium temperatures of ~780 K and ~630 K, respectively. We found that the inner planet TOI-1064 b has a radius of $R_\mathrm{b} = 2.59 \pm 0.04\,R_\oplus$ and a mass of $M_\mathrm{b} = 13.5^{+1.7}_{-1.8}\,M_\oplus$, while the outer one, TOI-1064 c, has a radius of $R_\mathrm{c} = 2.65 \pm 0.04\,R_\oplus$, and a 3σ upper limit mass of $8.5\,M_\oplus$.

Given the high precision of the radius, we performed an internal structure and atmospheric escape modelling. TOI-1064 b is one of the densest, well-characterized sub-Neptunes, with a tenuous atmosphere and a large volatile component by mass fraction. Atmospheric escape evolution modeling showed that TOI-1064 b likely lost its primordial atmosphere after migration through the protoplanetary disk. Given its low density, TOI-1064 c likely hosts an extended gaseous envelope. However, more RV data are needed to improve the mass and density estimates and confirm this scenario.

My contribution to the paper was to perform the frequency analysis of HARPS measurements in order to search for the Doppler reflection motion induced by the two transiting planets and look for additional signals associated with stellar activity and/or other companions orbiting the system. I wrote the relevant section of the paper. In addition, I performed a joint analysis of the transit and Doppler data to independently confirm the radii and masses of the planets.

8.3 TOI-544

In the paper by Osborne et al. (2024), we reported the precise radial velocity follow-up of the bright K star TOI-544 (V = 10.8). The star hosts a small transiting planet with an orbital period of 1.548352 ± 0.000002 days, recently discovered by TESS. We collected 122 HARPS and HARPS-N RV measurements to spectroscopically confirm the planetary nature of the transit signal detected by TESS and measure the mass of the planet. Our observations covered nearly 3 years and allowed us to unveil the presence of an additional, non-transiting planetary companion. For the inner transiting planet TOI-544 b we derived a radius of $R_\mathrm{b} = 2.018 \pm 0.076\,R_\oplus$ and a mass of $M_\mathrm{b} = 2.89 \pm 0.48\,M_\oplus$, which translate into a bulk density of $1.93^{+0.30}_{-0.25}$ g cm^{-3}. The outer planet TOI-

544 c has a minimum mass of $M_\mathrm{c} \sin i_c = 21.5 \pm 2.0\, M_\oplus$ and an orbital period of 50.1 ± 0.2 days.

The low density of TOI-544 b implies that it either has an Earth-like rocky core with a hydrogen atmosphere, or a composition that harbors a significant fraction of water. The interpretation of the composition is degenerate depending on the specific choice of planet interior models used. In addition, the location and equilibrium temperature of $T_\mathrm{eq} = 999 \pm 14\,\mathrm{K}$ of TOI-544 b places it in the predicted location of the radius valley, where few planets are expected. The radius valley describes the region in the radius distribution of exoplanets where a paucity of planets with radii between $1.5\, R_\oplus$ and $2.0\, R_\oplus$ has been found.

The valley, or "gap", was first identified by Fulton et al. (2017) and Van Eylen et al. (2018). Many theories have been proposed to explain this gap in planetary radii, including photo-evaporation (Owen & Wu 2017; Fulton et al. 2017; Van Eylen et al. 2018) and core-powered mass loss (Collier Cameron & Jardine 2018; Gupta & Schlichting 2019; Gupta & Schlichting 2021). Both scenarios involve the formation of planets generally with rocky cores and atmospheric layers composed of hydrogen and helium (H-He) of about 1% by mass. These planets, called mini-Neptunes, lie above the radius valley in the radius-period space, and the subsequent atmospheric loss reduces their radii and causes the planets to lie below the valley.

In the photo-evaporation scenario, the intense X-ray flux from the close-in host star could carry away the volatile layers, leaving behind a bare rocky core, the so-called super-Earth planet, with a radius below the radius valley (Owen & Wu 2017). The scenario of core-powered mass loss assumes that stored heat from the formation stage of the planet escapes from the core and heats the atmospheric layer from the inside, leading to the escape of gas (Gupta & Schlichting 2019). No significant observational evidence has yet been found to favour one model over the other. TOI-544 b is a top target for future atmospheric observations, e.g., with JWST, which would provide better constraints on the planet's composition.

I performed the RV analysis using a multidimensional GP approach to remove the impact of stellar activity and recover the planetary parameters. I modeled the S-index with the RVs simultaneously since both datasets showed a significant stellar rotation signal. I contributed to the writing of the relevant sections and to the revision of the manuscript.

8.4 K2-106

Masses and radii of USP planets can be determined to a higher precision than long-period planets. Indeed they are preferred targets to determine the density of planets and constrain their composition thanks to their ultra-short orbital period. As of January 2024, 35 USP planets with no extended atmosphere have been discovered in the mass range between $1\, M_\oplus$ and $25\, M_\oplus$, referred to as bare rocks. The formation mechanisms of these low-mass USP planets are still debated. In one scenario they could be the remnant cores of gas-giants that lost their atmospheres due to photo-evaporation, or Roche-lobe overflow (Mocquet et al. 2014; Armstrong et al. 2020). In a second scenario the USP planets could form in the innermost part of the protoplanetary disk through mass accretion (Petrovich et al. 2019). Finally, they could be the result of mantle stripping by giant impacts (Reinhardt et al. 2022).

The K2-106 system hosts two planets of nearly identical masses. The inner planet K2-106 b on a 0.57-day orbit, discovered by Adams et al. (2017), is one of the most massive rocky USPs known. Inconsistent mass and density estimates have been published in the last years (Sinukoff et al. 2017; Guenther et al. 2017; Dai et al. 2019; Singh et al. 2022; Rodríguez Martínez et al. 2022, 2023). K2-106 b has a very high maximum geometric albedo of 0.9 ± 0.3, consistent with a lava ocean (Rouan et al. 2011), and a maximum dayside temperature of 3620^{+56}_{-53} K (Singh et al. 2022). The outer planet K2-106 c on a 13.34-day orbit has a mass similar to that of K2-106 b, but a lower density.

In the paper by Guenther et al. (2024), we derived an improved stellar radius from Gaia DR3 parallax. With new ESPRESSO RV data we determined the masses of the two planets more precisely than previously done. We found a radius of $R_\mathrm{b} = 1.676^{+0.037}_{-0.037}\,R_\oplus$, and a mass of $M_\mathrm{b} = 7.80 \pm 0.71\,M_\oplus$, implying a density of $\rho_\mathrm{b} = 9.09 \pm 0.98\,\mathrm{g\,cm^{-3}}$ for K2-106 b. For K2-106 c, we derived $R_\mathrm{c} = 2.84^{+0.10}_{-0.08}\,R_\oplus$, $M_\mathrm{c} = 7.3^{+2.5}_{-2.4}\,M_\oplus$, and a density of $\rho_\mathrm{c} = 1.72^{+0.66}_{-0.58}\,\mathrm{g\,cm^{-3}}$.

I performed the joint analysis of the transit light curves and RV measurements to determine the planetary parameters of the two planets K2-106 b and K2-106 c. I wrote the relevant sections and revised the manuscript.

Chapter 9

Conclusions

We carried out an intensive RV follow-up of systems hosting transiting exoplanet candidates detected by the TESS space mission. Our observations allowed us to confirm and characterize new exoplanets, as well as to refine the parameter estimates of known systems. Most of the Doppler observations presented in this work were carried out by myself as part of my PhD project. Specifically, I observed for a total of 28 nights with the HARPS spectrograph mounted at the ESO-3.6m telescope at La Silla observatory, Chile. I performed a robust data analysis of the TESS systems GJ 367, TOI-4438, TOI-1801, TOI-1064, TOI-544, and the K2 system K2-106. Their main parameters are listed in Table 9.1. In Figure 9.1 I display the mass-radius and the density-radius diagrams of small exoplanets whose masses and radii are known with a precision better than 20 %. The planets characterized in the course of this thesis work, whose masses and radii and known with a precision better than 20 %, are included and shown with different colors[1].

Precise determinations of planetary masses and radii give us the opportunity to study the internal structure and composition of planets. Our intensive RV follow-up observations with world-class high-resolution spectrographs, along

---

[1] TOI-1064 c and K2-106 c have not been included in the plots due to the low precision in their mass determinations.

Table 9.1: Main parameters of the planets whose masses, radii, and bulk densities have been derived as part of this work. Values marked with a $*$ are minimum masses.

Name	**Period** (days)	**Mass** ($M_\oplus$)	**Radius** ($R_\oplus$)	**Density** ($\mathrm{g\,cm^{-3}}$)
GJ 367 b	0.3219225 ± 0.0000002	0.633 ± 0.050	0.699 ± 0.024	10.2 ± 1.3
GJ 367 c	11.543 ± 0.005	$4.13 \pm 0.36^*$	–	–
GJ 367 d	34.39 ± 0.06	$6.03 \pm 0.49^*$	–	–
TOI-4438 b	7.44628 ± 0.000009	5.4 ± 1.1	2.52 ± 0.13	$1.85^{+0.51}_{-0.44}$
TOI-1801 b	10.64387 ± 0.00006	5.74 ± 1.46	2.08 ± 0.12	3.70 ± 1.22
TOI-1064 b	6.443868 ± 0.000025	13.5 ± 1.8	2.587 ± 0.043	4.31 ± 0.55
TOI-1064 c	12.226574 ± 0.000045	$2.5^{+1.8}_{-2.0}$	2.651 ± 0.043	0.77 ± 0.55
TOI-544 b	1.548352 ± 0.000002	2.89 ± 0.48	2.018 ± 0.076	$1.93^{+0.30}_{-0.25}$
TOI-544 c	50.089 ± 0.24	$21.5 \pm 2.0^*$	–	–
K2-106 b	0.5713127 ± 0.0000055	7.8 ± 0.71	1.676 ± 0.037	9.09 ± 0.98
K2-106 c	13.33989 ± 0.00069	7.3 ± 2.4	2.84 ± 0.09	$1.72^{+0.66}_{-0.58}$

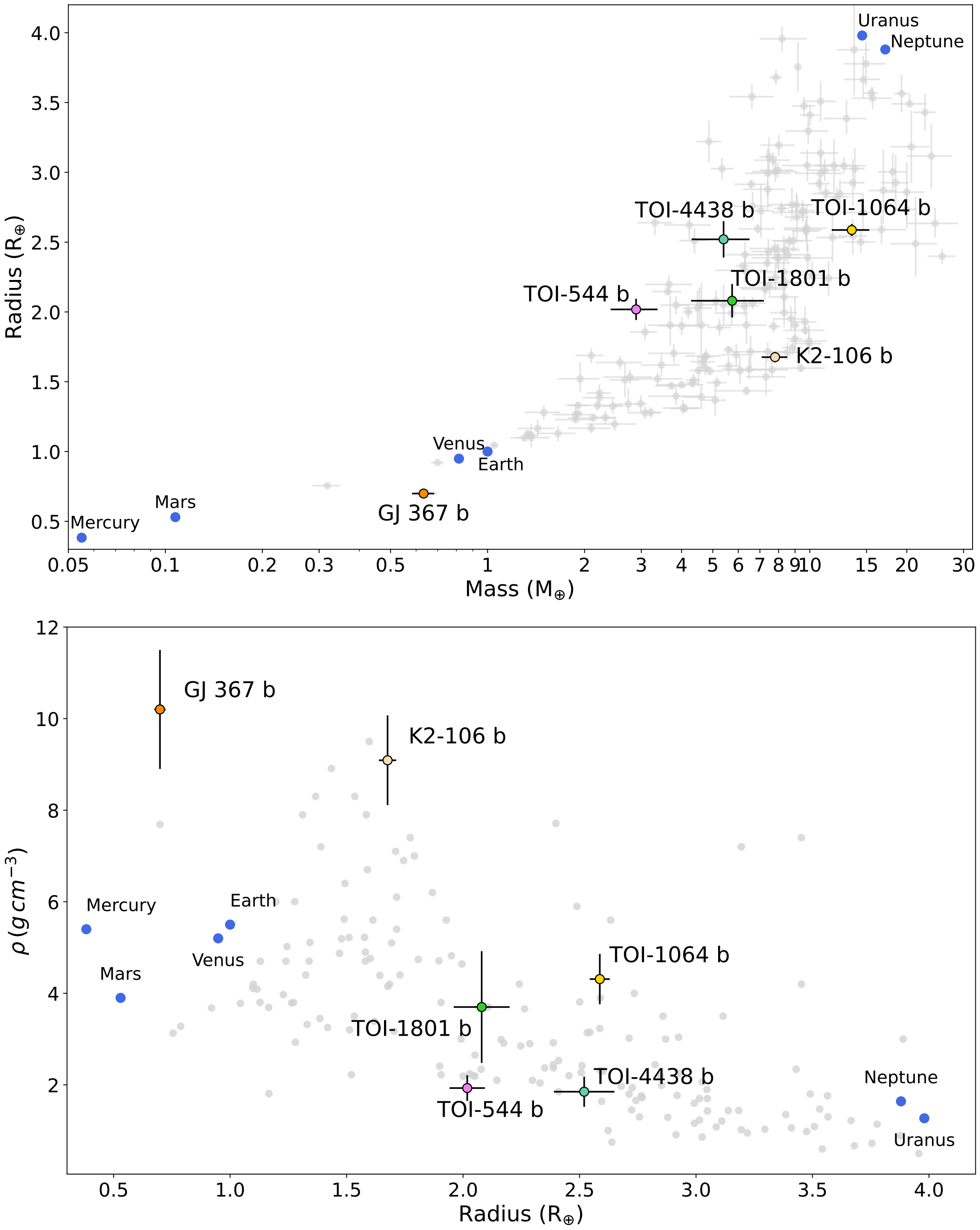

Figure 9.1: *Upper panel:* Mass-radius diagram of small exoplanets whose masses and radii are known with a precision better than 20 %. As of 14 February 2024, out of the 5573 planets confirmed to date, there are only 184 small planets with $M_\mathrm{p} < 30\,M_\oplus$ and $R_\mathrm{p} < 4\,M_\oplus$ whose masses and radii are known with a precision better than 20 %. The transiting planets characterized in the course of this work are shown with different colors (see also Chapters 6, 7, and 8, and Table 9.1). This plot has been created using planetary parameters retrieved from the Transiting Extrasolar Planet Catalogue (TEPCat; Southworth 2011). *Lower panel:* Density-radius diagram for the same sample of small exoplanets.

with our robust analyses, have allowed us to obtain high-precision planetary parameters. The transiting planets studied in the course of this thesis work are displayed in two mass-radius diagrams in Figure 9.2. The upper panel shows planets with masses $0.5\,M_\oplus < M_\mathrm{p} < 20\,M_\oplus$ and radii $0.5\,R_\oplus < R_\mathrm{p} < 3\,R_\oplus$, whereas the lower panel displays planets with masses $2\,M_\oplus < M_\mathrm{p} < 30\,M_\oplus$ and radii $1.5\,R_\oplus < R_\mathrm{p} < 4\,R_\oplus$. Composition models from Zeng et al. (2016, 2019) are plotted using different lines and colors.

I measured the mass and radius of GJ 367 b with a precision of 7.9 % and 3.4 %, respectively. The internal structure analysis suggests an iron core mass fraction of $0.91^{+0.07}_{-0.23}$, which makes GJ 367 b the densest ultra-short period small planet known to date (Figure 9.1, lower panel). The mass and radius of K2-106 b were estimated with a precision of ∼9 % and 2.2 %, respectively. Its position in the mass-radius diagram suggests that the planet has an Earth-like composition. However, K2-106 b is a USP planet and is expected to be different from Earth due to its proximity to the star. Many USPs could be bare rock, or could have, e.g., lava oceans or out–gassed or hybrid atmospheres of heavier non-volatile elements. In the case of TOI-4438 b, I measured its mass and radius with a precision of 20 % and 5 %, respectively. The analysis of its composition reveals a volatile-rich mini-Neptune likely featuring a H/He envelope mixed with HO_2, CO_2, and CH_4. The estimated mass (13 % precision) and radius (1.5 % precision) of TOI-1064 b suggests a mini-Neptune with a tenuous atmosphere and a large volatile component in terms of mass fraction. The mass (17 % precision) and radius (3.8 % precision) of TOI-544 b yield a low density of $1.93^{+0.30}_{-0.25}\,\mathrm{g\,cm^{-3}}$, suggesting that the planet has either a significant fraction of ice (∼30 % of its mass), or it is an Earth-like rocky core surrounded by an atmospheric H/He layer (∼0.5–1 % of its mass). These planets are either bare rocky cores (GJ 367 b and K2-106 b), or mini-Neptunes (TOI-544 b, TOI-1064 b and c, TOI-4438 b, TOI-1801 b, and K2-106 c) with different masses and radii, and, consequently, a wide variety of atmospheres.

The atmospheric composition and interior structure of small planets with radii $2\,R_\oplus \lesssim R_\mathrm{p} \lesssim 4\,R_\oplus$, the so-called mini-Neptunes, are not well understood yet. As shown in the lower panel of Figure 9.2, they could be explained by different composition models. Their bulk density could be compatible with either a high mass fraction of water, or an extended atmosphere. In this regard, follow-up atmospheric observations are needed to break the degeneracies between the models. Current and forthcoming telescopes, such as JWST or ARIEL, will allow us to explore the composition of the upper gaseous layer of exoplanets. Selecting the best targets for future atmospheric characterization is therefore crucial. TOI-4438 b and TOI-544 b have transmission spectroscopy metric (TSM) values of about 136 and 163, respectively, well above the recommended threshold value of 92 defined for the respective planetary categories (Kempton et al. 2018). They are among the most appealing targets for transmission spectroscopy characterization with JWST.

Our long-term RV monitoring with HARPS has also revealed new orbiting planets around the host stars, providing insights into their architecture, and, therefore, the formation mechanisms of the systems (see Chapter 6, and Sections 8.2, 8.3). For instance, the discovery of two outer low-mass companions around GJ 367 gives us clues on the possible formation and evolution scenarios that brought the ultra-dense iron "ball" GJ 367 b to its current location (see, e.g., high-eccentricity migration scenario, Chapter 6). GJ 367 joins the small group of well-characterized multi-planetary systems hosting a USP planet, be-

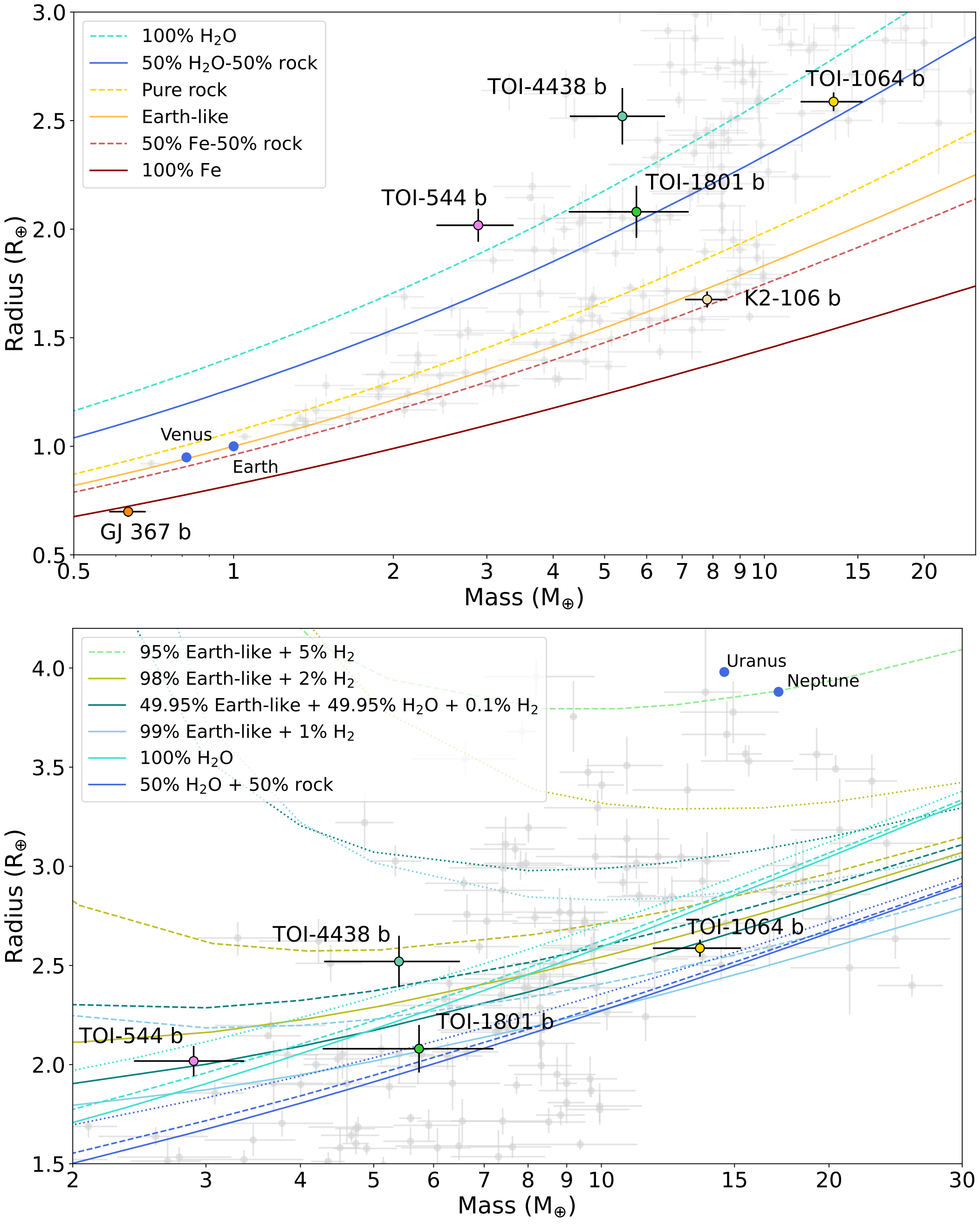

Figure 9.2: Same as Figure 9.1. *Upper panel:* solid and dashed curves are theoretical composition models from Zeng et al. (2016). *Lower panel:* solid and dashed curves are theoretical composition models from Zeng et al. (2019). For each color the set of solid, dashed, and dotted curves are calculated for an isothermal envelope at 300 K, 500 K, and 1000 K, respectively.

ing an extraordinary target for future investigations on the formation and migration scenarios of USP systems.

9.1 Future outlook

Over the last few decades, exoplanet research has gone from being mere speculation to becoming a rapidly developing established field. Nowadays, at least one new planet or planetary system is reported every week. However, our knowledge of exoplanets still needs more detailed and precise measurements. In the coming years, can we expect major technological advances that will lead to more discoveries using the transit and the RV method? At the current rate of use, the TESS spacecraft could still last and explore the sky for decades. It will be able to find planets on larger orbital periods. Its ESA's successor, PLATO (Rauer et al. 2014), will be able to observe continuously for longer periods, increasing the chances of finding Earth-like planets around Sun-like stars. To date, the CHEOPS space telescope (Benz et al. 2021) is refining the radii of known transiting planets, while recovering the orbital period of long-period planets with two non-consecutive transits seen in TESS photometry (Osborn et al. 2022), expanding our "horizon". JWST (Gardner et al. 2023) is carrying out deep investigations of the planetary atmospheres in unprecedented detail to measure their composition. The European Space Agency is building ARIEL, a space telescope that will perform a large-scale survey of the chemistry of exoplanet atmospheres (Tinetti et al. 2018).

But what about the future of Doppler observations? Remember that to discover an Earth-mass planet at 1 au around a sun-like star we need a precision of about 9 $\mathrm{cm\,s^{-1}}$. Current spectrographs are limited to a Doppler precision of about 50-100 $\mathrm{cm\,s^{-1}}$, and only ESPRESSO has been shown to be capable of approaching 10 $\mathrm{cm\,s^{-1}}$ (González Hernández et al. 2018). Therefore, in order to find small planets at large distances from their star, the precision of measurements must improve by an order of magnitude. With the current generation of spectrographs, the RV technique is limited by both the precision and stability of velocity measurements, as well as by stellar activity. ESO's ELT will be a revolutionary ground-based telescope with a 39-m main mirror, becoming the world's largest visible and infrared light telescope. The ELT's ultra-stable spectrographs, taking advantage of the telescope's large collecting power, will achieve measurement precision of about 1 $\mathrm{cm\,s^{-1}}$ over periods ranging from minutes to years.

A bright future for exoplanet science lies ahead. The discoveries made so far have revolutionized and challenged our understanding of planets and planetary systems – and this may only be the beginning. To phrase it with the words of Artie Hatzes:

Expect the unexpected!

Chapter 10

List of Publications

Publications included in this work:

1. **E. Goffo** et al., 2023, *Company for the ultra-short period sub-Earth GJ 367 b: discovery of two additional low-mass planets at 11.5 and 34 days*, ApJL, 955, L3.
2. **E. Goffo** et al., 2024, *TOI-4438 b: a transiting mini-Neptune amenable to atmospheric characterization*, Accepted for publication, A&A.
3. M. Mallorquin, **E. Goffo**, et al., 2023, *TOI-1801b: a temperate super-earth around a young M5 dwarf*, A&A, 680, A76.
4. T. G. Wilson, **E. Goffo** et al., 2021, *A Different-Twin Pair of Sub-Neptunes orbiting TOI-1064 Discovered by TESS, Characterised by CHEOPS and HARPS*, MNRAS, 511, 1043.
5. E. W. Günther, **E. Goffo** et al., 2024, *A new mass and radius determination of the ultra-short period planet K2-106b and the fluffy planet K2-106c*, Accepted for publication, MNRAS.
6. H. L. M. Osborne, V. Van Eylen, **E. Goffo** et al., 2023, *TOI-544 b: a potential water-world inside the radius valley in a two-planet system*, MNRAS, 527, 11138.

Other publications by the author, not included in this thesis:

7. I. Y. Georgieva, C. M. Persson, **E. Goffo**, et al., 2023, *TOI-733 b: a planet in the small-planet radius valley orbiting a Sun-like star*, A&A, 674, A117.
8. Van Eylen, V., et al., including **E. Goffo**, 2021, *Masses and compositions of three small planets orbiting the nearby M dwarf L231-32 (TOI-270) and the M dwarf radius valley*, MNRAS, 507, 2154.
9. Georgieva, I. Y. et al., including **E. Goffo**, 2021, *Hot planets around cool stars - two short-period mini-Neptunes transiting the late K-dwarf TOI-1260*, MNRAS, 505, 4684.
10. K. W. F. Lam et al., including **E. Goffo**, 2021,*GJ 367b: A Dense Ultra-Short Period Sub-Earth planet transiting a nearby M dwarf*, Science, 374, 1271.
11. A. P. Hatzes, et al., including **E. Goffo**, 2021, *A Radial Velocity Study of the Planetary System of Mensae: Improved Planet Parameters for π Mensae c and a Third Planet on a 125-d Orbit*, AJ, 163, 223.
12. A. M. S. Smith, et al., including **E. Goffo**, 2021, *K2-99 revisited: a non-inflated warm Jupiter, and a temperate giant planet on a 523-d orbit*

around a subgiant, MNRAS, 510, 5035.

13. J. Subjak, et al., including **E. Goffo**, 2022, *TOI-1268b: the youngest, hot, Saturn-mass transiting exoplanet*, A&A, 662, A107.
14. O. Barragán, et al., including **E. Goffo**, 2022, *The young HD 73583 (TOI-560) planetary system: Two 10-M mini-Neptunes transiting a 500-Myr-old, bright, and active K dwarf*, MNRAS, 514, 1606.
15. N. Zicher, et al., including **E. Goffo**, 2022, *One year of AU Mic with HARPS: I – measuring the masses of the two transiting planets*, MNRAS, 512, 3060.
16. Q. H. Tran et al., including **E. Goffo**, 2022, *TOI-1670 b and c: An Inner Sub-Neptune with an Outer Warm Jupiter Unlikely to have Originated from High-Eccentricity Migration*, AJ, 163, 225.
17. L. M. Serrano, et al., including **E. Goffo**, 2022, *A low-eccentricity migration pathway for a 13-h-period Earth analogue in a four-planet system*, Nature Astronomy, 6, 736.
18. P. Kabàth, et al., including **E. Goffo**, 2022, *TOI-2046b, TOI-1181b and TOI-1516b, three new hot Jupiters from TESS: planets orbiting a young star, a subgiant and a normal star*, MNRAS, 513, 5955.
19. C. M. Persson, et al., including **E. Goffo**, 2022, *TOI-2196 b: Rare planet in the hot Neptune desert transiting a G-type star*, A&A, 666, A184.
20. R. Luque, et al., including **E. Goffo**, 2022, *Precise mass determination for the keystone sub-Neptune planet transiting the mid-type M dwarf G 9-40*, A&A, 666, A154.
21. J. Orell-Miquel, et al., including **E. Goffo**, 2022, *HD 191939 revisited: New and refined planet mass determinations, and a new planet in the habitable zone*, A&A, 669, A40.
22. F. Murgas, et al., including **E. Goffo**, 2022, *HD 20329b: An ultra-short-period planet around a solar-type star found by TESS*, A&A, 668, A158.
23. E. Knudstrup, et al., including **E. Goffo**, 2023, *Radial velocity confirmation of a hot super-Neptune discovered by TESS with a warm Saturn-mass companion*, MNRAS, 519, 4.
24. E. Knudstrup, et al., including **E. Goffo**, 2023, *The low density, hot Jupiter TOI-640 b is on a polar orbit*, A&A, 671, A164
25. A. Bonfanti et al., including **E. Goffo**, 2023, *TOI-1055 b: Neptunian planet characterized with HARPS, TESS, and CHEOPS*, A&A, 671, L8
26. R. Luque et al., including **E. Goffo**, 2023, *A resonant sextuplet of sub-Neptunes transiting the bright star HD 110067*, Nature, 623, 932.
27. M. Zhang et al., including **E. Goffo**, 2024, *GJ 367b is a dark, hot, airless sub-Earth*, ApJL, 961, L44.

Acknowledgements

The me of 10 years ago would probably never have imagined doing a PhD in astrophysics. But here I am. It looks like I made it! It has been an incredible and winding journey, but it would not have been the same without all of you and all the experiences we shared. I have to be honest. I felt a bit overwhelmed writing this acknowledgments section. Because there are so many people to whom I should say 'thank you'. So, this is for you.

Thank you to those who have shown me the bright and dark side of science.

Thank you to those who have stood by me through thick and thin.

Thank you to those who have given me valuable scientific and life lessons.

Thank you to those with whom I shared countless laughs.

Thank you to those who made me feel at home.

Thank you to those with whom I shared good food and good talks.

Thank you to all the extraordinary people from all over the world I have met.

Thank you to those who give me continuous and unconditional support.

Thank you to all those who have believed in me.

Thank you to those who have helped to make these last few years unforgettable.

Ringraziamenti

La me stessa di 10 anni fa probabilmente non avrebbe mai immaginato di fare un dottorato in astrofisica. Ma eccomi qui. Sembra che ce l'abbia fatta! È stato un viaggio incredibile e tortuoso, ma non sarebbe stato lo stesso senza tutti voi e le esperienze che abbiamo condiviso. Devo essere sincera. Mi sono sentita un po' sopraffatta nello scrivere questa sezione di ringraziamenti. Perchè ci sono così tante persone a cui dovrei dire "grazie". Quindi, questo è per voi.

Grazie a coloro che mi hanno mostrato il lato bello e quello oscuro della scienza.

Grazie a coloro che mi hanno sostenuto nel bene e nel male.

Grazie a coloro che mi hanno dato preziose lezioni scientifiche e di vita.

Grazie a coloro con cui ho condiviso innumerevoli risate.

Grazie a coloro che mi hanno fatto sentire a casa.

Grazie a coloro con i quali ho condiviso buon cibo e buone chiacchierate.

Grazie alle persone straordinarie che ho incontrato in giro per il mondo.

Grazie a coloro che mi danno un sostegno continuo e incondizionato.

Grazie a tutti coloro che hanno creduto in me.

Grazie a coloro che hanno contribuito a rendere indimenticabili questi anni.

Bibliography

Adams, E. R., Jackson, B., Endl, M., et al. 2017, AJ, 153, 82

Adibekyan, V., Dorn, C., Sousa, S. G., et al. 2021, Science, 374, 330

Aguichine, A., Mousis, O., Devouard, B., & Ronnet, T. 2020, ApJ, 901, 97

Aigrain, S. & Foreman-Mackey, D. 2023, ARA&A, 61, 329

Aigrain, S., Llama, J., Ceillier, T., et al. 2015, MNRAS, 450, 3211

Anderson, D. R., Cameron, A. C., Hellier, C., et al. 2010, The Astrophysical Journal, 726, L19

Armstrong, D. J., Lopez, T. A., Adibekyan, V., et al. 2020, Nature, 583, 39

Baglin, A., Auvergne, M., Barge, P., et al. 2009, in Transiting Planets, ed. F. Pont, D. Sasselov, & M. J. Holman, Vol. 253, 71–81

Baglin, A., Auvergne, M., Boisnard, L., et al. 2006, in 36th COSPAR Scientific Assembly, Vol. 36, 3749

Barragan, O. 2018, PhD thesis, Universita degli studi di Torino

Barragán, O., Aigrain, S., Rajpaul, V. M., & Zicher, N. 2022, MNRAS, 509, 866

Barragán, O., Gandolfi, D., & Antoniciello, G. 2019, MNRAS, 482, 1017

Barragán, O., Gandolfi, D., Dai, F., et al. 2018, A&A, 612, A95

Batalha, N. M., Rowe, J. F., Bryson, S. T., et al. 2013a, ApJS, 204, 24

Batalha, N. M., Rowe, J. F., Bryson, S. T., et al. 2013b, ApJS, 204, 24

Beaulieu, J.-P., Bennett, D. P., Fouqué, P., et al. 2006, Nature, 439, 437440

Benz, W., Broeg, C., Fortier, A., et al. 2021, Experimental Astronomy, 51, 109

Binzel, R. P. 2006, Minor Planet Bulletin, 33, 106

Boccaletti, A. 2011, in Astronomical Society of the Pacific Conference Series, Vol. 450, Molecules in the Atmospheres of Extrasolar Planets, ed. J. P. Beaulieu, S. Dieters, & G. Tinetti, 163

Bond, I. A., Udalski, A., Jaroszyński, M., et al. 2004, ApJ, 606, L155

Borucki, W. J., Koch, D., Basri, G., et al. 2010, Science, 327, 977

Borucki, W. J., Koch, D. G., Basri, G., et al. 2011, ApJ, 736, 19

Brown, T. M. 2003, The Astrophysical Journal Letters, 593, L125

Caballero, J. A., Guàrdia, J., López del Fresno, M., et al. 2016, in Society of Photo-Optical Instrumentation Engineers (SPIE) Conference Series, Vol. 9910, Observatory Operations: Strategies, Processes, and Systems VI, ed. A. B. Peck, R. L. Seaman, & C. R. Benn, 99100E

Cameron, A. C. 2016, Extrasolar Planetary Transits, ed. V. Bozza, L. Mancini, & A. Sozzetti (Cham: Springer International Publishing), 89–131

Campbell, B., Walker, G. A. H., & Yang, S. 1988, The Astrophysical Journal, 331, 902

Charbonneau, D., Berta, Z. K., Irwin, J., et al. 2009, Nature, 462, 891

Charbonneau, D., Brown, T. M., Latham, D. W., & Mayor, M. 2000, The Astrophysical Journal Letters, 529, L45

Claret, A. 2018, Limb and gravity-darkening coefficients for the TESS satellite

Claret, A. 2018, VizieR Online Data Catalog

Collier Cameron, A., Ford, E. B., Shahaf, S., et al. 2021, MNRAS, 505, 1699

Collier Cameron, A. & Jardine, M. 2018, MNRAS, 476, 2542

Cosentino, R., Lovis, C., Pepe, F., et al. 2012, in Society of Photo-Optical Instrumentation Engineers (SPIE) Conference Series, Vol. 8446, Ground-based and Airborne Instrumentation for Astronomy IV, ed. I. S. McLean, S. K. Ramsay, & H. Takami, 84461V

Cretignier, M., Dumusque, X., Allart, R., Pepe, F., & Lovis, C. 2020, A&A, 633, A76

Dai, F., Howard, A. W., Batalha, N. M., et al. 2021, AJ, 162, 62

Dai, F., Masuda, K., Winn, J. N., & Zeng, L. 2019, ApJ, 883, 79

Demory, B.-O., Gillon, M., de Wit, J., et al. 2016, Nature, 532, 207209

Dullemond, C. P. & Monnier, J. D. 2010, ARA&A, 48, 205

Dumusque, X., Boisse, I., & Santos, N. C. 2014, ApJ, 796, 132

Dumusque, X., Cretignier, M., Sosnowska, D., et al. 2021, A&A, 648, A103

Evans, C., Puech, M., Afonso, J., et al. 2015, arXiv e-prints, arXiv:1501.04726

Fulton, B. J., Petigura, E. A., Howard, A. W., et al. 2017, The Astronomical Journal, 154, 109

Gandolfi, D., Barragán, O., Livingston, J. H., et al. 2018, Astronomy & Astrophysics, 619, L10

Gardner, J. P., Mather, J. C., Abbott, R., et al. 2023, PASP, 135, 068001

Gaudi, B. S., Stassun, K. G., Collins, K. A., et al. 2017, Nature, 546, 514518

Gelman, A., Carlin, J. B., Stern, H. S., & Rubin, D. B. 2004, Bayesian Data Analysis, 2nd edn. (Chapman and Hall/CRC)

Goffo, E., Chaturvedi, P., Murgas, F., et al. 2024, arXiv e-prints, arXiv:2403.09833

Goffo, E., Gandolfi, D., Egger, J. A., et al. 2023, ApJ, 955, L3

González Hernández, J. I., Pepe, F., Molaro, P., & Santos, N. C. 2018, in Handbook of Exoplanets, ed. H. J. Deeg & J. A. Belmonte, 157

Greene, T., Batalha, N., Bean, J., et al. 2019, BAAS, 51, 61

Guenther, E. W., Barragán, O., Dai, F., et al. 2017, A&A, 608, A93

Guenther, E. W., Goffo, E., Sebastian, D., et al. 2024, A new mass and radius determination of the ultra-short period planet K2-106b and the fluffy planet K2-106c

Gupta, A. & Schlichting, H. E. 2019, Monthly Notices of the Royal Astronomical Society, 487, 24

Gupta, A. & Schlichting, H. E. 2021, MNRAS, 504, 4634

Hall, J. C. 2008, Living Reviews in Solar Physics, 5, 2

Hastings, W. K. 1970, Biometrika, 57, 97

Hatzes, A. P. 2016, The Radial Velocity Method for the Detection of Exoplanets, ed. V. Bozza, L. Mancini, & A. Sozzetti (Cham: Springer International Publishing), 3–86

Hatzes, A. P. 2019, The Doppler Method for the Detection of Exoplanets

Hatzes, A. P., Cochran, W. D., Endl, M., et al. 2003, The Astrophysical Journal, 599, 1383

Hatzes, A. P., Dvorak, R., Wuchterl, G., et al. 2010, A&A, 520, A93

Hatzes, A. P., Fridlund, M., Nachmani, G., et al. 2011, ApJ, 743, 75

Haywood, R. 2017, in American Astronomical Society Meeting Abstracts, Vol. 229, American Astronomical Society Meeting Abstracts #229, 320.06

Haywood, R. D., Collier Cameron, A., Queloz, D., et al. 2014, MNRAS, 443, 2517

Henry, G. W., Marcy, G. W., Butler, R. P., & Vogt, S. S. 2000, ApJ, 529, L41

Hogg, D. W. & Foreman-Mackey, D. 2018, ApJS, 236, 11

Howell, S. B., Sobeck, C., Haas, M., et al. 2014, PASP, 126, 398

Huang, C. X., Burt, J., Vanderburg, A., et al. 2018, The Astrophysical Journal, 868, L39

Jenkins, J. M., Twicken, J. D., McCauliff, S., et al. 2016, in Proc. SPIE, Vol. 9913, Software and Cyberinfrastructure for Astronomy IV, 99133E

Kempton, E. M. R., Bean, J. L., Louie, D. R., et al. 2018, PASP, 130, 114401

Kipping, D. M. 2013, Monthly Notices of the Royal Astronomical Society, 435, 2152

Kipping, D. M., Bastien, F. A., Stassun, K. G., et al. 2014, The Astrophysical Journal Letters, 785, L32

Lam, K. W. F., Csizmadia, S., Astudillo-Defru, N., et al. 2021, Science, 374, 1271

Lecavelier des Etangs, A. & Lissauer, J. J. 2022, New A Rev., 94, 101641

Lee, E. J. & Chiang, E. 2017, The Astrophysical Journal, 842, 40

Lovis, C. & Pepe, F. 2007, A&A, 468, 1115

Mallorquín, M., Goffo, E., Pallé, E., et al. 2023, A&A, 680, A76

Mandel, K. & Agol, E. 2002, The Astrophysical Journal Letters, 580, L171

Mao, S. & Paczynski, B. 1991, ApJ, 374, L37

Marcy, G. W., Isaacson, H., Howard, A. W., et al. 2014, ApJS, 210, 20

Marois, C., Macintosh, B., Barman, T., et al. 2008, Science, 322, 1348

Marois, C., Zuckerman, B., Konopacky, Q. M., Macintosh, B., & Barman, T. 2010, Nature, 468, 1080

Mayor, M., Pepe, F., Queloz, D., et al. 2003, The Messenger, 114, 20

Mayor, M. & Queloz, D. 1995, Nature, 378, 355

Metropolis, N., Rosenbluth, A. W., Rosenbluth, M. N., Teller, A. H., & Teller, E. 1953, J. Chem. Phys., 21, 1087

Millholland, S. C. & Spalding, C. 2020, The Astrophysical Journal, 905, 71

Mocquet, A., Grasset, O., & Sotin, C. 2014, Philosophical Transactions of the Royal Society of London Series A, 372, 20130164

Mulders, G. D., Pascucci, I., Apai, D., Frasca, A., & Molenda-Żakowicz, J. 2016, AJ, 152, 187

Murdoch, K. A., Hearnshaw, J. B., & Clark, M. 1993, The Astrophysical Journal, 413, 349

Nagel, E., Czesla, S., Kaminski, A., et al. 2023, A&A, 680, A73

Narita, N., Fukui, A., Kusakabe, N., et al. 2019, Journal of Astronomical Telescopes, Instruments, and Systems, 5, 015001

Nicholson, B. A. & Aigrain, S. 2022, MNRAS, 515, 5251

Osborn, H. P., Bonfanti, A., Gandolfi, D., et al. 2022, A&A, 664, A156

Osborne, H. L. M., Van Eylen, V., Goffo, E., et al. 2024, MNRAS, 527, 11138

Owen, J. E. & Wu, Y. 2017, The Astrophysical Journal, 847, 29

Pepe, F., Cameron, A. C., Latham, D. W., et al. 2013, Nature, 503, 377

Pepe, F., Cristiani, S., Rebolo, R., et al. 2021, A&A, 645, A96

Pepe, F. A., Cristiani, S., Rebolo Lopez, R., et al. 2010, in Society of Photo-Optical Instrumentation Engineers (SPIE) Conference Series, Vol. 7735, Ground-based and Airborne Instrumentation for Astronomy III, ed. I. S. McLean, S. K. Ramsay, & H. Takami, 77350F

Perryman, M. 2011, *The Exoplanet Handbook* (Cambridge)

Petrovich, C., Deibert, E., & Wu, Y. 2019, The Astronomical Journal, 157, 180

Petrovich, C., Deibert, E., & Wu, Y. 2019, AJ, 157, 180

Pollacco, D. L., Skillen, I., Collier Cameron, A., et al. 2006, Publications of the Astronomical Society of the Pacific, 118, 1407

Pu, B. & Lai, D. 2019, Monthly Notices of the Royal Astronomical Society, 488, 35683587

Quirrenbach, A., Amado, P. J., Caballero, J. A., et al. 2014, in Proc. SPIE, Vol. 9147, Ground-based and Airborne Instrumentation for Astronomy V, 91471F

Quirrenbach, A., Amado, P. J., Ribas, I., et al. 2018, in Society of Photo-Optical Instrumentation Engineers (SPIE) Conference Series, Vol. 10702, Ground-based and Airborne Instrumentation for Astronomy VII, 107020W

Rajpaul, V., Aigrain, S., Osborne, M. A., Reece, S., & Roberts, S. 2015, MNRAS, 452, 2269

Rajpaul, V. M., Aigrain, S., & Buchhave, L. A. 2020, MNRAS, 492, 3960

Rasmussen, C. E. & Williams, C. K. I. 2006, Gaussian Processes for Machine Learning

Rauer, H., Catala, C., Aerts, C., et al. 2014, Experimental Astronomy, 38, 249

Reinhardt, C., Meier, T., Stadel, J., Otegi, J., & Helled, R. 2022, arXiv e-prints, arXiv:2204.04925

Reuyl, D. & Holmberg, E. 1943, The Astrophysical Journal, 97, 41

Ricker, G. R., Winn, J. N., Vanderspek, R., et al. 2015, Journal of Astronomical Telescopes, Instruments, and Systems, 1, 014003

Roberts, S., Osborne, M., Ebden, M., et al. 2013, Philosophical Transactions of the Royal Society A: Mathematical, Physical and Engineering Sciences, 371, 20110550

Rodríguez Martínez, R., Gaudi, B. S., Schulze, J. G., et al. 2023, AJ, 165, 97

Rodríguez Martínez, R., Gaudi, B. S., Schulze, J. G., et al. 2022, arXiv e-prints, arXiv:2208.07883

Rouan, D., Deeg, H. J., Demangeon, O., et al. 2011, ApJ, 741, L30

Sahu, K. C., Casertano, S., Bond, H. E., et al. 2006, Nature, 443, 534

Sanchis-Ojeda, R., Rappaport, S., Winn, J. N., et al. 2014, ApJ, 787, 47

Sanchis-Ojeda, R., Rappaport, S., Winn, J. N., et al. 2013, ApJ, 774, 54

Schlaufman, K. C., Lin, D. N. C., & Ida, S. 2010, ApJL, 724, L53L58

Seager, S. & Mallén-Ornelas, G. 2003, The Astrophysical Journal, 585, 1038

Sharma, S. 2017, Annual Review of Astronomy & Astrophysics, 55, 213

Silburt, A., Gaidos, E., & Wu, Y. 2015, The Astrophysical Journal, 799, 180

Singh, V., Bonomo, A. S., Scandariato, G., et al. 2022, A&A, 658, A132

Sinukoff, E., Howard, A. W., Petigura, E. A., et al. 2017, AJ, 153, 271

Smith, J. C., Stumpe, M. C., Van Cleve, J. E., et al. 2012, PASP, 124, 1000

Southworth, J. 2011, MNRAS, 417, 2166

Stevens, D. J. & Gaudi, B. S. 2013, PASP, 125, 933

Strand, K. A. 1943, Publications of the Astronomical Society of the Pacific, 55, 29

Struve, O. 1952, The Observatory, 72, 199

Stumpe, M. C., Smith, J. C., Catanzarite, J. H., et al. 2014, Publications of the Astronomical Society of the Pacific, 126, 100

Stumpe, M. C., Smith, J. C., Van Cleve, J. E., et al. 2012, PASP, 124, 985

Tinetti, G., Drossart, P., Eccleston, P., et al. 2018, Experimental Astronomy, 46, 135

Tingley, B., Bonomo, A. S., & Deeg, H. J. 2011, The Astrophysical Journal, 726, 112

van de Kamp, P. 1969, The Astronomical Journal, 74, 757

Van Eylen, V., Agentoft, C., Lundkvist, M. S., et al. 2018, arXiv:1710.05398 [astro-ph], arXiv: 1710.05398

Wilson, T. G., Goffo, E., Alibert, Y., et al. 2022, MNRAS, 511, 1043

Winn, J. N., Fabrycky, D., Albrecht, S., & Johnson, J. A. 2010, ApJ, 718, L145

Winn, J. N. & Fabrycky, D. C. 2015, Annual Review of Astronomy and Astrophysics, 53, 409

Wolszczan, A. & Frail, D. A. 1992, Nature, 355, 145

Zechmeister, M., Anglada-Escudé, G., & Reiners, A. 2014, A&A, 561, A59

Zechmeister, M. & Kürster, M. 2009, Astronomy & Astrophysics, 496, 577584

Zechmeister, M., Reiners, A., Amado, P. J., et al. 2018, Astronomy & Astrophysics, 609, A12

Zeng, L., Jacobsen, S. B., Sasselov, D. D., et al. 2019, Proceedings of the National Academy of Science, 116, 9723

Zeng, L., Sasselov, D. D., & Jacobsen, S. B. 2016, ApJ, 819, 127

Zhang, M., Hu, R., Inglis, J., et al. 2024, arXiv e-prints, arXiv:2401.01400

Zhu, W. & Dong, S. 2021, ARA&A, 59, 291